Suzaku Studies of Time Variable X-ray Spectra of Edge-On Active Galactic Nuclei

Takeshi Itoh

Department of Physics, School of Science, University of Tokyo,
7-3-1 Hongo, Bunkyo-ku, Tokyo 113-0033, Japan

Reprinted from the Thesis Submitted in
Partial Fulfillment of the Requirements
for the Degree of Doctor of Philosophy (Physics)
the University of Tokyo
December 2007

Abstract

In order to investigate the circum-nuclear environment of Active Galactic Nuclei (AGNs) in the local universe, we analyzed X-ray data of five type 2 Seyfert galaxies, taken with the *Suzaku* satellite in its Performance-Verification phase and in the cycle-1 Guest Observation phase. The selected AGNs, NGC 4388, Mkn 3, the Circinus galaxy, NGC 4945, and NGC 4258, all have water maser sources in their centers, and are known to harbor obscured active nuclei. Through the analysis of X-ray spectra and time variability utilizing the broad-band sensitivity of *Suzaku*, we successfully disentangled the observed X-ray emission (typically from a few keV to $\sim$ 100 keV) from each AGN into three components; (D) the highly absorbed intrinsic power-law emission; (R) the nuclear light reflected by a thick, cold material; and (S) the nuclear emission scattered by ionized matter. The origins of these components were identified in terms of the canonical Unified Scheme of AGNs.

We confirmed all the five nuclei to be obscured by considerable amounts of absorbing column, with equivalent hydrogen column densities of $N_{\rm H} = 10^{22.8-24.8}$ cm^{-2}. As a result, Component D can be observed only above $\sim$ 3–15 keV, and is strongly suffered from Compton scattering in two object where the absorbers are Compton-thick ($N_{\rm H} \gtrsim$ a few $\times$ 10^{24} cm^{-2}). Although the attenuation-corrected bolometric luminosity of the sample sources were found to distributes over a wide range as $L_{\rm bol} = 10^{41-44.5}$ erg s^{-1}, the spectral slope of Component D were found to be similar to one another, and to those of type 1 Seyfert galaxies. Component R was measured from at least four sources, more precisely than in any previous observation. It is characterized by three sub-components as; (R1) a hard "reflection" continuum observed in the energy range below $\sim$ 10 keV, accompanied by a sharp Fe-K edge; (R2) several narrow emission lines arising in neutral materials; and (R3) a spectral "hump" at energies around 20 keV, arising via Compton down-scattering of the primary X-ray photons. From both the spectral and time-variability aspects, these three features are consistent with originating in the same location, namely, a directly visible part of the circum-nuclear matter.

In two of our samples (NGC 4388 and Mrk 3), the strength of component R, with respect to the nuclear intrinsic emission (component D), $f_{\rm refl}$, have values as large as unity, which suggests that about 2π of the sky as seen from the central engine is covered by the reflector. Such a reflector with a large large covering factor can be readily identified with the putative "torus", introduced in the unification model of AGN. From both the time variability and energetics aspects, we found that the component D in one object (Circinus) should be identified with the nuclear light scattered by the obscuring material

into the line of sight, rather than the nuclear intrinsic emission. Such scattered-in photons are likely to dominate the hard X-ray emission, when the obscuring material covers a large solid angle as seen from the central source *and* our line of sight to the nucleus is blocked by the Compton-thick absorber. This in turn suggests the presence of putative "torus" with a large covering factor in Circinus.

We found that NGC 4945, another Compton-thick source, exhibits significant time variations in hard X-rays, showing that the contribution of scattered-in photons is much lower than in Circinus. This requires that the obscuring material do not have large covering factor to the central source. Furthermore, the value of $f_{\rm refl}$ have found to be smaller by about 2 orders of magnitude, compared to those in NGC 4388, Mrk 3, and Circinus. We also found that $f_{\rm refl}$ is smaller by more than an order of magnitude in NGC 4258, than in the three "thick torus" objects. Thus, the geometrically-thick torus is also unlikely in this source. Combining these facts, the obscuring material in NGC 4945 and NGC 4258 are likely to be localized to a limited solid angle (including our line of sight) around the nuclei. In other words, an inflated thick torus, as invoked in the simplest form of the Unified Scheme, is unlikely to be present in these objects.

Based on the intrinsic luminosity of the sample AGNs, as well as the geometry of the matter distribution as inferred above, we speculate that the accreting material assumes the putative toroidal shape, when the nucleus is in a gas-rich environment and hence the mass accretion rate is high. Then, the torus becomes at the same time the absorber for Component D, and the reflector for Component R. In contrast, when the nucleus is relatively gas-starved, the accreting matter is speculated to assume a geometrically-thin disk shape. This will suppress $f_{\rm refl}$, and the nuclear obscuration will occur only when our line of sight is grazing to the (possibly warped) thin disk.

Contents

1 INTRODUCTION **1**

2 REVIEW **5**

2.1 Active Galactic Nuclei and Their Properties 5

2.1.1 Active galactic nuclei 5

2.1.2 Observational classification of AGNs 6

2.1.3 Unified Scheme of AGNs 7

2.2 Supermassive Black Hole Hypothesis 10

2.2.1 Physical nature of AGNs 10

2.2.2 Eddington luminosity 11

2.2.3 Accretion disk models 12

2.2.4 Observational evidence for supermassive black holes 14

2.3 Mass Estimation 15

2.3.1 Estimation via stellar/gas motion 15

2.3.2 Reverberation mapping 16

2.3.3 Water maser 17

2.4 X-ray Spectral Properties of type 1 AGNs 19

2.4.1 Primary emission 19

2.4.2 Reflection components 20

2.4.3 Iron line 20

2.4.4 Warm absorbers 21

2.5 X-ray Spectral Properties of Obscured Seyferts 22

2.5.1 X-ray observation of hidden nuclei 22

2.5.2 Obscuration mechanism 23

2.5.3 Contribution to the cosmic X-ray background 24

2.5.4 Recent hard X-ray observations 25

3 INSTRUMENTATION
– The X-ray Observatory *Suzaku* – 29
3.1 Overview of the *Suzaku* Satellite . . . 29
3.2 X-Ray Telescope (XRT) . . . 31
3.3 X-ray Imaging Spectrometer (XIS) . . . 35
3.4 Hard X-ray Detector (HXD) . . . 39
3.4.1 System configuration of the HXD . . . 39
3.4.2 HXD-S . . . 41
3.4.3 HXD-AE . . . 43
3.4.4 HXD-DE . . . 47
3.5 In-orbit Performance of the HXD-PIN . . . 48
3.5.1 Energy scale . . . 50
3.5.2 Energy threshold . . . 51
3.5.3 Background reduction . . . 51
3.5.4 Response matrices . . . 54
3.6 In-orbit Performance of the HXD-GSO . . . 57
3.6.1 Energy scale . . . 57
3.6.2 Background reduction . . . 58
3.6.3 Energy response . . . 59
3.7 In-orbit Backgrounds of the HXD . . . 61
3.7.1 Common properties of non X-ray background of the HXD . . . 62
3.7.2 Background modeling of the HXD-PIN . . . 63
3.7.3 Background modeling of the HXD-GSO . . . 64
3.7.4 Comparison with other hard X-ray mission . . . 67

4 OBSERVATION 71
4.1 *Suzaku* Observations . . . 71
4.1.1 Performance verification observations . . . 71
4.1.2 Guest observations . . . 72
4.2 Data Reduction . . . 74
4.2.1 XIS data reduction . . . 74
4.2.2 HXD data reduction . . . 75
4.3 Target Selection . . . 76
4.4 Observations of Individual Targets . . . 79
4.5 Previous Studies on Individual Targets . . . 79

4.5.1 NGC 4388 79
4.5.2 Markarian 3 82
4.5.3 The Circinus galaxy 83
4.5.4 NGC 4945 84
4.5.5 NGC 4258 85

5 ANALYSIS AND RESULTS 87

5.1 NGC 4388 87
5.1.1 XIS data analysis 87
5.1.2 HXD data analysis 88
5.1.3 Broad-band spectrum 90
5.1.4 Baseline Continuum model of obscured AGNs 90
5.1.5 Spectral fitting 92
5.1.6 Derived parameters 93
5.1.7 Time variability 94
5.2 Mrk 3 101
5.2.1 XIS data analysis 101
5.2.2 HXD data analysis and broad-band spectrum 101
5.2.3 Spectral fitting 103
5.2.4 Derived parameters 105
5.2.5 Time variability 106
5.3 The Circinus Galaxy 111
5.3.1 XIS data analysis 111
5.3.2 HXD data analysis and broad-band spectrum 112
5.3.3 Spectral fitting below 10 keV 113
5.3.4 Wideband spectral fitting 118
5.3.5 Time variability 119
5.4 NGC 4945 124
5.4.1 XIS data analysis 124
5.4.2 HXD data analysis and broad-band spectrum 124
5.4.3 Spectral fitting with BC + lines model 127
5.4.4 Spectral fitting with BC + ionized plasma models 127
5.4.5 Derived parameters 129
5.4.6 Time variability 130
5.5 NGC 4258 135

5.5.1 XIS data analysis 135
5.5.2 HXD data analysis and broad-band spectrum 135
5.5.3 Spectral fitting 137
5.5.4 Time variability 138

6 DISCUSSION 145

6.1 Summary of Results 145
6.1.1 Spectral components observed in our sample objects 145
6.1.2 Time variability of the emission components 147
6.1.3 The Unified Scheme of AGNs 148
6.2 Reflector with Various Covering Factors 150
6.2.1 Reflection fraction vs time variability 150
6.2.2 Compton scattered-out/in through the obscuring material 154
6.3 Prospects 158

7 CONCLUSION 161

References 165

Chapter 1

INTRODUCTION

Active galactic nuclei (AGNs), which reside in the center of external galaxies, emit electromagnetic radiation energies as large as $10^{39} - 10^{48}$ erg s^{-1}, from a region only within ~ 1 pc. Such a huge amount of radiation energy can be explained only in terms of gravitational energy release via mass accretion onto a supermassive black hole. An integrated emission from numerous AGNs, located at large cosmological redshifts, are thought to be the origin of the Cosmic X-ray Background (CXB) which has remained a mystery since the early 1960's.

Although AGNs show complicated spectral properties, and hence are classified in various ways into various categories according to their spectral characteristics, there is a fairly well established view, called "Unified Scheme" (e.g., Antonucci and Miller 1985; Antonucci 1993), to explain the AGN variety. In addition to the two obvious parameters, namely the black hole mass and the mass accretion rate, this scheme employs two fundamental parameters which are radio loudness and our viewing direction to the accretion plane. When the nuclear emission is directly visible due to a relatively pole-on viewing, the object is called a "type 1" AGN, while it is classified as a "type 2" AGN when our line of sight is blocked by some part of the accreting material (often assumed to have a toroidal shape around the nucleus) due to a relatively edge-on viewing angle, and hence the intrinsic nuclear emission is considerably obscured. This scheme can explain much of the observational differences among AGNs of various kinds. However, its validity and the nature of the putative torus should still be examined.

X-ray observations of the obscured (type 2) AGNs are crucial, at least from the following three respects. Firstly, such observations enable us to test the validity of the Unified Scheme. Secondly, we can utilize the X-ray signals to diagnose the general environment of accreting massive black holes. In such objects, the obscuration of the glaring nuclear

X-ray emission allows us to observe and study secondary spectral components produced by circumnuclear regions, which would be outshined by the nuclear radiation in type 1 sources. Particularly interesting is to study "reflection" of the nuclear X-rays off the circumnuclear matter, which may well be some part of the accretion flow. In type 2 AGNs, such circumnuclear materials, neutral or ionized, will manifest themselves via Compton scattering of the primary nuclear X-rays, and via copious X-ray lines due to fluorescence. Finally, many X-ray observations have revealed the presence of a large number of heavily obscured AGNs in the local universe, so that much of the spectral peak the CXB at around 30 keV should be produced by such objects. Therefore, measuring precisely the energy spectra of obscured AGNs by itself has an important implication to the synthesis models of the CXB, even though the CXB modeling is beyond the scope of the present thesis.

Much of the pioneering works on the obscured X-ray AGNs have been conducted by Japanese astrophysicists since 1980's, making the best use of the *Ginga* and *ASCA* satellites. The *Chandra* and *XMM-Newton* satellites promoted the study in further details, but their limited observable energy range ($\sim 0.3 - 10$ keV) often limit the study mainly to the reprocessed low-energy signals, leaving the primary X-ray radiation sometimes undetectable. The *BeppoSAX* satellite in contrast, with its sensitivity covering hard X-rays up to ~ 100 keV, succeeded in measuring the intrinsic nuclear emission even in the extremely obscured cases, and demonstrated the general presence of the primary and reprocessed X-ray components. However, it lacked sensitivity at lower energies where the signal provide a crucial information on the reprocessing material.

The *Suzaku* satellite is the most promising X-ray mission to reveal the nature of the obscured AGNs, since it has high throughput throughout the wide energy range of $\sim 0.3 - 200$ keV, together with excellent spectroscopic capability in the $0.5 - 10$ keV range where a number of atomic lines and edges are present. It is expected to be capable of spectrally disentangling all the emission components, and of precisely measuring their parameters. The unprecedented high sensitivity for hard X-rays, realized by the Hard X-ray Detector (HXD), would also provide information on hard X-ray variability of obscured AGNs. Given these, we analyze in the present thesis X-ray spectra and time variability of five edge-on AGNs, all of which are water maser sources.

In Chapter 2, we review the properties of AGNs with emphasis on the obscured sources. Chapter 3 describes detailed performance of the *Suzaku* satellite, including the HXD instrumentation to which the author made a big contribution. Chapter 4 briefly introduces our sample. Our detailed analysis and the results are presented in Chapter 5. Then, we

discuss the obtained results in Chapter 6, followed by a brief summary and conclusion in Chapter 7.

Chapter 2

REVIEW

2.1 Active Galactic Nuclei and Their Properties

2.1.1 Active galactic nuclei

The universe is made up of over a hundred billion galaxies, with many of them containing in turn more than a hundred billion stars each. A few percent of the galaxies are called "active" galaxies, and possess an amazing source of energy at its nucleus (e.g., Ormes 1996), which generates a power comparable to that emitted by a thousand normal galaxies. Direct imaging observations revealed that the huge optical luminosity of an active galaxy is mostly emitted from an extremely small region at the galaxy center (or "nucleus"). Such nuclei are called "active galactic nuclei (AGNs)".

In general, AGNs emit not only visible light, but also electromagnetic radiation over a wide spectral range from radio to γ-rays. In particular, AGNs emits huge luminosities in the X-ray band. Their multi-frequency emission spectra indicates that the emission mechanism of AGNs is totally different from that of ordinary stars. Although an AGN is usually too small to be resolved by ordinary astronomical techniques, most AGNs are quite variable in X-ray and optical frequencies, on time scales of hours, days, to years. This allows us to infer that an AGN has a size comparable to the Solar System. These facts lead us to the hypothesis, which is now widely believed, that the massive black holes are present in the central power-houses, and that the accretion of matter onto such black holes is the origin of their high radiation power (§2.2).

In addition to the electro-magnetic radiation, an AGN sometimes generates collimated jets extending far beyond the host galaxy; the jet is sometimes terminated at shocks and inflates to a lobe (e.g., Isobe et al. 2002), which extends many tens of kpc. Since such a

lobe consists mainly of relativistic particles and tangled magnetic fields both supplied by the jet, a strong synchrotron radio emission is observed. The integrated stellar light from a galaxy is emitted mainly in the IR/optical bands, with a minor ($\sim 10^{-4}$) fraction and relatively little of it is in the X-ray band. Furthermore, the most rapid time variability in AGN is observed in the X-ray to γ-ray bands. Therefore, X-ray observations are an extremely important tool to "look" inside the active galaxies.

2.1.2 Observational classification of AGNs

The great majority of all AGNs display strong emission lines in their optical UV, and even X-ray spectra. Only relatively rare objects (e.g., BL lac object, Figure 2.1) exhibit no lines at all, or have lines whose equivalent widths are very small. Indeed, simple properties of the optical emission lines including Lyα, Hα and Hβ, etc. have allowed the construction of a rather well-defined AGN classification system.

AGNs are roughly categorized based on their luminosities. Quasars are the most powerful AGNs with the B-band magnitude $M_{\rm B} < -23$ mag (Greenstein and Schmidt 1964). In X-rays, where $\sim 10\%$ of the bolometric luminosity of a typical AGN is emitted, they exhibit a typical luminosity in the range of 10^{44-47} erg s^{-1}. The other extreme class of AGNs are Low luminosity AGNs (LLAGNs), namely those with the Hα luminosity of $< 10^{40}$ erg s^{-1}, corresponding to a bolometric luminosity of $\lesssim 10^{42}$ erg s^{-1}.

Independently, on the spectral grounds, AGNs are classified into several categories as shown in Figure 2.1. They are first divided into "radio loud" and "radio quiet" objects by their activity and/or luminosity in the radio band. About 10% of AGNs are radio loud, and the jet structure most frequently appears in their radio VLBI images. Radio quiet AGNs which are not accompanied by jet structure, include Seyfert galaxies (Seyfert 1943) and Low Ionization Nuclear Emission Regions (LINERs; Heckman 1980). Based on the intensity ratios among prominent optical emission lines, Seyferts are usually defined as those with [OI] ≥ 0.08 Hα, [NII] ≥ 0.6 Hα, [SII] ≥ 0.4 Hα, and [OIII]/H$\beta \geq 3$. In control, LINERs are characterized by lower-ionization lines, with [OI] ≥ 0.17 Hα, [NII] $\geq$ 0.6 Hα, [SII] ≥ 0.4 Hα, and [OIII]/H$\beta < 3$ (Veilleux and Osterbrock 1987).

Seyfert galaxies are less luminous than quasars, with an X-ray luminosity in the range of 10^{43-45} erg s^{-1}. They are further categorized into two types; type 1 (Seyfert 1s) and type 2 (Seyfert 2s). Seyfert 1s show extremely broad permitted-emission lines with the line widths (in terms of Doppler velocities) reaching $\sim 1,000$–25,000 km s^{-1}, while Seyfert 2s show only narrow ones with a few hundred km s^{-1}. X-ray observation revealed that

Seyfert 2s suffer from strong absorptions, while Seyfert 1s show weak/no absorptions.

Radio galaxies are radio-loud counterparts of Seyfert galaxies, with a similar X-ray luminosity range of 10^{43-45} erg s^{-1}. X-ray spectroscopy also showed that some of those galaxies suffer from absorption, while the other do not. In X-ray range, the jet emission of radio galaxies is not so strong and the emission from the nucleus is the main contributer, as Seyfert galaxies. In BL Lac objects and Optically Violently Variable (OVV) quasars, on the other hands, the jet emission overwhelms the nuclear emission over the all frequency ranges. These objects are called blazers.

Generally, except for quasars, the radio-quiet AGNs are found in spiral galaxies, while the radio-loud AGNs are in elliptical galaxies or S0 galaxies. Quasars often reside in the elliptical galaxies, even if they are radio-quiet.

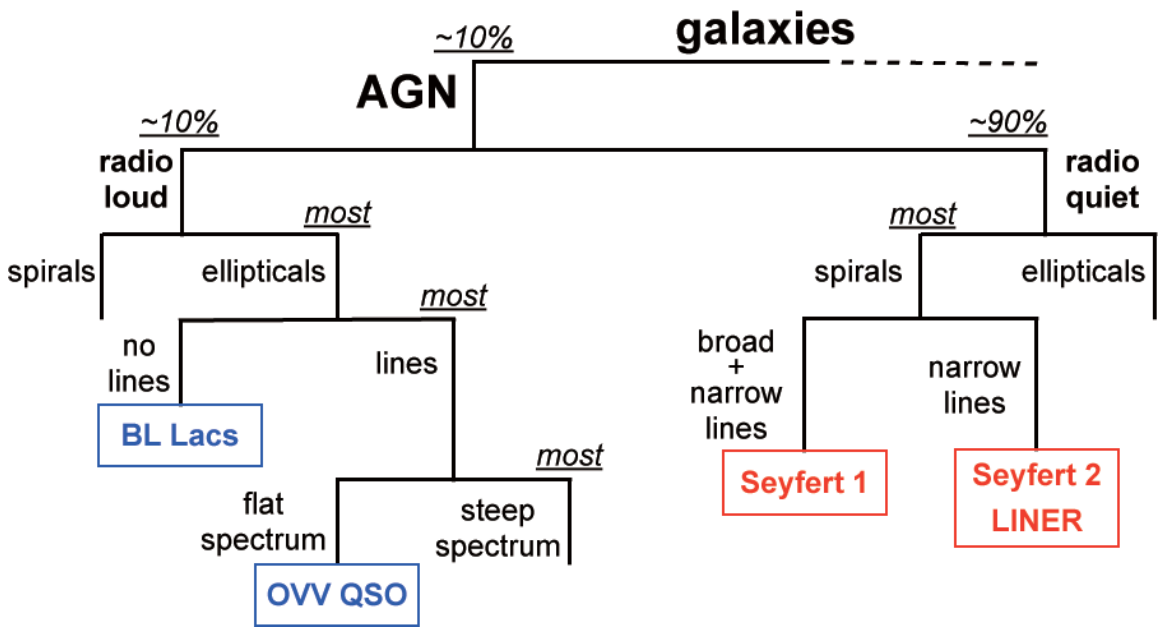

Figure 2.1: A classification of AGNs. About a few % of galaxies have active nuclei at their center.

2.1.3 Unified Scheme of AGNs

Intensive studies to unify AGNs have successfully impose some order on many types of AGNs (e.g., Antonucci 1993). As summarized in §2.1.2, the optical emission line spectra in some AGNs have both narrow lines (with widths corresponding to velocities of several hundred km s^{-1}) and broad line (with widths of up to 10^4 km s^{-1}), while those in other AGNs have only the narrow lines. This difference itself leads to the sub-class of the AGN :

type 1 and type 2. Current picture of the Unified Scheme assumes that type 1 and type 2 AGNs are physically the same objects, but in the Type 2s the BLR is obscured from our view, probably by dust in a torus surrounding the central source. In this case, the observer looking at the nucleus along the torus axis sees the central source, the BLR and the NLR and identifies the galaxy as a type 1. In contrast, another observer observing the same galaxy but in the plane of the torus sees only the narrow lines and a relatively weak nuclear source.

The basis of this picture is the detection of weak broad emission lines in the linear polarization spectrum of the Seyfert 2 galaxy NGC 1068 and other sources (e.g, Antonucci and Miller 1985). We cite in Figure 2.2 the nuclear spectrum of NGC 1068: top panel shows the total flux, while the bottom panel shows the linearly polarized flux (Miller et al. 1991). The polarization spectrum could be identified as that of a Seyfert 1 galaxy; the Balmer lines are broad, and Fe II blends (which are characteristic of broad-line but not narrow-line galaxies) are seen. A polarized spectrum can result from scattering or reflection of the AGN continuum, either by dust or by free electrons. Thus, NGC 1068 apparently has a Seyfert 1 nucleus that we do not view directly, but only in scattered (and thus polarized) light. This observation demonstrated that there are at least some Seyfert 2 galaxies that are intrinsically Seyfert 1s. Other similar cases have also been found among Seyfert 2s with polarized continua (e.g., Tran et al. 1992).

Figure 2.3 shows a schematic picture of the unifying scheme of AGNs, where key parameters are the radio loudness and the viewing angle (in addition, of course, to the mass and the mass accretion rate). The left panel summarizes the radio-loud objects without jets, while the right is for the case of radio-loud objects with jets. The nucleus and regions responsible for the optical emission lines are surrounded by a molecular torus. Narrow line region (NLR) is the place where the optical lines with narrow widths are thought to be emitted. Broad line region (BLR) is believed to be inner part of the NLR, where a number of molecular clouds are thought to produce the optical emission lines under the excitation by ultraviolet and X-ray photons from the AGN. Then, the large line widths are taken as evidence for high velocities of the clouds that must be moving around/toward the central black hole. When the line of sight is between the jet axis and the torus plane, both the broad line region and the narrow line region are visible. For galaxies with radio emission, these would be classified as broad line radio galaxies. Especially when we see the jet right to the end, the objects are identified as blazers since the jet emission is enhanced and blue-shifted by the beaming effect due to its relativistic bulk velocity. This beaming effect also leads to the enhanced time variability. When the

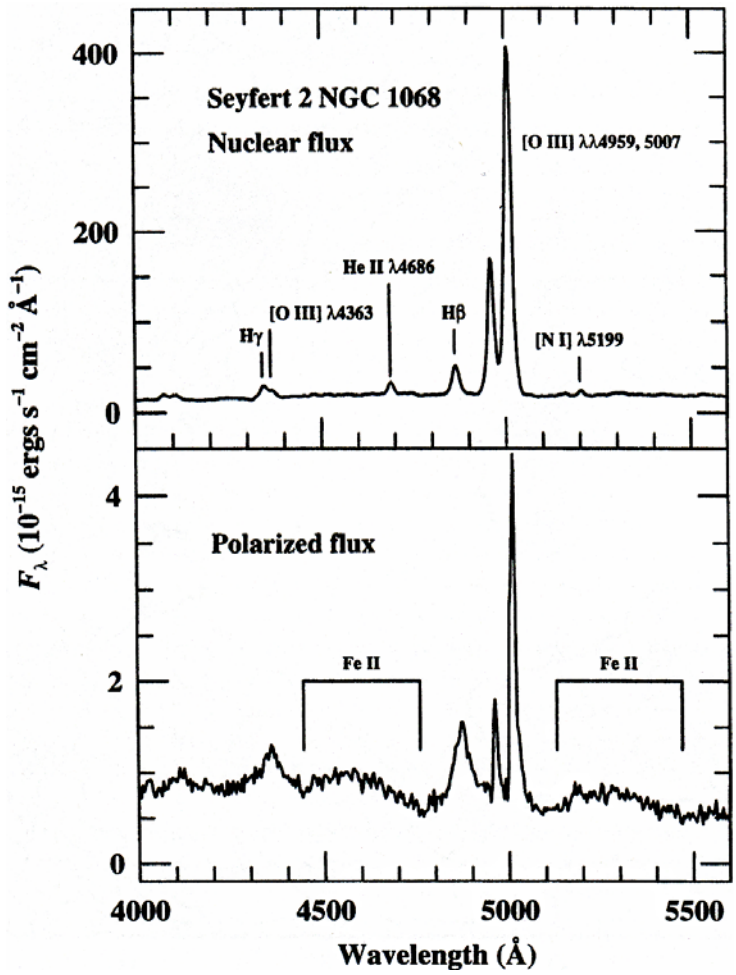

Figure 2.2: Nuclear emission line spectrum of the Seyfert 2 galaxy NGC 1068. (top) The total-flux nuclear spectrum. (bottom) The linearly polarized flux. This figure is adopted from Miller et al. (1991).

broad line region is obscured by the torus, object is observed as a narrow line galaxy.

Again, in this context, type 1 and type 2 Seyfert galaxies have intrinsically the same objects, and the observational differences between them are interpreted by the difference of line of sight between the torus axis and the plane (e.g., Antonucci 1993). And this holds independently of their radio loudness.

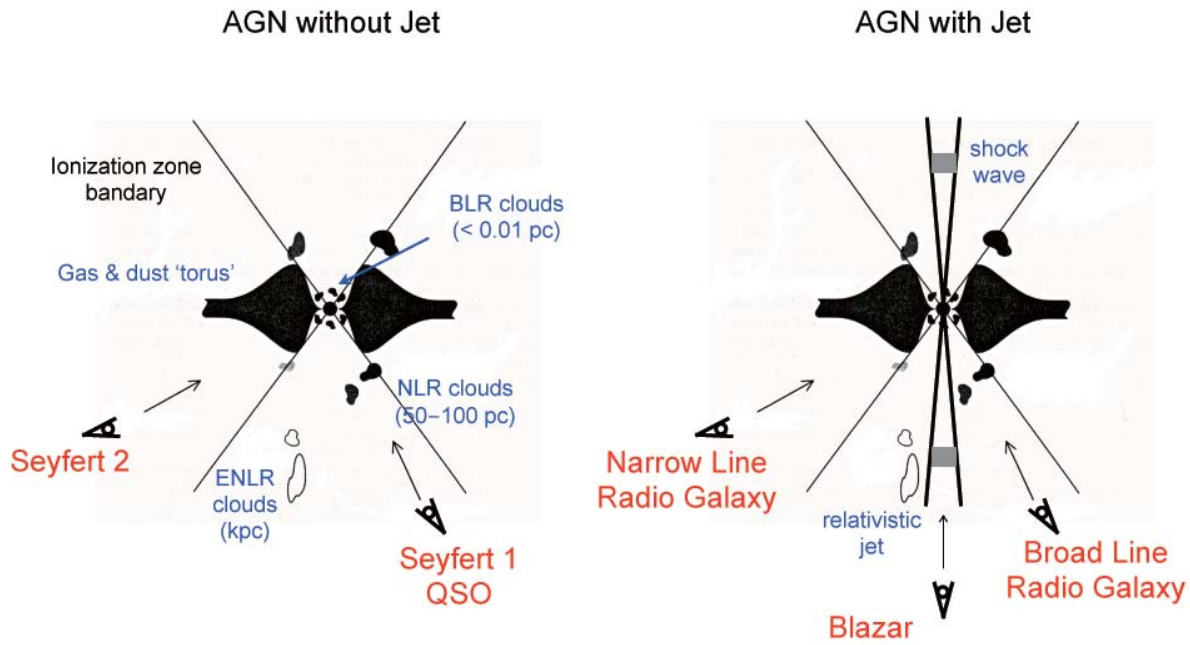

Figure 2.3: Unified Scheme of all types of AGNs. (left) AGNs without jet. (right) AGNs with jet.

2.2 Supermassive Black Hole Hypothesis

2.2.1 Physical nature of AGNs

It is now widely accepted that the huge radiation power of AGNs are produced by mass accretion onto a central supermassive black hole. Several observational techniques are utilized to estimate the mass of the central black hole (see §2.3), and the estimated mass ranges over 10^{4-10} times the solar mass. Around such massive objects, the potential energy of infalling materials is converted into kinetic energy, and partially into radiation. Since the infalling material generally have some angular momentum, they are expected to form an axisymmetric accretion disk around the black hole. The materials are then

heated via viscous drag within the accretion disk, and the disk (especially the innermost part) radiates ultraviolet to X-ray photons.

A black hole itself is characterized by only three parameters; its mass, spin and charge. When we consider the mass accretion onto a black hole, physical processes involved there should be characterized primarily by these quantities, or those derived from them. Although a black hole has no physical surface, its event horizon, namely the Schwarzschild radius, provides a characteristic size of the black hole. It is given as

$$\begin{aligned} R_s &= \frac{2GM_{\rm BH}}{c^2} \\ &\approx 3\times10^{13}\frac{M_{\rm BH}}{10^8 M_\odot}\ {\rm cm} \approx 10^{-2}\frac{M_{\rm BH}}{10^8 M_\odot}\ \text{light days}, \end{aligned} \tag{2.1}$$

where $M_{\rm BH}$ is the black hole mass, $M_\odot = 1.989\times10^{33}$ g is the solar mass, c is the speed of light, and G is the gravitational constant. Since $R_{\rm s}$ is proportional to $M_{\rm BH}$, any other lengths around the black hole are, generally, characterized by (or scaled to) $R_{\rm s}$, and hence its mass. For example, the innermost stable Keplerian orbit of a non-rotating black hole is $3R_{\rm s}$.

Let us consider a proton accreting onto a black hole. By falling into the gravitational potential well, a proton release its potential energy by

$$E = \frac{GM_{\rm BH}m_{\rm p}}{3R_{\rm s}} = \frac{m_{\rm p}c^2}{6} \tag{2.2}$$

until it reaches $3R_{\rm s}$ where $m_{\rm p}$ is the proton mass. This suggests that an order of ~ 0.1 times the proton rest-mass energy could be converted into radiation. Thus, the accretion onto a black hole can be an order of magnitude more efficient than fusion of hydrogen to helium, where only $\sim 0.6\%$ of the rest-mass energy can be utilized. Since E is independent of $M_{\rm BH}$, the radiation efficiency is not dependent on $M_{\rm BH}$ either. Consequently, the radiation power acquired per unit accreting mass is independent of $M_{\rm BH}$. This leads to a fact that when mass is accreting constantly, the luminosity L is proportioned to $\dot{M}$, and independent of $M_{\rm BH}$. However, the emergent spectral energy distribution depends on $M_{\rm BH}$.

2.2.2 Eddington luminosity

The accreting matter is governed by two forces in opposite directions; the inward gravitational force from the black hole, and outward radiation pressure. From a condition that the former must exceed the latter, we can derive a critical luminosity for a simple

spherical accretion. This luminosity, called Eddington luminosity, is qualitatively given as

$$L_{\rm Edd} = \frac{4\pi c G M_{\rm BH} m_{\rm p} \mu}{\sigma_{\rm T}} = 1.3\mu \times 10^{38} \left(\frac{M_{\rm BH}}{M_\odot}\right) \ {\rm erg}, \tag{2.3}$$

where $\sigma_{\rm T}$ is the Thompson cross-section, and μ is a number ratio of nucleon to electron of the accreting matter; i.e., $\mu = 1$ for Hydrogen, $\mu = 2$ for Helium, and ~ 1.2 for materials with the cosmic abundance. When we consider a typical AGN with a bolometric luminosity of $L \sim 10^{12} L_\odot = 3.8 \times 10^{45}$ erg s^{-1} ($L_\odot = 3.85 \times 10^{33}$ erg s^{-1} is the solar luminosity), the black hole mass is calculated as $3 \times 10^7\ M_\odot$, on condition that L is close to $L_{\rm Edd}$. If the luminosity is significantly lower than the Eddington limit, the mass must be larger. Thus, the black hole must be supermassive.

Given the definition of $L_{\rm Edd}$, and the accretion rate $\dot{M} = L/\eta c^2$, where η is the efficiency of converting gravitational potential energy to electromagnetic radiation, we can define several other useful quantities. Thus the "Eddington accretion rate", $\dot{M}_{\rm Edd}$, is the accretion rate required to produce $L_{\rm Edd}$,

$$\dot{M}_{\rm Edd} = \frac{L_{\rm Edd}}{\eta c^2} \simeq 3 \left(\frac{M_{\rm BH}}{10^8 M_\odot}\right) \left(\frac{\eta}{0.1}\right)^{-1} \ M_\odot \ {\rm yr}^{-1}, \tag{2.4}$$

The "Eddington time", $t_{\rm Edd}$, is the typical time associated with this accretion rate and is given by

$$t_{\rm Edd} = \frac{M_{\rm BH}}{\dot{M}_{\rm Edd}} \simeq 4 \times 10^8 \eta \ {\rm yr}. \tag{2.5}$$

When the accretion continues with $\dot{M}_{\rm Edd}$, the black hole mass grows exponentially on this time scale, regardless the initial mass. This terminology allows us to express the relative accretion rate (accretion rate per unit mass of the BH) as

$$\frac{L}{L_{\rm Edd}} \propto \frac{\dot{M}}{\dot{M}_{\rm Edd}} \propto \frac{\dot{M}}{M_{\rm BH}}. \tag{2.6}$$

The normalized Eddington accretion rate, $\dot{m} \equiv \dot{M}/\dot{M}_{\rm Edd}$, is a dimensionless quantity independent of $M_{\rm BH}$. Hereafter, we generally use the term "accretion rate" to refer to this normalized value.

2.2.3 Accretion disk models

It is thought that an accretion disk plays a crucial role in the conversion of gravitational energy into radiation around compact objects (Lynden-Bell 1969; Shakura and Syunyaev 1973). In theoretical studies of accretion disks, three typical solutions have been proposed to describe different regimes in $\dot{m}$.

- Shakura and Syunyaev (1973) provided a prototypical formalism called a standard disk (or "thin disk"), which is thought to be appropriate for $\dot{m} \sim 0.1$. This optically-thick, geometrically-thin accretion disk is a very efficient conversion system of gravitational energy of accreting gas into radiation energy. Mitsuda et al. (1984) gave a simple mathematical approximation to the radiation spectrum integrated over a standard disk. Called "multi color disk (MCD)" model, it is expressed as a particular superposition of many blackbody emission components up to a certain maximum color temperature, $T_{\rm in}$, which is realized at the innermost disk boundary. Since a standard disk around a typical stellar-mass ($\sim 10\ M_\odot$) black hole has $T_{\rm in} \sim 10^7$ K, its emission appears predominantly in the X-ray energy. Actually, this MCD model has been shown to give a successful physical description of soft state X-ray spectra of X-ray binaries (BHBs); as reported by e.g., Makishima et al. (1986), Ebisawa et al. (1993), and Kubota et al. (1998). In the case of AGNs, luminous objects such as quasars have spectral energy distributions (SEDs) more weighted toward lower frequencies, with a "big blue bump" in their optical/UV soft X-ray band (Koratkar and Blaes 1999). Since most of the energies of such AGNs emerge in that energy range, this bump feature is thought to be the primary emission from a standard accretion disk.

  Luminosity of the black-body radiation relates to the temperature T and to the emission region S as $L = \sigma T^4 S$, where σ is the Stefan-Boltzmann constant. Since $S \propto {R_{\rm s}}^2 \propto M_{\rm BH}^2$ and $L \propto L_{\rm Edd} \propto M_{\rm BH}$ under a constant $\dot{m}$, the temperature becomes $T \propto {M_{\rm BH}}^{-1/4}$. This is the reason why emission from the standard accretion disk in a BHB is observed in X-rays, while that of an AGNs is generally in the optical/UV.

- A slim disk ($\dot{m} \gtrsim 1$; e.g., Abramowicz et al. 1988) is a theoretical solution to a super-Eddington accretion system. In a black hole, an optically-thick accretion flow can become super-Eddington for two reasons: the flow is axisymmetric rather than spherical, and the matter can be swallowed into the black hole without much liberating the potential energy into radiation. In such an optically thick accretion flow, the radiation energy is trapped in the flow and advected inward. Since the trapped radiation energy can fall onto the black hole with the accreting gas without being radiated away, a radiative efficiency is reduced. Because the emergent luminosity is thought to saturate at $\sim L_{\rm Edd}$, the model is considered appropriate for Narrow Line Seyfert 1s (NLS1s) which are thought to be systems rapidly accreting onto relatively

small ones among super-massive black holes (e.g., Leighly 1999, Boroson 2002, and references therein). Recent studies (e.g., Ebisawa et al. 2003) suggested that this model may be applied for accounting for the measured spectra of the Ultra Luminous X-ray sources (ULXs), assuming that that they are accreting intermediate mass ($\sim 10^{2-3}\ M_\odot$) black hole.

- An advection-dominated accretion flow (ADAF; $\dot{m} \ll 1$; Ichimaru 1977, Narayan and Yi 1994, Abramowicz et al. 1995) is very radiatively inefficient. The ADAF is a widely accepted model in accounting for the low/hard state of galactic BHBs or LLAGNs, with its unusual low-luminosities given relatively abundant accretion rate. This is because almost all of viscously dissipated energy is stored in the flow and advected beyond the event horizon rather than radiated away. The dissipated energy is mainly transferred to ions, and subsequently electrons are heated, up to $\sim 10^{10}$ K, due to Coulomb collisions with the hot ions and advection of electrons themselves. On the other hand, the electrons are cooled mainly via three radiation mechanisms: Bremsstrahlung, synchrotron radiation, and Comptonization of the synchrotron photons. The accretion flow is optically-thin, but optically-thick only in the radio band. Hence, the self-absorbed synchrotron emission is expected to achieve a color temperature of $\sim 10^{9.5}$ K, which can be detectable with VLBIs.

A standard disk and slim disk can produce only quasi-blackbody spectrum at optical-UV regime, while an ADAF can generate both radio and hard X-ray emission from AGNs. To explain a hard spectral component in SEDs of luminous AGNs, several composite configurations have been proposed: outer standard disk + inner ADAF (e.g., Esin et al. 2001), standard disk + disk corona (e.g., Liu et al. 2002), and slim disk + disk corona (e.g., Wang and Netzer 2003).

2.2.4 Observational evidence for supermassive black holes

While the black hole model for the AGN central engine has a high degree of plausibility, it has remained unproven by any reasonable scientific standard since the early days of AGN research. The wide acceptance of this model has been at least in part due to the absence of serious contenders until 1990's. In the last ~ 10 years, however, stronger evidence for the existence of supermassive ($M_{\rm BH} > 10^7 M_\odot$) objects in the centers of galaxies has emerged as a result of the following mass estimation observations (§2.3). (a) Dynamical studies of stellar and gas motions in the nucleus of M 31 (Kormendy 1988) and M 87 (Ford et al.

1994), respectively. (b) Megamaser kinematics in M106 (Miyoshi et al. 1995), which is now well-established as a *bona fide* AGN (Wilkes et al. 1995). (c) A reverberation mapping of the broad-line regions in AGNs (e.g., Korista et al. 1995).

Another very important, direct evidence has been provided by an X-ray observation; *ASCA* (Tanaka et al. 1994) observed a Seyfert 1 galaxy at a distance of 31 Mpc, MCG-6-30-15, and discovered a gravitationally red-shifted iron K fluorescent line in its X-ray spectrum. Tanaka et al. (1995) performed a very deep observation of the galaxy by *ASCA* in 1994 July, and found a quite broadened iron line, corresponding to a Doppler velocity of $\sim 0.2c$. The line was also asymmetric, being extended to the red wing, as shown in Figure 2.4. The only explanation seems to be that the line originates from inner accretion disk, where the line is subject to the rotational (transverse and longitudinal) Doppler shifts and gravitational red shift. A supermassive black hole nicely fits the picture. Since this discovery, more than ten Seyfert 1 galaxies has been found to possess similar broad iron lines (e.g., Nandra et al. 1997). *Suzaku* satellite (§3.1) has, not only confirmed the broadness of the line, but also strengthened the perspective by detecting the reprocessed signal above 10 keV which is also considered to originate in the disk (Miniutti et al. 2007).

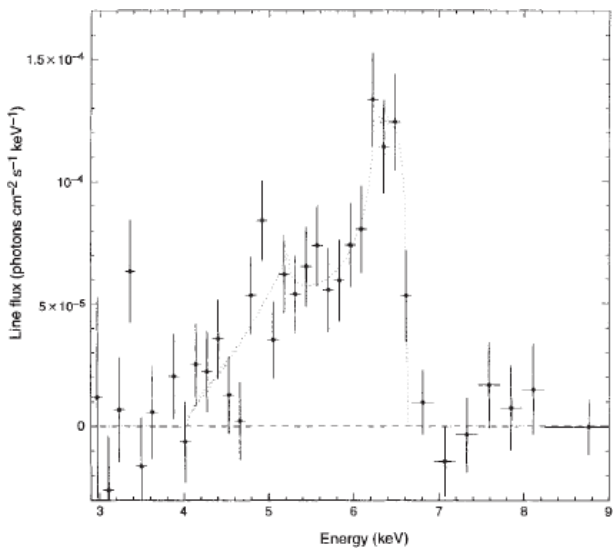

Figure 2.4: The line profile of iron Kα in the X-ray spectrum The best fit continuum spectrum has been subtracted from the data. The dotted line shows the best fit line profile from a model of Fabian et al. (1989), an extremely-illuminated accretion disk orbiting a Schwarzschild black hole. This figure was adopted from Tanaka et al. (1995).

2.3 Mass Estimation

2.3.1 Estimation via stellar/gas motion

Studies of stellar motions in the very center of nearby galaxies and Our Galaxy provide promising opportunities to estimate the mass concentrated at its center. Kormendy (1988) extracted from optical observation data the radial velocity of stars at the central region of M 31 (or Andromeda Nebula) located at a distance of 0.7 Mpc. They found that the starts are orbiting around the M 31 nucleus with a very high velocity, whose radial profile can be modeled by a Keplerian motion (Figure 2.5). It implied a mass of $\sim 3 \times 10^7\ M_\odot$ is contained within the $\sim$ 4 pc of the nucleus, suggesting that the central object is a supermassive black hole. In the same way, Genzel et al. (1997) and Genzel et al. (2000) estimated the mass contained in the center of Our Galaxy as $(2.6 - 3.3) \times 10^6\ M_\odot$. Using this method, supermassive black holes with masses $\sim 10^{6-10}\ M_\odot$ have been detected at the centers of nearby galaxies (e.g., Kormendy and Richstone 1995; Pinkney et al. 2003). Instead, it is valid for non-active galaxies unlike reverberation technique (§2.3.2) or water maser mapping (§2.3.3), but cannot be applied if the AGN emission so luminous that it overwhelms the starlight.

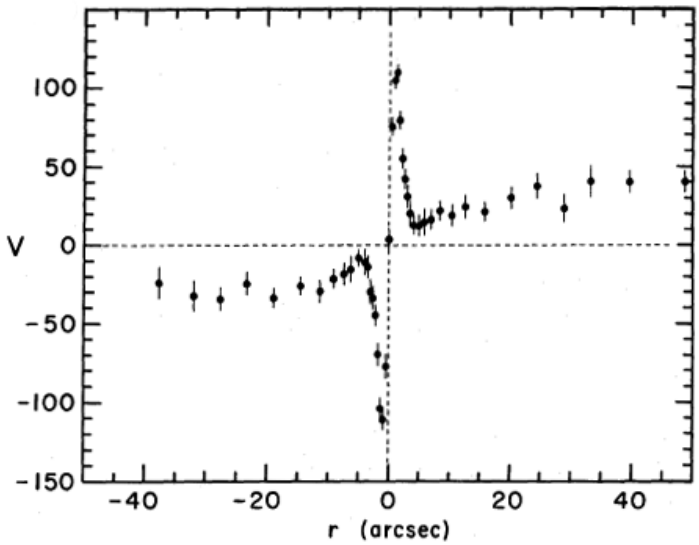

Figure 2.5: The radial velocity profile of the stars at the center of a galaxy M 31. This figure is cited from Kormendy (1988).

From dynamical studies of gas-disk around the AGN nucleus, we can also estimate the mass within the disk. Especially, when the gas velocity varies with distance from the nucleus obeying the Kepler's law, the motion is supposed to reflect the gravitational

potential. Using the Hubble Space Telescope, Ford et al. (1994) observed the nuclear region of M 87, a nearby giant elliptical galaxy at a distance of 15 Mpc. They found from spectra at several positions around the nucleus that the gas is rotating in a Keplerian manner, around an estimated mass of $2.4 \times 10^9 M_\odot$ within the 18 pc of the nucleus.

2.3.2 Reverberation mapping

Another technique is so called "reverberation mapping" (Kaspi et al. 2000, Nelson 2000). In principle, the size and structure of the BLR can be obtained by observing the response of emission lines to continuum variations. The emission-line response to a continuum change is delayed and spread out in time by light travel-time effects within the BLR. The BLR thus appears to "reverberate" in response to the continuum variations. If, e.g., we consider a central black-hole mass of 3×10^7 $M_\odot$, a typical line width of 5000 km/s, when interpreted as the Keplerian velocity, places the BLR at $\sim 2 \times 10^{16}$ cm or ~ 6 light days from the nucleus.

Indeed, monitoring the variability of the continuum and emission line fluxes in broad line AGNs shows that both intensities are highly correlated, but that of the emission line lags behind the continuum. The lag, by times ranging from days to months, is best explained as a light travel time from the nucleus to the BLR, and can be used to estimate the size of broad line region (BLR). If we further assumes that the BLR kinematics are nearly Keplerian, we can use the line widths as a characteristic velocity to determine the total mass contained within the BLR. The reverberation studies have now yielded the mass of numerous Seyfert 1 galaxies and quasars (e.g., Wandel et al. 1999).

2.3.3 Water maser

Water maser signals, at 22 GHz have provided unprecedented insight to the circum-nuclear environment of low luminosity AGNs, like Seyfert and LINER nuclei. Luminous extragalactic H_2O masers were discovered in the late 1970's, and it was quickly recognized that they are more commonly found in active spirals than in other types of galaxies. The landmark extragalactic H_2O maser source has been NGC 4258. The integrated maser spectrum is rich with a group of bright, blended lines near the systemic velocity of the host galaxy, and also a number of high-velocity, "satellite" lines offset by roughly ± 1000 km s^{-1} from systemic. The masers will be most efficiently amplified along pencil beams through the disk with the smallest spread of Doppler velocities.

The near-systemic H_2O maser lines of NGC 4258 drift towards higher Doppler veloci-

ties with time but the satellite lines remain fixed in velocity. It was recognized by several groups that this pattern of radial acceleration is consistent with centripetal acceleration of an edge-on, rotating ring of molecular gas. Follow-up VLBA observations by Miyoshi et al. (1995) showed that the maser spots trace a linear structure spanning $\sim$ 0.5 pc across the nucleus. The position-velocity diagram of the maser spots, cited in Figure 2.6, precisely matches the profile expected from an edge-on disk undergoing Keplerian rotation around a central mass concentration of 3.5×10^7 $M_\odot$ within the inner 0.13 pc (the inner radius of the maser spots). Based on detailed kinematic models of the maser spot distribution and Doppler velocities, the disk must be geometrically-thin, gently warped, and viewed nearly edge-on. Proper motion studies later confirmed that the maser spots undergo rotation.

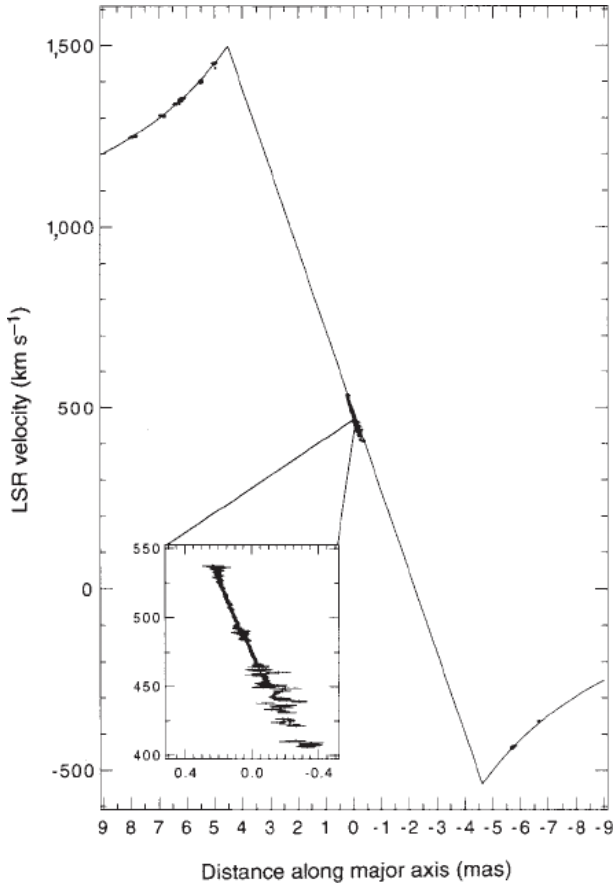

Figure 2.6: Line-of-sight velocity versus distance along the major axis of NGC 4258, derived with the H_2O maser observation. Inset: data near the systemic velocity of the galaxy. The line represents the best fitted curve of the Keplerian rotation model. This figure is cited from Miyoshi et al. (1995).

2.4 X-ray Spectral Properties of type 1 AGNs

The X-ray properties of bright, optically selected quasars have been intensively studied over the last ~ 30 years (Elvis et al. 1978, Zamorani et al. 1981), mostly with broad-band but low resolution spectra. The X-ray emission from quasars extends from the Galactic absorption cut-off at ~ 0.1 keV up to ~ 300 keV. Laor et al. (1997) analyzed the *ROSAT* soft X-ray (0.5–2 keV) observations of the sample of local ($z < 0.4$) PG quasars, and a subsample of these objects has been studied with *ASCA* in the 2–10 keV band (George et al. 2000), and with *BeppoSAX* in the 1–100 keV band (Mineo et al. 2000). Recent studies of samples of bright Seyfert 1 galaxies are reported in George et al. (1997; *ASCA* observations) and in Perola et al. (2002; *BeppoSAX* observations). Through these huge number of X-ray studies performed over the past 3 decades, we can now understand X-ray spectra from typical Type 1 AGNs (both quasars and Seyfert 1s) as illustrated in Figure 2.7. Thus, the spectrum is dominated by a primary component emergent from a close vicinity (e.g., an accretion disk) of the central BH, but superposed on it are secondary (or reprocessed) components such as iron emission lines and "Compton reflection hump". In addition, the low-energy region is strongly affected by "warm absorber", and contaminated by a "soft excess" component. Below, we describe these constituent components.

2.4.1 Primary emission

The intrinsic continuum X-ray emission of quasars and Seyfert 1s is to first order a power-law, extending from about 1 keV to over 100 keV. However, as higher resolution and better signal-to-noise spectra have become available, emission and absorption features have been found that mask a direct view of this "power-law" over virtually the whole X-ray band (see Figure 2.7). Hence, slight curvatures may be present but unseen. The typical photon index is between $\alpha = 1.8$ to $\alpha = 2.0$, both for low luminosity Seyfert galaxies and high luminosity quasars. Radio-loud AGN have a somewhat flatter spectrum (α between 1.5 and 1.7). Here, the photon index α is defined such that the number of X-ray photons emitted over a unit energy interval is given as $\propto E^{-\alpha}$ (usually $\alpha > 0$), with E representing the X-ray energy. This is thought to be due to the additional hard component emitted by relativistic electrons in the jet via inverse-Compton scattering on the radio-synchrotron photons (Williams et al. 1992), but this is not fully established.

There is now increasing evidence, mostly from *BeppoSAX*, for a roughly exponential cut-off to the power-law at energies of $\sim$ 80–300 keV. This is presumably due to a cut-off in the energy distribution of the electrons responsible for the X-ray emission. Such a high-

energy cut off is well established in hard X-ray spectra of Galactic black-hole binaries. It is still debated, however, whether the spectral index depends on the red-shift, or luminosity, or the BH mass (Zamorani et al. 1981; Avni and Tananbaum 1982; Avni and Tananbaum 1986; Bechtold et al. 2002; Vignali et al. 2003).

In addition to the main power-law continuum component, a soft emission component with thermal emission lines from ionized atoms is often observed, with characteristic temperature k$T \sim 0.2 - 1$ keV. The physical origin of this component is not clear: it could be emitted by some warm gas located in the accretion disk, or in the broad line region (it could be the confining medium of the broad emission line clouds), or in a region farther from the center. Such a warm gas could be ionized either collisionally, or via photoionization by the primary X-rays. Alternatively, this "soft excess" could be an extension of the big blue bump to higher energies, e.g., via Compton scattering in a hot accretion disk corona (Czerny and Elvis 1987).

2.4.2 Reflection components

The primary emission of AGN can be "reflected", i.e., Thomson scattered by electrons in neutral or ionized gas. If the reflector has a column density $N_{\rm H} > 1.5 \times 10^{24} cm^{-2}$ (i.e., $\sim 1/\sigma_{\rm T}$) and is not fully ionized, the reflected component has a spectrum like the one shown in Figure 2.7 (the actual shape slightly varies, depending on the geometry and chemical composition of the reflector). The main features of this reflection component are a continuum due to electron scattering with a peak at $\sim$ 30 keV, the iron K-edge absorption, and a cut-off below 4–5 keV due to photoelectric absorption of the lower energy incident radiation. The low-energy absorption is less abrupt than the case of a simple photoelectric absorption, because the incident photons are reflected back from various depths of the reflector, and hence with different absorbing column densities. The reflection efficiency is typically a few percent in the 2–10 keV range because of photoelectric absorption, rising to $\sim$ 30% at the 30 keV peak if the reflector is Compton thick and covers a significant fraction of the solid angle around the nucleus (Ghisellini et al. 1994). The efficiency drops if the reflecting medium is Compton-thin, or the reflector subtends a smaller solid angle; in these cases, part of the incident radiation escapes without interaction.

2.4.3 Iron line

The most prominent narrow feature in the 2–10 keV X-ray spectra of AGNs is an iron emission line at an energy of 6.4 keV, corresponding to the $n = 2 - 1$ transition of K-shell electrons in "cold" (i.e., $\leq$ Fe XVII) iron atoms. The line is usually thought to arise when an incident X-ray photon with energy > 7.2 keV is photoelectrically absorbed by an iron atom, presumably in the inner part of the accretion disk, followed by an emission of a fluorescent K-line photon. The line has a typical EW 100–200 eV (Makishima et al. 1986). As shown in Figure 2.4, the Fe-K line in some Seyfert galaxies exhibit a broad "red wing" extending to lower energies (Tanaka et al. 1995; Turner et al. 1997; Miniutti et al. 2007). Once thought to be ubiquitous, XMM-Newton results suggest that this red wing is seen only in a few objects, with MCG-6-30-15 being the clearest example (Vaughan and Fabian 2004). Such a broad line would be one of the best tools to look for general relativistic effects in strong gravity (§2.2.4).

Regardless of the presence/absence of the broad Fe-K line wing, a narrow component of the Fe-K line is very clearly present in most AGNs. The width of this "narrow" line (unresolved in the CCD spectra with *ASCA* , *Chandra* ACIS, or *XMM-Newton* EPIC) is a few thousand km s^{-1} or smaller, as measured with a dispersive spectrograph on *Chandra* . This is similar to the width of the optical and UV broad emission lines. This narrow component does not vary when the continuum varies, even on delay times of days. Coupled with the line width, this suggests an origin well beyond a few R_s, although a small radius is not fully ruled out (Fabian et al. 2002).

If the reflector is highly ionized, the peak energy of this line can be shifted toward high energies. This is because the Kα line (n = 2–1 transition) energy of heavy ions increase gradually as the ion gets further ionized, and hence electrostatic screening of the nuclear charge is weakened. The energy becomes 6.68 keV for helium-like iron, and 6.96 keV for hydrogen-like ones. It is also possible that two narrow components are present in the spectrum, one emitted by a cold reflector and the other by an ionized reflector.

2.4.4 Warm absorbers

As illustrated in Figure 2.7, the AGN continuum below ~ 2 keV often deviates negatively from a simple power-law form. However, this is likely to be extrinsic to the primary nuclear emission, because the flux deficit involves local structures attributable to edges (and resonant absorption lines) of ionized ions. This property is expressed as the presence of "warm absorber" somewhere close to the nucleus. The warm absorber features are

present in the soft X-ray spectra of half of the bright Seyfert 1 galaxies observed with *ASCA* (Reynolds 1997). Such warm absorbers are considered to be such gas that is photo-ionized by the strong X-ray emission from the nucleus. Their column densities are typically observed as $N_{\rm H} = 10^{21}$–10^{23} cm^{-2}, sometimes showing time variability.

Recently, the availability of high resolution soft X-ray spectra, obtained with the grating instruments onboard *Chandra* and *XMM-Newton* , showed that this component is formed by an outflowing gas. Krongold et al. (2003) obtained the highest signal-to-noise high resolution spectrum with a long observation of the Seyfert 1 galaxy NGC 3783 (see their Figure 3). and succeeded in reproducing all of the observed lines with a two-phase absorber, with the two phases in pressure equilibrium.

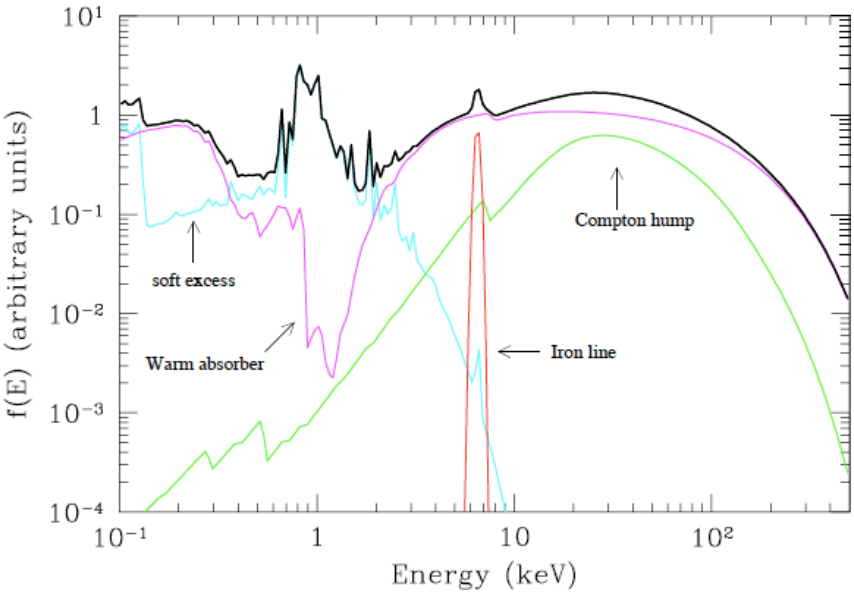

Figure 2.7: Average total spectrum (thick black line) and main components (thin color lines) in the X-ray spectrum of a type 1 AGN. This figure is adopted from Risaliti & Elvis (2004).

2.5 X-ray Spectral Properties of Obscured Seyferts

2.5.1 X-ray observation of hidden nuclei

As described in §2.1.3, current picture of Seyfert nuclei relies on the Unified Scheme (Antonucci and Miller 1985), which assumes that the central source— a black hole, an accretion disk, and broad line region— is embedded within an optically thick molecular

torus located at a distance larger than ~ 0.1 pc. Over a certain luminosity range, the structure of these main ingredients are considered almost identical in all active galactic nuclei (AGNs), and the apparent differences among individual objects are ascribed to their orientation with respect to our line of sight; the object is classified as a Seyfert 1 if the line of sight lies within the opening angle of the torus, and as a Seyfert 2 if observed through the obscuring material.

Because the nuclear intrinsic light in the optical, ultraviolet, and soft X-ray frequencies is absorbed by the torus, Seyfert 2 AGNs can be seen at these energies only through reprocessed emission. The optical to UV band continuum emission of Seyfert 2s is heavily absorbed by dust, hence the nucleus is only seen through reprocessed emission at longer wave length. As a result, the observed continuum is dominated by the stellar contribution of the host galaxy and/or scattered emission, which can only be disentangled through the polarized light. In heavily obscured AGN, when only emission lines are seen, it can be even difficult to distinguish an AGN from a starburst. Since only (hard) X-rays can penetrate the obscuring material, observations in such energy range are crucial to investigate the nature of hidden nuclei, or even to establish the presence of AGN in a galaxy.

Many of pioneering works on this field were done with Japanese *Ginga* satellite, with its hard X-ray sensitivity up to ~ 30 keV. For example, Koyama et al. (1989) observed NGC 1068, finding a quite flat X-ray spectrum followed by a strong iron emission line with EW of ~ 2 keV; Awaki et al. (1990) discovered a highly obscured ($N_{\rm H} \sim 10^{24}$ cm^{-2}) intrinsic nuclear emission in Mrk 3. Many of other works showed that the direct AGN emission, thus observed in hard X-rays, were highly absorbed even by $N_{\rm H}$ of $\gtrsim 10^{24}$ cm^{-2} (e.g., Awaki and Koyama 1993;Ueno et al. 1994a; Iwasawa et al. 1993).

The *ASCA* satellite allowed us a more precise investigation of reprocessed signal in X-ray range, such as strong iron line complex and quite flat continua in energies from a few keV to 10 keV (e.g., Iwasawa et al. 1994; Ueno et al. 1994b). *ASCA* has also contributed with its high sensitivity, in founding obscured nuclei whose activity had been suggested by other wavelength. At some epoch as the exciting radio results on NGC 4258 (§2.3.3), Makishima et al. (1994) discovered, using *ASCA* , a rather obscured hard X-ray source in NGC 4258, with a intrinsic 2–10 keV luminosity of $\sim 4 \times 10^{40}$ erg s^{-1}. This demonstrated that the nucleus of this galaxy is "weakly active", with the X-ray luminosity $\sim 2 \times 10^{-4}$ times the Eddington luminosity indicated by the H_2O-determined mass. Thus, NGC 4258 has become a prototypical low-luminosity AGNs which are characterized by extremely low accretion rates.

2.5.2 Obscuration mechanism

If we see the emission of a type 1 Seyfert through a significant column of dust and/or gas, its observed Spectral Energy Distributions (SEDs) would be significantly distorted over wide energy range. The observed SEDs would thus show further spread, depending both on the intrinsic emission (which has a large dispersion) and on the characteristic of the absorber such as the amount, composition, and geometry. In general, the main absorption mechanisms in AGN are the following;

1. Line absorption due to atomic transitions. The strongest features observed in AGN spectra, i.e. "Narrow and Broad absorption lines" in the UV, and "Warm absorption" in the soft X-rays, are mainly due to resonant absorption lines.

2. Continuum absorption in the IR to UV due to dust.

3. Continuum absorption (or scattering) in the X-rays due to photoelectric absorption (dominant below ~ 3 keV) and Compton scattering (dominant above ~ 7) by dust and gas.

Furthermore, the physical state (temperature, density), column density, and metallicity of the gas, the chemical composition of the dust, the dust-to-gas ratio, and the composition of the dust grains are all elements that affect the observed SED.

2.5.3 Contribution to the cosmic X-ray background

It now appears that different types of sources produce the majority of the Cosmic X-ray Background (CXB; Boldt 1987) in different X-ray energy bands. In the soft (0.5–2 keV) band, Seyfert 1 galaxies and quasars are the dominant contributors (Schmidt et al. 1998). These sources, however, have steep X-ray spectra and cannot account for the flat slope of the CXB spectrum at higher energies. (e.g., Mushotzky et al. 1980; Nandra and Pounds 1994). Seyfert 2 galaxies have thus emerged as the most promising candidates for the origin of the hard (2–10 keV) CXB (Awaki and Koyama 1993). Since their emission suffer from heavy obscuration by dense molecular gas, their observed X-ray spectra are substantially flatter than those of unobscured AGN (Awaki et al. 1991). CXB models based on AGN Unified Scheme have demonstrated that the combined emission of absorbed and unabsorbed source, integrated over all redshifts, can account for the intensity and spectrum of the hard CXB (e.g., Setti and Woltjer 1989; Madau et al. 1993; Comastri et al. 1995). According to these models, the sources responsible for most of the flux

in the hard X-ray band are expected to have absorption column densities in the range $N_{\rm H} \approx 10^{23} - 10^{24}$ cm^{-2}.

Such AGN based CXB models depend on a number of assumptions and free parameters: (a) the universality of the Unified Scheme, i.e., all Seyfert 2 galaxies are obscured Seyfert 1 galaxies, (b) the ratio of obscured to unobscured source, (c) the distribution and luminosity dependence of the absorption column densities in AGN, and (d) the luminosity extent and redshift evolution of the X-ray luminosity function for obscured AGN. These assumptions, in principle, can be (and should be) verified or constrained observationally. As to (a), optical spectropolarimetry surveys, which can reveal broad emission lines in the polarized flux spectra of Seyfert 2 galaxies, have demonstrated that at least $\sim 50\%$ of such sources are indeed hidden Seyfert 1 galaxies (Moran et al. 2000; Moran et al. 2001; Lumsden et al. 2001; Tran 2001). Given the generally low polarizations of Seyfert 2 galaxies make the survey difficult (e.g., Kay 1994), it is probably safe to assume that most Seyfert 2 galaxy are obscured Seyfert 1 galaxies. For (b), the observed space density of Seyfert 2 galaxies are observed at about 3 times higher than that of Seyfert 1s, which in turn means that the torus must block out about 3/4 of the sky as seen by the central source. Intensive studies on (c) and (d) are still continued (e.g., Risaliti et al. 1999 for c, Miyaji et al. 2000 and Ueda et al. 2003 for d).

2.5.4 Recent hard X-ray observations

Recently, *BeppoSAX* and *RXTE* observed the hard X-ray emission from a number of Seyfert 2 nuclei in the $\sim$ 10–100 keV range (e.g., Ikebe et al. 2000, Matt et al. 1997b, Malizia et al. 2003 and references therein). Most of them has column densities below $\sim 1.5 \times 10^{24}$ cm^{-2}, which produce a photoelectric cut-off at energies between 1 and 10 keV (in this case, the source is "Compton-thin"). Whereas in a fraction of them, the obscuring material was found to be even opaque to Compton scattering, with $N_{\rm H} \times \sigma_{\rm T}$ reaching a few, where $\sigma_{\rm T}$ is the Thomson cross section. In such "Compton-thick" AGNs, accurate measurements of the intrinsic emission are quite difficult, since it appears only above $\sim$ 10 keV with a strongly absorbed spectrum. In the most extreme cases, the direct AGN emission is completely hidden even up to $\sim$ 100 keV.

In heavily absorbed sources ("Compton-thick", $N_{\rm H} > 10^{24}$ cm^{-2}), the two main spectral features are a prominent; iron Kα emission line with EW $\sim$ 1–3 keV, and a reflected and/or scattered continuum. In less obscured sources, the EW of the iron line depends on the fraction of the intrinsic continuum emission absorbed at the line energy;

for $N_{\rm H} < 10^{23}$ cm^{-2}, values typical of type 1 AGN are observed (EW $\sim$ 100–300 eV), in agreement with the Unified Scheme. The reflected/scattered component is the same as described for type 1 AGN. In Figure 2.8, we plot the 1–100 keV spectra of two representative obscured AGN: MCG-5-23-16 ($N_{\rm H} = 10^{22}$ cm^{-2}, Risaliti 2002), and NGC 1068 ($N_{\rm H} > 10^{25}$ cm^{-2}, Matt et al. 1997b). MCG-5-23-16 is "Compton-thin", i.e., they are dominated by the primary emission down to a few keV. In MCG-5-23-16, a cold reflection component also gives a measurable contribution. The continuum of the Compton-thick source NGC 1068 (Matt et al. 1999b) in the 2–10 keV range, as compared with the Compton-thin sources, shows a quite hard spectrum due to cold reflection and a warm reflection component. Equivalent widths of the iron line are $\sim$ 100 eV in MCG-5-23-16, and $\sim$ 2 keV in NGC 1068.

Although the above results show variety of X-ray spectra of obscured AGNs, they can be explained by the concept of the Unified Scheme: we are seeing the same object, with the apparent difference being come from simply the viewing angle. Recently, interesting results has appeared from a combination of *Swift* and *Suzaku* satellite. Ueda et al. (2007), using *Suzaku* , observed an obscured AGN found by the hard X-ray survey with *Swift* BAT instrument. The X-ray spectrum of the source suggested that the central source is covered by a dust torus, with a much smaller opening angle than assumed in the Unified Scheme. This result clearly implies the distribution of the absorption column densities of Seyfert 2s (and its possible dependence of other physical parameters such as $M_{\rm BH}$, luminosity, redshift) is the remaining questions to be settled.

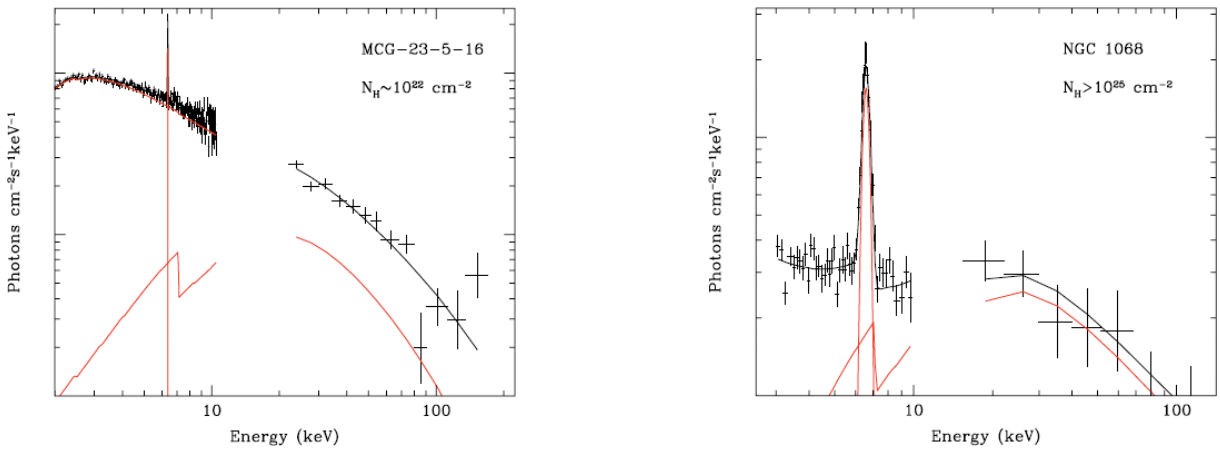

Figure 2.8: 2–100 keV *BeppoSAX* best fit X-ray spectra of two representative Seyfert 2 galaxies. Main components of the best fit models are also shown. MCG-5-23-16 is a "Compton-thin" source, i.e., its spectrum is dominated by the primary emission down to a few keV. Whereas NGC 1068 is a "Compton-thick" source, whose spectrum is dominated only by the reprocessed signals.

Chapter 3

INSTRUMENTATION
– The X-ray Observatory *Suzaku* –

3.1 Overview of the *Suzaku* Satellite

The *Suzaku* satellite (Mitsuda et al. 2007) is the fifth Japanese X-ray astrophysical observatory, which was launched on 2005 July 10 with the M-V (mu-five) launch vehicle from Uchinoura, Japan. After deploying the solar paddles and extending its extendible optical bench (EOB), *Suzaku* performed perigee-up orbit maneuver for $\sim$ 10 days, to obtain its altitude of 570 km and an inclination of 31°. It has a near circular orbit with an orbital period of $\sim$ 96 minutes. The remarkable characteristic of *Suzaku* is its high throughput over a broad-band energy coverage from 0.3 to 600 keV.

Figure 3.1 shows a schematic drawing and a side view of *Suzaku* . The spacecraft at launch has a weight of 1706 kg, and a length of 6.5 m along the telescope axis when the EOB is extended. In order to perform three-axis attitude control, it utilizes four reaction wheels (one for redundancy). The attitude is measured by three gyroscopes and two star trackers. The absolute pointing accuracy is nominally $\sim 0'.24$ with a stability better than $0'.022$ per 4 sec, which is a half of typical exposure time of the XIS (Serlemitsos et al. 2007). Observations are interrupted when the satellite passes through the South Atlantic Anomaly (SAA), where particle background drastically increases. The normal mode of operations requires the spacecraft pointed to a single direction of the sky for at least a quarter day (which corresponds to an observable exposure of $\sim$ 10 ksec). With this constraint, most targets will be occulted by the Earth for about one third of each orbit, while some objects near the orbital poles can be observed nearly free from the occultations.

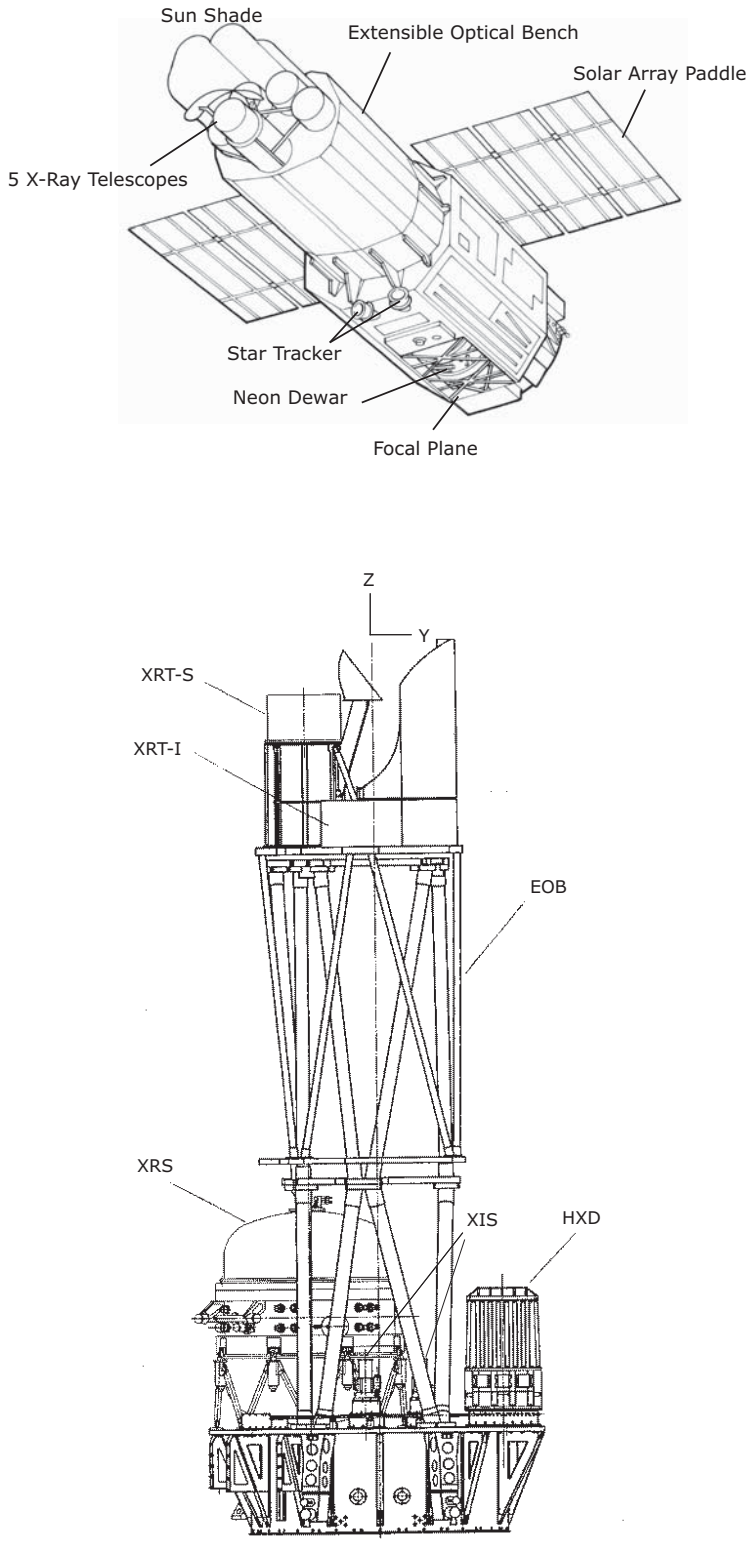

Figure 3.1: A schematic drawing of the *Suzaku* satellite (top), and its side-view (bottom).

The satellite has five reflective X-ray imaging optics, collectively called the X-ray Telescope (XRT) mounted on top of the EOB, and corresponding five focal plane detectors on the base panel of the spacecraft. One of the detectors is the X-ray Spectrometer (XRS) and the remaining four are the X-ray Imaging Spectrometer (XIS). They observe X-rays from ~ 0.3 to ~ 10 keV. The third instrument, the Hard X-ray Detector (HXD; Takahashi et al. 2007) is also mounted on the base panel. It is a non-imaging, collimated detector for higher energies, working from ~ 10 keV to ~ 600 keV without using optics. Although the XRS has stopped its operation soon after the launch, on 2005 August 8, the remaining two instruments are now providing us a series of new observational data, fully utilizing their broad-band capability. In the present thesis, we no longer describe the XRS, nor the XRT that is coupled to it.

3.2 X-Ray Telescope (XRT)

Figure 3.2 shows schematic drawing of the XRT and a photograph of one of the four XRT modules which are coupled to the XIS (XRT-I). The XRT employs Wolter-I type telescopes, which are also used in many previous missions; *Einstein* , *ROSAT* , *ASCA* (Tanaka et al. 1994), *XMM-Newton* (Jansen et al. 2001), *Swift* (Gehrels et al. 2004) and some others. An X-ray telescope of this type is usually made up of nested sets of co-axial grazing-incidence reflectors, each in turn consists of a paraboloid and a hyperboloid sections which reflect incident X-rays in series. The *Suzaku* XRT is made of very thin ($\sim$ 178 μm) foils to achieve light-weight and high-throughput performance over a wide energy range up to ~ 12 keV, with conical approximations to the paraboloid and hyperboloid sections. This, together with shape errors of the foils, results in a moderate angular resolution.

As shown in Figure 3.2, an XRT module has a cylindrical structure with the following components layered along the optical axis;

1. a thermal shield at the entrance aperture to reduce temperature gradient;
2. a pre-collimator mounted on metal rings for stray light elimination;
3. a primary stage (or "paraboloid" section) for the first X-ray reflection;
4. a secondary stage (or "hyperboloid" section) for the second X-ray reflection;
5. a base ring for structural integrity and interface with the EOB of the spacecraft.

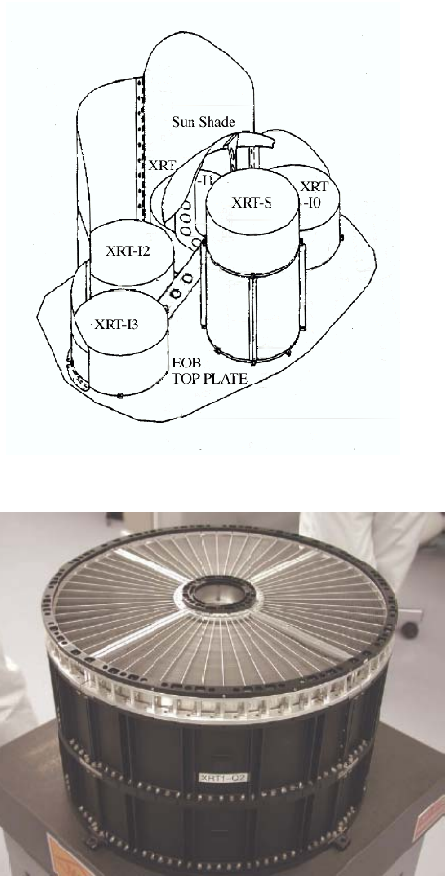

Figure 3.2: A schematic drawing of the X-Ray Telescope (XRT) mounted on the EOB (top), and a photograph of one XRT module (bottom).

All these components, except for the base rings, are fabricated in 90°segments, called "quadrants". Four quadrants are coupled together by interconnect-couplers and also by the top and base rings. The telescope housings are made of aluminum to achieve an optimal strength-to-mass ratio. Each reflector consists of a substrate also made of aluminum, and an epoxy layer that couples the reflecting gold surface to the substrate.

We summarize basic parameters of XRT-I in Table 3.1. The XRT has a typical angular resolution of $\sim 2'0$ in terms of half-power diameter (HPD), which is nearly independent of the X-ray energy. This resolution is significantly worse than those of *Chandra* and *XMM-Newton* , because of the conical approximation and of shape errors in the aluminum substrate foils. Except for this drawback, the employed replication method allows a mirror shell to be thin, and hence to realize a light-weight telescope with a large effective area. Figure 3.3 shows the effective area of an XRT module. Although a single XRT module has a smaller effective area than the *Chandra* and the *XMM-Newton* telescopes, it keeps a high reflectivity up to 10 keV.

The optical axis of each XRT module was determined by in-orbit observations of the

Crab Nebula at various off-axis angles. The derived axes are shown in Figure 3.4, where the off-axis angles are refer to the detector coordinate system (Ishisaki et al. 2007). Since the optical axes moderately scatter, the origin of Figure 3.4 was adopted as a nominal reference position, called "XIS-nominal" position. In contrast, the optical axis of the HXD deviates by $\sim 5'$ in the negative Det-X direction. Due to this misalignment, the observation efficiency of HXD-PIN, when the target is placed at the XIS-nominal position, reduces by $\sim 10\%$ compared to the on-axis value. Therefore, another pointing position is provided for HXD-oriented observations at (Det-X, Det-Y) = $(-3'.5, 0'.0)$. At this pointing position, called "HXD-nominal" position, the efficiency of the XIS reduces to $\sim 88\%$ of the on-axis value.

Verification observations of the imaging capability of the XRT have been performed with a moderately bright point source, SS CYG. In Figure 3.5, we show the image, point-spread function (PSF), and Encircled-energy fraction (EEF) of each XRT module. The net exposure time used here is 9.1 ks. The EEF is normalized to unity at the edge of the CCD chip. With this normalization, the obtained HPD of XRT-I0 through I3 is $1'.8$, $2'.3$, $2'.0$, and $2'.0$, respectively.

Table 3.1: Basic parameters and performance of the *S*uzaku XRT-I.

Number of Telescopes	4
Substrate (thickness)	Aluminum (155 μm)
Mirror coating	Gold
Total height	279 mm
Weight	19.5 kg
Number of nested shells	175
Mirror diameter (outer/inner)	39.9 / 11.8 cm
Focal length	4.75 m
Plate scale	0.724 mm arcmin^{-1}
Geometrical area	873 cm^2
Effective area (@ 1.5, 8 keV)	440, 250 cm^2
Field of view (@ 1.5, 8 keV)	17, 13 arcmin
Angular resolution (HPD)	2 arcmin

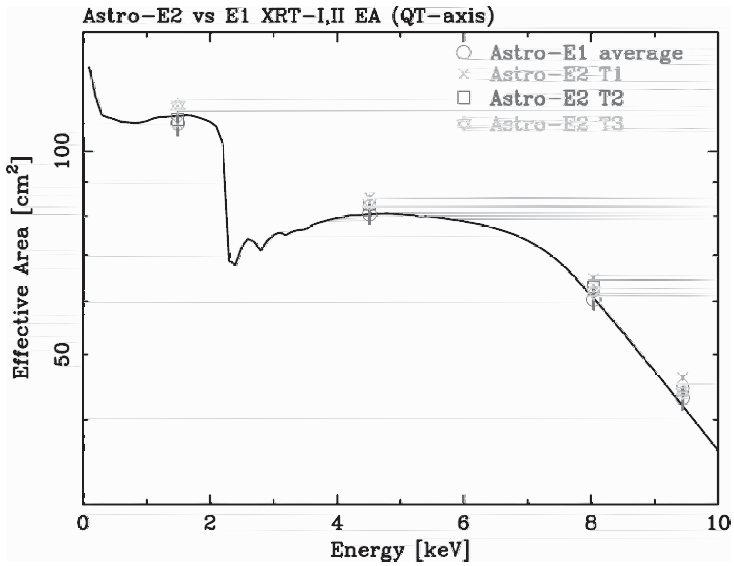

Figure 3.3: The effective area of the *S*uzaku XRT-I. The predicted response is compared to pre-launch measurements of three different XRT modules performed at particular energies.

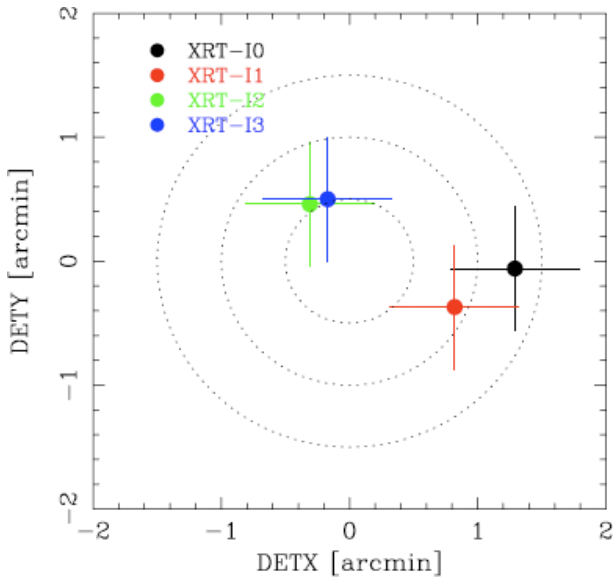

Figure 3.4: Locations of the optical axis of each XRT module on the focal plane, determined from the observations of the Crab Nebula. The dotted circles are drawn every 30″ in radius from the XIS-nominal position.

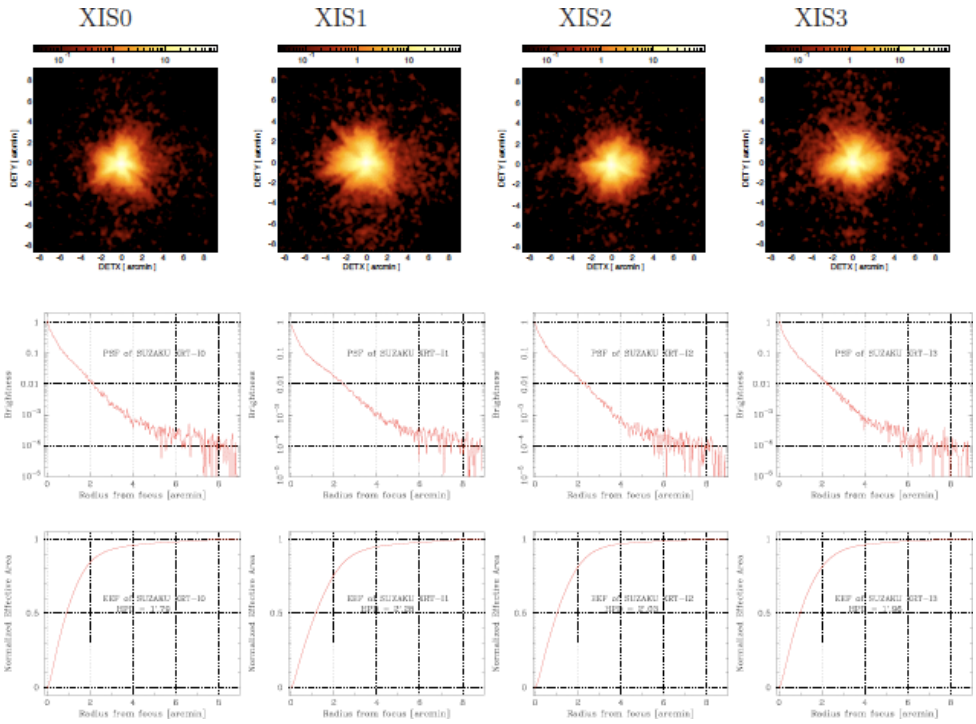

Figure 3.5: Image, Point-Spread-Function (PSF), and Encircled-Energy Fraction (EEF) of the XRT modules on the focal plane.

3.3 X-ray Imaging Spectrometer (XIS)

As described in §3.2, *Suzaku* has four XIS sensors designated as XIS0, 1, 2 and 3, each located at the focal plane of the corresponding XRT module (XRT-I0, I1, I2 and I3, respectively). Figure 3.6 is a photograph of one of them. As illustrated schematically in Figure 3.7, each XIS sensor utilize of a single CCD chip with a format of 1024 × 1024 pixels, and covers a region of $17'.8 \times 17'.8$ on the sky. Each CCD chip is further divided into four segments and a frame store region. Two corners of each sensor are illuminated by built-in calibration ^{55}Fe radio-isotopes. Unlike ordinary optical CCDs which accumulate large number of photons in each pixel over an exposure, these X-ray CCDs operate in single-photon detection mode, assuming that multiple photons do not fall in the same pixel in a single exposure.

Three XIS sensors, XIS0, 2 and 3, employ front-illuminated (FI) chips, while XIS1 a back-illuminated (BI) one. Basic parameters of the XIS-FI and BI detectors are summarized in Table 3.2. As shown in Figure 3.8, major difference between their performance appears in their effective areas at lower energies. The effective area of the BI chip exceeds that of FI by nearly an order of magnitude at 0.4 keV, while the FI effective area becomes

larger at energies above $\sim$ 4 keV. A single FI chip has an effective area of 147 cm^2 at 8 keV; hence the sum of the three XIS-FI sensors becomes $\sim$ 440 cm^2, which is comparable to that of the *XMM-Newton* -pn detector.

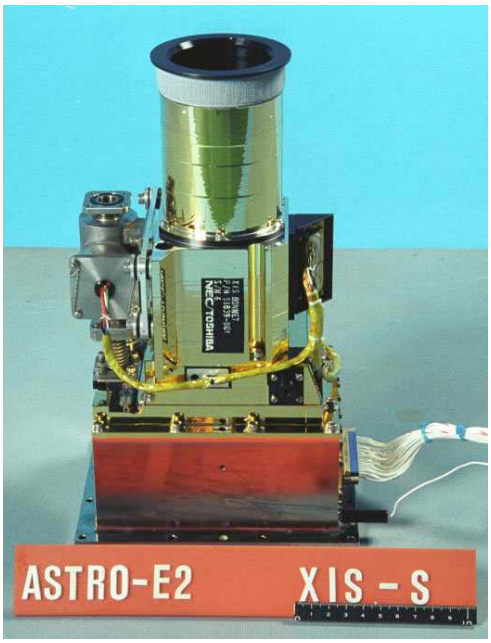

Figure 3.6: A photograph of one of the four *Suzaku* XIS sensors.

A notable feature of the *Suzaku* XIS, compared to the previous CCD-based instruments, is its improved energy resolution; $\sim$ 60 eV at 1 keV and $\sim$ 130 eV at 6 keV. In addition, XIS-BI realizes simultaneously the good energy resolution and the large effective area at lower energies, since it has an improved charge collection efficiency for soft X-ray photons. Another advantage of the XIS is its low and stable background level. Because *Suzaku* orbits inside the radiation belt of the Earth, it is free from background flares which affect missions with highly elongated orbits, including *Chandra* and *XMM-Newton* . Figure 3.9 shows background levels of various missions, normalized by the instrumental effective area and further by the field of view. The *ASCA* -SIS has the lowest background among the instruments shown here, and the *Suzaku* XIS (FI and BI) achieves a level next to it. The low background of the XIS enables us to achieve a high sensitivity especially for spatially extended sources.

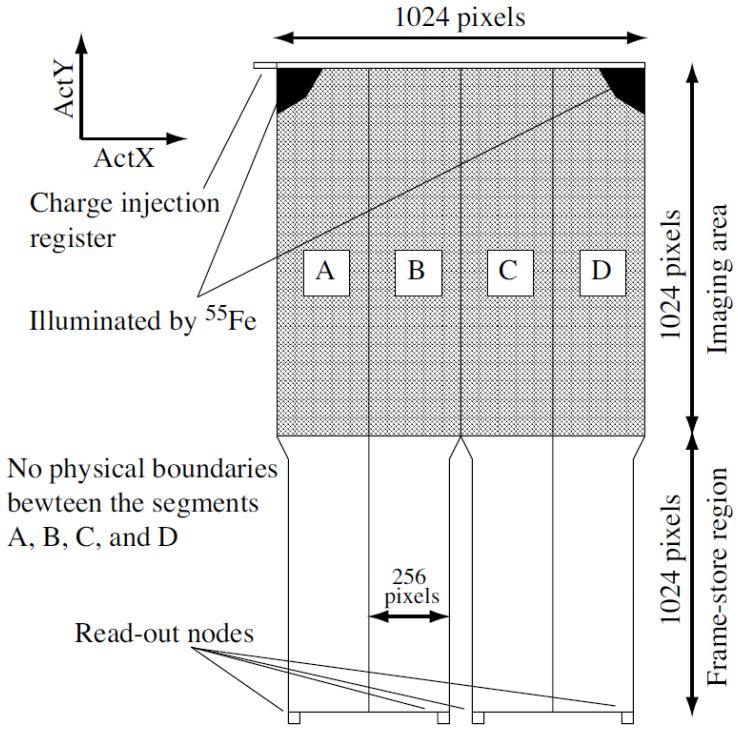

Figure 3.7: The structure of each CCD chip employed by the *Suzaku* XIS.

Table 3.2: The characteristics of the *Suzaku* XIS.

Pixel grid	1024×1024 pixels
Pixel size	24 μm $\times$ 24 μm
Field of view	18×18 arcmin
Effective area (@ 1.5 keV)	344 cm^2 (FI), 393 cm^2 (BI)
Effective area (@ 8 keV)	147 cm^2 (FI), 103 cm^2 (BI)
System noise	$<$ 2 electrons per pixel
Time resolution (Normal/ P-sum mode)	8 s / 7.8 ms
Depletion layer	50–70 μm
Dark current	$<$ 0.1 electrons s^{-1} pixel^{-1}
Readout noise	$<$ 3–4 electrons rms, typical

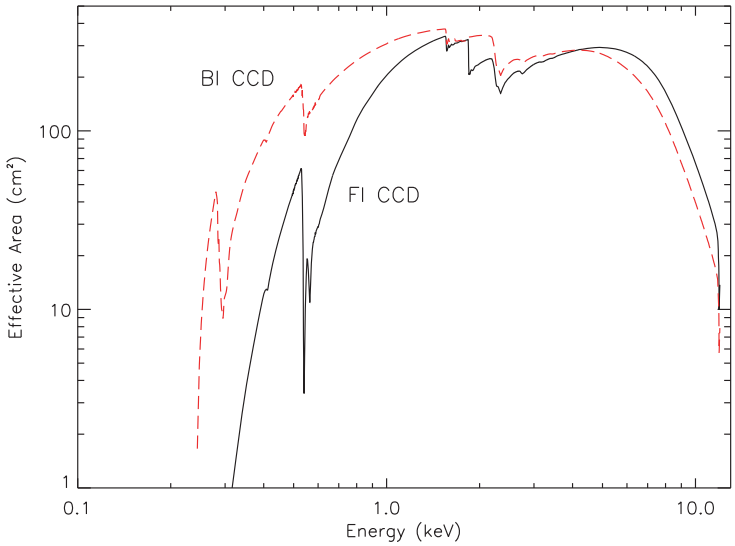

Figure 3.8: Effective areas of a single *Suzaku* XIS-BI (red dashed line) and FI (black solid line) sensor, including the telescope (XRT-I) response.

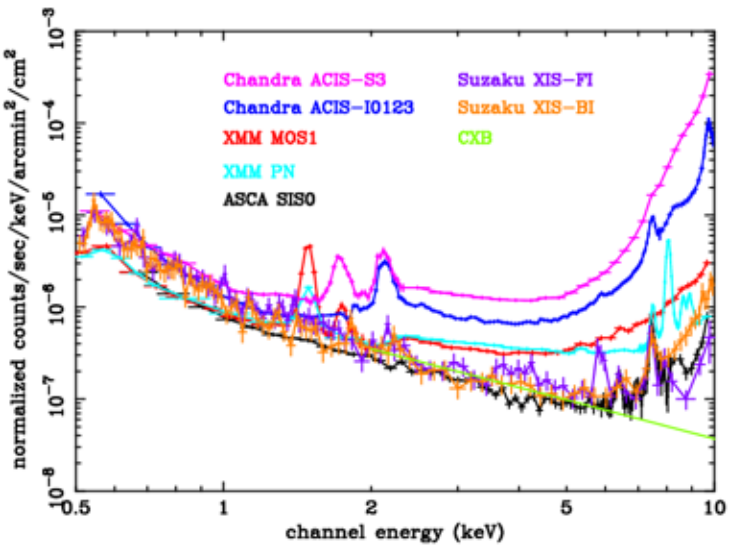

Figure 3.9: XIS background counting rate normalized both with the effective area and the field of view, presented as a function of energy. Those of other X-ray CCDs on-board *ASCA* , *Chandra* , and *XMM-Newton* (Kataoka et al. 2004) are shown for comparison.

3.4 Hard X-ray Detector (HXD)

3.4.1 System configuration of the HXD

The third instrument, the Hard X-ray Detector (HXD) covers higher energy range; from ~ 10 to ~ 600 keV. Figure 3.10 is a photograph of the HXD sensor. It is a non-imaging, collimated hard X-ray instrument which was designed to achieve an unprecedented high sensitivity. The whole HXD system is composed of three parts; a sensor part (HXD sensor or HXD-S), an analog electronics system (HXD-AE), and a digital electronics system (HXD-DE). Figure 3.11 shows a block diagram of the HXD system with a signal flow between components. Analog signals from HXD-S are send to HXD-AE, where only proper events are selected and are digitized. HXD-DE receives the digitized data and formats the data packets to send them to the ground via the satellite data processor (DP). Commands to the HXD are sent to peripheral interface unit (PIM) from the satellite data-handling unit, then sent to HXD-DE. All power driving the HXD system is supplied from a power-supply unit (HXD-PSU). The basic characteristic of the HXD are summarized in Table 3.3.

Figure 3.10: A photograph of the sensor part (HXD-S) of the *Suzaku* Hard X-ray Detector (HXD).

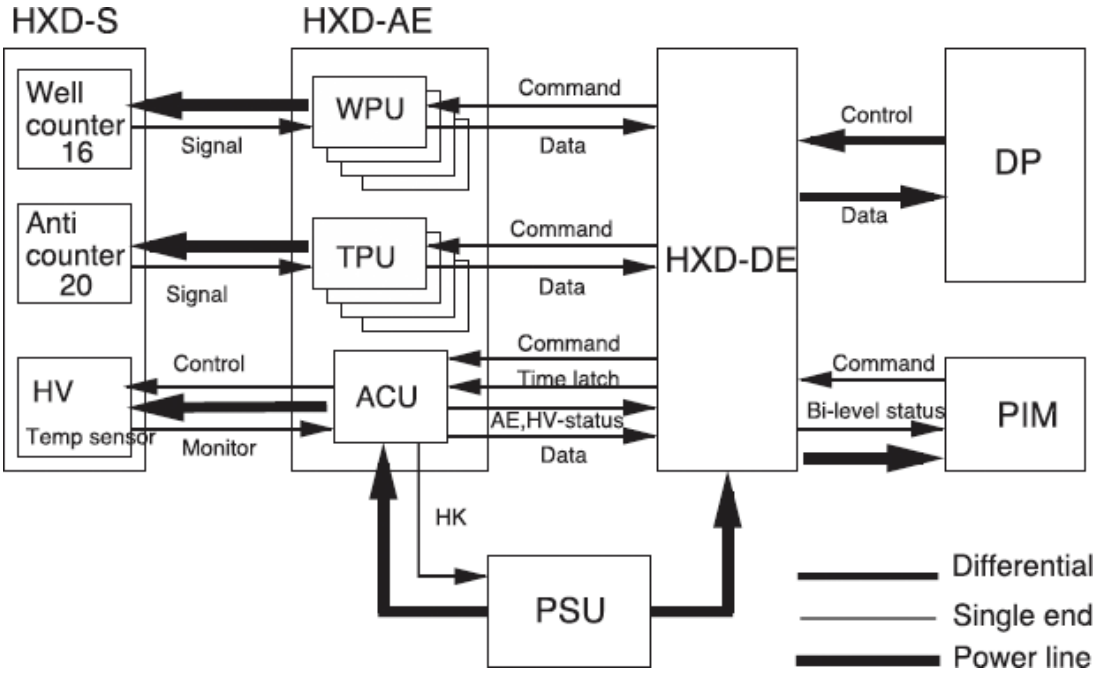

Figure 3.11: Block diagram of the HXD system.

Table 3.3: The characteristics of the *Suzaku* HXD.

Field of View	$34' \times 34'$ ($\lesssim$ 100 keV)
	$4^\circ.5 \times 4^\circ.5$ ($\gtrsim$ 100 keV)
Energy Range	10 – 600 keV
PIN	10 – 70 keV
GSO	40 – 600 keV
Energy Resolution (FWHM)	
PIN	$\sim$ 4.0 keV
GSO	$7.0/\sqrt{E_{\rm MeV}}\%$
Effective Area	$\sim$ 160 cm^2 (at 20 keV)
	$\sim$ 260 cm^2 (at 100 keV)
Time Resolution	61 μs or 31 μs

3.4.2 HXD-S

Overview of the HXD-S

As schematically shown in Figure 3.12, the main part of HXD-S consists of 16 identical detectors, called "Well" units. They are surrounded by 20 "Anti" units. Figure 3.12 (bottom) illustrates a single Well unit. Its main detection part has two types of detectors; four GSO (Gd_2SiO_5:Ce 0.5% mol) crystal scintillators and four 2 mm-thick silicon photo diodes, both surrounded by BGO ($Bi_4Ge_3O_12$) crystal scintillation. Softer photons (typically below $\sim$ 40 keV) are detected mainly by the PIN diodes, while harder photons are likely to penetrate PIN and are detected by GSO. The basic characteristics of Well units are summarized in Table 3.3.

In the hard X-ray and soft γ-ray range, observations suffer high backgrounds due mainly to charged particles, cosmic diffuse γ-rays, secondary γ-rays produced in the environment, and activation caused by cosmic protons. Since the background level thus sets the sensitivity limit in the hard X-ray range, the HXD is designed to minimize its background. Among various techniques employed, two key schemes are the following:

- Well-type active shield: In a Well unit, the main detection part, GSO crystals, has a faster decay time than the shielding part, BGO crystals. Signals from both crystals are extracted by a single photomultiplier, and discriminated using pulse-shape discrimination (§3.4.3). This technique, called "phoswich" technique, has been employed intensively in previous cosmic experiments, but drastic improvement is that the shield is shaped so that it also acts as an active collimator (well-type active shield), narrowing the field of view (FOV) of the Well unit without additional passive materials. Thus, the main detection part (GSO and PIN diodes), located at the bottom of the well, have an active shield of almost 4π of its surrounding.

- Compound eye configuration: As described above, HXD-S has a modular design, consisting of a number of units. Each well unit has a simple shape and operates independently at a modest count rate. The well units are arranged in a tightly packed 4×4 array (compound eye configuration), allowing each unit to act as an active shield for adjacent units. The 20 thick anti-coincidence BGO counters, each of which works independently as an active shield, provide additional shielding for the outermost well units. The configuration also reduces the possible dead time by implementing parallel processing of signals from them.

Well Unit

As schematically shown in Figure 3.12 (bottom), each Well unit consists of six components; GSO scintillators, BGO active shield,a a photomultiplier coupled to them, PIN diodes, fine collimators, and front-end electronics. Each unit weights 4.63 kg. The four GSO scintillators comprising the main detector part of the Well unit attains a very low background level.

The GSO and BGO crystals have very different scintillation decay times; $\sim$ 706 ns and $\sim$ 122 ns respectively, at a temperature of $-20°$C (Kamae et al. 1992). This allows an easy discrimination of valid GSO signal from those of the BGO shield, so that a single photomultiplier can tell from which scintillators the light pulse has come. Any particle events or Compton events that are registered by both BGO and GSO can be rejected by this phoswich technique. The 64 GSO crystals in the 16 Well units, as viewed by 16 photo-tubes, are collectively called HXD-GSO.

While HXD-GSO covers an energy range of 40–600 keV, the other main part of each Well unit, 2 mm-thick silicon PIN diodes, provide the lower energy response of the HXD. Each silicon PIN diode is placed in front of a GSO crystal to form a PIN-GSO pair, which observes hard X-rays from $\sim$ 10–600 keV without a gap. The PIN detectors absorb X-rays with energies up to $\sim$ 70 keV, but gradually becoming transparent in energies above $\sim$ 30 keV. The PIN diodes can be fully depleted at a bias voltage of $\sim$ 500 V due to their high resistivity (20–30 kΩcm^{-1}). The geometrical area of a PIN diode, including a guard ring, is 21.5 mm $\times$ 21.5 mm. All the 64 PIN diodes in HXD-S have a leakage current of less than 2.2 nA at 500 V and $-20°$C, and do not show any breakdown even under a bias voltage up to 1000 V. We call the 64 PIN diodes collectively HXD-PIN.

In the HXD-PIN energy range, the background is dominated by the cosmic X-ray background (CXB; Boldt 1987). The most effective method to reduce the CXB contribution is to narrow the field of view. For this purpose, passive collimators are inserted above the PIN diodes, inside the BGO well-type collimator. The collimator, called "fine collimator", has a length of 30 cm, and is made of 50 μm-thick phosphor bronze foils arranged to form a square array of 8×8 channels or 3 mm $\times$3 mm. Below $\sim$ 100 keV, the fine collimator passively defines a $34' \times 34'$ square FOV (in full-width half-maximum; FWHM). At higher energies, the fine collimator gradually becomes transparent, and the BGO active collimator defines $4.°5 \times 4.°5$ FWHM square opening. We show in Figure 3.13 the angular response measured by γ-ray lines from radio isotope located at a limited but large distance.

Figure 3.14 shows the effective area of 16 Well units, which refers to the photo-peak efficiency calculated by Monte Carlo simulations, and takes into account photoelectric absorption by materials in front of the Well units. The total geometrical areas of the HXD-PIN and HXD-GSO are 160 cm^2 and 350 cm^2, respectively. From Figure 3.14, it is clear that the overlapping energy region between PIN and GSO is well covered.

Anti Unit

The outermost Well units are further surrounded by 20 additional BGO shields, called Anti units. Each Anti unit is made of thick (average 2.6 cm) BGO pillars, and weights each 4.12 kg (for 16 units, except for corner units which is 2.72 kg in weight). This shielding reduces the cosmic proton flux on the main detection part by an order of magnitude. It also reduces Compton-scattered evens as well as nuclear activation background events.

The Anti wall has a geometrical area of $\sim$ 800 cm^2 per one side, providing an effective area of $\sim$ 400 cm^2 even for 1 MeV γ-rays. Therefore, it also works as an excellent γ-ray burst (GRB) detector in an energy range between 50 keV and 5 MeV. When regarded as an uncollimated detector rather than an active shield, the Anti units are alternatively called Wide-band All-sky Monitor (WAM). By comparing signal counts from the four sides of WAM, we can determine one-dimensional position of a GRB with an accuracy of $\sim 5^\circ$. A detailed description of WAM and its in-flight performance are described in Yamaoka et al. (2006) and Tashiro et al. (2007).

3.4.3 HXD-AE

The total number of signal channels extracted from HXD-S reaches 116, where 96 channels are from the Well units and 20 channels from the Anti units. The electronic system of the HXD is required to process these many channels in a robust and stable way, under a limited resources for space experiment such as a severe power limitation. Since it thus plays a crucial role in realizing the best performance of the HXD, it has been carefully designed (e.g., Takahashi et al. 1998; Tanihata et al. 1999; Itoh et al. 2005).

HXD-AE consists of three types of circuit boards; one Analog Control Unit (ACU) board, four Well-Processing Unit (WPU) boards, and four Transient Processing Unit (TPU) boards. ACU is a control board; it is provided with power from HXD-PSU, and controls the power lines to the other electronic boards in HXD-AE and HXD-S. Each WPU and TPU handles four well units and five Anti units, respectively. In order to take advantage of the compound eye configuration of HXD-S, we need to acquire information

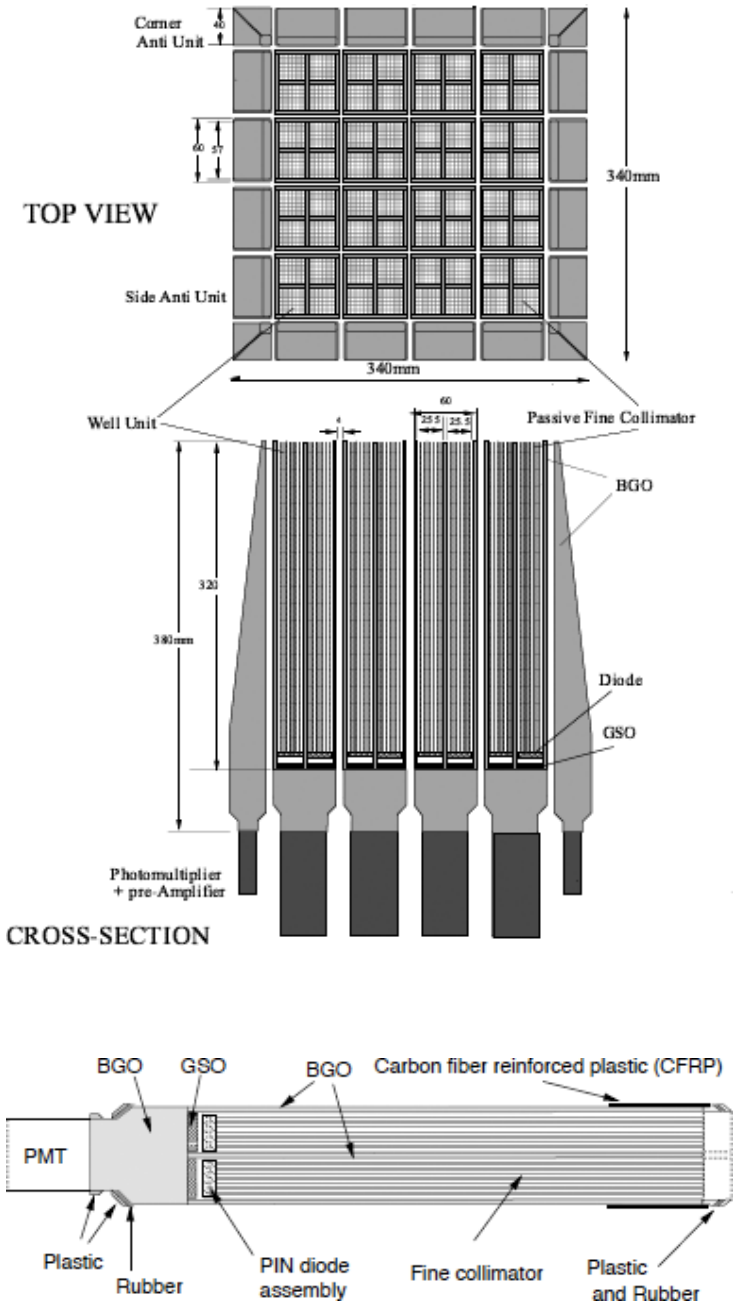

Figure 3.12: A schematic view of the HXD-S. Top and middle figures shows the side and top views of the sensor layout. Bottom figure shows a cross-sectional view of a single Well unit.

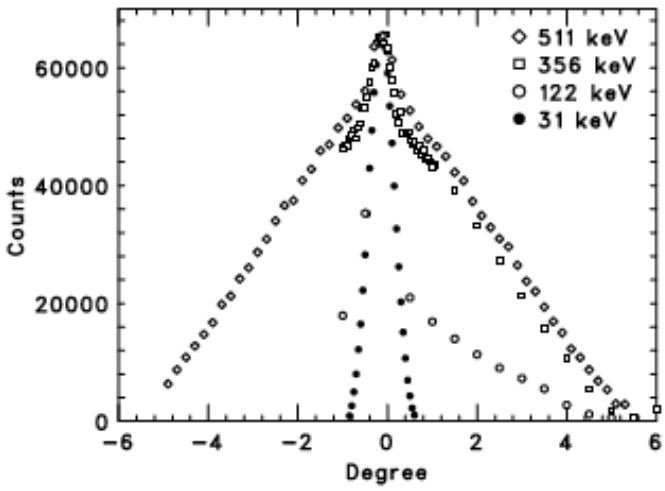

Figure 3.13: Angular responses of a single Well unit, measured by γ-ray irradiation from radio isotopes placed 280 cm away.

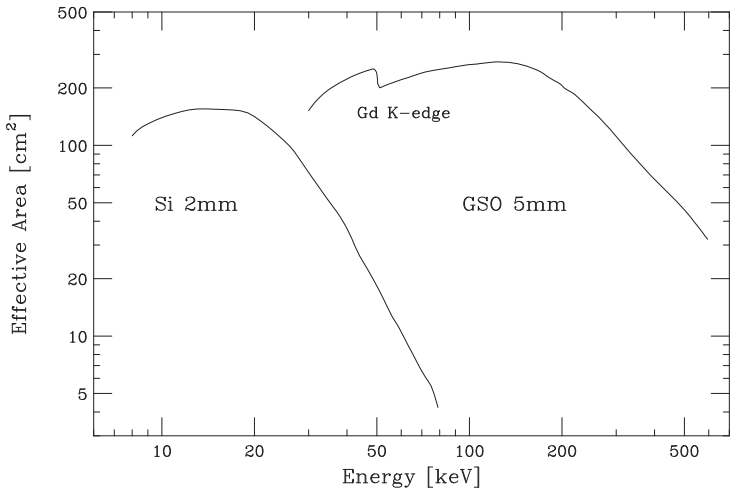

Figure 3.14: The effective area of HXD-PIN and HXD-GSO, shown as a function of energy.

on the presence or absence of hits in all the 36 units. This information is called hit pattern, and is shared by all electronic boards through a "hit-pattern bus" running through the backplane.

We show in Figure 3.15 signal flows from a single Well unit to a WPU board. Thus, the signals from a photomultiplier anode are directly fed into a fast current amplifier in HXD-AE to generate fast pre-trigger signals. In contrast, the last-dynode signal is first amplified by a charge-sensitive amplifier (preamplifier) which is contained in the HXD-S front-end electronics. In HXD-AE, this preamplifier output is split and fed into two different shaping amplifiers; one with a time constant of 150 ns (fast shaper), and the other 1000 ns (slow shaper). Then, each of the shaper output is peak held and sent to analog to digital converters (ADCs). Since scintillation light from GSO has a fast decay time of $\sim$ 122 ns, whole GSO signal will be integrated by both shapers, yielding the same outputs between the two peak-holders. In contrast, BGO has a slower decay time of $\sim$ 706 ns, so that only part of its signal will be integrated by the fast shaper. Thus, the outputs from the two peak-holders will be different for a BGO signal. We can thus discriminate GSO pulses from BGO events, and realize a function of pulse shape discrimination (PSD). This particular PSD method has several advantages over other methods (e.g., constant-fraction measurement, bipolar plus zero-cross method etc.); it is less affected by noise, and the results depend less on the signal pulse height.

Figure 3.16 (top) is called "fast-slow diagram" or "two-dimensional spectrum", in which outputs from the two shaping chains are plotted; the vertical and horizontal axes represent the slow and fast shaping pulse heights, respectively. In the diagram,events from ^{22}Na isotope form two major branches, corresponding to photoelectric absorption in GSO and BGO. A fainter which connects them is formed by those events which hit both GSO and BGO in the same unit (Compton-scattered events). In HXD-AE, we can filter out BGO events simply by comparing the two pulse heights. However, this hardware discrimination is left rather loose, to allow further filtering to be done by software in HXD-DE and in ground analysis.

While the PSD selection can reject Compton-scattered events in a single unit, we can utilize the hit-pattern information attached to each event to filter out Compton scattered events that hit multiple units. Every time a valid event is acquired from any Well unit, the hit-pattern information from all the 36 unit is latched. The rejection condition based on the hit pattern can be specified by software, either in HXD-DE or in the course of ground analysis. Effects of the PSD and hit pattern selections are described in Kawaharada et al. (2004).

As shown in Figure 3.15, signals from the four PIN diodes in a single Well unit are individually fed into a low noise charge-sensitive preamplifiers, which are mounted underneath the PMT in HXD-S. Their outputs are then sent to HXD-AE. In order to joint the observable energy ranges between the XIS and the HXD, analog electronics for HXD-PIN is designed to achieve an energy threshold of 10 keV and an energy resolution of 3 keV (FWHM), under a power consumption of 107 mW for the preamplifier per PIN diode. Since a PIN diode has a typical leakage current of $\sim$ 2 ns at $-20°$C, and a relatively large capacitance of $\sim$ 50 pF (including that of the cable), we used a low-noise preamplifier with a capacitance gradient of $\sim$ 15 eV pF^{-1}.

Besides processing signals from HXD-S, another important task of the electronic system is to measure electronic dead time. Accurate dead time measurements are crucial especially when the celestial object is faint and hence the non-celestial background dominates the source signal, because an accurate live time is required to subtract the background properly. A dead time measurement is done individually for each Well unit by counting the number of "pseudo" event pulses, which are generated periodically in the ACU module. These pseudo pulses are fed into the trigger-handling block of each WPU, activates the trigger logic in the same way as other trigger sources (PMT and PIN signals), but with a specific flag in the trigger pattern. As the pseudo events are treated equally as other normal events, some fraction of them are lost due to dead times in that WPU. Thus, we can accurately measure the dead time fraction, by comparing, over a given exposure the total number of injected pseudo pulses and those actually recorded in a finite exposure.

3.4.4 HXD-DE

HXD-DE is a CPU-based signal processing part of the HXD. It works as the primary interface with the satellite data processor for command and telemetry, as well as a controller of the acquisition and formatting of the data from HXD-AE. It is also designed to react to events such as γ-ray burst. HXD-DE has two CPU boards, with one board working while the other idling for backup purpose. Mounted on each board is a CPU 80C386 running at 12 MHz. The clock rate is thus set unusually low, just in order to reduce the power consumption of HXD-DE down to $\sim$ 5.1 W.

While HXD-DE is operated at a rather low CPU speed to reduce the power consumption, it must be able to process scientific data without loss, even from sources several times as bright as the Crab Nebula. This requires that HXD-DE works properly at an

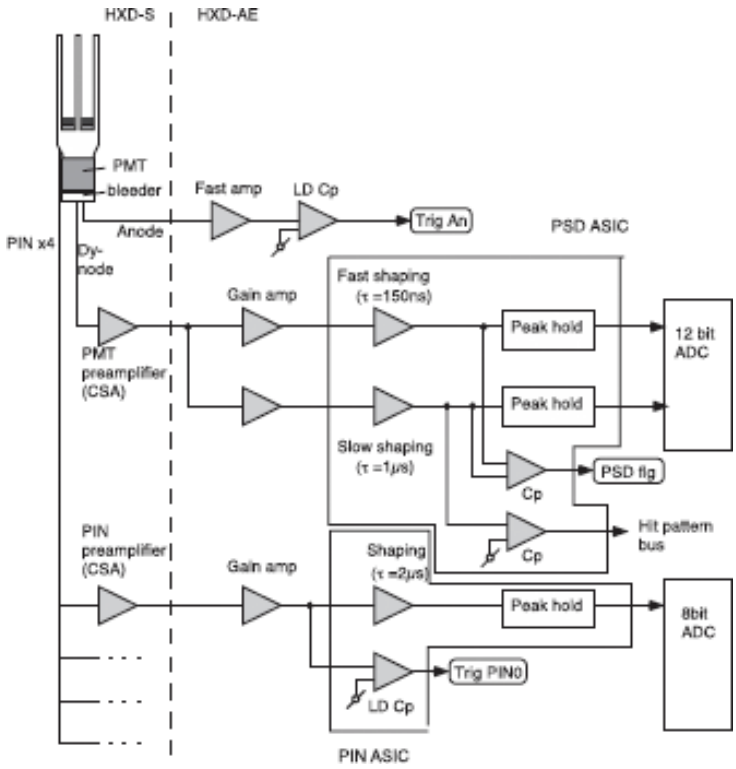

Figure 3.15: Signal flows from a Well unit to a WPU board.

acquisition rate of at least several hundred events per second. Thus, the minimum processing speed of the system has been set at 4000 events per second. In order to achieve this high acquisition rate with limited hardware resources, we uses a fast real-time operating system specially designed for this experiment, in conjunction with a circuit capable of receiving data from HXD-AE by a direct memory access (DMA) mode.

Another important capability of HXD-DE is to further filter (background) events which leaked through the hardware selection in HXD-AE. This allows a low-background capability while keeping a high signal throughput capability, and is realized by processes called "PI programs". The PI programs can do the event selection via several different algorithms, which can be chosen by commands. For example, (1) a program can select events based on the hit-pattern information of the surrounding units; (2) using another program, a finer and more flexible pulse shape discrimination can be applied on the fast-slow diagram, than that in HXD-AE. Other tasks of the PI program are to collect calibration data, and to notify γ-ray burst triggers to the TPU modules.

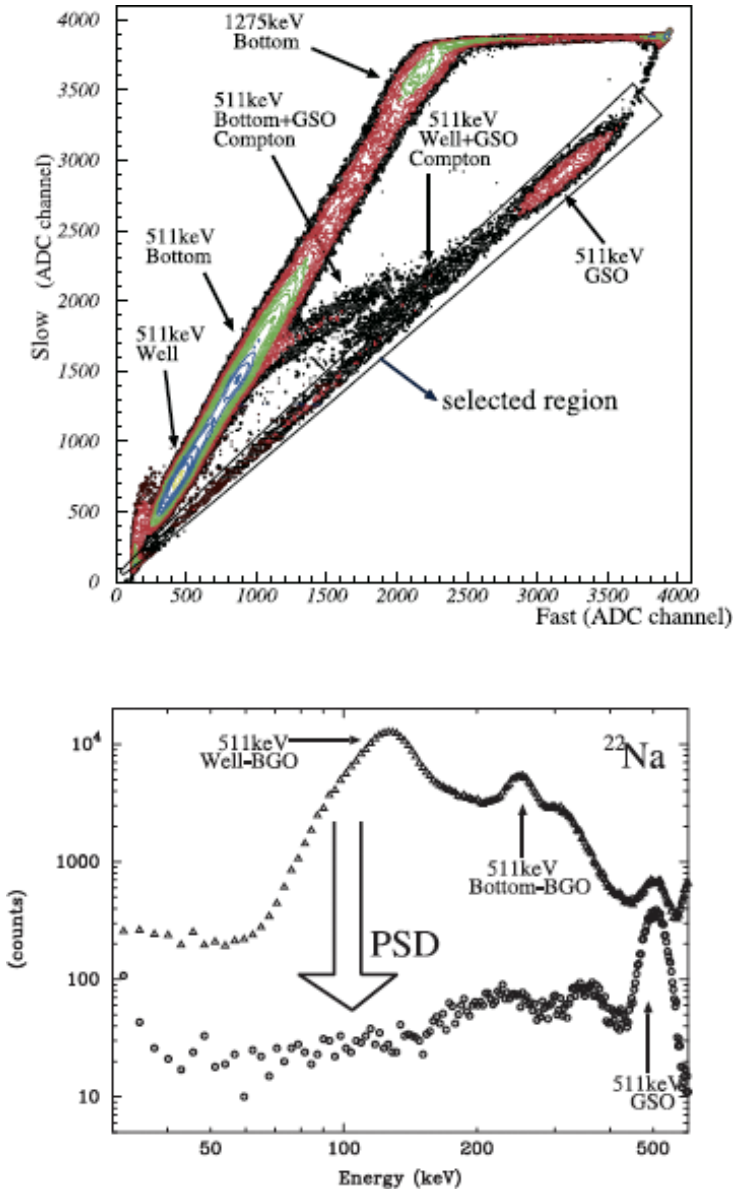

Figure 3.16: (Top) Fast-slow diagram for a single Well unit, taken with ^{22}Na irradiation. (Bottom) PSD selection effect on the GSO spectrum.

3.5 In-orbit Performance of the HXD-PIN

In this section we describe in-orbit calibration and obtained performance of the HXD-PIN detector, in the following three steps. (1) Estimation of the absolute energy scales, energy resolution, and optimal lower energy thresholds for individual 64 PIN diodes. (2) Optimization of the event selection criteria to minimize the residual non X-ray background (NXB). (3) Generation of response matrices of individual 64 PIN diodes. Another important issue, estimation of the in-orbit background is described in §3.7.

3.5.1 Energy scale

As described in Takahashi et al. (2007), the energy scales of the individual 64 PIN diodes were measured on ground with radio isotope irradiations, to an accuracy of $\lesssim 1\%$. Although these measured energy scales are not expected to change significantly by the launch, we re-confirmed the scales using actual data taken in orbit. The fluorescent X-rays from gadolinium (Gd-Kα, 42.7 keV) and bismuth (Bi-Kα, 76.2 keV) in the GSO and BGO scintillators, respectively, have been used to reconfirm the absolute energy scales. Since the fluorescent events are rejected via the normal event selection, we extracted spectra by selecting only coincidence events between PIN diodes and scintillators in the same well-counter unit.

Figure 3.17 shows in-orbit energy spectrum of a PIN detector, where such coincident events are accumulated over half a year. As shown there, the pulse height spectrum clearly reveals Gd-Kα and Gd-Kβ lines. We fitted it with a background continuum, and four Gaussians, representing Kα_1, Kα_2, K$\beta_1 + \beta_3$ and Kβ_2 fluorescent lines from Gd. Thus, the peak channels of the Kα_1 line and the energy resolution were obtained for each PIN diode. Figure 3.18 compares the energy resolution of the 64 PIN diodes thus measured in-orbit, against the on-ground measurements, which utilized radio isotope ^{1}52Eu (Sm-Kα, 40.1 keV fluorescent line). The typical in-orbit energy resolution at the Gd-Kα_1 line is $\sim$ 4 keV, which is roughly consistent with those obtained on the ground. The energy scale at $\sim$ 40 keV was confirmed to agree within 0.2% with the pre-launch calibration.

In order to accurately calibrate the energy scales especially at lower energies, we need another anchor point in addition to the two (relatively higher energy) fluorescent lines. We used "pedestal channel" as the point, that is, the peak channel of noise spectrum obtained by the random triggers from scintillators. Since the pedestal channel is determined by the noise of the peak-hold circuit, it should be proportional to the energy resolution of the relevant PIN diode. With a flight-equivalent PIN diode, we found that the energy

resolution of $\sim$ 4 keV corresponds to a pedestal channel equivalent to 2 keV. Thus, we assign 2.0 keV to the measured pedestal channel of each PIN diode. The energy scale over the whole 2–76 keV band was then derived by fitting a spline curve to the three anchor points. The accuracy of this scale is estimated to be $\sim$ 1%, based on deviations of the calibration points from the fitted curves.

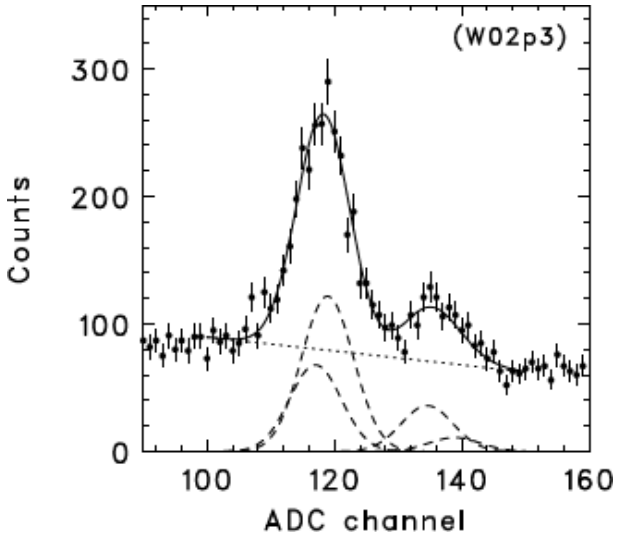

Figure 3.17: An energy spectrum of a single PIN diode, where the events coincident between PIN and GSO were accumulated over half a year. Dashed lines show Gaussians fitted to gadolinium fluorescent lines; Kα_1 (43.0 keV), Kα_2 (42.3 keV), Kβ_1+β_3 (48.6 keV) and Kβ_2 (50.0 keV).

3.5.2 Energy threshold

The PIN signals are screened by on-board analog and digital lower discriminators (LDs). Although these LDs are set at appropriate levels to generally discard thermal and electrical-interference triggers, the pulse heights of these noise events in some PIN diodes exceed the LDs, producing a noise component in the spectrum as exemplified in Figure 3.20. In order to filter these noise events out, we apply an additional LD level in the course of on-ground analysis. As indicated in the figure,the level is determined in each PIN spectrum at the crossing point between the noise component and non-celestial background events. Therefore, combined with the calibrated energy scale this "software LD" determines the actual lower-limit energy observable with the relevant PIN diode. Among the 64 PIN diodes, this lower threshold energy distributes from 9 to 14 keV, with an average of $\sim$ 10 keV.

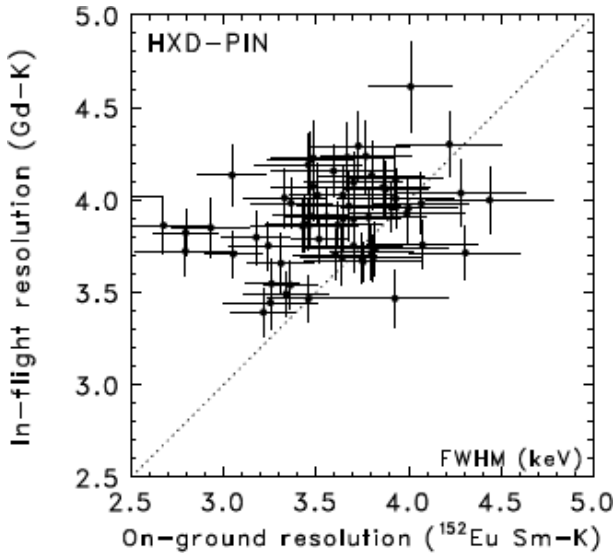

Figure 3.18: Comparison between the energy resolutions of the 64 PIN diodes measured on-ground and in-orbit.

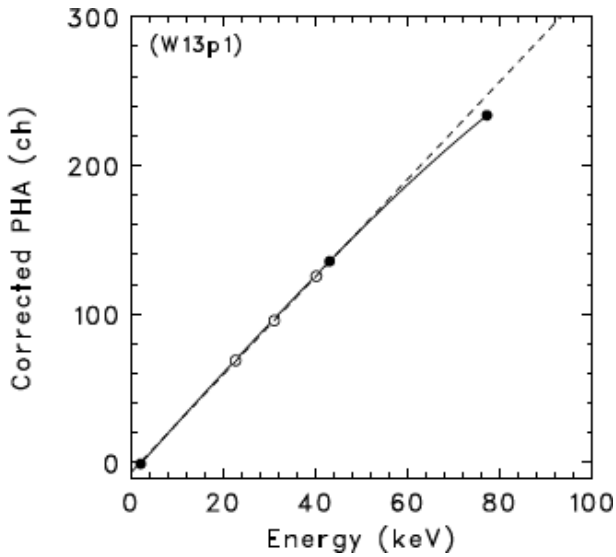

Figure 3.19: Energy vs. pulse height relation of a single PIN diode. Open and filled circles show on-ground and in-orbit data, respectively. Solid line shows a spline curve fitted to the in-orbit data, and the dashed line the linear energy scale determined with the on-ground experiment. The vertical axis shows the ADC channel (PHA).

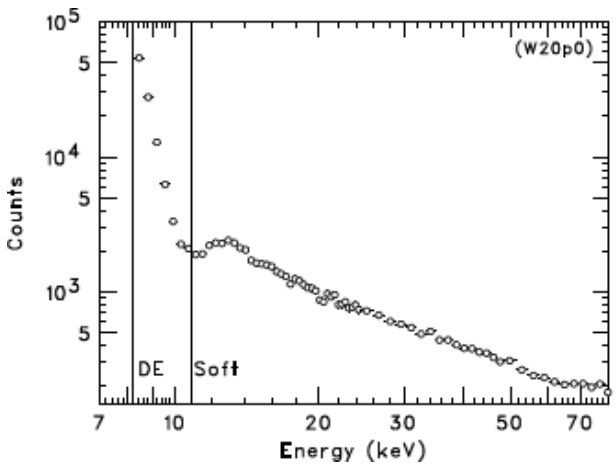

Figure 3.20: An in-orbit background spectrum of a single PIN diode. Two vertical lines indicate the LD level applied in HXD-DE, and the energy threshold used in the on-ground analysis software.

3.5.3 Background reduction

After screening events by the software LD, remaining background events of the PIN detector can be further reduced drastically by the applying anti-coincidence method described in §3.4.2. Figure 3.21 shows background spectra summed over the 64 PIN diodes, under different anti-coincidence conditions. There, the spectrum with the highest count rate was obtained when the PMT high-voltages were set zero, so that the BGO scintillators were working only as passive shields. When the BGO active shields is working and the PSD screening in HXD-AE is enabled, those events that deposits significant energy in BGO are rejected. Thus the background decreases by a factor of 3 (open triangle). The background is further decreased when rejecting events that carry the hit-pattern flag from either the photo-tube on the other three PIN diodes of the same unit (filled triangle).

In orbit, the whole HXD system is always exposed to energetic cosmic-ray particles whose rigidity is higher than several GV, with a typical flux of ~ 1 particle s^{-1} cm^{-2}. When they penetrate the HXD, secondary radiation is likely to be promptly generated, which in turn adds background events to surrounding units. Since most of the particles are charged, their penetration usually causes simultaneous hits to multiple units. Therefore, such background events can be efficiently rejected using "multiplicity", N, which is defined as the number of units with simultaneous hits besides the relevant triggering unit itself. N ranges from 0 up to 35. If we require a valid event to have rather small values of N, the background will decrease, but the actual celestial signal will also decrease due to an

increase of accidental coincidence. In orbit, each unit suffer a raw counting rate of ~ 1 k cts s^{-1}. With a coincidence width of 5.6 μs, we found that accepting only events with $N \leq 1$ is the optimal selection criteria; spectrum after this selection is plotted with open circles in Figure 3.21.

Further optimization studies showed that the following is the optimal anti-coincidence condition (Kitaguchi et al. 2006); requiring $N = 0$ in the surrounding 8 units around the triggering one, and $N \leq 1$ in the remaining 27 units. The final background spectrum is shown with filled circles in Figure 3.21. The net count rate at this condition is only ~ 0.5 cts s^{-1}.

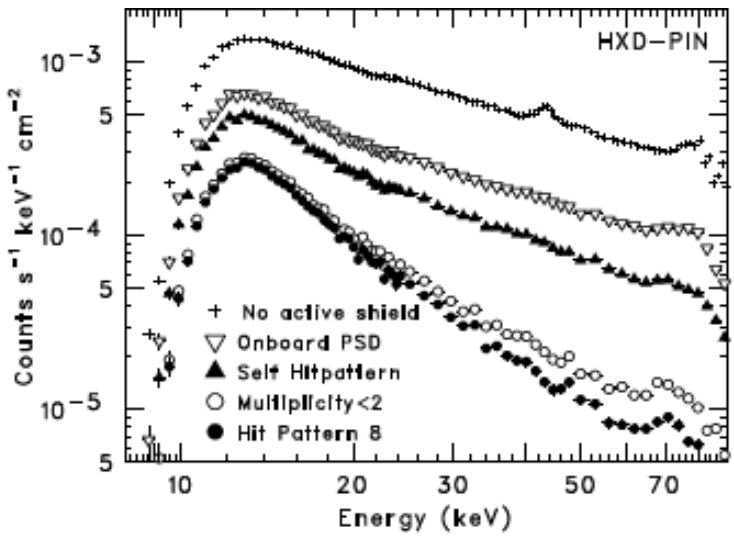

Figure 3.21: The background spectra summed over the 64 PIN diodes, extracted under various anti-coincidence conditions (see text). The spectra are normalized to the total geometrical area of the whole 64 PINs.

3.5.4 Response matrices

A detector response matrix is essential to infer the incident photon spectrum from the raw pulse height spectrum. A raw spectrum $g(P)$, a function of pulse height P, is related to the incident spectrum, $f(E)$, a function of energy E, as

$$g(P) = \int R(E, P) f(E) \mathrm{d}E, \tag{3.1}$$

where $R(E, P)$ is the detector response. Since the pulse heights are obtained as discrete values in an actual detector, the relation becomes

$$\begin{pmatrix} g(P_1) \\ \vdots \\ g(P_m) \end{pmatrix} = \begin{pmatrix} r_{11} & \cdots & r_{1n} \\ \vdots & \ddots & \vdots \\ r_{m1} & \cdots & r_{mn} \end{pmatrix} \begin{pmatrix} f(E_1) \\ \vdots \\ f(E_n) \end{pmatrix}. \tag{3.2}$$

The $n \times m$ matrix r_{ij} is called a detector response matrix.

It is impractical to generate the response matrices based only on experimental data, since we would need to irradiate the detector with X-rays of all possible energies and incident directions. Instead, Monte Carlo simulations provide an essential and powerful tool for constructing response matrices of hard X-ray detectors. Thus, we have developed a Monte Carlo simulator for the HXD, named "simHXD", based on Geant4 toolkit (Geant4 Collaboration et al. 2003). Geometrical parameters are precisely described, together with a chemical composition of each material. Properties of the sensor devices and electronics are also implemented. In-orbit calibration results, such as the energy scale, energy resolutions, and LD levels, are imported into simHXD. The outputs of the simulator can be analyzed in the same way as the actual instrumental data.

The response matrices of HXD-PIN are generated from outputs of simHXD. If we input a number of photons with a particular energy into the detector model of simHXD, we obtain a probability distribution of output pulse heights for that energy. Therefore, by repeating this procedure with energies fully covering the observable bandpass, we obtain the response matrix.

The PIN diodes used in HXD is so thick, ~ 2.0 mm, that their full depletion needs a bias voltage around 700 V (Ota et al. 1999). At the nominal operation voltage of ~ 500 V, which was chosen for safety reasons, the actual thickness of the depletion layer can vary among the 64 PIN diodes. We calibrated the thickness with the following steps; (1) we analyzed the spectra of the Crab Nebula for its slope in an energy range of 45–78 keV, where the diode thickness has little effects. This has given the Crab photon index of 2.12, which is consistent with the canonical value (Kirsch et al. 2005). (2) The overall 15–78 keV Crab spectra were fitted individually by a single power-law model, and the effective thickness was adjusted individually so that every PIN spectrum can be reproduced by the photon index obtained in the previous step.

In order to examine the whole HXD-PIN response, the 64-PIN summed spectrum of the Crab Nebula was fitted with a summed response. Since *Suzaku* has two nominal pointing positions, XIS-nominal and HXD-nominal, corresponding two response matrices

were generated. Figure 3.22 shows the Crab spectra in comparison with predictions of the best-fit power-law models, obtained at these two positions. The fitting was carried out in an energy range of 12–70 keV, by adjusting the model normalization and the model slope, so as to minimize the fit chi-squared. The model parameters obtained in this way, are summarized in Table 3.4. The spectra are well reproduced within a few % over the energy range used in the fitting, while the deviation becomes larger up to $\sim 10\%$ around 10 keV.

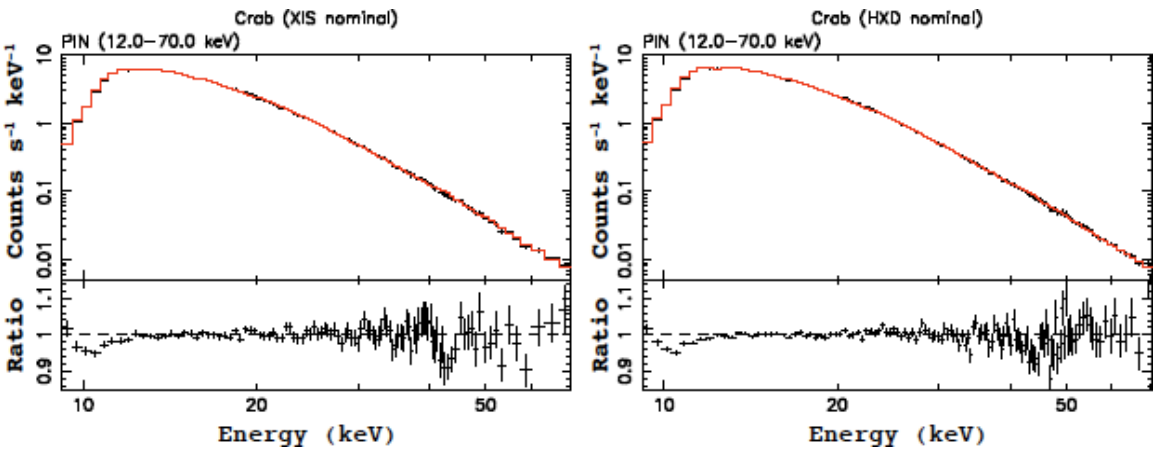

Figure 3.22: HXD-PIN spectra of the Crab nebula obtained at the XIS-nominal (left) and the HXD-nominal (right) positions. The best-fit power-law model, convolved with the response matrix, is shown with red lines. The lower panels show the data-to-model ratios.

Table 3.4: The best-fit parameters and 90% confidence errors for the spectra of the Crab Nebula.

Pointing Position	Photon Index	Normalization	χ^2_ν/ν
XIS-nominal	2.11 ± 0.01	11.7 ± 0.1	1.03 / 152
HXD-nominal	2.10 ± 0.01	11.2 ± 0.1	1.24 / 152

3.6 In-orbit Performance of the HXD-GSO

3.6.1 Energy scale

A pulse height of a GSO event is determined by the light yield of individual scintillators, the PMT gain, the preamplifier capacitance, and the amplifier settings in HXD-AE. The former two factors depends on working temperature. Although the GSO energy scales were calibrated on-ground before the launch, they have changed across the launch (due mainly to vibration effects on the PMT), and are changing since then. Part of this variation is attributed to the temperature fluctuations of HXD-S, but there remains additional unit-dependent short-term and long-term variations which could be occurring in the PMTs.

Similar to the HXD-PIN case, the in-orbit GSO energy scales can be determined using several instrumental lines in background spectra. Figure 3.23 shows a typical GSO background spectrum of a single unit, obtained in orbit. There, there is a broad line feature around 350 keV with a count rate of ~ 0.16 cts s^{-1} per well unit (Takahashi et al. 2007). This line is attributed to α particles from a natural radioactive isotope ^{152}Gd in GSO.

Since the whole HXD volume is exposed to high energy particles including geomagnetically trapped protons in the SAA, several radioactive isotopes are created in GSO. When these activated isotopes decay via electron-capture (EC) and other processes, spectral lines with well defined energies are produced. Indeed, we can see several peaks in Figure 3.23, which have been identified with corresponding isotopes. The most prominent one around 150 keV is attributed to EC decay of ^{153}Gd, with a half life of 241 days. This line can be used as the second calibration anchor. Some of the activated isotopes in GSO and BGO also decay via β^+ decay process, followed by a production of a pair of annihilation lines. Such events are usually detected as "multi-hit" events, since the two 511 keV photons are likely to escape from the relevant unit and hit neighboring units. Thus, by accumulating such events, the 511 keV peak is clearly detected as shown in Figure 3.23.

Thus, the in-orbit background data provides at least three calibration anchor points; 511 keV, 350 keV, and 153 keV. By fitting them with a linear function, we can obtain a first approximation of GSO energy scale for each of the 16 well units. However, the GSO light yield and the HXD-AE performance are known to involve significant non-linearity in energies below $\sim$ 100 keV (Kawaharada et al. 2004). In order to take this effect nonlinearity into account, we express the GSO energy as

$$P = a_i E - b_i + c_i \exp(-E/d_i), \tag{3.3}$$

where E is the photon energy, P is the pulse height (in ADC channel), $a_i, \cdots, d_i$ are positive parameters with $i = 0, \cdots, 15$ representing the unit number. We determine a_i and b_i first using the three anchor points, while c_i and d_i using the activation line at 70 keV and Gd K-edge energy (50 keV), under a condition that P coincides with the pedestal ADC channels.

Figure 3.24 shows the derived energy scale of a single well-counter unit (dashed curve), where the in-orbit calibration data points are overlaid. This empirical energy scales accounts for the calibration points within ±3%, in each unit, over the entire energy range of 50–600 keV.

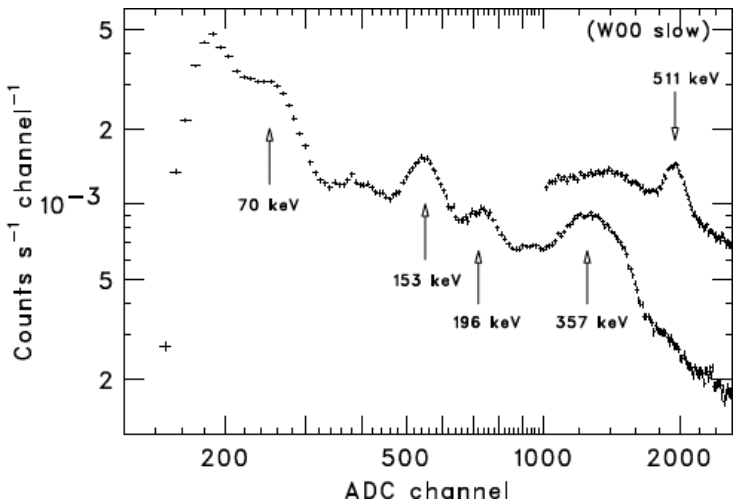

Figure 3.23: A typical in-orbit GSO background spectrum of a single Well unit. Lower data points represent events obtained in the full anti-coincidence condition, while the higher ones indicate those rejected by the condition. The latter spectrum is shown only above 1000 channel for clarity.

3.6.2 Background reduction

As described in §3.4.3 and §3.4.4, GSO background events, namely BGO events or Compton scattered events, can be filtered out in the orbit by the PSD function in HXD-AE and HXD-DE, in an effective and flexible manner. However, there still remains some room for tightening the PSD criteria, in order to acquire spectra with the highest signal to noise ratio. This can be done in the coarse of on-ground analysis, through a process called "software PSD". Kitaguchi et al. (2006) analyzed the two dimensional fast-slow diagram of the Crab Nebula in detail, to find the optimal PSD cut criteria. They successfully

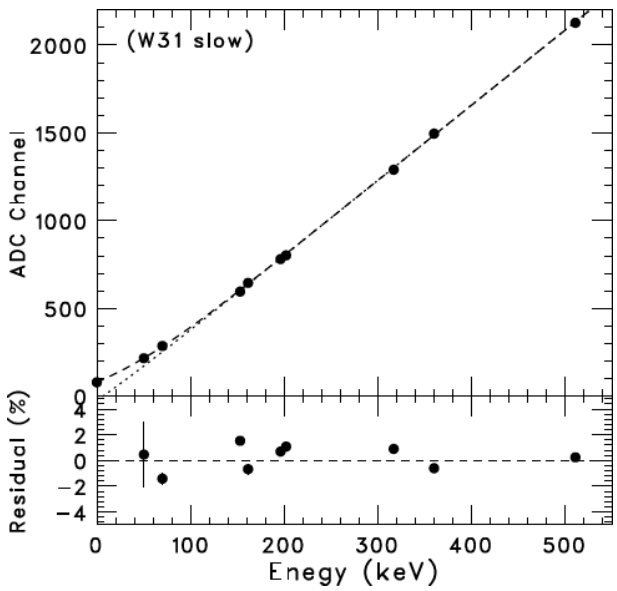

Figure 3.24: GSO energy scale in a single well-counter unit, compared with the calibration points (filled circles). Dashed curve shows the best-fit relation of eq. (3.3). The lower panel shows residuals from the dashed curve.

(HXD-AE plus HXD-DE) halved the GSO background compared to the on-board screening, while keeping the acceptance of celestial signals at 96%. The effects of various PSD cuts on the GSO spectrum is illustrated are Figure 3.25.

Similar to the case of HXD-PIN (§3.5) Kitaguchi et al. (2006) also optimized the anti-coincidence condition for GSO events. They find that the GSO events satisfying either of the following two conditions should be rejected (the same as that for HXD-PIN); (1) It has a simultaneous hit in at least one of the 8 units surrounding the relevant triggering unit. (2) It has at least two simultaneous hits in any units other than the relevant triggering unit. Figure 3.26 illustrates how the anti-coincidence condition reduces the background events, after the PSD cuts are applied. As clearly seen there, it particularly reduces the 511 keV lines, because they are mostly produced by pair annihilation photons which follows nuclear β^+ decays.

3.6.3 Energy response

Response matrices of HXD-GSO are generated in the same way as the HXD-PIN case (§3.5). The employed method, namely Monte Carlo simulation, is particularly important in energies above $\sim$ 100 keV, where most input photons are likely to be Compton-Scattered, hence the off-diagonal elements of the response matrices becomes significant.

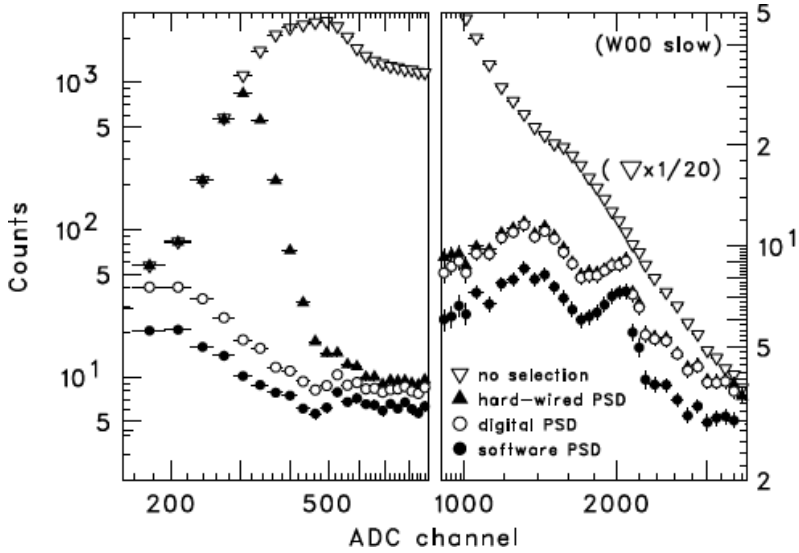

Figure 3.25: Background spectra of scintillators from a single well-counter unit, under various PSD cut conditions; no PSD selection (open triangles), after applying only the hard-wired PSD by HXD-AE (filled triangles), after applying in addition the digital PSD by HXD-DE (open circles), and after further incorporating the software PSD by off-line analysis (filled circles). A rough energy scale in keV is obtained by multiplying the ADC channel by 0.25.

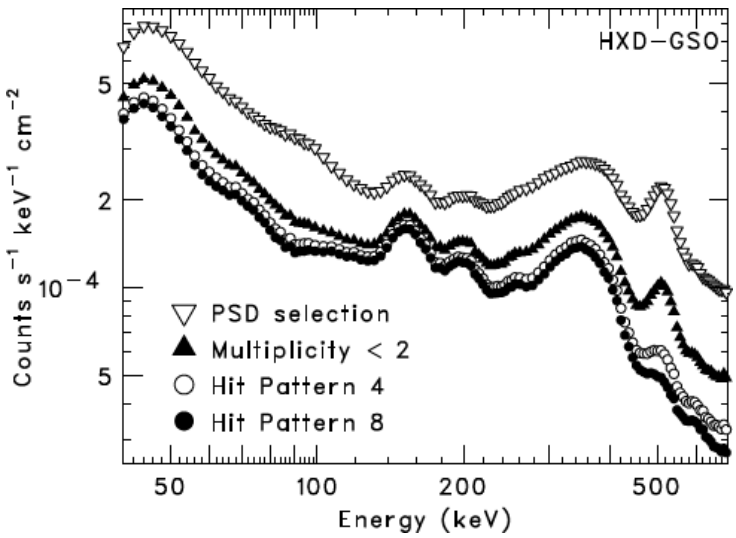

Figure 3.26: GSO background spectra processed with various anti-coincidence conditions, summed over 16 well-counter units.

We show in Figure 3.27 background-subtracted GSO spectra (summed over the 16 units) of the Crab Nebula, taken at the two nominal pointing positions. The backgrounds were taken on the next days of the Crab observations, by pointing onto a blank sky. A single power-law model was fitted to each spectrum, using the corresponding response matrix. The fitting is performed in an energy range of 100–300 keV, to avoid poor signal-to-noise ratio at higher energies, and insufficient tuning of the simulator parameters at lower energies. In this range, the data are successfully reproduced within ±10% by a power-law function, using the best-fit parameters summarized in Table 3.5.

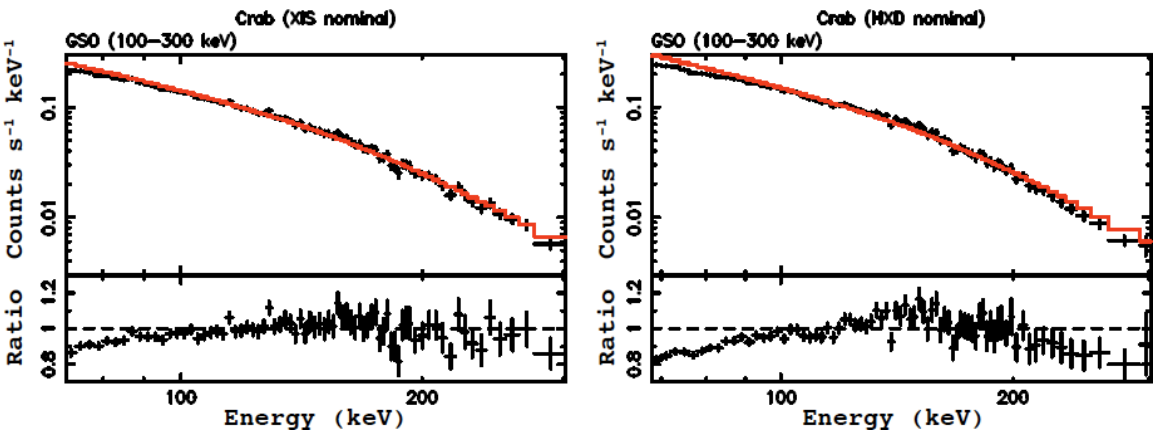

Figure 3.27: Background-subtracted GSO spectra (summed over the 16 Well units) of the Crab Nebula, taken at the XIS (left) and the HXD (right) nominal pointing positions. Overlayed lines (red) are predictions of the best-fit power-law model. The lower panels show the data-to-model ratio.

Table 3.5: The best-fit parameters and 90% confidence errors of the power-law model determined by the 100-300 keV GSO spectra of the Crab Nebula.

Pointing Position	Photon Index	Normalization	χ^2_ν/ν
XIS-nominal	2.12 ± 0.03	10.6 ± 1.4	1.07 / 98
HXD-nominal	2.15 ± 0.03	11.7 ± 1.4	1.50/ 96

3.7 In-orbit Backgrounds of the HXD

As described in Takahashi et al. (2007), the backbone concept in the HXD design is to reduce the background as much as possible to achieve a high signal-to-noise ratio. Unlike

other hard X-ray instruments such as the *BeppoSAX* PDS and the *RXTE* HEXTE, the HXD has been designed to use neither offset detectors (which require extra mass), nor on-off rocking observations (which require extra observing time). Instead, background subtraction of the HXD is performed by modeling the residual non X-ray background (NXB), utilizing such pieces of information as the satellite position, and upper-discriminator count rates. In this section, we first describe basic properties of the actually observed HXD non X-ray background, and then the modeling methods of both PIN and GSO backgrounds.

3.7.1 Common properties of non X-ray background of the HXD

Basically, the NXB of the HXD (PIN and GSO) can be attributed to the following three components (Kokubun et al. 2007);

1. Delayed emissions from radio-active isotopes inside the detector, activated by nuclear interactions mainly by geomagnetically trapped protons.
2. Secondary emissions following interactions between cosmic-ray particles and the spacecraft.
3. Emissions from natural radioactive isotopes in the detector materials.

The third component should stay constant throughout the mission, while the former two components show significant time variations in orbit, in response to the depth of the SAA passage and changes in the cosmic-ray flux. In order to know information on the high energy particles that cause these variations, counting rates of upper discriminator (UD) of the PIN detectors provide a good real-time flux monitor. We show in Figure 3.28 a typical light curve of the PIN-UD count rate, along with the PIN and GSO event rate (after all the screening procedure), and geomagnetic cut-off rigidity (COR) along the spacecraft passage.

The sharp peaks around ~ 2000 cts s^{-1} seen in the PIN-UP rate (top panel of Figure 3.28) indicate the SAA passages, which occur every spacecraft orbit except in ~ 6 "SAA-free" orbits out of the daily 15 revolutions of *Suzaku* . In the middle panel, the real background shows a rather complicated variations than the PIN-UD count rate. This is because the first background component is contributed by many radioactive isotopes with different half lives. The light curve involves at least two major components; (1) "short-nuclides" with half lives shorter than $\sim$ 100 min, which cause a rapid decrease after every SAA passage, (2) "middle-nuclides" with half lives longer than the orbital period ($\sim$ 95 min) but shorter than a day, which produce a gradual increase and decline over

the SAA and SAA-free orbits. In addition, "long nuclides" with half lives of more than a few days are gradually accumulated, until they individually achieve equilibria between the decay and production. This longest component is visible only when we study the background on time scales of months or longer.

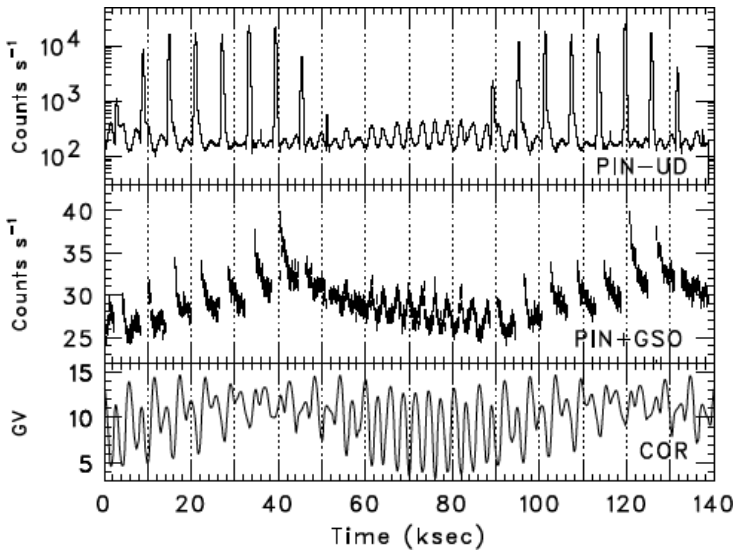

Figure 3.28: Light curves of (top) the PIN-UD count rate summed over the 16 units, (middle) "cleaned" events of PIN plus that of GSO, and (bottom) geomagnetic cut-off rigidity, taken from an observation of a blank sky field.

3.7.2 Background modeling of the HXD-PIN

In the middle panel of Figure 3.28, the PIN+GSO background shows a rather periodic behavior, in addition to the structures related to the SAA. To examine this, in Figure 3.29 (top) we produced a light curve of background events folded with an elapsed time from the SAA (T_SAA), which is reset to zero when the satellite passes through the SAA. Since only data during earth occultations are accumulated in the figure, the CXB is not included. An averaged COR is also plotted (bottom panel). A strong anti-correlation between the NXB and COR is clear, while the NXB is rather weakly correlated with T_SAA itself. This means that the SAA-related variations in the PIN+GSO background occurs mainly in GSO, where the PIN background varies mainly two cycles per orbit in anti-correlation with COR. The latter fact further implies that the NXB of PIN is dominated by secondary emission following interactions between cosmic rays and the spacecraft, rather than short-lived radio isotopes induced during the SAA passages.

An empirical NXB model of HXD-PIN is constructed using actual background data. Since the data should contain neither target sources nor the CXB, an ideal background database is provided by earth occultation data, whose average exposure is $\sim$ 15 ks per day. In the modeling, counts of PIN-UD is used as a monitor of real-time particle flux. The PIN-UD level corresponds to $\sim$ 90 keV, and its hit rate can be regarded as the number of cosmic-ray charged particle penetrating the device. Although the real time PIN-UD count rate can thus be used as a good indicator of the NXB component which directly correlate with COR. Although the overall events in the earth-occultation database may be combined into a single PIN NXB spectrum of very high statistics, it represents a mere long-term average, and cannot describe the factor $\sim$ 2 variations in the PIN NXB (Figure 3.29 bottom). Therefore, we need to divide the overall background events in a series of subsets, each representing a particular condition of data acquisition. As a leading parameter to define the subsets, we have chosen instantaneous hit rates, $u(t)$, of the PIN-UD, set at $\sim$ 90 keV, because this can be regarded as proportional to the cosmic-ray flux, and hence expected to parameterize the COR-dependent changes in the PIN NXB. In addition, to express NXB variations that are correlated with T_SAA but not with COR, we introduced another parameter defined as,

$$v(t) = \int_{-\infty}^{t} u(t_0) \exp\left(-\frac{t-t_0}{\tau}\right) \mathrm{d}t_0, \tag{3.4}$$

where τ is various values of time constant τ was tried between 5000–10000s, and $\tau = 8000$ s was found to best describe the behavior of the earth occultation data. Typical light curves of $u(t)$ and $v(t)$ are shown in Figure 3.30.

In order to make a modeled background spectrum, we first construct the NXB database by accumulating and sorting the earth occultation data by these two parameters. That is, we obtain a template background spectrum $B(E, u_{\mathrm{i}}, v_{\mathrm{j}})$, which is acquired under a condition of $u = u_{\mathrm{i}}$ and $v = v_{\mathrm{j}}$. If an observation with an exposure of $T_0 = \sum_{\mathrm{ij}} T_{\mathrm{ij}}$, where T_{ij} is the on-source exposure attained under $u = u_{\mathrm{i}}$ and $v = v_{\mathrm{j}}$, is carried out, the background $B(E)$ is estimated as $B(E) = \sum_{\mathrm{ij}} \frac{T_{\mathrm{ij}}}{T_0} B(E, u_{\mathrm{i}}, v_{\mathrm{j}})$. The reproducibility of this model is examined by Mizuno et al. (2006), and found to be $\sim$ 4% for a 40 ks exposure.

3.7.3 Background modeling of the HXD-GSO

Unlike the PIN NXB, the GSO NXB is expected to evolve through the mission lifetime, due to the "long-live nuclides". Thus, modeling of the GSO NXB is significantly more difficult than that of the PIN NXB, which does not show evolution after $\sim$ 1 year of

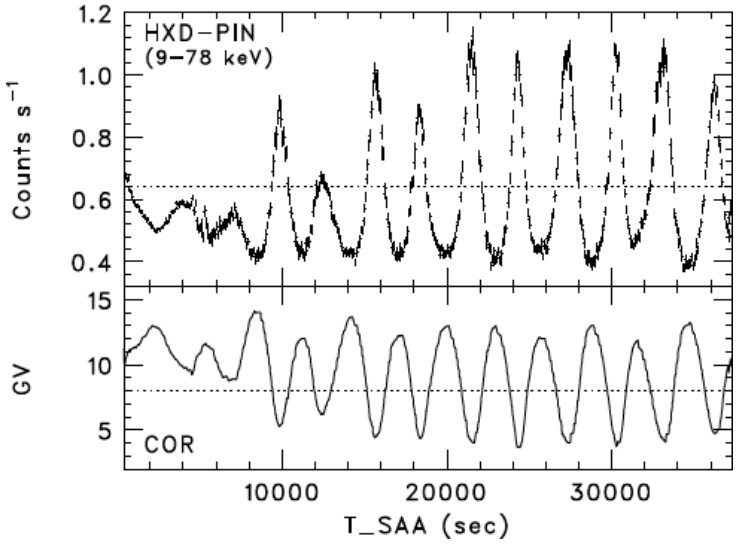

Figure 3.29: Light curves of (top) 9-78 keV PIN NXB folded with T_SAA, accumulated over $\sim$ half a year, and (bottom) COR which is experienced by *Suzaku* , folded in the same way as a function of T_SAA.

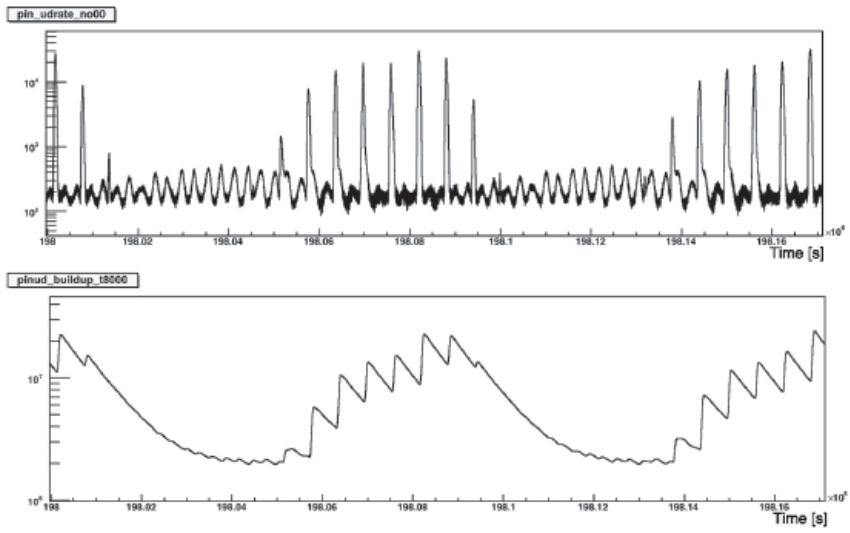

Figure 3.30: Typical light curves of $u(t)$ (top), and $v(t)$ defined by eq. (3.4) (bottom).

operation (Kokubun et al. 2007). We show in Figure 3.31 daily averaged GSO NXB spectra measured at 40, 70, 130 and 220 days after the launch. Several spectral peak, as well as the continuum below $\sim$ 400 keV have kept evolving on a time scale of several months.

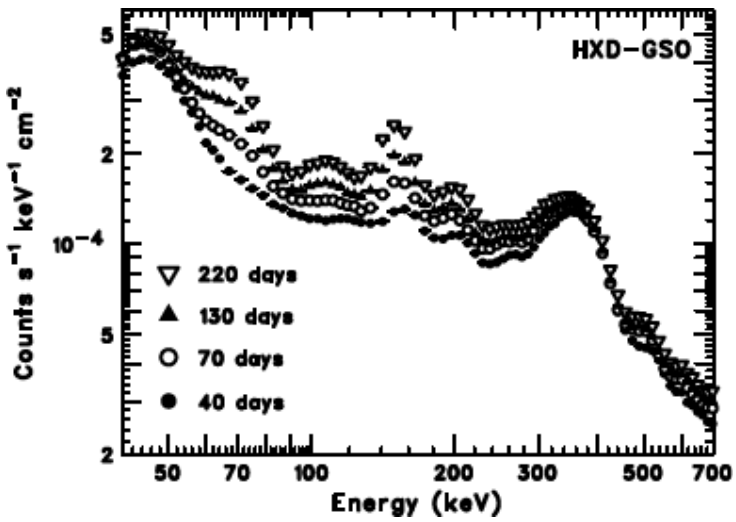

Figure 3.31: A long-term evolution of averaged GSO NXB spectra during the first half year in orbit. Each spectrum has been accumulated for more than a day.

Like in the PIN case, the GSO NXB depends on the COR in energies below 100 keV, but the dependence becomes weaker toward higher energies. Instead, the GSO NXB exhibits much stronger variations as a result of activation induced during the SAA passages. These variations are strongly energy-dependent, because many activated nuclei emit various gamma-ray lines together with the continuum. Therefore, in constructing the NXB model, we directly fit the GSO NXB light curve over an appropriate time period ($\sim$ 1 month) with an empirical model, assuming that the actual NXB of HXD-GSO can be described as a sample functional of $u(t)$, $v(t)$, and a few other parameters. Then, the model is interpolated to estimate the NXB count rate at any given time.

The GSO background light curve to be fitted, is produced typically every month. This is because the GSO NXB gradually evolves, constructing a single and universal NXB database would not be sufficient, unlike the case of PIN. We thus accumulate the GSO NXB data during earth occultations, and extract light curves of in 32 energy bands, with 200-sec binning. Note that this modeling can be applied to the PIN NXB as well; in fact, a part of the public PIN NXB model is based on this modeling, rather than the method described in §3.7.2. There the PIN light curve is analyzed in a single 11–70 keV energy band.

Then we fit each light curve with an empirical model. Various studies derived the empirical model function of the i-th energy band as (Fukazawa et al. 2007);

$$\begin{aligned}\mathrm{NXB_i}(t) &= a_i + \sum_{k=0}^{3} b_{k,i} \int \left(1 + c_{k,i}\frac{90^\circ - \theta_B(t')}{90^\circ}\right) \cdot u(t') \exp\left(-\frac{t-t'}{\tau_k}\right) \mathrm{d}t' \\ &\quad + d_i\ u(t) + e_i\ u(t)^2 \\ &\quad + f_i\ G(t) \left\{1 + g_i \exp\left(-\frac{t - t_{\mathrm{SAA}}}{\tau_g}\right)\right\} \\ &\quad + h_i. \end{aligned} \tag{3.5}$$

Here, $G(t)$ represents GSO count rate in an energy range of 450–700 keV, where celestial signals are less than 0.2% even during the Crab observation. t_{SAA} is an elapsed time from the end of the latest SAA. θ_{B} is an angle between the geomagnetic field and the HXD field of view. This parameter affects the background level, since the SAA particles are expected to enter the tight HXD "wells" more easily when θ_{B} is small. τ_g is set at 10000 sec, and four time constants ($\tau_k, k = 0, \cdots, 3$) are typically set at 1–2 ksec, 10–20 ksec, a few days, and several tens days, depending on the energy bands. Coefficients a_i, $b_{k,i}$, $c_{k,i}$, d_i, e_i, f_i and g_i are the model parameters to be adjusted. The last term in this model, h_i, is a correction bias introduced in order to reduce the current uncertainty as much as possible.

After the model is fitted to the earth occultation data, we create the background light curve in each energy band. Then, fake background events are created, with their pulse heights determined by a Monte-Carlo method referring to the model-predicted counts at a particular time. As shown in Figure 3.32, the pulse height is uniformly and randomly distributed within each energy band. Therefore, users are advised to use exactly the same energy boundaries as the present model, when binning the GSO spectra. According to Mizuno et al. (2007), the reproducibility of this NXB model is 1–2% for a 40 ks observation.

3.7.4 Comparison with other hard X-ray mission

The in-flight background of the HXD is shown in Figure 3.33, in comparison with those of the non-imaging hard X-ray instruments. The background count rate is normalized to the effective area of each instrument. The HXD background spectrum shown here is averaged over August 2005 to March 2006. In the 15–70 keV and 150–500 keV ranges, the HXD thus achieves the lowest background level. In addition, if we employ only non-SAA orbits instead of the averaged HXD spectra, the background can be reduced by 2–20%, especially in the GSO range below 100 keV.

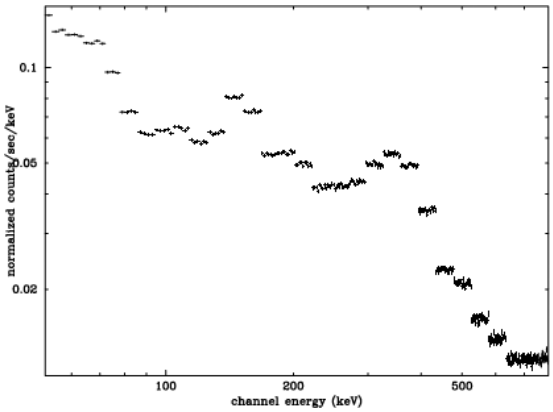

Figure 3.32: An example of fake GSO NXB spectra, derived from the background model.

In order to demonstrate the low-background characteristic of the HXD, we show in Figure 3.34 the spectrum of the Crab nebula obtained with the HXD-PIN and GSO, shown together with the in-orbit background spectrum. The background signals are only a few % of the celestial signal in the 10–50 keV range (HXD-PIN). Even in the HXD-GSO energy range, the celestial signals exceeds the background signals by ~ 5 times up to ~ 100 keV, and are clearly detected up to 400 keV.

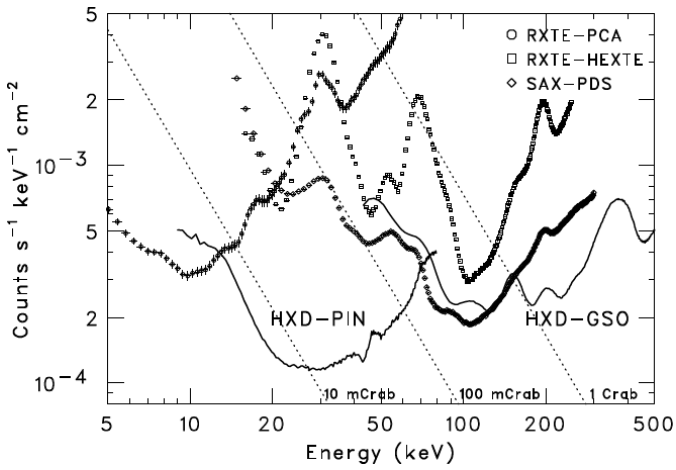

Figure 3.33: A comparison of in-orbit detector background of the HXD with those of *RXTE* (the PCA and HEXTE) and the *BeppoSAX* PDS.

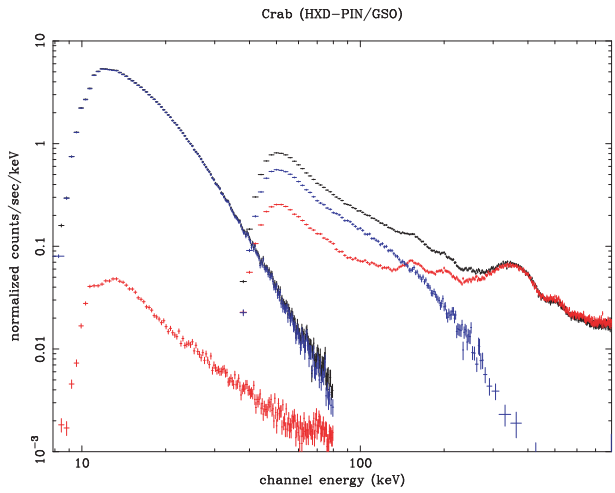

Figure 3.34: The hard X-ray spectra of the Crab nebula, obtained with the *Suzaku* HXD-PIN (< 90 keV) and GSO (> 40 keV). The observed spectra (black) are shown together with the background spectra taken in the orbit (red). The background subtracted spectra are represented by blue crosses.

Chapter 4

OBSERVATION

4.1 *Suzaku* Observations

4.1.1 Performance verification observations

In the first several months after the launch of an astrophysical satellite, it is most important to calibrate the instruments by observing well-understood celestial sources, and to drive the newest scientific results from highlight objects. Such series of observations, performed to verify and demonstrate the expected performance of the satellite, are called "Performance Verification" (PV) observations. The data acquired in this phase are exclusively utilized by "Project Team" for a limited length of time (about 9 months for *Suzaku*), but made publicly available after that. The definition of the Project Team varies, and in the case of *Suzaku* , it consists primarily of those scientists who contributed to the development of the spacecraft and/or instrument (either hardware or software), plus those who help the spacecraft operation. Graduate students supervised by a team member are regarded as "associate" members. After initial start-up operations which took place over ~ 2 months after the launch, *Suzaku* devoted itself to the PV observations until the end of 2006 March, performing more than 200 sets of observations. The targets have been initially selected before launch focusing on the XRS, since its superb capability had been the most anticipated feature of the satellite, and it had a limited cryogenic life time. The XRS, however, was lost unfortunately soon after the launch, due to unexpected evaporation of the cryogenic liquid helium. Therefore, the performance verification targets were re-selected by the Science Working Group of *Suzaku* in 2005 September.

As described in §3.4, the *Suzaku* HXD has a superior sensitivity above 10 keV, compared to other previous hard X-ray instruments. In addition, the *Suzaku* XIS achieves the

high energy resolution (though not as good as the XRS), in conjunction with the large effective area toward higher energies at (4–10 keV), and a very low background (§3.2, §3.3).

Including Seyfert galaxies, AGNs in general have hard energy spectra extending up to hundreds of keV, as well as remarkable iron line and edge complex features around 4–8 keV. Some of them also show the Compton hump around 20–40 keV (§2.4), where HXD-PIN achieves an unprecedented sensitivity. Observing both the line complex and hump is thought to be one of the key techniques to resolve the condition of accreting materials around black hole. Furthermore, simultaneous observations of the two structure are crucial, since the AGN emission is variable. Thus, combining the two working instruments, *Suzaku* is thought to be one of the best observatories to promote the AGN science. As a result, a number of AGN observations were proposed, and 16 have been observed in the PV observation phase. These targets are summarized in Table 4.1.

4.1.2 Guest observations

After the series of PV observations, astrophysical satellite generally enters an open-use phase, and accept observation proposals from astronomical community world-wide. In this way, we can collect brilliant scientific ideas widely to utilize the satellite in the most effective way, and to benefit the community. The submitted proposals are competitively refereed, and only accepted ones will be performed. Such series of observations are called "Guest Observations" (GO). In the case of *Suzaku* , the GO phase started in 2006 April, based on the first announcement opportunity (GO-1) issued in 2005 October.

As described in §2.2, accretion onto a black hole can be to first order characterized by the black hole mass $M_{\rm BH}$ and the normalized mass accretion rate $\dot{m}$. Although the AGN sample observed in the PV phase includes various types of objects, they have rather moderate normalized luminosity, $L/L_{\rm Edd}$. This is because they are required to be well-known, hence X-ray (or hard X-ray) "bright" objects, in order to verify and demonstrate the instrumental capability.

Low luminosity AGN (LLAGN) are known to be radiating with quite low values of $L/L_{\rm Edd}$, by more than an order of magnitude than those ($L/L_{\rm Edd} = 10^{-2} - 10^{-1}$) of typical AGNs. In order to cover objects with significantly lower $L/L_{\rm Edd}$, we thus proposed observations of two Seyfert galaxies which are known to harbor low luminosity AGNs, NGC 4258 and M 81: from previous observations, both AGNs are estimated to radiate at $L/L_{\rm Edd} \lesssim 10^{-3}$. Both AGNs have successfully been observed during the early stage of the

Table 4.1: *Suzaku* observation log of active galactic nuclei during the performance verification phase, together with M 81 and NGC 4258 observed by our GO-1 proposal.

Target name	Type[a]	Start date of observation	Exposure[b] (ks)
ARP 220	Sy2	2006/01/07	100
Cen A	RG	2005/08/19	40
MCG–5-23-16	Sy2	2005/12/07	100
		2005/11/19	40
		2005/12/13	40
MCG–6-30-15	Sy1	2005/08/17	50
		2006/01/09	200
		2006/01/23	50
		2006/01/27	50
MRK 3	Sy2	2005/10/22	100
NGC 2110	Sy2	2005/09/16	100
NGC 3516	Sy1.5	2005/10/12	150
NGC 2992	Sy1.9	2005/11/06	40
NGC 4051	NLS1	2005/11/10	150
NGC 4388	Sy2	2005/12/24	130
NGC 4945	Sy2	2006/01/15	100
		2005/08/22	40
PG 1211+143	NLS1	2005/11/24	100
SWIFT J0746.3+2548	Blazer	2005/11/04	100
0836+714	Blazer	2006/03/15	50
1H 0707–495	NLS1	2005/12/03	100
3C 120	BLRG	2006/02/09	160
M 81	Sy1.8	2006/05/07	100
NGC 4258	LINER/Sy1.9	2006/06/10	100

[a] Allocated maximum exposure; the actual net exposure may be different by $\sim 10\%$, according to the (orbital) condition of the individual observation.

[b] Activity type from the NASA Extragalactic Database (NED). Sy : Seyfert, NLS1 : Narrow line Seyfert 1, BLRG : Broad line radio galaxy, RG : Radio galaxy.

GO-1 phase (Table 4.1). Although the scientific data obtained in the GO phase belong exclusively to the proposer, they will be made public after ~ 1 year after the observation. Thus some of those data obtained in the early stage of GO-1 observations have actually been made public on 2007 October 28th.

4.2 Data Reduction

Scientific data files from X-ray satellites are generally distributed in so called "FITS" format. The files include all the detected "photon events" (including background events), each of them being tagged with such pieces of information as the energy, position, arrival time, event grades, etc. In order to extract the image, for example, we arrange these photon events (usually using only those in a specified energy range) over the sky plane. Similarly, we can make an X-ray energy spectrum by sorting the events (usually using only those in a specified sky region) along the energy axis. In order to extract "proper" (or "the best") scientific images or spectra, however, event screening is necessary in general. In this section, we briefly summarize the event screening criteria for the XIS and the HXD, to be employed in the subsequent stages of the present thesis.

First of all, event files from both instruments were processed using version 1.2 of the *Suzaku* pipeline processing, where the rawest event information is calibrated with the newest gain maps, charge transfer inefficiency, timing information file and so on. Secondly, based on the assembled value such as event grades or satellite attitude, we need to screen the events further (e.g., excluding un-appropriate orbital periods).

4.2.1 XIS data reduction

We used only events with grades 0, 2, 3, 4 and 6, in the XIS event files. Hot and flickering pixels in each of the CCD chip were removed using `cleansis` software. Using `aeattcor` software (Uchiyama et al. 2007), we corrected the event positions for attitude fluctuation due to thermal spacecraft wobbling. Then, we defined Good Time Intervals (GTIs), excluding those observation periods which fulfill at least one of the following conditions:

1. Attitude is not controlled in the pointing mode, or the spacecraft is under a maneuver operation.

2. Distance from the mean pointing position is larger than 1.5 arcmin.

3. Data transfer rate is "low", or the data transfer suffered telemetry saturation,

4. The target elevation angle is less than 5° from the night-time Earth rim, or less than 20° from the day-time Earth rim.

5. The satellite is passing through the South Atlantic Anomaly (SAA), or within 256 sec after an exit from the SAA,

6. The geomagnetic Cut-Off Rigidity (COR) is < 6 GV.

The source spectrum and light curves are extracted from a circular region centered on the source (with a radius of a few arcmin, see §4.4), while backgrounds are from annuli around the source region or other source free regions on the same CCD chip.

4.2.2 HXD data reduction

Either of the proper PIN or GSO events are selected using event grades: 1 for PIN and 0 for GSO. Similar to the XIS case, we made GTIs by excluding those periods that fulfill at least one of the following conditions: (1)–(3): The same as the XIS case. (4) The Earth elevation angle is less than 5°. (5) The satellite is passing through the SAA, or within 500 sec after an exit from the SAA, or within 180 sec to the beginning of the next SAA. (6) The geomagnetic Cut-Off Rigidity (COR) is < 8 GV. Compared to the XIS screening, that of the HXD employs a looser elevation angle condition, while tighter SAA and COR constraints. Therefore the XIS and HXD data use slightly different sets of GTIs.

Even after these careful screenings, the HXD events are rather dominated by residual non X-ray background (NXB) events. In order to estimate and subtract the NXB, we use a time-dependent instrumental background event files provided by the instrumental team (see §3.7), process the fake background events exactly in the same manner as the on-source data, using the same set of GTIs. Then, we can derive, e.g., a pair of spectra (or light curves), one from the on-source event list while the other from that of background. The derived source spectra and light curves need to be further corrected, before the background subtraction, for the detector dead time by counting the "pseudo events" observed in the same intervals (§3.4.3). For sources of moderate brightness, the dead time is usually $\lesssim 5\%$. The NXB spectra and light curve may also need to be corrected for the dead time in the same manner, depending on the method of NXB modeling (§3.7). After these dead-time corrections, we can finally subtract a background spectrum (or a light curve) from the corresponding on-source spectrum (or a light curve).

In addition to the NXB, the contribution of cosmic X-ray background (CXB; Boldt 1987) must be taken into account in the HXD-PIN case. We simulate it using the HXD-

PIN response for diffuse emission, and the widely accepted CXB surface-brightness spectrum (e.g., Gruber et al. 1999) given as

$$N_{\rm CXB}(E) = 10.8 \times 10^{-9} \cdot (E/3\ {\rm keV})^{-0.29} \times \exp\left(-E/40\ {\rm keV}\right)\ {\rm erg\ cm^{-2}\ s^{-1}\ str^{-1}\ keV^{-1}}, \quad (4.1)$$

where E is the photon energy. The CXB count rate is typically 3–8 % of that of the NXB in the HXD-PIN band. On the other hand, the CXB contribution is negligible in the HXD-GSO energy range,

4.3 Target Selection

In the present thesis, we focus on the X-ray observation of edge-on active nuclei in Seyfert galaxies. This is because the primary emission in such objects are usually obscured by the line-of-sight reprocessing material (putative "torus"), and hence, emission from the reprocessing matter can be seen more clearly in such sources than in un-obscured sources. If we follow the AGN Unified Scheme (§2.1.3), a type 2 Seyfert galaxy is expected to harbor rather edge-on nucleus. Previous X-ray observations, however, showed that not all of the Seyfert 2 nuclei suffer strong obscuration in the energy range (Risaliti 2002).

Water maser emission ($\lambda = 1.3$ cm), detected to date in approximately 60 nuclei, is currently the only resolvable tracer of warm dense molecular gas in the inner parsec of AGNs. The great majority of them are classified optically as Seyfert 2 or LINER (e.g., Braatz et al. 1996; Braatz et al. 2004; Greenhill et al. 2003b; Henkel et al. 2005; Kondratko et al. 2006; Zhang et al. 2006). Very Long Baseline Interferometry (VLBI) maps of seven water maser sources have been interpreted in the context of a model in which the maser emission traces a nearly edge-on disk of molecular material 0.1–1 pc from a supermassive black hole (Braatz et al. 1997; Greenhill et al. 1997; Greenhill and Gwinn 1997; Trotter et al. 1998; Ishihara et al. 2001; Greenhill et al. 2003a). As a consequence of these studies, it is believed that maser emission is detected preferentially in edge-on parsec-scale disks. In each object, the maser emission "spots" are arranged in two preferred locations; one along the diameter perpendicular to the line of sight, and the other close to the line of sight toward the center. Indeed, there is an empirical observation that water maser sources are found preferentially in nuclei with large hydrogen column densities ($N_{\rm H} > 10^{24}$ cm^{-2}; Braatz et al. 1997; Madejski et al. 2006; Zhang et al. 2006). Furthermore, the mappings by the spectral line interferometer data with milliarcsecond resolution have provided by far the most accurate measurements of the disk rotation

velocities as a distance from the center, as well as the central engine masses, warp shapes, and disk orientations (e.g., Greenhill and Gwinn 1997; Greenhill et al. 2003a; Herrnstein et al. 2005). We may even obtain distances to the host galaxies kinematically, without using any standard candles (Herrnstein et al. 1999).

By limiting our sample to water maser sources, therefore, we can exclusively pick up edge-on nuclei, and can at the same time know the black hole mass of some of them. This is quite useful, since we will then be free from systematic differences in the viewing angle, and can precisely estimate $L/L_{\rm Edd}$. Thus, we picked up four water maser sources from the AGN samples in Table 4.1. The selected objects and their basic properties are summarized in Table 4.2 where we have added the Circinus galaxy. This source, a canonical megamaser galaxy with Seyfert 2 activity, was observed in the GO-1 phase (PI : Wilson, A.), and the data have already been archived. In three of the five sources, namely Circinus, NGC 4258, and NGC 4945, the information on the mass and distance is available from H_2O maser mappings by VLBI observations. In the subsequent section, we focus on these five sources.

Table 4.2: The selected sample sources and their properties.

Target	D (Mpc)	redshift z	α (J2000.0)	δ (J2000.0)	$\log L_{\mathrm{H_2O}}$ [a] ($L_\odot$)	M_{BH} ($M_\odot$)	References for maser emission
NGC 4388	17 ± 1	0.008419	12 25 46.7	+12 39 44.0	1.1	$\sim 1 \times 10^7$ [b]	(1)
Mrk 3	$\sim 54 \pm 4$	0.013509	06 15 36.3	+71 02 15.0	1.0	$\sim 4.5 \times 10^8$ [c]	(1)
Circinus	4.0 ± 0.8	0.001448	14 13 10.0	−65 20 21.2	1.3	$(1.7 \pm 0.3) \times 10^6$ [d]	(2),(3)
NGC 4945	3.7 ± 0.3	0.001878	13 05 26.1	−49 28 15.0	1.7	$\approx 1.4 \times 10^6$ [d]	(4),(5)
NGC 4258	7.2 ± 0.3	0.001494	12 18 57.5	+47 18 14.3	1.9	$(3.9 \pm 0.1) \times 10^7$ [d]	(6),(7)

(α, β) refer to the detected maser position. The units of right ascension are hours, minutes, and seconds, and declination are degrees, arcminutes, and arcseconds.

[a] Inferred isotropic luminosity of the maser emission.

[b] Estimated from the relation between the bulge K-magnitude and black hole mass (Peng et al. 2006).

[c] Estimated from the stellar velocity dispersion of the galaxy (Woo and Urry 2002).

[d] Enclosed mass within the innermost maser emission, traced by VLBI mappings.

(1) Braatz et al. (2004); (2) Freeman et al. (1977); (3) Greenhill et al. (2003a); (4) Greenhill et al. (1997); (5) Mauersberger et al. (1996); (6) Miyoshi et al. (1995); (7) Herrnstein et al. (1999);

4.4 Observations of Individual Targets

We summarize in Table 4.3 the *Suzaku* observation logs of our sample galaxies. Although the total exposures differ by up to a factor of 2 among the observations, each of them achieves net exposures of $\sim$ 100 ks with the XIS and $\sim$ 80 ks with the HXD. This is mainly because periods when the target is occulted by the earth differ among the observations, depending on the target's position in the sky and the spacecraft orbit at that time.

Figure 4.1–4.5 show images of the sources taken with *Suzaku* XIS 2, extracted in two energy ranges: 0.3–2 keV, 2–10 keV. In the lower energy band, Galactic diffuse emission or other point sources are commonly seen. Above 2 keV, in contrast, the active nuclei can be identified as the most prominent source in the field of view. This in turn implies that all the nuclei are obscured in the lower energy range, exhibiting their signals predominantly at higher energies.

Table 4.3: *Suzaku* observation log of the five water maser AGNs.

Target	Observation Start (UT)	Total Exposure (ks)	Net Exposure (ks) XIS	Net Exposure (ks) HXD	Aiming Position
Circinus	2006/07/21 12:29:57	132.0	108.3	80.5	XIS
NGC 4258	2006/06/10 12:59:29	187.5	99.9	83.6	HXD
NGC 4388	2006/12/24 09:04:19	248.2	125.9	94.4	XIS
NGC 4945	2006/01/15 08:04:39	227.1	90.9	69.7	HXD
MRK 3	2005/10/22 02:02:09	188.6	95.0	81.3	XIS

4.5 Previous Studies on Individual Targets

4.5.1 NGC 4388

NGC 4388 is a low-redshift ($z = 0.00842$), nearly edge-on ($i \sim 78°$) spiral galaxy (Phillips and Malin 1982; Filippenko and Sargent 1985), located near the core of the Virgo cluster. It is optically classified as type 2 Seyfert, with permitted and forbidden emission lines of the same width (Khachikian and Weedman 1974). Hard X-ray observations in early 1990 revealed its nuclear activity similar to that of type 1 Seyferts (Hanson et al. 1990;

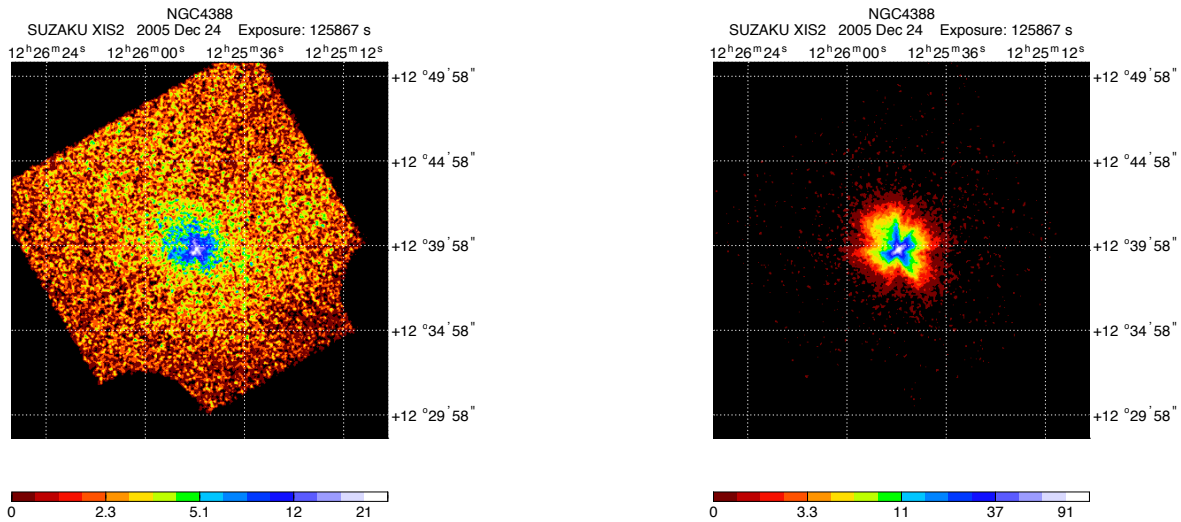

Figure 4.1: *Suzaku* XIS 2 images of NGC 4388, in energy ranges of 0.3–2 keV (left) and 2–10 keV (right).

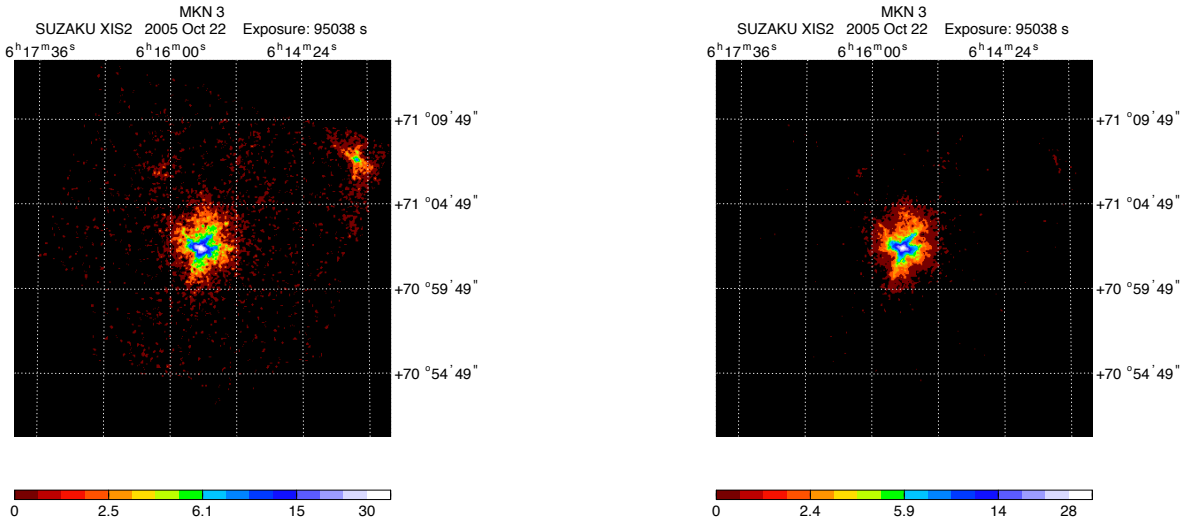

Figure 4.2: The same as Figure 4.1, but for MKN 3.

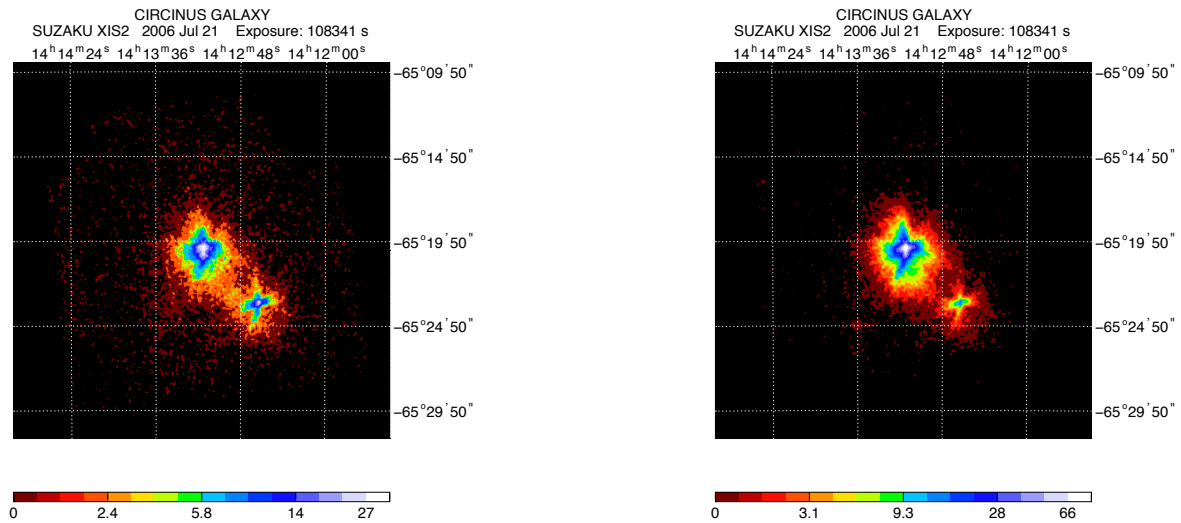

Figure 4.3: The same as Figure 4.1, but for the Circinus galaxy.

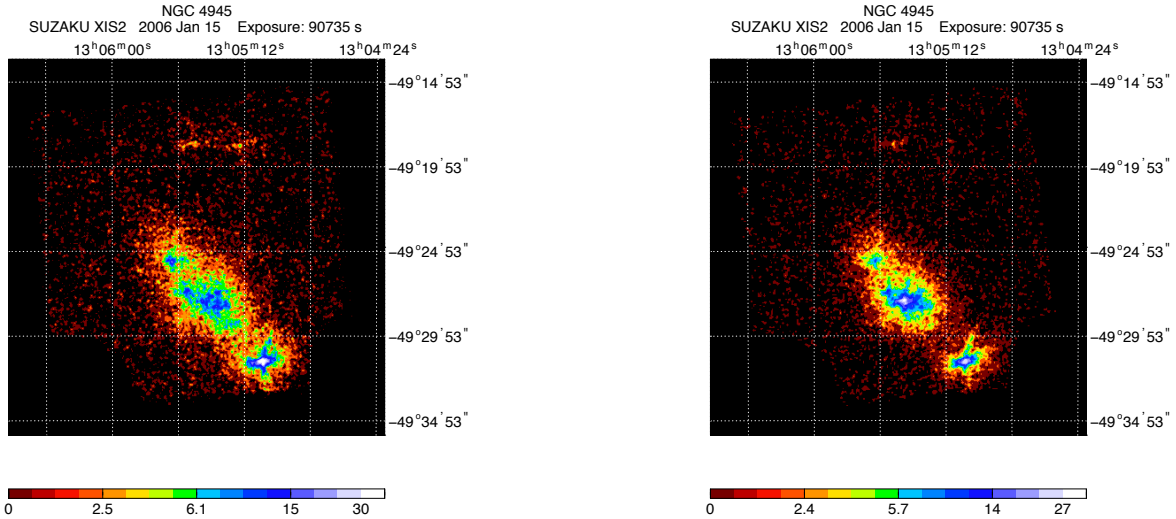

Figure 4.4: The same as Figure 4.1, but for NGC 4945.

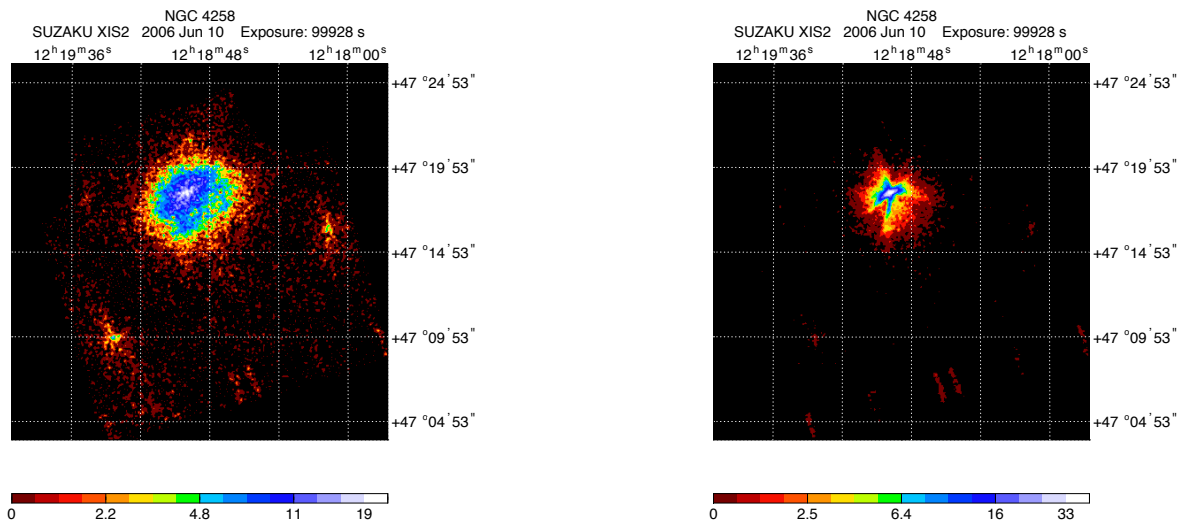

Figure 4.5: The same as Figure 4.1, but for NGC 4258.

Takano and Koyama 1991). Since then, the energy ranges up to ~ 4 keV has been well studied with X-ray missions such as *ROSAT* (Antonelli et al. 1997) and *ASCA* (Iwasawa et al. 1997; Forster et al. 1999). From these observations, it is known to exhibit a strongly absorbed but bright X-ray continuum with an absorption column density of $N_{\rm H} \sim$ a few $\times 10^{23}$ cm^{-2}, and thus the direct nuclear emission appears only above a few keV.

Spectral studies of the hardest X-ray energies up to hundreds of keV have been performed by SIGMA (Paul et al. 1991), and by the OSSE experiment (Johnson et al. 1993) on the Compton Gamma Ray Observatory (CGRO; Gehrels et al. 1993). Similar observations up to 150 keV were performed by the Phoswich Detector System (PDS; Frontera et al. 1997) on board *BeppoSAX* (Butler and Scarsi 1990; Boella et al. 1997). The two *BeppoSAX* observations in 1999 and 2000 showed a high-energy spectrum with a power-law of $\Gamma = 1.6$ and 1.5, respectively. Triggered by the All Sky Monitor onboard the *Rossi X-ray Timing Explorer* (*RXTE*), Elvis et al. (2004) discovered a drastic change of absorbing column: roughly an order of magnitude variation within only 4 hours. This rapid variability corresponds to a scale of a few hundreds Schwarzschild radii, putting some difficulties for a parsec-scale obscuring torus. Recently, Shirai et al. (2008) analyzed the *Suzaku* wide band X-ray spectrum ranging from a few keV up to ~ 100 keV, and found a signature of a reflected emission from near neutral material.

Extended thermal emission in soft X-ray was detected with *ASCA* and *Chandra* (Iwasawa et al. 1997; Iwasawa et al. 2003). The source of this emission is likely to be a photoionized gas with low ionization parameters. In the *Suzaku* soft X-ray image (Figure 4.1), the extended emission as large as ~ 6 arcmin can be seen.

4.5.2 Markarian 3

Markarian 3 (hereafter Mrk 3) is a S0 galaxy at a low red shift of $z = 0.013509$ (Tift and Cocke 1988), and is among a small sample of Seyfert 2 galaxies which show broad emission lines in polarized light; this suggests the presence of a "hidden Seyfert 1 nucleus" (e.g., Miller and Goodrich 1990; Tran 1995). Other evidence in favor of heavy obscuration includes the discovery of a biconical extended narrow line region (Pogge and De Robertis 1993); the low flux of ionizing photons inferred from the directly observed UV continuum, compared to the ionizing photons required to produce the observed Hβ emission (Haniff et al. 1988, Wilson et al. 1988); the low $L_{\rm X}/L$[OIII] ratio (0.14; Bassani et al. 1999); and the observation of heavy X-ray obscuration.

Ginga data showed that the spectrum of Mrk 3 is flat ($\Gamma \sim 1.3$), absorbed by a thick column density of $N_{\rm H} \sim 6 \times 10^{23}$ cm^{-2}, and is accompanied by a strong iron line with an equivalent width (EW) of $\sim$ 500 eV (Awaki et al. 1991). At higher energies, Mrk 3 was detected by the OSSE for the first time in March 1994 at a flux level of $\sim 2.8 \times 10^{-11}$ erg cm s^{-1} in the 50–150 keV energy band (Cappi et al. 1999). *ASCA* observations revealed that the Fe Kα line emission decreased by a factor of 3 in response to a flux decline by a factor of 6 (Iwasawa et al. 1994). *ASCA* also resolved the iron line into a 6.4 keV component of EW $\sim$ 900 eV and a 6.7 keV one of EW $\sim$ 190 eV (Iwasawa et al. 1994). Because of the large column density of intervening cold matter, the intrinsic X-ray continuum is hardly visible directly. Instead, the X-ray studies with *ASCA* (Turner et al. 1997) and *BeppoSAX* (Cappi et al. 1999) have suggested that the observed X-ray flux over the 2–10 keV band is dominated by indirect radiation; "reflected" (i.e. redirected by scattering in optically-thick matter) into the line of sight.

Measurements at lower X-ray energies revealed the presence of a soft excess and also indicated the presence of prominent soft X-ray emission lines (Kruper et al. 1990; Turner et al. 1993; Iwasawa et al. 1994). An extended soft X-ray emission component was resolved in an early *Chandra* observation (Sako et al. 2000a), which also showed the soft X-ray spectrum to be dominated by blue-shifted line emission from highly ionized gas.

4.5.3 The Circinus galaxy

The Circinus galaxy (hereafter Circinus) is a highly inclined ($\sim 65°$) SA(s)b galaxy harboring a type 2 Seyfert active nucleus as well as a nuclear starburst. At about 4 Mpc distance (1 arcsec $\sim$ 20 pc, Freeman et al. 1977), the galaxy is among the nearest AGN and hence it is an ideal object to study the nuclear region of active galaxies. This galaxy was discovered rather recently, in 1977 (Freeman et al. 1977), because it is located almost behind the Milky Way. The galaxy can be considered as a prototypical Seyfert 2 object due to the presence of narrow emission lines (Oliva et al. 1994), broad emission lines in polarized light (Oliva et al. 1998), an ionization cone traced by [OII], Hα and [SiVII] (Veilleux and Bland-Hawthorn 1997; Maiolino et al. 2000; Wilson et al. 2000; Prieto et al. 2004), an outflow observed in CO (Curran et al. 1998; Curran et al. 1999), and bipolar radio lobes (Elmouttie et al. 1998). The ionization cone, the outflow and the radio lobes have a position angle of about $-40°$, which is roughly perpendicular to the disk of the galaxy, to the circum-nuclear star forming rings and to the nuclear rings of molecular gas.

Greenhill et al. (2003a) performed a VLBI mapping of H_2O maser emission, constructed from data obtained with the Australia Telescope Long Baseline Array. The maser emission traces a warped, edge-on accretion disk between radii of 0.11 ± 0.02 and ~ 0.40 pc, as well as a wide-angle outflow that extends up to ~ 1 pc from the estimated disk center. The disk rotation is close to Keplerian ($v \propto r^{-0.5}$), with the maximum detected rotation speed is 260 km s^{-1}. This yields a central mass of $(1.7 \pm 0.3) \times 10^6\ M_\odot$.

The first X-ray observation was performed during the *ROSAT* All Sky Survey (Brinkmann et al. 1994). A reflection dominated spectrum was revealed by *ASCA* , together with a prominent neutral iron Kα line and a number of other lines from lighter elements (Matt et al. 1996b). The spectrum is fully consistent with reflection from the inner surface of a mildly ionized material, and the same matter is likely to be responsible for the absorption of the nuclear radiation. The *BeppoSAX* observation added a precious piece of information: detection of the direct nuclear emission above ~ 10 keV, absorbed at lower energies by a Compton-thick ($N_{\rm H} \gtrsim 4 \times 10^{24}$ cm^{-2}) material, which is usually identified with the torus envisaged in unification models (Matt et al. 1999a; Guainazzi et al. 1999).

4.5.4 NGC 4945

NGC 4945 is a nearby (located at a distance of ~ 3.7 Mpc, Mauersberger et al. 1996) almost edge-on (with an inclination $i \sim 78°$, Ott et al. 2001) spiral galaxy classified as SB(s)cd. It exhibits both a prominent dust lane crossing its plane, and an H_2O megamaser (Dos Santos and Lepine 1979). It is the third brightest extragalactic source in the IRAS point source catalog, and most of its infrared emission is concentrated in a compact nuclear region (Rice et al. 1988; Brock et al. 1988). It shows starburst emission (Heckman et al. 1990; Koornneff 1993). A region of extended optical-line emitting gas protrudes from the nucleus along the galaxy minor axis (Nakai 1989; Heckman et al. 1990). It is associated with a cavity open by a star-burst superwind (Moorwood et al. 1996b).

At wavelengths longer than 1 keV, all its observational properties can be accounted for by the starburst activity alone, despite its classification as a Seyfert in the Veron-Cetty and Veron (1989) catalog. For instance, a mass-to-light ratio of 0.18 is consistent with the parameter space solely occupied by starbursts (Oliva et al. 1999). Also, in the Genzel et al. (1998) ISO diagnostic planes, NGC 4945 is located in the regions occupied by starbursts. However, the presence of a strong continuum radio source and studies of the off-nuclear optical spectra have suggested the presence of a LINER (Whiteoak and Gardner 1979; Moorwood et al. 1996b).

Greenhill et al. (1997) presented the interferometer map of the water maser in NGC 4945, observed with VLBI. Unlike NGC 4258, the observed emission does not trace a smooth rotation curve expected from a well ordered disk. But assuming this irregular, clumpy distribution still traces orbital motion gives an estimate of the central black hole mass of $\sim 1.4 \times 10^6\ M_\odot$. X-ray observations provided the final proof for the presence of an active nucleus. X-ray observations with *Ginga* unveiled a highly obscured, strongly variable X-ray source (Iwasawa et al. 1993). This demonstrates that hard X-ray emission can be the most efficient wavelength to identify the nature of obscured AGNs (see e.g., the discussion in Vignati et al. 1999). Actually, in the 100 keV sky, NGC 4945 turned out to be the brightest Seyfert 2 and the second brightest radio-quiet AGN after NGC 4151 (Done et al. 1996). While the *Ginga* spectrum above $\sim$ 10 keV revealed the highly absorbed hard nuclear emission, a softer component below $\sim$ 10 keV was successfully fitted with a simple power-law with a photon index of about 1.7, interpreted as scattering of the primary nuclear continuum (Iwasawa et al. 1993). The same description fits also the non-simultaneous OSSE spectra (Done et al. 1996). An iron line with a huge equivalent width of 1–1.5 keV has been observed as well, whose centroid energy is consistent with Kα fluorescence from neutral or mildly ionized iron. Observation by *ASCA* revealed a hard continuum below $\sim$ 10 keV, and strong iron line complex, showing that the reprocessed emission dominates in that energy range (Turner et al. 1997). Using *XMM-Newton*, Schurch et al. (2002) found both neutral and ionized iron lines in the reprocessed nuclear emission, but their origins (especially of the latter one) remain rather unclear even with the superb spatial resolution of *Chandra* (Done et al. 2003).

4.5.5 NGC 4258

NGC 4258 (M 106) is a highly inclined (72°, Tully 1988) SABbc spiral galaxy located nearby at a distance of 7.2 Mpc, i.e., $1'' = 35$ pc (Herrnstein et al. 1999). It is spectroscopically classified as a 1.9 Seyfert galaxy (Ho et al. 1997). The strong polarization of the relatively broad optical emission lines (Wilkes et al. 1995) supports the existence of an obscured active nucleus in NGC 4258. Turner and Ho (1994) detected a very bright radio continuum nuclear source, showing, in observations from March 1985 through to May 1990, long term time variability by 47% both at 6 and 20 cm (Hyman et al. 2001).

The water maser emission of NGC 4258 is remarkable because the disk is extremely well described by a relatively simple dynamical model (Miyoshi et al. 1995; Greenhill et al. 1995a; Greenhill et al. 1995b). The maser emission has been mapped from radii

of 0.14–0.28 pc, indicating the presence a massive nuclear black hole with the mass of $3.6 \times 10^7\ M_\odot$. Maser positions, line-of-sight velocities and accelerations, and proper motions are all measurable, and they fit a simple geometrically thin, highly inclined ($\sim 83°$), and slightly warped Keplerian disk model to high accuracy (Herrnstein et al. 1999).

In X-rays, *ROSAT* PSPC and HRI observations of NGC 4258 (Pietsch et al. 1994; Cecil et al. 1995; Vogler and Pietsch 1999) resolved diffuse emission mostly connected to an "anomalous" arms around the center, and emission from point sources in the galaxy. However, due to the soft energy band (0.1–2.4 keV) only upper limits can be derived for emission from the nucleus. *ASCA* observations of NGC 4258 extended the energy coverage to 10 keV with improved spectral resolution. Makishima et al. (1994) discovered, for the first time, a hard, highly absorbed point-like component that could be modeled by an absorbed power-law , with $N_{\rm H} \sim 1.5 \times 10^{23}$ cm^{-2}, photon index of $\Gamma \sim 1.78$, and unabsorbed luminosity of $\sim 4 \times 10^{40}$ erg s^{-1} in the 2–10 keV band. They also found an iron Kα emission line with an equivalent width of 250 ± 100 eV. Further *ASCA* observations improved on the spectral parameters of the hard component, confirming a narrow iron Kα emission line at $6.45^{+0.10}_{-0.07}$ keV with an equivalent width of 107^{+42}_{-37} eV (Reynolds et al. 2000). Recent observations from *XMM-Newton* tend to find much lower EWs and, in many cases, only upper limits (Pietsch and Read 2002; Fruscione et al. 2005).

Time variability of the 5–10 keV flux and probably also the absorbing column of the hard component has been seen on timescales from 19 days to years, with little change in the power-law index (Reynolds et al. 2000; Terashima et al. 2002; Fruscione et al. 2005). *BeppoSAX* observations extended the spectral coverage of the power-law component to 70 keV (Fiore et al. 2001). Wilson et al. (2001) have recently reported the results of a *Chandra* observation optimized to investigate the X-ray emission from the "anomalous arms".

Chapter 5

ANALYSIS AND RESULTS

5.1 NGC 4388

5.1.1 XIS data analysis

We choose NGC 4388 as our first source to be analyzed, because it is known as a typical Seyfert 2 AGN with a moderate absorbing column ($N_{\rm H} \sim 10^{23}$ cm^{-2}). Although the *Suzaku* results on this object have already published by Shirai et al. (2008), we re-analyzed the data for consistency with the other targets.

Suzaku XIS0 images of NGC 4388 are shown in Figure 5.1, in the two energy ranges of 0.3–3 keV and 3–10 keV. The soft band image reveals an apparently diffuse emission extending up to $\sim 6'$ toward the north of the nucleus. In contrast, the emission from the nucleus is quite dominant in the hard band image, and no other emission components are indicated considering the PSF of the telescope. Indeed, soft X-ray studies utilizing higher spatial resolution instruments, such as *ROSAT* (Antonelli et al. 1997), *XMM-Newton* (Beckmann et al. 2004), and *Chandra* (Iwasawa et al. 2003) indicate that the extended soft X-ray morphology represents thermal emission from a hot plasma with a temperature of $T \simeq 0.8$ keV, associated with a host galaxy or the Virgo cluster in which NGC 4388 is located. The thermal emission, with a soft energy spectrum and without variability over years, does not contribute to the spectrum above 3 keV (Beckmann et al. 2004). Since these thermal emissions are beyond the scope of the present thesis, we use data only above 3 keV in the subsequent analysis.

After appropriate event screening (§4.2), we obtained a total net exposures of ~ 126 ks from each XIS sensor. We extracted the source events within a circular region indicated by a black solid circle in the images, with a radius of $4'.34$, where more than 99% of

the source events are contained. This radius corresponds to 6 mm on the CCD chip, and to 21.5 kpc in physical size at a distance of 17 Mpc. The background events were extracted from annulus regions surrounding the source regions in the same CCDs. In order to avoid high background and response uncertainly at high energies, we restrict our spectral modeling to 3.0–9.0 keV for the FI chips and to 3.0–8.0 keV for the BI chip. The background count rates in the relevant energy ranges are $\sim 7\%$ of the total events for the FI chips and $\sim 10\%$ for the BI chip. In the same energy range, we obtained the background subtracted count rates of 1.055 ± 0.003 cts s^{-1} and 0.283 ± 0.003 cts s^{-1} for the FI and BI, respectively.

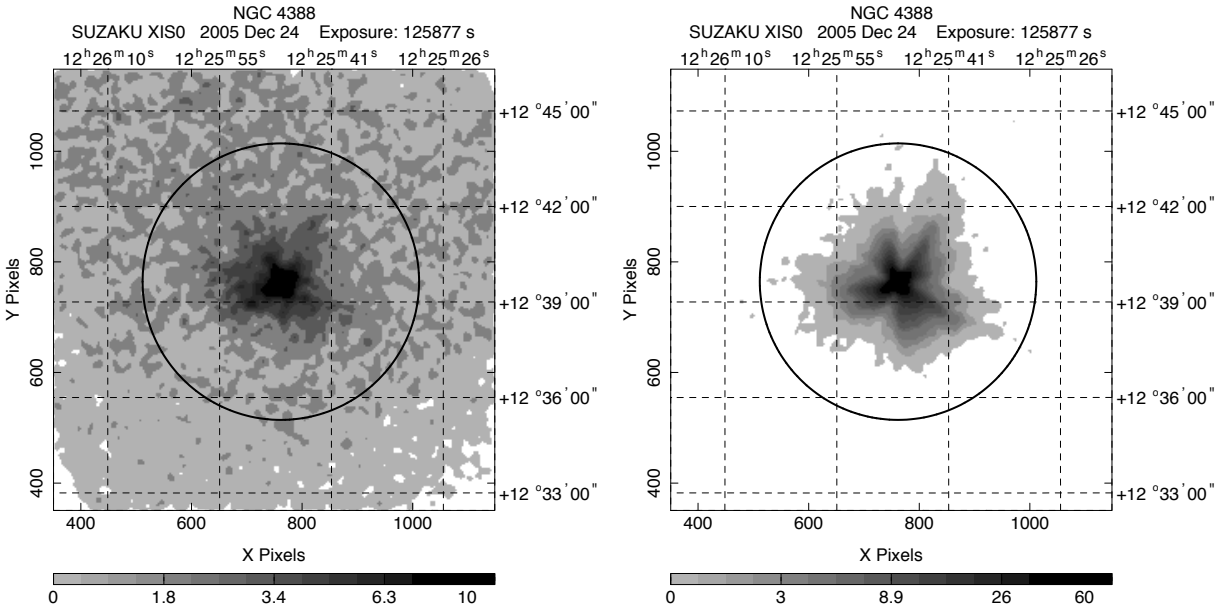

Figure 5.1: Background-inclusive *Suzaku* XIS images of NGC 4388, in the 0.3–3.0 keV (left) and 3-9.0 keV (right) band. Only events from XIS0 sensor are used. The source events are extracted within the black solid circles whose radius is $4'.3$, corresponding to 6.0 mm on the sensor.

5.1.2 HXD data analysis

Figure 5.2 shows the energy spectra of NGC 4388 taken with HXD-PIN (below 60 keV) and HXD-GSO (above 50 keV), in comparison with their backgrounds. The background spectrum of HXD-PIN includes not only the non X-ray background (NXB; §3.7), but also the contribution from the CXB. The CXB count rate is estimated to be only $\lesssim 7\%$ of the NXB, and hence $\sim 5\%$ of the net source signals. The HXD-GSO background does not include the CXB since it is negligible in the relevant energy range.

As indicated by the lower panel of Figure 5.2, the net source count rate of HXD-PIN

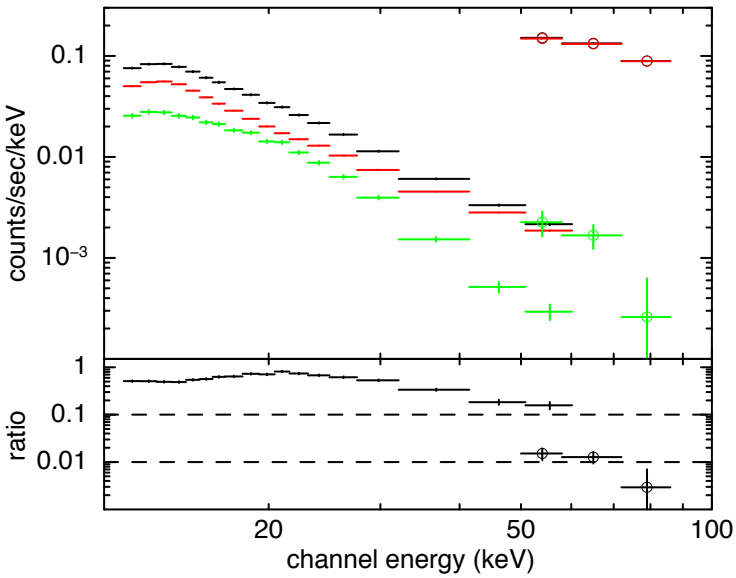

Figure 5.2: HXD-PIN and HXD-GSO spectra of NGC 4388. In the upper panel, the total spectra (source plus background) are shown in black, the estimated background (NXB+CXB) spectra in red, and the net source (total minus background) spectra in green. The lower panel shows the ratio of the net source to the background spectra. In both panels, crosses and circles correspond to data points of HXD-PIN and HXD-GSO, respectively.

exceed, over its whole energy range, 10% of the NXB rate. According to Mizuno et al. (2007) who compared Earth-occultation data with the modeled NXB spectra (§3.7.2), the systematic error in the NXB modeling is $\pm \lesssim 3\%$ for a typical observation period of 1 day. Since our net exposure is three times longer than the typical one utilized by Mizuno et al. (2007), the systematic NXB uncertainty must be even smaller. In the following spectral analysis, we therefore use the entire energy range of HXD-PIN, where the systematic NXB uncertainty is estimated to be smaller than the statistical errors. The background-subtracted source count rate in the energy range, with statistical errors, is 0.290 ± 0.003 cts s^{-1}, which is $\sim 53\%$ of the background rate (NXB plus CXB, 0.543 cts s^{-1}).

In the HXD-GSO spectrum, the net source counts are only $\sim 1\%$ of the background even in the 50–100 keV range. In a similar way to the HXD-PIN case, the current NXB uncertainly of HXD-GSO is estimated to be $\sim 2\%$ for a 1 day observation. Considering this, we cannot claim the source detection with HXD-GSO. We therefore do not include the HXD-GSO data in our subsequent spectral fitting.

5.1.3 Broad-band spectrum

Before actually analyzing the X-ray spectra from our target sources, let us briefly describe a "reference object" in the X-ray sky, namely the Crab Nebula. The Crab nebula is a remnant of a supernova which occurred in 1054, whose explosion itself was historically recorded by Chinese astronomers. As first discovered by Gursky et al. (1963), it is one of the brightest objects in the X-ray to gamma-ray sky. Unlike other strong X-ray sources (mostly accreting objects), the Crab exhibits no X-ray variations (except the 30 Hz pulsations with an amplitude of a few percent), because the emission comes from an extended (a few light years) region via synchrotron process. Over $\sim$ 0.1–100 keV, the X-ray spectrum of the Crab is well reproduced by a simple absorbed power-law with a photon index of 2.12 (e.g.,§3.5.4; Kirsch et al. 2005). From these characteristics, the Crab nebula has been used as a calibration target by many X-ray/hard X-ray astronomical instruments. *Suzaku* has also observed the Crab several times, typically every 6 months.

Since the Crab has a single power-law spectrum with a photon index of $\sim$ 2, if a source energy spectrum is normalized to that of the Crab nebula, the ratio spectrum can be regarded as an approximate $\nu F\nu$ spectrum. Such a ratio plot is quite useful, since we can grasp the overall spectral feature without knowing the detector response. Hereafter we call such ratio spectrum a "Crab ratio" of the relevant target.

Figure 5.3 shows the 3–80 keV Crab ratio of NGC 4388. At the first glance, the spectrum below 6 keV is impressive with its steep decline toward lower energies. This is considered to provide the evidence that the underlying nuclear emission is obscured by a considerable degree of the absorbing column. There are also remarkable features around 6–8 keV, including an emission line and a sharp edge. Such structures indicate the presence of reprocessed emission of the nuclear primary continuum. The slope around 7 keV is still hard but gradually softens toward $\sim$ 20 keV, implying that the intrinsic power-law emerges because the cross section of photoelectric absorption decreases roughly as E^{-3} as a function of the X-ray energy E. The ratio shows a slight convexness around 20–50 keV, suggesting the presence of a Compton hump, which is also a characteristic associated with a reflected continuum.

5.1.4 Baseline Continuum model of obscured AGNs

In order to approximate the overall X-ray continua of obscured AGNs, we introduce a rather simple model to be called Baseline Continuum (BC) model. It consist of an absorbed power-law continuum with high energy exponential cutoff ($\gtrsim$ 100 keV), and a

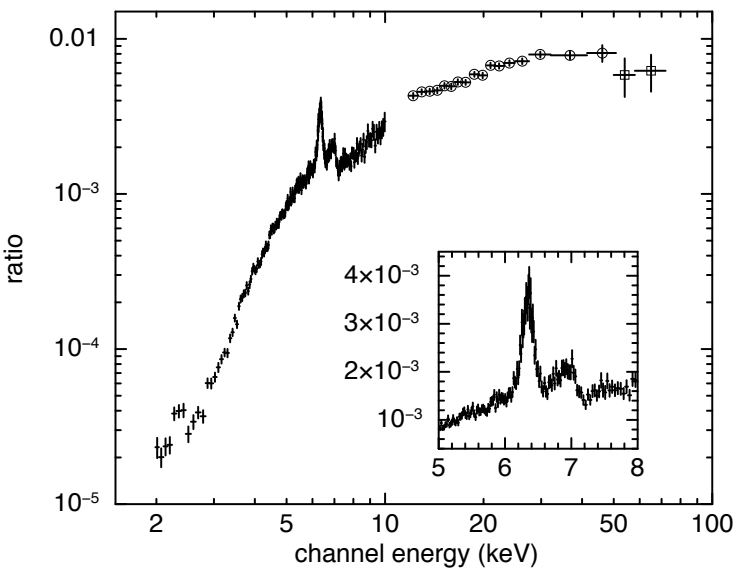

Figure 5.3: The background-subtracted *Suzaku* spectra of the nucleus of NGC 4388, normalized to those of the Crab nebula. The XIS-FI , HXD-PIN and HXD-GSO data points are marked with crosses, circles and boxes, respectively. (Insert) A zoom of the 5–8 keV band, with the flux in linear scale. The XIS-BI data are omitted just for clarity.

reflection continuum by a cold matter which is absorbed by the column of our Galaxy only. We multiply the first component by an energy-dependent factor of the form $\exp\{-N_{\rm H}\sigma(E)\}$, where the cross-section $\sigma(E)$ generally includes the effects of both photo-electric absorption and Compton scattering. The latter component is based on an assumption that some fraction, $f_{\rm refl}$, of the primary power-law is reflected from cold (neutral) materials, and reaches us without further absorbed by the obscuring matter that affects the first component.

We calculated the cold reflection in the BC model using a model called `pexrav` in XSPEC (Magdziarz and Zdziarski 1995), which reproduces a reflected continuum and a neutral iron edge structure at ~ 7.1 keV. Note that it does not account for any fluorescent lines although they are physically expected. This model assumes a situation where the intrinsic power-law from the nucleus is reflected by a slab of neutral matter, which extends a solid angle of Ω as seen from the central source. The spectral slope and exponential cutoff energy of the assumed incident emission is set equal to those of the intrinsic power-law. This model, thus, has three free parameters; the reflection fraction ($f_{\rm refl} \equiv \Omega/2\pi$), cosine of the inclination angle of the slab as seen from the observer ($\cos\theta$, $\cos\theta \sim 0$ for face-on view and ~ 1 for edge-on), and iron abundance ($A_{\rm Fe}$). While the strength of the reflected component scales roughly as $\propto \cos\theta$, its spectral shape does not depend strongly

on $\cos\theta$. As a result, the value of $\cos\theta$ degenerate with $f_{\rm refl}$, and is not well constrained by the data. In the following spectral fitting throughout this chapter, therefore, we fix $\cos\theta$ at 0.5. We also fix $A_{\rm Fe}$ at 1.0, unless otherwise stated.

5.1.5 Spectral fitting

We first fitted the background-subtracted XIS and HXD-PIN spectra of NGC 4388 simultaneously with the BC model. We fixed the absorbing column of our Galaxy toward NGC 4388 at 2.62×10^{20} cm^{-2}. Here, the energy range between 6.0 and 8.0 keV was not used in the fitting, in order to avoid the emission line/edge complex. The data, the best-fit BC model, and the fit residuals are shown in Figure 5.4, where we restore data in the 6.0–8.0 keV range to highlight the complex structure there. As seen in the figure, this model roughly reproduced the overall continuum shape, with a fit statistics of $\chi^2/\nu = 246.0/198$. The absorbing columns, photon index of the intrinsic power-law, and the reflection fraction were estimated to be $N_{\rm H} \sim 3.5 \times 10^{22}$ cm^{-2}, $\Gamma \sim 1.75$, and $f_{\rm refl} \sim 1.9$, respectively. The right panel of Figure 5.4 compares the data and the model in the iron-complex energy region which was excluded in determining the model. The figure reveals evidence of several emission lines at $\sim$ 6.40, 7.05 and 7.47 keV in the source rest frame energy. It also indicates the presence of an absorption line at $\sim$ 6.70 keV. Hereafter throughout this thesis, we refer to the line energies in the source rest frame.

When the data in the 6.0–8.0 keV band are restored, the BC model as determined above became totally unacceptable ($\chi^2/\nu = 3159.9/325$), due to the emission/absorption lines as seen in Figure 5.4 (right). Adding a Gaussian line at $\sim$ 6.4 keV in the model and readjusting the model parameters, the fit drastically improved with $\Delta\chi^2 = -2689.7$, against three more free parameters, i.e., center energy, width and normalization. Therefore, the added model component is statistically highly significant. The center energy of the Gaussian is derived at $\sim$ 6.40 keV, which is consistent with the fluorescent line from neutral iron (Fe I Kα). In the same manner, we added two more Gaussian emission lines at $\sim$ 7.05 and 7.47 keV, and an absorption line at $\sim$ 6.70 keV, with their width set equal to the first one. They can be identified with Fe I Kβ, Ni I Kα and Fe XXV Kα lines, respectively. Each line significantly improved the fit at $> 99.9999\%$ level, and the fit χ^2/ν reached 356.0/316. The ionized iron absorption line indicate the presence of an ionized reprocessing material in the line of sight, as well as the cold matter. At this point, there still remained line like residuals around 3.7 and 4.0 keV. We included two more Gaussians at these energies, to find that they are significant at similar levels as above. The line at

3.7 keV can be identified as Ca I Kα (3.69 keV), which is physically expected from the cold reflection continuum as well as the neutral iron lines. The line at 4.0 keV can be identified as Ar I Kβ, which is also expected to arise from the reprocessing medium.

With the BC + six Gaussian components, the fit reached an acceptable level with $\chi^2/\nu = 317.3/312$. We finally replaced the model for the Fe I Kα line, with a more sophisticated model named `kalpha`. It consists of two Gaussian components representing Kα_1 and Kα_2, and also includes a Compton down-scattered shoulder which is physically expected when the line is produced either in a reflection or by transmission through optically-thick materials (Matt 2002). The profile of the shoulder is calculated according to Illarionov et al. (1979). This model has one additional free parameter compared to a Gaussian, $f_{\rm CS}$, the ratio between the intensity of the shoulder and that of the narrow core. The replacement improved the fit goodness with $\Delta\chi^2 = 5.8$, which is significant at a $\sim 99\%$ level. The derived center energy of the Fe I Kα_1 is 6.405 ± 0.003, in agreement with the expected value (6.404 keV). Indeed, fixing the center energy of the `kalpha` model at the expected value gives an equally good fit ($\chi^2/\nu = 312.5/312$). Therefore in this section, we hereafter fix the model center energy in the fitting. We call this model the BC + lines model.

5.1.6 Derived parameters

The data, the best-fit BC + lines model, and the fit residuals are shown in Figure 5.5, and the best-fit parameters and their errors are summarized in Table 5.1. The errors are quoted in 90% confidence of one interesting parameter. Since some of the parameters are correlated with each other in the fitting, we show in Figure 5.6 confidence contours of Γ vs $N_{\rm H}$, and the width vs $f_{\rm CS}$ of Fe I Kα.

As inferred in §5.1.3, the primary nuclear emission is obscured by a high degree of absorption, and emerges above $\sim$ 3–5 keV, while the reflection from cold material becomes dominant around 20–50 keV. The observed and absorption-corrected intrinsic fluxes in the 2–10 keV range, calculated for the best fit model, are $F^{\rm obs}_{2-10} = 1.9 \times 10^{-11}$ erg s^{-1} cm^{-2} and $F^{\rm int}_{2-10} = 4.7 \times 10^{-11}$ erg s^{-1} cm^{-2}, respectively. These correspond to the luminosities of $L^{\rm obs}_{2-10} = 8.2 \times 10^{41}$ erg s^{-1} and $L^{\rm int}_{2-10} = 2.0 \times 10^{42}$ erg s^{-1}, assuming a distance of 17 Mpc. According to the bolometric correction factor derived by Marconi et al. (2004), the bolometric luminosity is estimated to be $\sim 3 \times 10^{43}$ erg s^{-1}, which corresponds to $\sim 2\%$ of the Eddington luminosity for a 10^7 $M_\odot$ black hole.

The cold reflection continuum is observed significantly, with a reflection fraction of

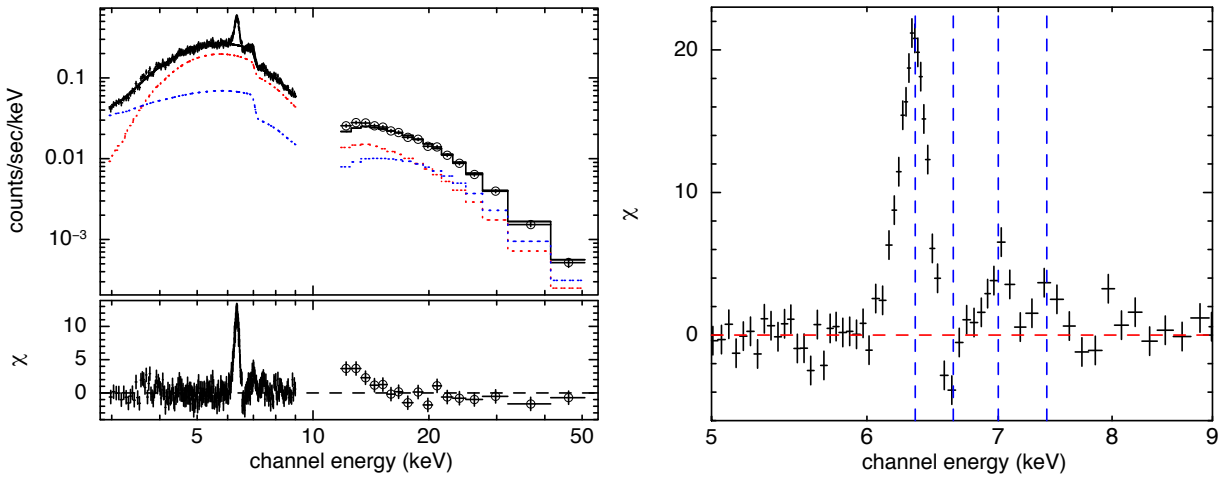

Figure 5.4: The broad-band (3.0–50 keV) spectra of NGC 4388, compared with the BC model which was determined by ignoring the 6.0–8.0 keV band. (Left) The spectrum is shown as the raw count rate of the detector. The black crosses and circles show the data points from XIS-FI and HXD-PIN, respectively. The dashed color lines represent the BC model components: the absorbed intrinsic power-law in red, and reflection in blue. The lower panel shows the residuals from this fit. (Right) A zoom of the residuals in the 5–9 keV band. The blue lines specify 6.40, 6.70, 7.05, 7.47 keV in the source rest frame.

$f_{\rm refl} \sim 1.8$. Emission lines from neutral materials also suggests the existence of a cold reprocessing material around the nucleus. Since these reprocessed signals are considered to have the same origin, we can calculate the expected equivalent widths of the lines with respect to the reflection continuum. The derived EW of $0.90^{+0.12}_{-0.15}$ keV is slightly smaller than the expected value (1.3–2.5 keV, Matt et al. 1996a). This suggests sub-solar abundance of the reflecting material. The derived fraction of Compton shoulder, ~ 0.12 is consistent with the picture that the iron line is originating in the optically-thick material, which likely to be the matter responsible for the reflection (Matt 2002).

5.1.7 Time variability

Observation of time variability can provide a clue to investigate the circum-nuclear environment of an AGN. From numerous observations of Seyfert 1 galaxies by *ASCA* , O'Neill et al. (2005) found that the time variability is an ubiquitous feature of Seyfert 1 AGN, with their RMS variability amplitude well connected to the black hole mass. Thus, we may also expect some intrinsic time variability in Seyfert 2 galaxies. We show in Figure 5.9 light curves of NGC 4388 in five energy ranges taken with the *Suzaku* XIS and HXD-PIN. Those in the upper four panels are extracted from the XIS, with data from

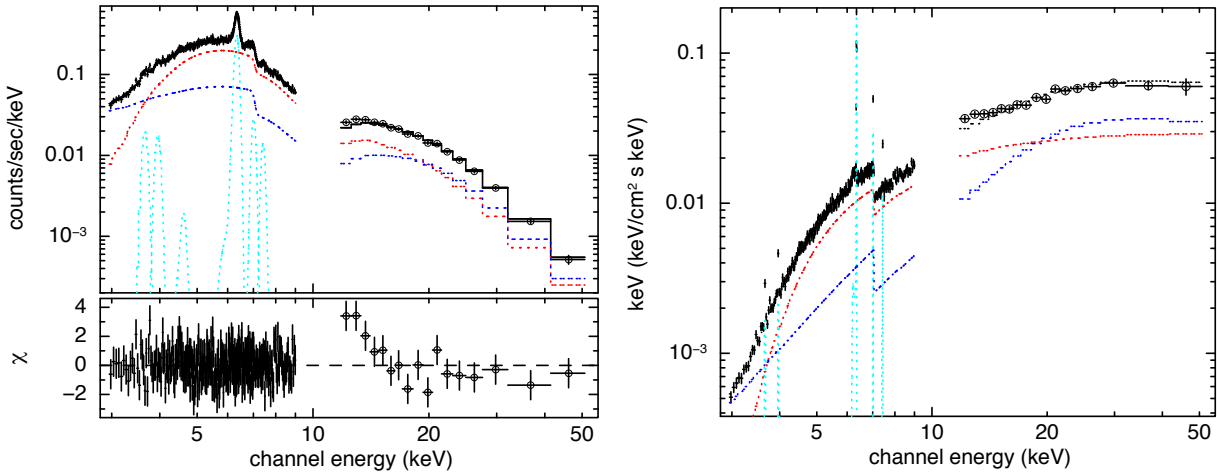

Figure 5.5: The same as Figure 5.4, but under the final model (see text). Emission lines are illustrated in cyan. The right panel shows the same results in a deconvolved $\nu F\nu$ form. The dashed color lines represent model components: the absorbed intrinsic power-law in red, reflection in blue, and emission lines in cyan.

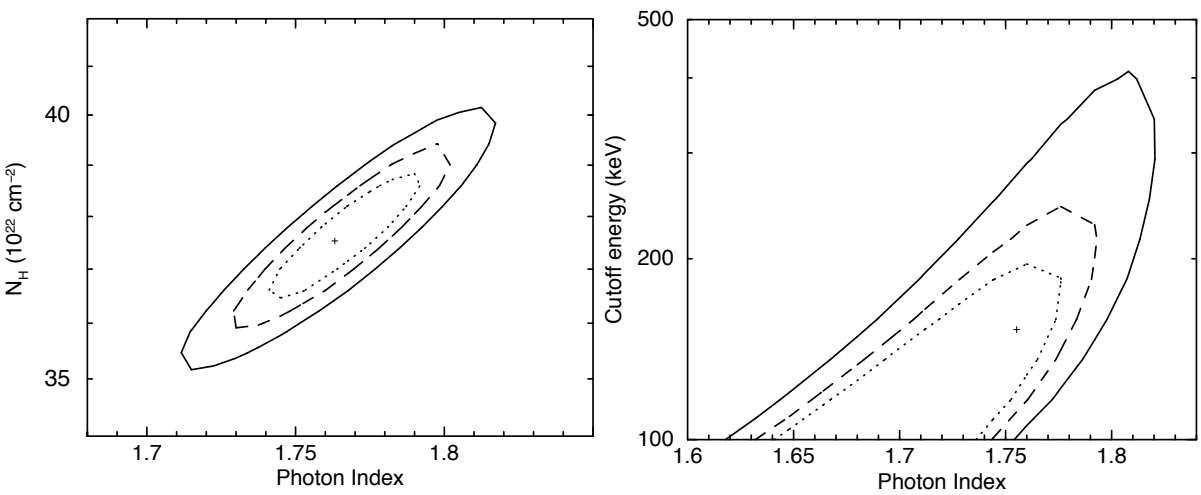

Figure 5.6: Confidence (68%, 90%, 99%) contours of the photon index of the primary continuum vs. the absorbing column (left), and those of the photon index vs. high cutoff energy (right).

Table 5.1: Best-fit parameters of *Suzaku* spectrum of NGC 4388 over 3.0–50 keV, derived with the final model.

Model Component	Parameter	Average	High	Low
Intrinsic PL	Γ	$1.76^{+0.06}_{-0.04}$	$1.84^{+0.08}_{-0.06}$	$1.64^{+0.08}_{-0.10}$
	$N_{\rm PL}{}^{a}$	$1.31^{+0.16}_{-0.15}$	$1.90^{+0.42}_{-0.37}$	$0.88^{+0.21}_{-0.18}$
	$N_{\rm H}{}^{b}$	$3.75^{+0.14}_{-0.13}$	$3.63^{+0.23}_{-0.15}$	$3.74^{+0.25}_{-0.24}$
Reflection	$f_{\rm refl}$	$1.82^{+0.28}_{-0.37}$	$1.50^{+0.24}_{-0.55}$	$2.02^{+0.33}_{-0.56}$
Fe I Kα	$E_{\rm c}{}^{c}$	fixed (see text)	fixed	fixed
	σ^{d}	26^{+15}_{-26}	30^{+20}_{-30}	23^{+23}_{-23}
	I^{e}	$83.9^{+2.9}_{-5.2}$	$85.0^{+5.0}_{-7.3}$	$79.0^{+4.0}_{-6.0}$
	$EW_{\rm int}{}^{f}$	$0.17^{+0.02}_{-0.03}$	$0.11^{+0.03}_{-0.04}$	$0.23^{+0.04}_{-0.03}$
	$EW_{\rm refl}{}^{g}$	$0.90^{+0.12}_{-0.15}$	$0.87^{+0.14}_{-0.20}$	$0.92^{+0.15}_{-0.23}$
Compton Shoulder	$f_{\rm CS}$	$0.12^{+0.10}_{-0.05}$	$0.11^{+0.09}_{-0.07}$	$0.14^{+0.10}_{-0.05}$
Fe I Kβ	$E_{\rm c}{}^{c}$	$7.072^{+0.025}_{-0.030}$	$7.075^{+0.069}_{-0.069}$	$7.073^{+0.039}_{-0.038}$
	I^{e}	$9.3^{+2.0}_{-2.1}$	$10.5^{+5.2}_{-5.2}$	$7.9^{+3.2}_{-3.8}$
Ni I Kα	$E_{\rm c}{}^{c}$	$7.48^{+0.02}_{-0.02}$	$7.45^{+0.06}_{-0.06}$	$7.52^{+0.04}_{-0.04}$
	I^{e}	$5.2^{+2.1}_{-2.3}$	$6.2^{+5.2}_{-5.0}$	$5.8^{+3.2}_{-3.8}$
Fe XXV Kα	$E_{\rm c}{}^{c}$	$6.66^{+0.04}_{-0.04}$	$6.63^{+0.13}_{-0.11}$	$6.68^{+0.06}_{-0.05}$
	I^{e}	$6.2^{+2.0}_{-2.3}$	$6.4^{+5.2}_{-3.4}$	$5.8^{+4.5}_{-4.0}$
	EW^{f}	$0.06^{+0.03}_{-0.03}$	$0.04^{+0.05}_{-0.03}$	$0.08^{+0.04}_{-0.04}$
Ca I Kα	$E_{\rm c}{}^{c}$	$3.69^{+0.03}_{-0.02}$	$3.70^{+0.05}_{-0.06}$	$3.68^{+0.04}_{-0.05}$
	I^{e}	$3.78^{+0.70}_{-0.75}$	$3.69^{+0.92}_{-0.91}$	$3.88^{+0.82}_{-0.85}$
	$EW_{\rm refl}{}^{g}$	$0.06^{+0.02}_{-0.02}$	$0.06^{+0.03}_{-0.02}$	$0.06^{+0.02}_{-0.02}$
χ^2/d.o.f.		312.4/312	310.5/312	315.3/312

[a] 10^{-3} photons keV^{-1} cm^{-2} s^{-1} at 1 keV. [b] 10^{23} cm^{-2}. [c] Line center energy in keV.

[d] Line width in eV. [e] Line intensity in 10^{-6} photons cm^{-2} s^{-1}.

[f] EW with respect to the absorption-corrected intrinsic power-law in keV.

[g] EW with respect to the cold reflection in keV. par

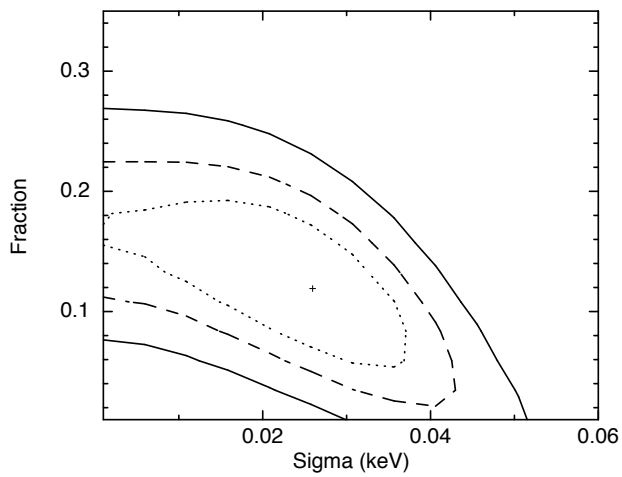

Figure 5.7: Confidence (68%, 90%, 99%) contours of of the width of Fe I Kα vs. the fraction of the Compton shoulder $f_{\rm CS}$.

the four sensors co-added. Each time bin corresponds to a continuous time interval which is free from any data gap. The bin length is typically 1000–3000 sec, since the satellite is suffered from approximately two data gaps in one orbital period, mainly due to the COR variation and the SAA. We discarded data points whose exposure is less than 128 sec, since they have too large statistical errors. The light curves in the bottom panel was extracted from the HXD-PIN data. We show the net source count rates (black) along with the background-inclusive raw count rates (red) and the estimated background (NXB + CXB) rates (blue). Each time bin corresponds to the continuous time interval of the HXD-PIN data. In this case, we discarded those bins with the exposure less than 512 s.

The light curves below 3 keV do not show any significant variation, which agree with the idea that the thermal diffuse emission dominates in this energy range. In the energy ranges above 3 keV, in contrast, the source flux varied by a factor of $\sim$ 2 within $\sim$ 40 ks, accompanied by random, slight variations in the hardness ratio. Such short-term variability has been detected by this *Suzaku* observation for the first time from this source (Shirai et al. 2008). It is known that the variability time scale of AGNs correlates with the central black hole mass (e.g., O'Neill et al. 2005; Iyomoto and Makishima 2001; Hayashida et al. 1995), and the black hole mass in NGC 4388 is inferred, from its bulge K-magnitude, to be $\sim 10^7\ M_\odot$. A black hole in this mass range is expected to vary on a time scale of $\sim 10^{4-5}$ s, with which the present observation is consistent.

In order to investiate energy dependence of the time variability, we introduce a frac-

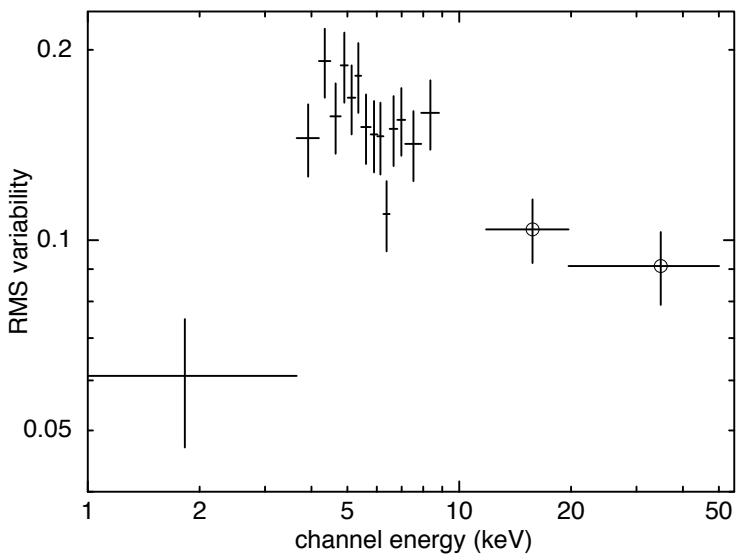

Figure 5.8: A fractional RMS variability of NGC 4388. Crosses and circles represent data points derived from the XIS (with four sensors co-added) and HXD-PIN light curves, respectively.

tional variability, $F_{\rm var}$, defined as

$$F_{\rm var} = \sqrt{\frac{S^2 - \langle \sigma_{\rm err}^2 \rangle}{\langle X \rangle^2}}, \tag{5.1}$$

where $\langle X \rangle$ is the average counts, S^2 is the variance of the binned data comprising the light curve, and $\langle \sigma_{\rm err}^2 \rangle$ is the average of square of the Poisson errors within individual time bin. Detailed description on the fractional variability and derivation of its uncertainty can be obtained in Edelson et al. (2002). Figure 5.8 plots the fractional RMS variability against the energy. Thus, the variability above ~ 3 keV tends to decrease toward higher energies. Compared to those in the neighboring energy bins, $F_{\rm var}$ in the Fe I Kα band is also smaller. These facts imply that the only absorbed primary emission is varying while the reprocessed signal stays rather constant on the relevant time scales. That is, the variability is suppressed by a factor of ~ 2 in the 12–50 keV range compared to that in the 3–10 keV range, since the variable primary emission contributes only about a half of the total flux at the former energy range (see Figure 5.5).

In order to more directly examine the spectra for intensity-correlated changes, we defined "high flux" and "low flux" phases, according to the 3–10 keV count rate: the "high flux" and "low flux" phases comprise those time bins when the count rates are higher than 1.50 cts s^{-1} and lower than 1.22 cts s^{-1}, respectively. The net exposure is 55.3 ks (XIS) and 43.1 ks (HXD) for the high phase, and 60.1 ks (XIS) and 53.5 ks

(HXD) for the low phase. We separately derived the spectra of the two phases, and fitted them with the final model in §5.1.5. As in the time averaged spectrum, the fits were acceptable in both cases. The resultant fit and the best-fit parameters are summarized in Table 5.1. Thus, the photon index of the primary power-law, as well as its normalization, significantly changes between the two phases. The flux of reflection continuum do not vary, while the reflection fraction $f_{\rm refl}$ changes in response to the variation of the incident power-law. The Fe I Kα line flux also stays constant within errors. These results clearly indicate that only the primary power-law is variable while the reprocessed signal stays rather constant. This inference is well consistent with the picture that the cold reflector is located at a distance of ~ 0.1 pc from the central source (a putative "torus").

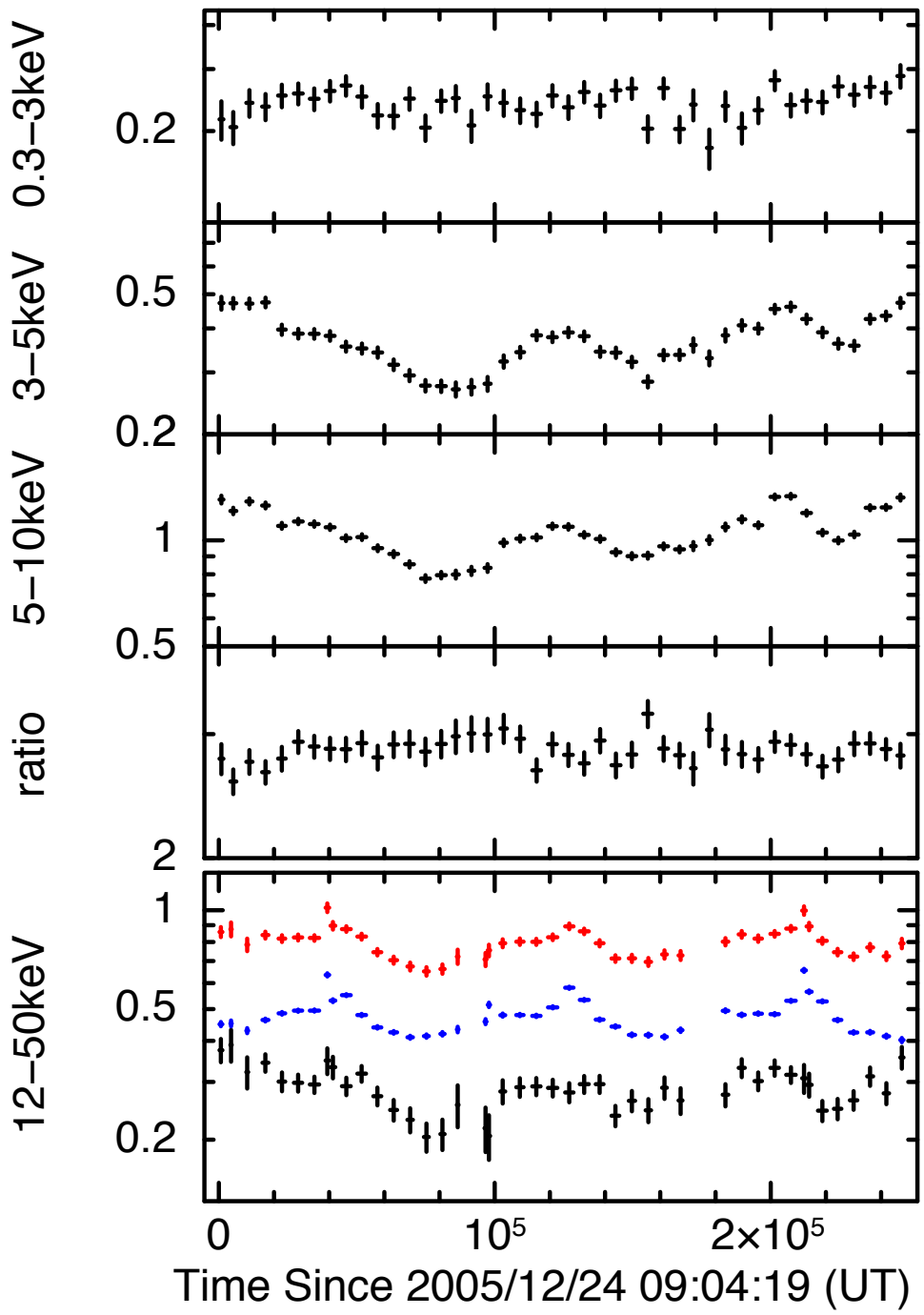

Figure 5.9: Background-subtracted light curves of NGC 4388 taken with *Suzaku* . The upper three panels show those in 0.3–3 keV, 3.0–5.0 keV and 5.0–10.0 keV, respectively, taken with the four XIS sensors. The fourth panel shows the hardness ratio between 5.0–10.0 keV and 2.0–5.0 keV. Each bin corresponds to a continuous time interval without data gaps. The bottom panel shows the HXD-PIN light curves in the 12–40 keV band: the red points indicates background-inclusive raw count rates, blue the modeled background (NXB + CXB), and black the net source count rates. Each bin corresponds to a continuous time interval without data gaps, which can be different from those in the upper panels.

5.2 Mrk 3

5.2.1 XIS data analysis

We show in Figure 5.10 *Suzaku* XIS0 images of Mrk 3, in two energy ranges of 0.3–2 keV and 2–9 keV. Besides its nucleus, *Suzaku* detected no significant X-ray source in either energy band up to $\sim 4'$ from the center of the galaxy. Therefore, we extracted the source events within a circular region with a radius of $4'.34$, indicated by black solid circles in the images. This radius corresponds to 6 mm on the CCD chip, and to 68 kpc in physical size at a distance of 54 Mpc. Indeed, soft X-ray studies with higher special resolution instruments (e.g., *ROSAT*; Colbert and Ptak 2002) found in our extraction region only one faint X-ray source, IXO 30, about $30''$ off the nucleus. Using *XMM-Newton* and *Chandra*, Bianchi et al. (2005b) found that the X-ray spectrum of IXO 30 is represented by a single power-law with a photon index of ~ 1.8, and reported that its flux stayed constant over a 2-year monitoring period. Based on their result, the possible contamination to the nuclear emission from IXO 30 is estimated to be only $\sim 7\%$, even in the 0.4–2 keV band.

The soft X-ray spectrum of Mrk 3 in the ~ 0.2–2.5 keV band is known to be dominated by a numerous emission lines and radiative recombination continua, which are most likely to be originating in materials photo-ionized by the nuclear X-ray irradiation (e.g., Bianchi et al. 2005b; Guainazzi and Bianchi 2007). Utilizing the high energy resolution and large effective area of the *Suzaku* XIS-BI, we conducted detailed studies of the soft X-ray emission from Mrk 3 nucleus, and reported the results in Awaki et al. (2008). In the present thesis, we focus on the nuclear hard X-ray emission and the reflection continuum, which are prominent above ~ 3 keV. Thus, hereafter we restrict our spectral analysis to the energy ranges above this threshold.

The background events were extracted from annulus regions surrounding the source regions in the same CCDs. In our spectral fittings, we used energy ranges of 3.0–9.0 keV for the FI chips and 3.0–8.0 keV for the BI chip. After event screening (§4.2), we obtained a total net exposures of ~ 95.0 ks from each XIS sensor. The background count rates in the relevant energy ranges were found to be $\sim 12\%$ of the total events in the FI chips, and $\sim 18\%$ in the BI chip. After subtracting these backgrounds, we obtained signal count rates of 0.351 ± 0.002 cts s^{-1} and 0.088 ± 0.001 cts s^{-1} with the FI and BI, respectively.

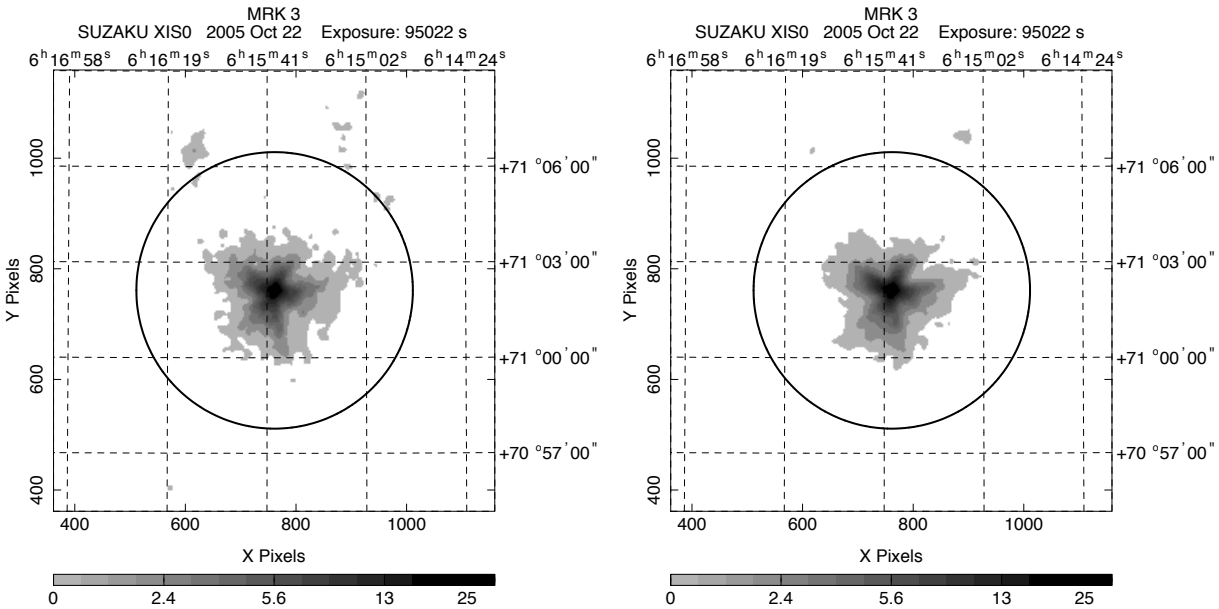

Figure 5.10: The same as Figure 5.1, but for Mrk 3, in the 0.3–2.0 keV (left) and 2.0-9.0 keV (right) band. The source events are extracted within the black solid circle with a radius of $4'.3$.

5.2.2 HXD data analysis and broad-band spectrum

As in §5.1.2, Figure 5.11 shows the energy spectra of Mrk 3 taken with the HXD-PIN (below 60 keV) and HXD-GSO (above 50 keV), in comparison with their backgrounds. The lower panel indicate that the net source count rates of HXD-PIN reaches several tens percent of that of its background, over its whole energy range. Therefore, the systematic errors in the PIN NXB can be neglected. In the following spectral analysis, we thus use the entire energy range of HXD-PIN. In the energy range, the background-subtracted source count rate with statistical errors, is 0.178 ± 0.003 cts s^{-1}, which is $\sim 25\%$ of the background rate (NXB plus CXB, 0.539 cts s^{-1}).

In the HXD-GSO spectrum, the net source counts are ~ 1.5–2% of the background in the 50–100 keV range. We can therefore claim the source detection in 50–100 keV with GSO, considering its background uncertainly (§3.7.3). In contrast, the GSO detection above 100 keV is marginal. The background-subtracted source count rate in the 50–100 keV energy range is 0.024 ± 0.005 cts s^{-1}. The current response uncertainty of the HXD-GSO is rather large ($> 10\%$) at its lowest energy range (< 70 keV), mainly because the non-linear responses of both the scintillators and analog electronics become dominant there. We therefore incorporate the HXD-GSO data only in the 70–100 keV range (corresponding to one energy bin) in our subsequent spectral fitting.

We show in Figure 5.12 the Crab ratio of Mrk 3 in the 2–150 keV band. The iron

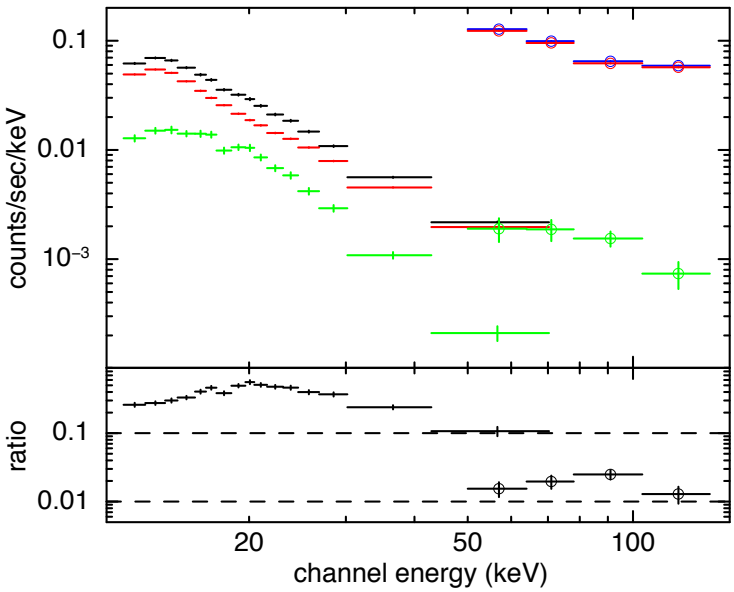

Figure 5.11: The same as Figure 5.2, but for Mrk 3.

line and edge structures around 6–7 keV appear to be more prominent than those in NGC 4388. This suggests that the intrinsic emission is more obscured than that of NGC 4388 so that the cold reflection continuum is more apparent up to $\sim$ 10 keV. The extremely hard continuum at 6–10 keV followed by a roll-over around $\sim$ 15 keV supports this idea; i.e., the intrinsic emission appears only above $\sim$ 6 keV, while the lower energy range is dominated by the reflection. The continuum above $\sim$ 20 keV appear rather straight, without significant signature of the Compton hump or high-energy curvature, although the GSO data points should be viewed with reservation as mentioned in §5.2.2.

5.2.3 Spectral fitting

As in §5.1.5, we first adopted a BC model to simultaneously fit the background-subtracted XIS, HXD-PIN and HXD-GSO spectra. The energy range between 6.0 and 8.0 keV was not utilized in the fitting. We fixed the absorbing column of our Galaxy toward Mrk 3 at 8.7×10^{20} cm^{-2} (Stark et al. 1992). We also fixed the hard-band cutoff energy at 300 keV, which is a canonical value for Seyfert galaxies (e.g., Cappi et al. 1999). The data, the best-fit BC model, and the fit residuals are shown in Figure 5.13. As seen in the figure, the BC model roughly reproduce the overall continuum shape, with a fit goodness of $\chi^2/\nu = 98.8/77$. The absorbing column, photon index of the intrinsic power-law, and the reflection fraction are estimated to be $N_{\rm H} \sim 1.4 \times 10^{23}$ cm $^{-2}$, $\Gamma \sim 2.0$, and $f_{\rm refl} \sim 1.3$, respectively. The derived value of $N_{\rm H}$ is significantly higher than that in NGC 4388, while

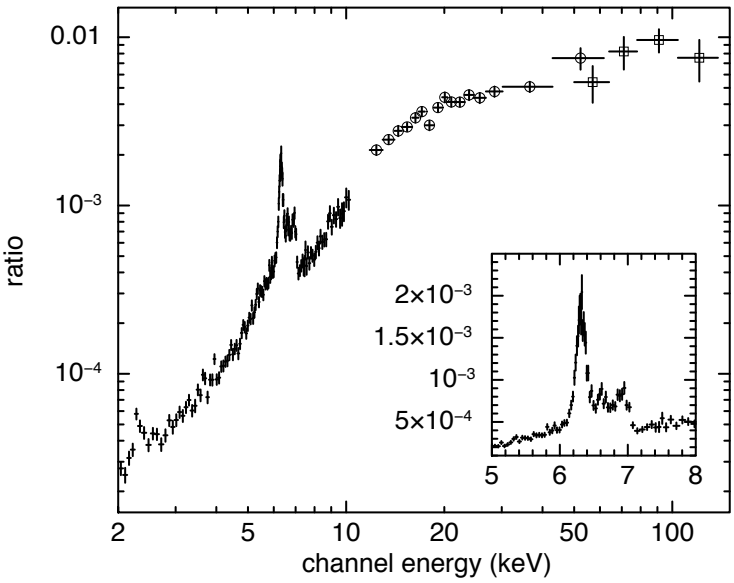

Figure 5.12: The same as Figure 5.3, but for Mrk 3.

the reflection fraction is similar between the two sources, in agreement with the inference obtained in §5.2.2. The right panel of Figure 5.4 shows the residuals around the iron line region, which reveals evidence of several emission lines at $\sim$ 6.40, 6.70, 7.05 and 7.47 keV.

Next, in the same procedure as in §5.1.5, we added to the model the Gaussian lines one by one, to reproduce the whole energy spectrum. We found that 5 emission lines are statistically significant: Fe I Kα, Fe I Kβ, Ni I Kα, Fe XXV Kα and Ca I Kα. The Compton shoulder of the Fe I Kα lines was also significant in this source, so we replaced the Gaussian to `kalpha` model (§5.1.5) to reproduce it.

At this stage, the fit goodness still remained somewhat poor at $\chi^2/\nu = 141.8/120$. This is mainly due to systematic positive residuals seen below $\sim$ 4 keV, suggesting that there is another continuum buried. We thus added another power-law with its photon index tied to that of the intrinsic emission (Awaki et al. 2008). Such a soft continuum emission was actually observed in this source, from analysis of soft X-ray spectra of *XMM-Newton* (Bianchi et al. 2005b) along with emission lines from photo-ionized emission material. Its origin is thought to be the nuclear light Thomson scattered by the same material as is responsible for the ionized lines. Since the highly ionized material act as a "mirror" to the incident emission, the scattered continuum has the same spectral slope as the intrinsic nuclear emission. The inclusion of the scattered continuum improved the fit significantly with $\Delta\chi^2 = -8.0$. The ratio between the normalization of the scattered continuum to that of the intrinsic power-law is hereafter denoted as $f_{\rm scat}$; a fraction $f_{\rm scat}$ of the nuclear light is scattered by a ionized matter into our line of sight.

In this source, the iron edge is more prominent than in NGC 4388, which could further allow us to determine the iron abundance. Since the absorption and the reflection both produce the edge, we constrained these two components to have the same, but free, iron abundance. A slightly sub-solar (~ 0.85) iron abundance improved the fit significantly ($\chi^2/\nu = 127.2/118$), and the iron abundance is obtained to be ~ 0.8. We hereafter take this model as the final one for this source, and call "BC + lines + scattering model".

5.2.4 Derived parameters

The best-fit parameters under the BC + lines + scattering model are summarized in Table 5.2. The left panel of Figure 5.15 shows the confidence contours of Γ vs. $N_{\rm H}$. Additionally, we tried to constrain the cutoff energy describing the high-energy continuum bending. Allowing the cutoff energy to vary did not improve the fit. Figure 5.15 gives the derived confidence ranges of the cutoff energy against the slope of the intrinsic emission, which indicates that the cutoff energy is marginally constrained to be > 100 keV. The observed and unabsorbed intrinsic flux are obtained to be $F^{\rm obs}_{2-10} = 6.7\times10^{-12}$ erg s^{-1} cm^{-2} and $F^{\rm int}_{2-10} = 4.0 \times 10^{-11}$ erg s^{-1} cm^{-2}, corresponding to luminosities of $L^{\rm obs}_{2-10} = 2.3 \times 10^{42}$ erg s^{-1} and $L^{\rm int}_{2-10} = 1.4 \times 10^{43}$ erg s^{-1}, respectively, assuming a distance of 54 Mpc. The bolometric luminosity is thus estimated to be $\sim 3 \times 10^{44}$ erg s^{-1} (Marconi et al. 2004), or $\sim 0.5\%$ of the Eddington luminosity for a 4.5×10^8 $M_\odot$ black hole.

The derived absorbing column of $N_{\rm H} = 1.17^{+0.07}_{-0.10} \times 10^{23}$cm^{-2} is a factor of ~ 3 higher than that in NGC 4388, while the fraction of the cold reflection, $f_{\rm refl} \sim 1.3$, is close to that of NGC 4388. This implies that the two nuclei are covered by the reflectors subtending similar solid angles, while the absorber (putative torus) is likely to be viewed more edge-on in Mrk 3. The equivalent width of the Fe I Kα, estimated to be $0.85^{+0.15}_{-0.16}$ keV, is again smaller by several tens percent than the expected value for a solar abundance (Matt et al. 1996a). The value instead agree with the iron abundance estimated from the iron edge profile, ~ 0.8, which supports the picture that the cold reflection continuum and the neutral emission lines arise in the same location. The derived $f_{\rm CS} \sim 0.1$, shown in Figure 5.16, is also consistent with the reflection continuum and the neutral lines having the same origin.

The ionized scattering fraction has been estimated as $f_{\rm scat} \sim 1\%$, which is quite close to that obtained from the *Suzaku* soft X-ray spectrum (Awaki et al. 2008), and that by Bianchi et al. (2005b). This fraction is approximately written as $f_{\rm scat} \sim (\Delta\Omega/4\pi) \cdot N_{\rm H}^{\rm scat} \cdot \sigma_{\rm T}$, where $\Delta\Omega$ and $N_{\rm H}^{\rm scat}$ is the solid angle (seen from the nucleus) and column density of

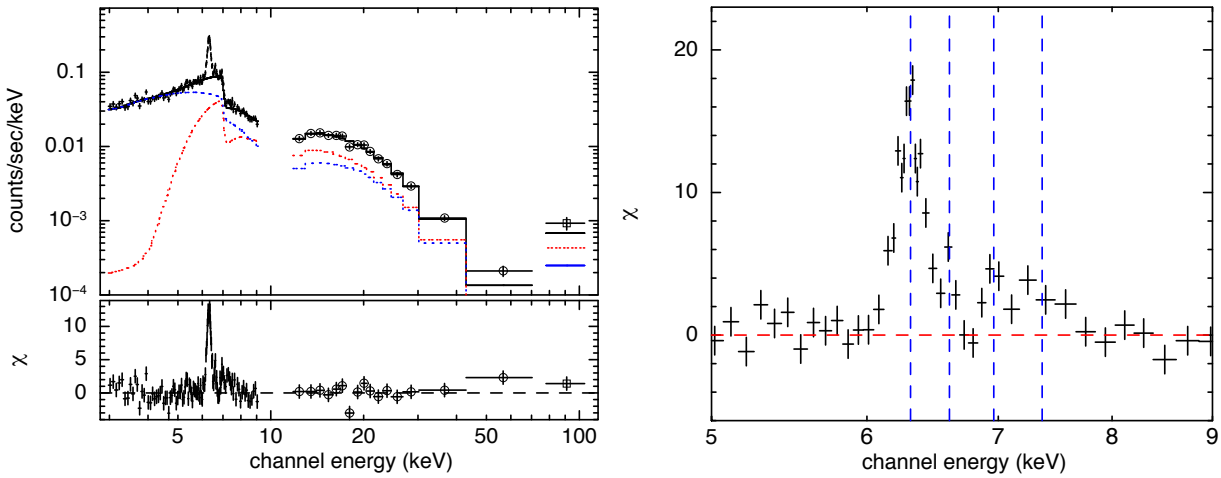

Figure 5.13: The same as Figure 5.4, but for Mrk 3. (Right) A zoom of the residuals in the 5–9 keV band. The blue lines correspond to energies of 6.40, 6.70, 7.05, 7.47 keV in the source rest frame.

the assumed scatterer, respectively. If we take $\Delta\Omega/4\pi \sim 0.3$ as a representative case, the observed value of $f_{\rm scat} \sim 0.01$ can constrain $N_{\rm H}^{\rm scat}$ as

$$N_{\rm H}^{\rm scat} = f_{\rm scat} \cdot \left(\frac{\Delta\Omega}{4\pi}\right)^{-1} \cdot \sigma_{\rm T}^{-1} = 4.5 \times 10^{22} \left(\frac{f_{\rm scat}}{0.01}\right) \left(\frac{\Delta\Omega/4\pi}{0.3}\right)^{-1} \ {\rm cm}^{-2}. \tag{5.2}$$

Equivalently, the ionized scatterer is inferred to have a Thomson optical depth of

$$\tau \simeq N_{\rm H}^{\rm scat} \cdot \sigma_{\rm T} \simeq 0.3 \left(\frac{f_{\rm scat}}{0.01}\right) \left(\frac{\Delta\Omega/4\pi}{0.3}\right)^{-1} \tag{5.3}$$

As in the case of cold reprocessors, we can utilize the equivalent widths of the ionized lines to examine whether the lines and the scattered continuum arise in the same material. The observed equivalent width of Fe XXV Kα is $1.5^{+0.3}_{-0.3}$ keV, with respect to the scattered continuum. This value agree with that inferred from the calculation, assuming $N_{\rm H}^{\rm scat} \sim 10^{22}$ cm^{-2} (Bianchi and Matt 2002; Bianchi et al. 2005a). Therefore, the ionized lines and the scattered continuum can be regarded as arising from the same ionized gas.

5.2.5 Time variability

Figure 5.17 shows light curves of Mrk 3 taken with *Suzaku* in five energy ranges, extracted in the same was as in §5.1.7. The upper four panels are those of the XIS (four sensors co-added), while the bottom panel shows the HXD-PIN light curve. According to the chi-squared tests, none of the light curves in the three bands below 10 keV nor the hardness ratio show any significant variability; each curves are consistent with being constant at least $\gtrsim$ 95% level.

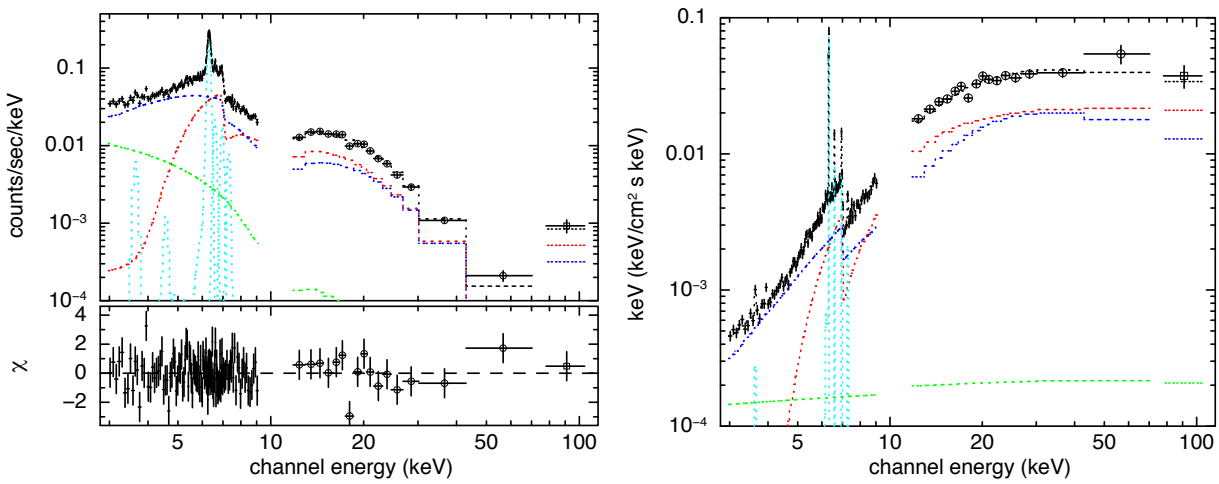

Figure 5.14: The same as Figure 5.13, but with the final model (see text). The dashed color lines represent model components: the absorbed intrinsic power-law in red, reflection in blue, emission lines in cyan, and scattered power-law in green.

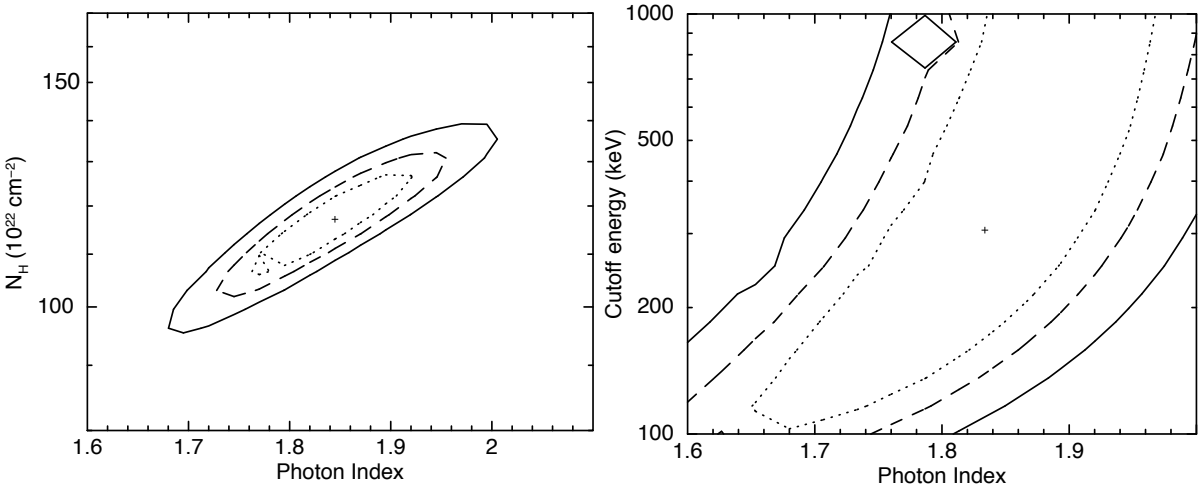

Figure 5.15: The same as Figure 5.6, but for Mrk 3.

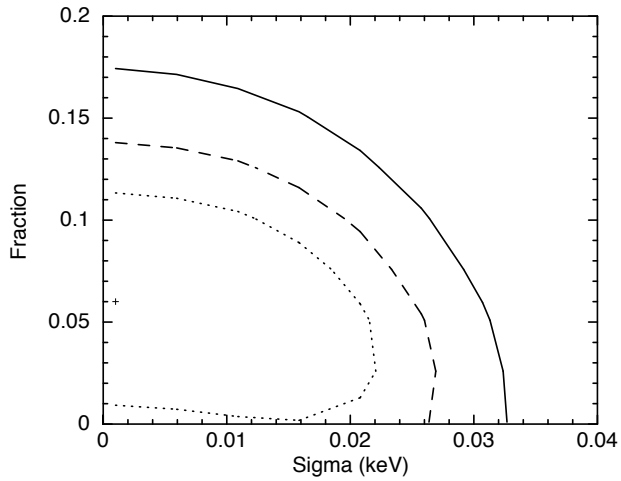

Figure 5.16: The same as Figure 5.7, but for Mrk 3.

Table 5.2: The Best-fit parameters of the *Suzaku* spectrum of Mrk 3 over the 3.0–110 keV range, derived under the BC + lines + scattering model (see text).

Model Component	Parameter	Value
Intrinsic PL	Γ	$1.85^{+0.06}_{-0.07}$
	$N_{\rm PL}{}^{a}$	$1.25^{+0.05}_{-0.06}$
	$N_{\rm H}{}^{b}$	$1.17^{+0.07}_{-0.10}$
Reflection	$f_{\rm refl}$	$1.31^{+0.31}_{-0.35}$
	$A_{\rm Fe}{}^{c}$	$0.84^{+0.25}_{-0.21}$
Scattering	$f_{\rm scat}$	$0.010^{+0.003}_{-0.003}$
Fe I Kα	$E_{\rm c}{}^{d}$	$6.400^{+0.002}_{-0.003}$
	σ^{e}	< 23
	I^{f}	$50.0^{+1.8}_{-2.0}$
	$EW_{\rm int}{}^{g}$	$0.12^{+0.04}_{-0.03}$
	$EW_{\rm refl}{}^{h}$	$0.85^{+0.15}_{-0.16}$
Compton Shoulder	$f_{\rm CS}$	$0.06^{+0.05}_{-0.06}$
Fe I Kβ	$E_{\rm c}{}^{d}$	$7.057^{+0.020}_{-0.022}$
	I^{f}	$5.2^{+1.2}_{-1.4}$
Ni I Kα	$E_{\rm c}{}^{d}$	$7.40^{+0.07}_{-0.06}$
	I^{f}	$2.8^{+1.1}_{-1.2}$
Fe XXV Kα	$E_{\rm c}{}^{d}$	$6.688^{+0.021}_{-0.023}$
	I^{f}	$5.6^{+1.5}_{-1.2}$
	$EW_{\rm scat}{}^{i}$	$1.5^{+0.3}_{-0.3}$
Ca I Kα	$E_{\rm c}{}^{d}$	$3.68^{+0.04}_{-0.05}$
	I^{f}	$3.88^{+0.82}_{-0.85}$
	$EW_{\rm refl}{}^{h}$	~ 0.03
χ^2/d.o.f.		127.1/118

[a] 10^{-3} photons keV^{-1} cm^{-2} s^{-1} at 1 keV.

[b] 10^{23} cm^{-2}. [c] Iron abundance tied to that of the absorber. [d] Line center energy in keV

[e] Line width in eV. [f] Line intensity in 10^{-6} photons cm^{-2} s^{-1}.

[g] EW with respect to the absorption-corrected intrinsic power-law in keV.

[h] EW with respect to the cold reflection in keV.

[i] EW with respect to the ionized scattering in keV.

In contrast to the lack of variation in softer energies, the HXD-PIN light curve is not consistent with being constant at $\gtrsim 99.5\%$ level via the chi-squared test. However, this should be taken with reservations, considering the uncertainty of the modeled NXB. In fact, the variation in the count rate is only $\lesssim \pm 0.02$ cts s^{-1}, which is similar to the NXB uncertainty (at 1σ level) in this energy band with a time bin length of ~ 1000 sec (Mizuno et al. 2007). Conservatively regarding the observed variation as possibly instrumental, the 90% upper limit on the fractional RMS variability (§5.1.7) is obtained as < 0.05, which is much lower than those in NGC 4388. Thus, we should conclude that we found no significant time variation from the *Suzaku* observation, in any energy range, from Mkn 3. The black hole mass in MKN 3 has been estimated as $\sim 4.5 \times 10^8\ M_\odot$, from optical observations (Woo and Urry 2002). Then, the RMS variability for a two day observation is expected to be $\sim 2 \times 10^{-2}$ from a relation between $M_{\rm BH}$ and $\sigma^2_{\rm rms}$ (e.g., O'Neill et al. 2005). Therefore, our non detection of variability is consistent with the black hole mass.

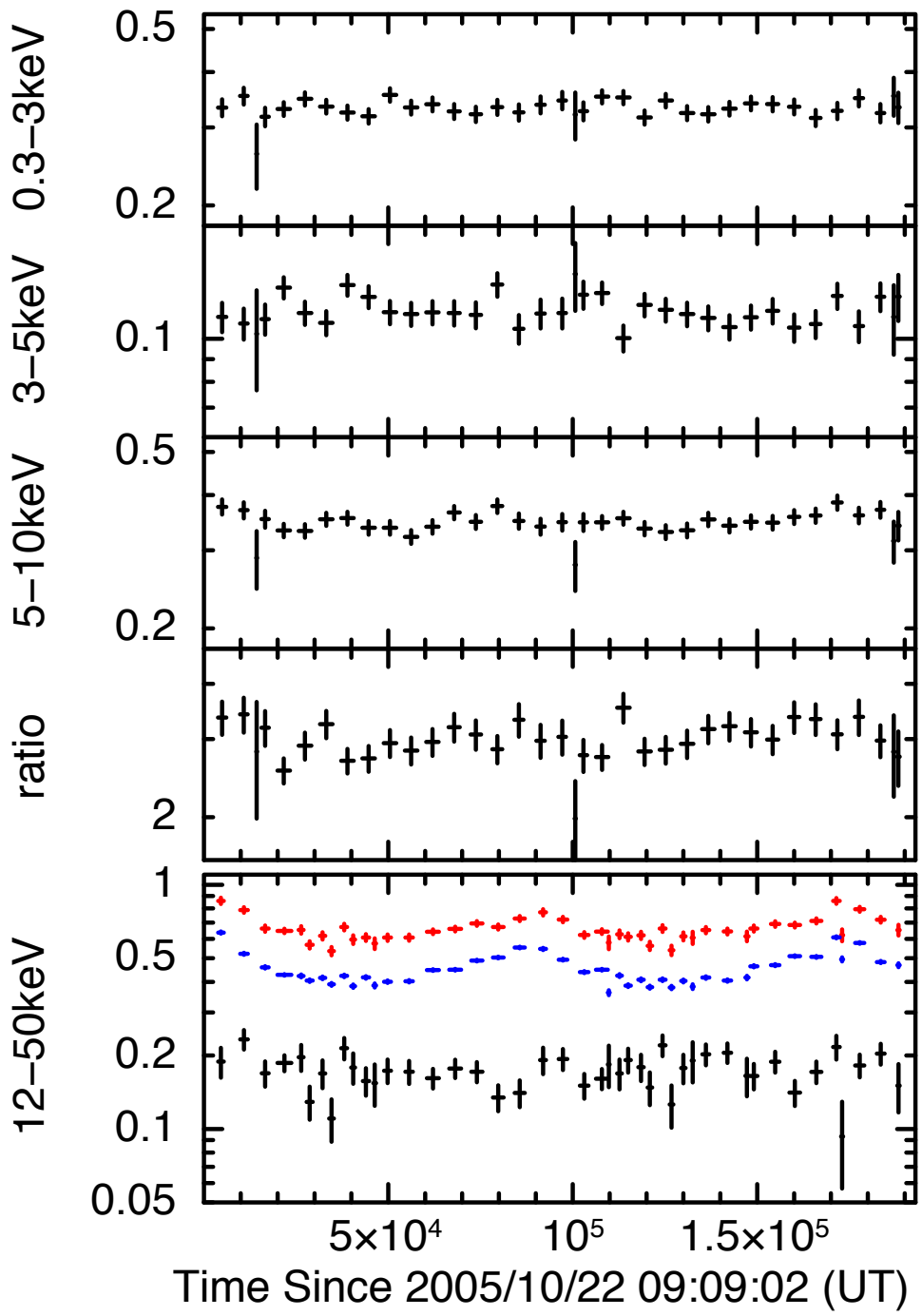

Figure 5.17: Background-subtracted light curves of Mrk 3 taken with *Suzaku* . The upper three panels show those in 0.3–3 keV, 3.0–5.0 keV and 5.0–10.0 keV, respectively, taken with the four XIS sensors. The fourth panel shows the hardness ratio between 5.0–10.0 keV and 2.0–5.0 keV. Each bin corresponds to a continuous time interval without data gaps. The bottom panel shows the HXD-PIN light curves in the 12–50 keV band: the red points indicates background-inclusive raw count rates, blue the modeled background (NXB + CXB), and black the net source count rates. Each bin corresponds to a continuous time interval without data gaps, which can be different from those in the upper panels.

5.3 The Circinus Galaxy

5.3.1 XIS data analysis

We show in Figure 5.18 *Suzaku* XIS0 images of the Circinus galaxy, in two energy ranges of 0.3–3 keV and 3–9 keV. The *Suzaku* data were acquired for a net exposure of $\sim$ 108 ks with each XIS sensor. The brightest source at the center of the images is the nucleus, while a second brightest source at $\sim 5'$ off the center is apparent in both energy ranges. This source was discovered by *ASCA* (Matt et al. 1996b), and is also present in the *ROSAT* HRI image. Total counts of the second source is $\sim$ 40% of that of the nucleus in the lower energy range, while it decreases to only $\sim$ 10% in the higher one. From the *Suzaku* XIS data, the spectrum of the second source can be well fitted either by a power-law with $\Gamma \sim 2.3$ and $N_{\rm H} \sim 1.1 \times 10^{22}$ cm^{-2}, or by a thermal bremsstrahlung with k$T \sim 5$ keV and $N_{\rm H} \sim 4.5 \times 10^{21}$ cm^{-2}. In either cases, the extrapolation to the HXD-PIN band lies more than two orders of magnitude below the total PIN counts, so its contribution to the HXD can be neglected compared to the AGN emission.

To avoid contamination from the second source, we extracted source events within $2'.60$ of the nucleus, where more than 95% of the AGN events are included. This radius, indicated by black solid circles in the images, corresponds to 3.6 mm on the CCD chip, and to 2.9 kpc in physical size at a distance of 3.8 Mpc. The background events were extracted from the source free regions in the same CCDs. Similar to Mrk 3 (§5.2.1), the soft X-ray spectrum of Circinus is dominated by plenty of emission lines likely to be originating in a photo-ionized plasma (Sako et al. 2000b; Bianchi et al. 2001). Although the *Suzaku* XIS data could make a precious contribution to the soft X-ray spectroscopy of this source, we restrict our analysis above 3 keV, as we focus on the harder spectral components in this thesis. In this energy range, the contamination from the second source to the nuclear spectrum can be neglected ($<$ 1%). After the background subtraction, the net signal counts were obtained as 1.019 ± 0.003 cts s^{-1} with the XIS-FI chips (3.0–9.0 keV), and 0.273 ± 0.002 cts s^{-1} with the BI chip (3.0–8.0 keV). The background count rates are $\sim$ 2.8% and $\sim$ 4.0% of the total events in the FI and BI, respectively.

Using *Chandra*, Sambruna et al. (2001) and Bauer et al. (2001) found 15 X-ray sources within $1'$ of the nucleus. Most of them are very faint and have soft spectra, but two sources, CG X-1 and CG X-2, are found to be bright enough to individually contaminate the *Suzaku* spectrum up to $\sim$ 20% in the $3-5$ keV band. CG X-1 exhibits periodic variations with a $\sim$ 27 ks period, and its average spectrum is well reproduced by a MCD model with $T_{\rm in} \sim 1.5$ keV and $N_{\rm H} \sim 1 \times 10^{22}$ cm^{-2} (Bauer et al. 2001; Weisskopf

et al. 2004). Among $\sim$ 10 observations by *ROSAT*, *Chandra*, and *XMM-Newton* over $\sim$ 6 years, its flux varied by a factor of $\sim$ 2 (Bianchi et al. 2002). The spectrum of CG X-2 can be reproduced by a power-law with $\Gamma \sim 1.8$ and $N_{\rm H} \sim 1 \times 10^{22}$ cm^{-2}, without any short term or long term variability. It is considered to be a young supernova remnant (Bauer et al. 2001). Since *Suzaku* cannot resolve these sources spatially, we included model components in our spectral analysis in §5.3.3 to account for their contamination. We used the spectral parameters described above, with the CG X-1 normalization allowed to vary while that of CG X-2 fixed constant.

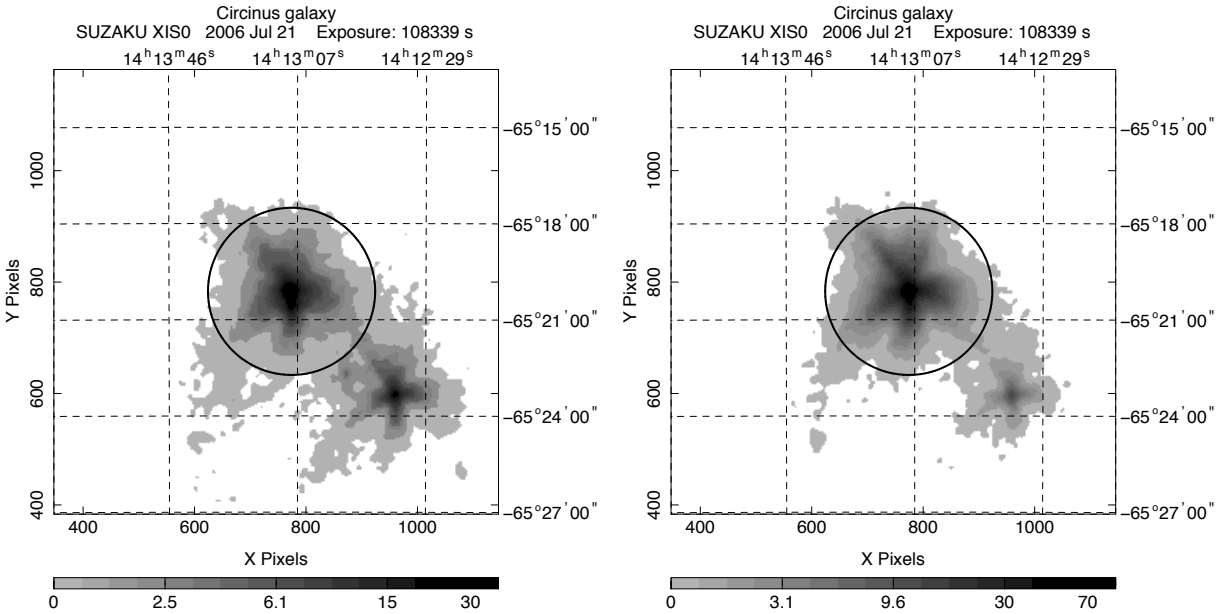

Figure 5.18: The same as Figure 5.1, but for Circinus, in the 0.3–3.0 keV (left) and 3.0-9.0 keV (right) band. The source events are extracted within the black solid circle whose radius is 2′.6, corresponding to 3.6 mm on the sensor.

5.3.2 HXD data analysis and broad-band spectrum

Figure 5.19 shows the energy spectra of Circinus taken with HXD-PIN (below 60 keV) and HXD-GSO (above 50 keV), in comparison with their backgrounds. Thus, the net source count rate of HXD-PIN exceeds 20% of the background rate over the 10–55 keV range. Below, we use the HXD-PIN data in the 10–55 keV range, where the signal count rate, 0.402 ± 0.003 cts s^{-1}, amounts to $\sim$ 40% of the background rate (NXB plus CXB, 0.506 cts s^{-1}). In the HXD-GSO spectrum, the net source counts are $\sim$ 1–2% in the 50–100 keV range. To minimize the response uncertainty (§5.2.2), we use in our subsequent spectral fitting the GSO data summed into a single energy bin covering 70–100 keV. The background-subtracted source count rate in the energy range is 0.047 ± 0.007 cts s^{-1}.

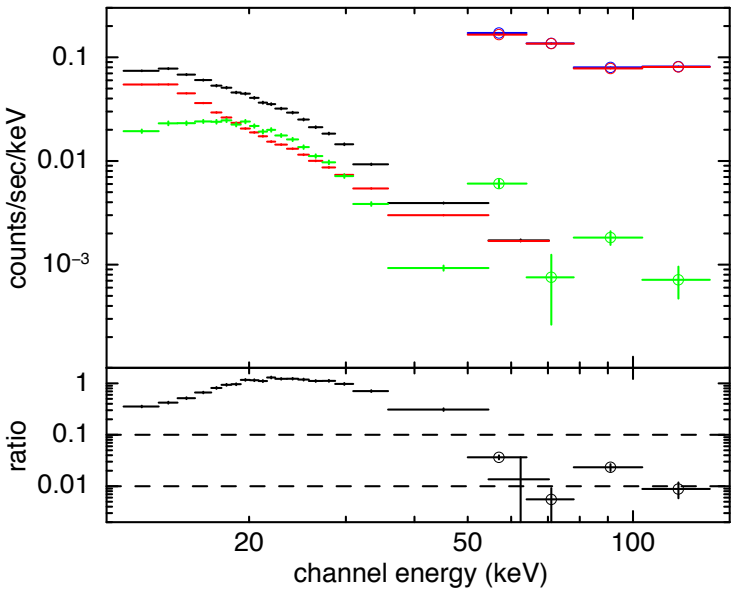

Figure 5.19: The same as Figure 5.2, but for Circinus.

Figure 5.20 shows the Crab ratio of Circinus in the 2–150 keV band. The huge line complex around the 6–8 keV as well as the extremely hard continuum up to $\sim$ 30 keV are even more amazing than in the two sources studied so far. This clearly suggests that the reprocessed emission dominate the spectrum up to at least $\sim$ 10 keV. There is a hump-like feature around $\sim$ 30 keV. Although this hump could be interpreted as either Compton hump or spectral cutoff, it could have other yet unknown origin.

5.3.3 Spectral fitting below 10 keV

As suggested in §5.3.2 and previous studies (e.g., Matt et al. 1996b; Sako et al. 2000b), the intrinsic nuclear emission of Circinus emerges only above 10 keV, so that the spectrum below this energy is considered to be totally dominated by reprocessed emission. Therefore, we begin the analysis with spectrum below 10 keV, in order to quantify the reprocessed signal in detail. We fitted the 3.0–9.0 keV spectrum only with the cold reflection continuum (`pexrav`), but excluding the energy ranges of 6.0–8.0 keV and 3.5–4.0 keV, where line complex are apparent in the Crab ratio. The Galactic absorbing column was set to 5.0×10^{21} cm^{-2}, the photon index of the incident power-law at 1.80, and the cutoff energy at 100 keV. The spectra of CG X-1 and CG X-2 were modeled as described in §5.3.1.

As shown in Figure 5.21, the model poorly reproduced the data (χ/ν = 417.7/201) even in this limited energy range, although the relatively steeper 3–5 keV slope (compared

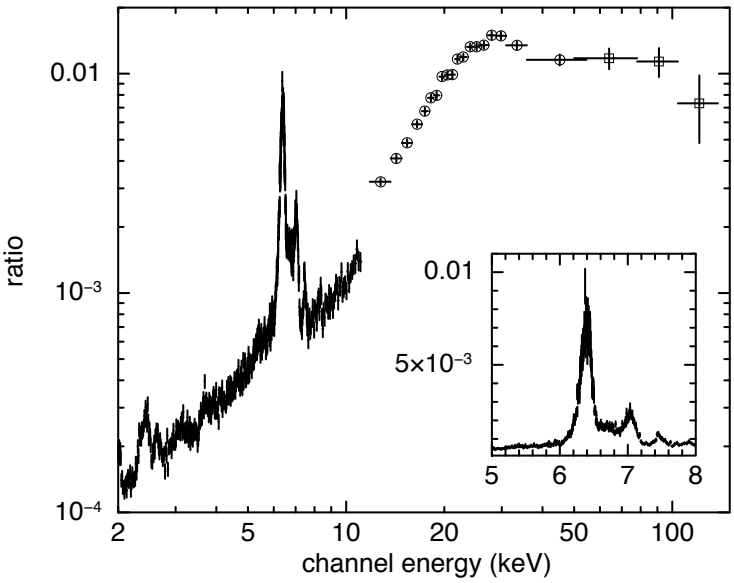

Figure 5.20: The same as Figure 5.3, but for Circinus.

to the previous two AGNs) were successfully accounted for by the CG X-1 and CG X-2 contributions. In the residual spectra, several line-like features besides the iron line region (6–8 keV) are clearly seen. The blue lines show the expected line energies from various kinds of neutral materials: Ar, K, Ca, Sc, Cr, Fe, Ni, as well as that of ionized Fe. Interestingly, the huge emission line at 6.4 keV, attributable to Fe-I Kα fluorescence, has a dent-like structure around its center, which can imply a possible absorption line feature.

Next, we added to the model Gaussian lines one by one, up to as many as the data require. We then found that eleven emission and two absorption lines make the fit almost acceptable with $\chi^2/\nu = 457.3/410$. The best fit model and the residuals are shown in Figure 5.21, and the line properties are summarized in Table 5.3. Among the emission lines, ten lines can be identified as Kα or Kβ lines from neutral material, and one as Fe XXV Kα line. The equivalent width of the neutral lines with respect to the reflection continuum are roughly consistent with the expected value, calculated for an optically-thick reflecting material (Matt et al. 1996a, Matt et al. 1997a). Thus they are most likely to originate in the same material which is responsible for the cold reflection continuum. The two absorption line in the table are statistically significant, but their center energies are closest to those of Fe I Kα and Fe I Kβ emission lines. Since we cannot expect absorption lines from these species, it is very likely that the dent-like feature of the emission lines should be attributed to other physical processes. But we do not focus on it in this thesis. The quoted equivalent widths of Fe I Kα and Fe I Kβ emission lines are calculated for the net number of photons in the relevant emission feature, i.e., number of photons in the

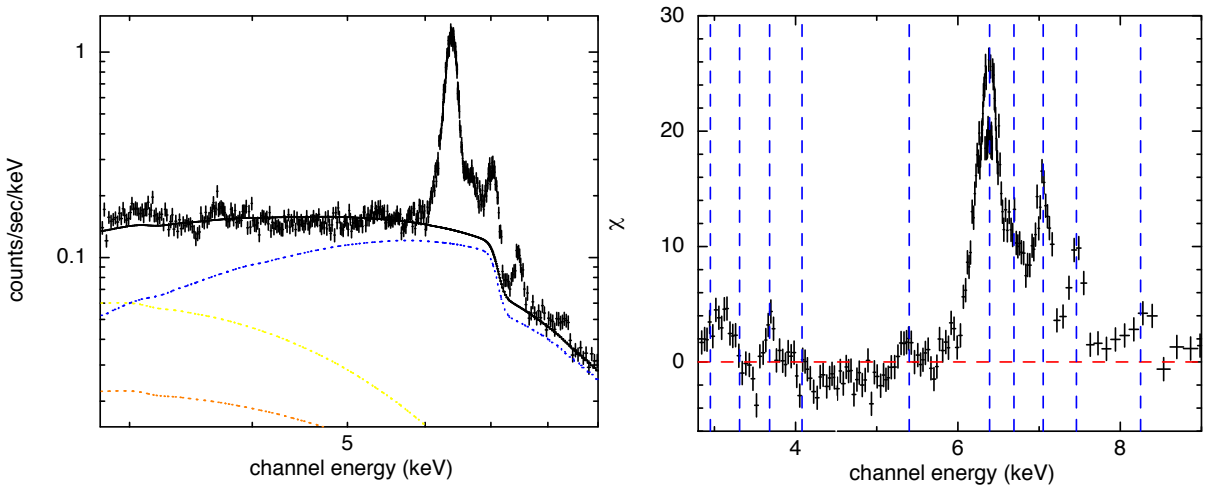

Figure 5.21: (Left) The XIS raw count rate spectra of Circinus on which cold reflection model are superimposed. The data in the 6.0–8.0 and 3.5–4.0 keV band are not used in the fit. The black crosses shows the data points from XIS-FI, while the dashed blue lines represent the reflection model. The yellow and brown liens represent the model for CG X-1 and CG X-2. (Right) The residuals from the fit, with the energy in linear scale. The blue lines correspond to energies of 2.96, 3.31, 3.69, 4.09, 5.41, 6.40, 6.70, 7.05 and 7.47 keV in the source rest frame, respectively. Assignments of these energies to atomic lines are given in Table 5.3

modeled emission line minus that of the absorption line.

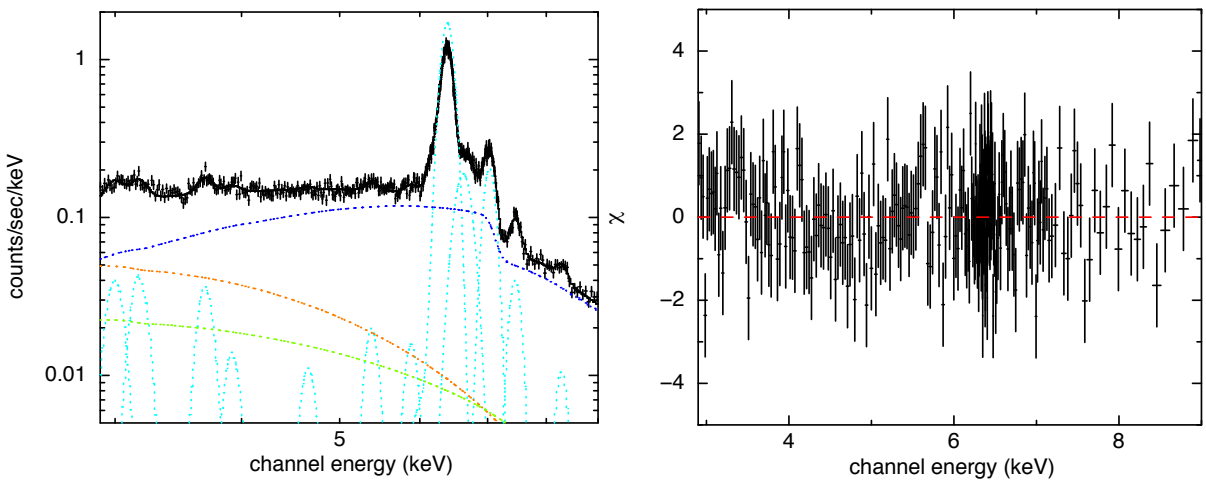

Figure 5.22: The same as Figure 5.21, but for the cold reflection plus 11 emission lines and two absorption lines model (see text). The emission lines are colored in cyan.

Table 5.3: The line profiles observed in the 3.0–9.0 keV XIS spectrum of Circinus.

Element	Line energy (keV) observed	Line energy (keV) expected	Intensity (10^{-5} ph s^{-1} cm^{-2})	Width[a] (eV)	$EW_{\rm refl}$[b] (eV) observed	$EW_{\rm refl}$[b] (eV) expected[c]
Emission lines						
Fe I Kα	$6.400^{+0.002}_{-0.003}$	6.400	571^{+50}_{-42}	< 20	$1.3^{+0.1}_{-0.2} \times 10^3$	1.0–2.7 $\times 10^3$
Compton shoulder	-	-	20^{+5}_{-5}%	-	-	-
Fe I Kβ	$7.041^{+0.008}_{-0.006}$	7.058	83.6^{+10}_{-12}	-	580^{+53}_{-62}	-
Fe XXV Kα	$6.635^{+0.008}_{-0.007}$	6.668/6.701	94.8^{+15}_{-14}	90^{+60}_{-70}	-	-
Ni I Kα	$7.465^{+0.015}_{-0.016}$	7.472	$19.3^{+1.8}_{-2.2}$	-	190^{+22}_{-30}	80–120
Ni I Kβ	$8.30^{+0.05}_{-0.06}$	8.265	$7.6^{+1.0}_{-1.1}$	-	76^{+8}_{-9}	-
Ar I Kα	$3.00^{+0.04}_{-0.05}$	2.957	$10.0^{+1.2}_{-1.1}$	-	102^{+10}_{-11}	45–70
Ca I Kα	$3.69^{+0.06}_{-0.05}$	3.690	$8.5^{+1.0}_{-0.9}$	-	73^{+7}_{-6}	40–60
Cr I Kα	$5.39^{+0.12}_{-0.11}$	5.412	$5.0^{+0.8}_{-0.9}$	-	33^{+4}_{-6}	25–35
Mn I Kα	$5.90^{+0.12}_{-0.13}$	5.895	$4.4^{+0.8}_{-1.0}$	-	27^{+6}_{-7}	-
Ar I Kβ	$3.92^{+0.13}_{-0.12}$	4.089	$3.1^{+0.6}_{-0.5}$	-	26^{+5}_{-6}	-
S I Kβ	$3.17^{+0.10}_{-0.08}$	3.313	11.0^{+3}_{-2}	-	103^{+23}_{-25}	-
Absorption lines						
.....	$6.417^{+0.007}_{-0.005}$	-	308^{+62}_{-85}	77^{+42}_{-61}	-	-
.....	$7.066^{+0.018}_{-0.022}$	-	$21.3^{+4.5}_{-4.3}$	-	-	-

[a] Line widths of the neutral emission lines are tied to each other. Those of the absorption lines are also tied to each other.

[b] Equivalent width with respect to the cold reflection. [c] Via Matt et al. (1996a); Matt et al. (1997a);

5.3.4 Wideband spectral fitting

In Figure 5.4, we found that the direct nuclear emission of NGC 4388 emerges at $\gtrsim 3.5$ keV above the reflected continuum, through an absorber with $N_{\rm H} = 3.7 \times 10^{23}$ cm^{-2}. In the case of Mrk 3 (Figure 5.13), this cross-over locates at the highest end of the XIS spectrum, because of the heavier absoption with $N_{\rm H} \sim 1.2 \times 10^{-24}$ cm^{-2}. In Circinus, we do not find such evidence of the direct nuclear emission up to ~ 9 keV (Figure 5.22). This implies that the absorbing column density in Circinus is even higher than 1×10^{24} cm^{-2}, and is likely to be Compton-thick. Then, are the HXD signals (Figure 5.20) accounted for entirely by the reflected signals, or do we start observing the direct nuclear emission at higher energies? In order to examine this possibility, we extrapolated the XIS-determined reflection spectrum to the HXD band, to find a huge excess emission as shown in Figure 5.23. Although the Circinus galaxy happens to lie close to the Galactic plane at ($l \simeq 311°, b = -3.8°$), there is no known bright hard X-ray source in the HXD field of view. Therefore, we must be observing another component in the Circinus spectrum, which is most likely to be the nuclear radiation piercing throughtout a very large column density absorber.

We then fitted the spectrum over the whole energy band, including a highly absorbed power-law to the model. We show in Figure 5.24 the best fit model and the residuals, and the best fit parameters in Table 5.4 (Model 1). The model reproduced the whole band spectrum roughly successfully with $\chi^2/\nu = 510.5/427$. Thus, the solution implies the transmitted nuclear radiation to overwhelm the reflection above ~ 15 keV.

The observed total flux in the 20–100 keV is 2.0×10^{-10} erg s^{-1} cm^{-2}, which makes the Circinus one of the brightest AGN in hard X-rays. However, the estimation of the intrinsic AGN luminosity is subject to a large uncertainty, for the following reason. The absorber columns density derived with the above model reaches $N_{\rm H} \sim 7 \times 10^{24}$ cm^{-2}, confirming that the abosorber is quite Compton-thick ($\tau \sim 4$). This implies that the photons which eventually emerge may have suffered one or more Compton scatterings. If the absorber subtends an infinitely small solid angle as seen from the central source, a considerable fraction of the intrinsic emission is scattered out from the line of sight, and its flux must be suppressed by a factor of $\exp(-N_{\rm H}\sigma_{\rm T})$ for an observer located at infinity. If, instead, the Compton-thick absorber covers a large solid angle, a significant fraction of the intrinsic emission would be scattered back into the line of sight. Thus, under such a Compton-thick condition with $N_{\rm H}\sigma_{\rm T}$ reaching a few, the two extreme assumptions provide quite different intrinsic flux to explain the observed flux; they can even differ by two orders of magnitude (Matt et al. 1999b). If we assume the former case (absorber subtending small solid angle),

the absorption corrected 2–10 keV flux is estimated to be $\sim 4 \times 10^{-8}$ erg s^{-1} cm^{-2}, yielding a 2–10 keV luminosity $L_{2-10}^{\rm int} \sim 8 \times 10^{43}$ erg s^{-1} and a bolometric luminosity of $\sim 2 \times 10^{45}$ erg s^{-1}. The latter is even about ~ 8 times the Eddington luminosity for the $1.7 \times 10^6 M_\odot$ black hole. Therefore, the small solid angle assumption is physically unlikely and large covering fraction is required in this source. On the other hands, if we assume a Compton-thick absorber with a large covering fraction (and thus significant scattering-in of the nuclear emission), the bolometric luminosity of only $\sim 1 \times 10^{43}$ erg s^{-1} (or $\sim 5\%$ of the Eddinton luminosty) is required (Matt et al. 1999b). This scenario is, therefore, physically more plausible. Indeed, the derived bolometric luminosity agree with the integrated infrared luminosity of $\sim 4 \times 10^{43}$ erg s^{-1}, a large fraction of which being probaly reprocessing of the nuclear radiation (Moorwood et al. 1996a; Maiolino et al. 1998). In this case, the reflection fraction is estimated to be $f_{\rm refl} \sim 0.3$.

Although the emergence of the AGN component at $\gtrsim 15$ keV successfully explains the HXD spectrum, there remains yet another interpretation denoted Model 2 in Table 5.4, in which the additional component emerging in the HXD-PIN band is simply a fraction of the total reflection component, but affected by an additional absorption i.e., the reflecting matter is partially covered. This case would represent a scenario in which the line of sight towards the nucleus is completely blocked (i.e., $N_{\rm H}$ in excess of $\sim 10^{25}$ cm^{-2}), but the optical depth diminishes at higher torus latitudes, so permitting transmission of some of the radiation reflected by the far side of the torus. This model gives statistically as good fit as Model 1. No estimate of the nuclear luminosity nor $f_{\rm refl}$ is possible in this model. Thus, $f_{\rm refl}$ in Circinus is quite ambiguous; it can be as large as an order of unity.

5.3.5 Time variability

Although the spectra do not allow us to distinguish the three alternatives (a small solid angle in Model 1, a large solid angle in Model 1, and Model 2), we may discriminate them using time variations. In a situation that a Compton-thick absorber subtends a large solid angle as seen from the nuclear source, the scattered-in photons would dilute the intrinsic variability, and hence smaller or no time variation would be observed. The Model 2 case is essentially the same. With a small covering fraction absorber, instead, the intrinsic variability would be observed without being diluted. Considering the $1.7 \times 10^6 M_\odot$ black hole in Circinus, we may expect intrinsic time variation with a time scale of as fast as ~ 20 ks, which can be observed with the 2 days observation if the small solid angle is the case.

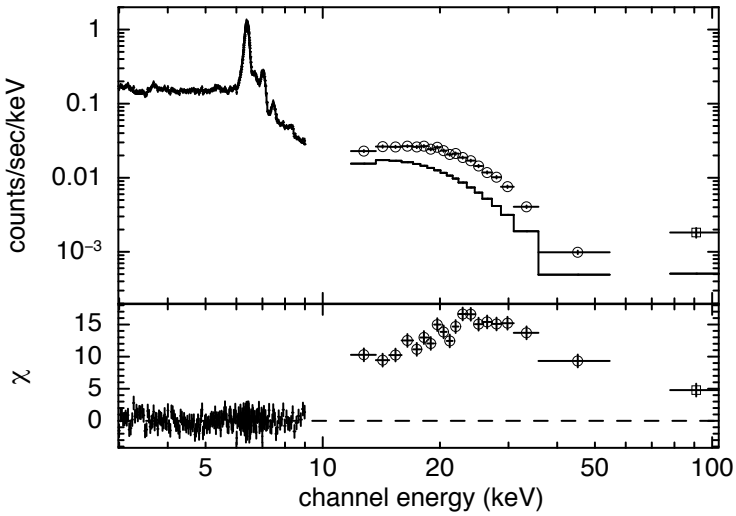

Figure 5.23: The XIS + HXD spectrum of Circinus in detector raw count rate. Crosses, circles and boxes correspond to data of XIS-FI, HXD-PIN and HXD-GSO, respectively. The XIS best fit model extrapolated to the HXD data is shown by black line.

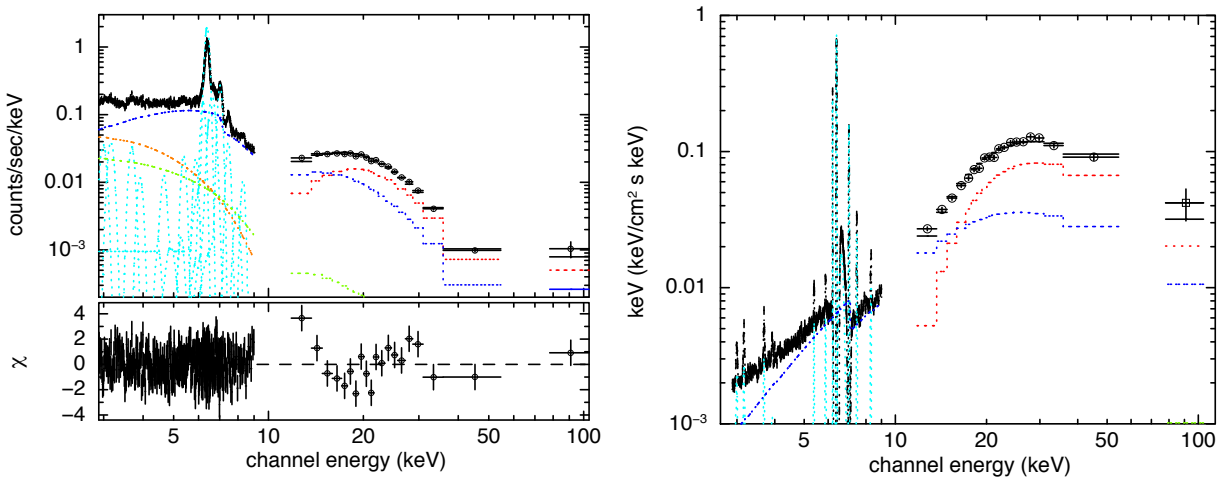

Figure 5.24: The same as Figure 5.21, but under the wideband modeling incorporating a highly attenuated intrinsic AGN emission (see text). The dashed color lines represent model components: the absorbed intrinsic power-law in red, reflection in blue, emission lines in cyan.

Table 5.4: Best-fit continuum parameters of wideband spectrum of Circinus over the 3.0–110 keV range.

Model Component	Parameter	Model 1	Model 2
Intrinsic PL	Γ	$2.0^{+0.1}_{-0.2}$	$2.0^{+0.1}_{-0.2}$
	$N_{\rm PL}{}^{a}$	$0.20^{+0.07}_{-0.06}$	-
	$E_{\rm cut}$	37^{+8}_{-15}	43^{+10}_{-14}
	$N_{\rm H}{}^{b}$	$7.3^{+0.7}_{-1.0}$	$6.3^{+0.6}_{-0.8}$
Reflection	$f_{\rm refl}$	$0.3^{+0.2}_{-0.1}$	-
	$A_{\rm Fe}{}^{c}$	$0.72^{+0.28}_{-0.25}$	$0.64^{+0.32}_{-0.24}$
χ^2/d.o.f.		510.5/427	510.3/427

[a] ph keV^{-1} cm^{-2} s^{-1} at 1 keV. [b] 10^{24} cm^{-2}.

[c] Iron abundance of the reflector and absorber.

Figure 5.25 shows *Suzaku* XIS light curves of the Circinus in five energy ranges, which has been extracted in the same way as in §5.1.7. The light curves below 4 keV show variation by $\sim$ 20%, exhibiting an apparent apparent periodicity with a $\sim$ 30 ks period. This variation can be attributed to that of CG X-1, because it is known to almost completely disappear every $\sim$ 30 ks (Weisskopf et al. 2004), and its contribution is $\sim$ 20% of the nucleus (see §5.3.1) in the energy ranges. The flux variation becomes smaller in the higher energy ranges: we observe a slight, statistically significant variation by $\sim$ 10% in the 4–6 keV band, while no variation above the energy, suggesting that the contamination by CG X-1 becomes smaller at higher energies. These facts concerning CG X-1 are consistent with our spectral model in §5.3.3 and §5.3.4 to account for its contamination.

Figure 5.26 shows the HXD-PIN light curves in its whole (12–60 keV), soft (12–25 keV) and hard (25–60 keV) energy ranges, as well as the hardness ratio (12–25 keV/25–60 keV). We show in each energy ranges, the total, background and net count rates. The background-subtracted light curves apparently show a time variability by $\sim$ 10%, while they are only marginally significant ($\sim$ 95% in the 12–60 keV band). Instead, the hardness ratio shows a slight variability. If this time variation is real, it means that at least some fraction of the observed flux is the nuclear intrinsic emission which have not undergone scattering by the absorber. If so, the Model 2 scenario is ruled out, and furthermore, the Compton-thick absorber is inferred to have relatively small solid angles.

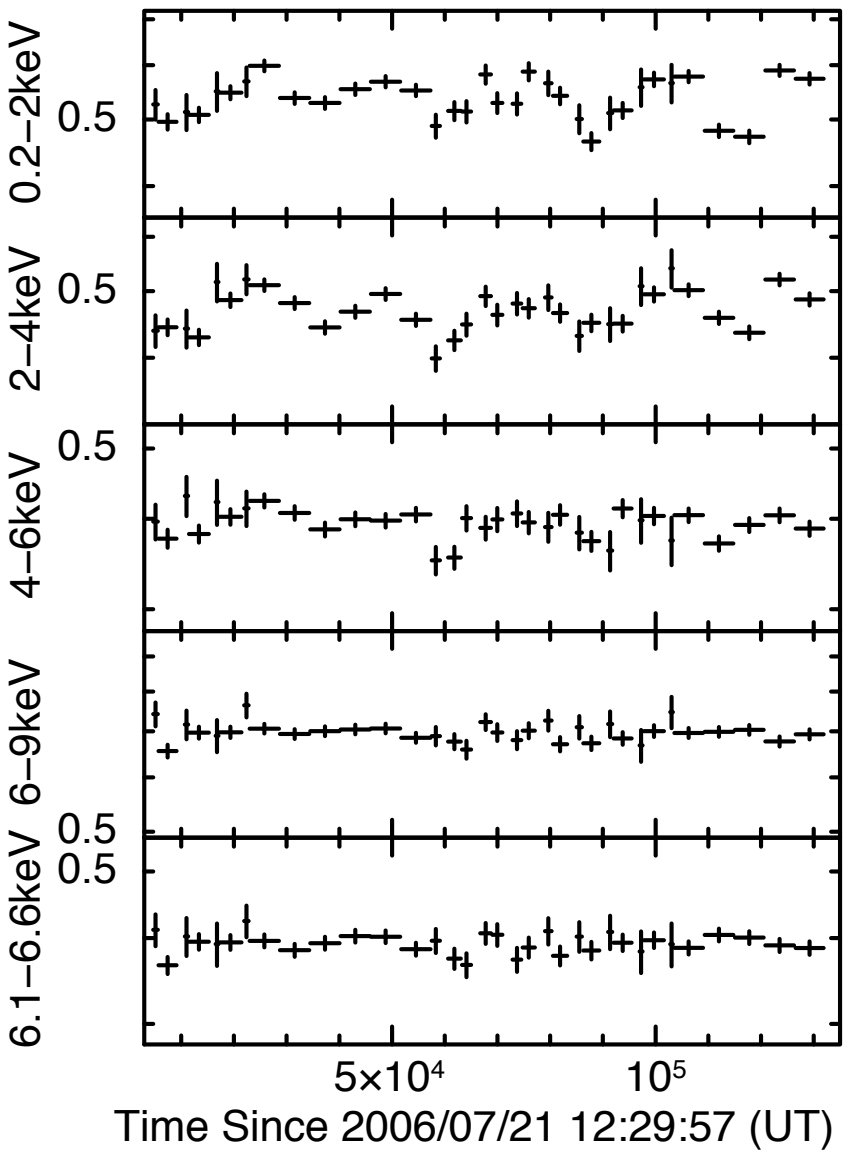

Figure 5.25: Background-subtracted light curves of Circinus taken with *Suzaku* XIS, in the energy ranges of 0.2–2, 2–4, 4–6, 6–9, and 6.1–6.6 keV. Data from the four XIS sensors are co-added. Each bin corresponds to a continuous time interval without data gaps.

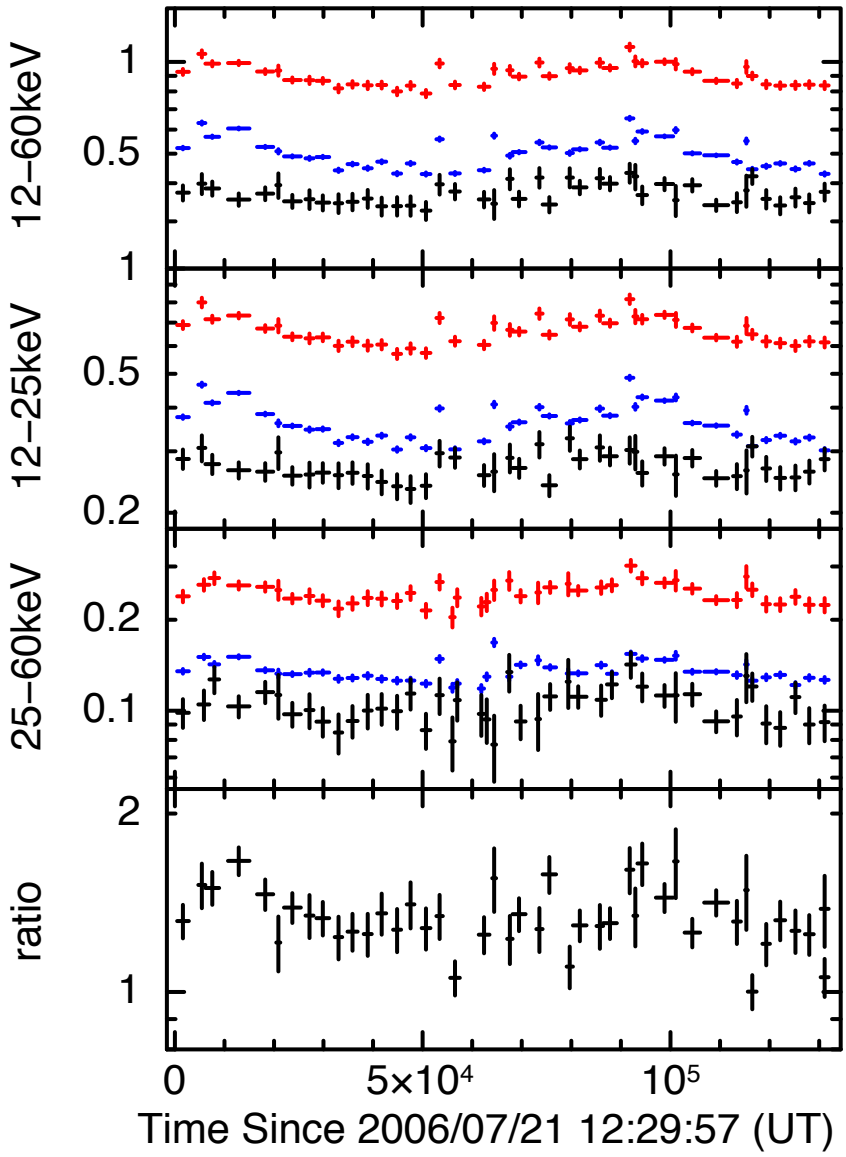

Figure 5.26: Background-subtracted light curves of Circinus taken with *Suzaku* HXD-PIN, in the energy ranges of 12–60, 12–25 and 25–60 keV. Each bin corresponds to a continuous time interval without data gaps.

5.4 NGC 4945

5.4.1 XIS data analysis

Figure 5.27 shows the XIS image of NGC 4945, in energy ranges of 0.3–4.5 keV (left) and 4.5–9.0 keV (right). The AGN is located at the center of the images. While several other X-ray sources can be seen in the lower energy band, the AGN emission is dominant in the higher energy band. In the same region, Schurch et al. (2002) detected non-nuclear point sources which are indicated with white arrows in Figure 5.27 (left). We analyzed the *XMM-Newton* data of these sources, to find that their contamination to the *Suzaku* AGN spectra are negligible in energies higher than ~ 4.5 keV. The bright source in the SW region in Figure 5.27 has not been observed by any previous observations. According to its luminosity, this transient source could be a ultra luminous X-ray source (ULX) associated with NGC 4945. Detailed analysis and results of this source are reported in Isobe et al. (2008), together with a discussion on its nature. Even though this source is the second brightest in the image, it has a thermal spectrum with a temperature of ~ 1.5 keV. Thus, its emission becomes much smaller ($\lesssim 1\%$) than that of the AGN in the HXD band.

In order to avoid the contamination from the two bright sources in the region, while collecting the source events as much as possible, we extracted AGN spectra from the four XIS sensors within a circular region of $1'.45$ radius (corresponding to 2 mm on the sensor, or 1.56 kpc in physical size at a distance of 3.7 Mpc), indicated by a black circle in the images. The background spectra were extracted from source free regions of the same CCDs. In the following spectral analysis, we use data over an energy range of 4.5–9.0 keV and 4.5–8.0 keV for FI and BI chips, respectively, to avoid possible contamination by other sources in lower energies. A total net exposure of ~ 90.8 ks was obtained from each XIS sensor, with source count rates of $(8.83 \pm 0.1) \times 10^{-2}$ cts s^{-1} for the three FI chips and $(1.88 \pm 0.05) \times 10^{-2}$ cts s^{-1} for the BI chip.

5.4.2 HXD data analysis and broad-band spectrum

Figure 5.28 shows the energy spectra of NGC 4945 observed with HXD, in comparison with their backgrounds. As shown in the lower panel of Figure 5.28, the net source counts exceed $\sim 20\%$ of the background over the entire HXD-PIN energy range. In the following spectral analysis, we use an energy range of 12–60 keV, in which the net signal counts become 0.299 ± 0.003 cts s^{-1}, or $\sim 65\%$ of the background rate (NXB plus CXB,

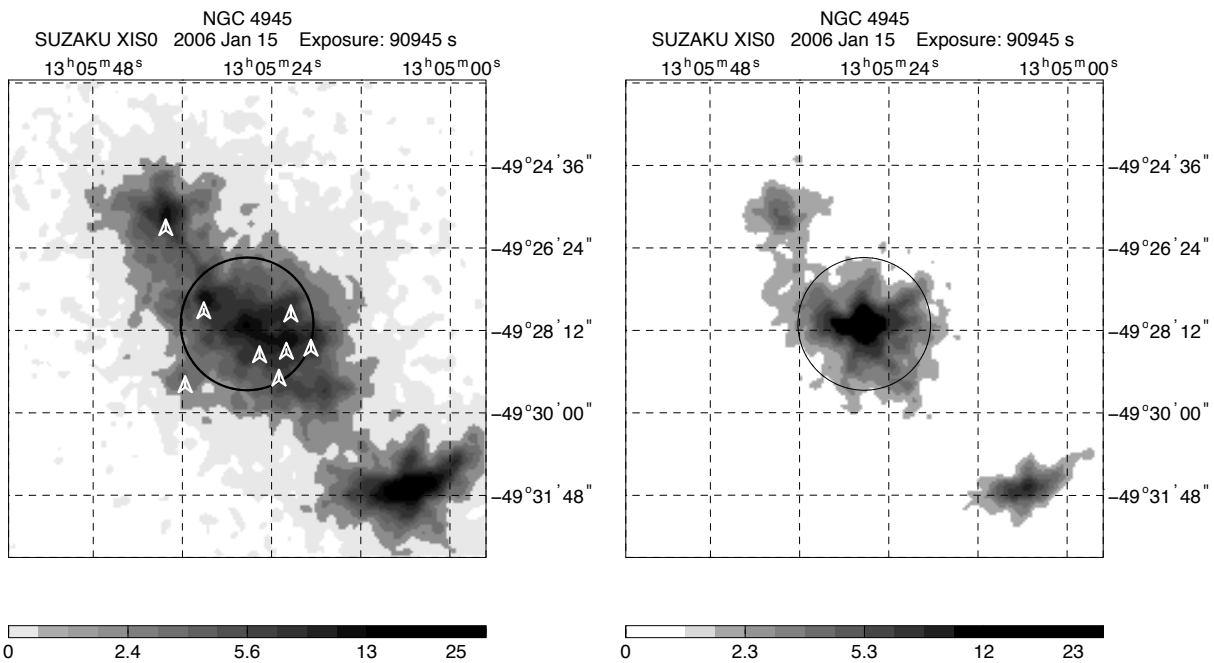

Figure 5.27: The same as Figure 5.1, but for NGC 4945, in the 0.3–4.5 keV (left) and 4.5-9.0 keV band (right). White arrows in the left panel indicate individual point sources detected by *XMM-Newton* (Schurch et al. 2002). Black circle in the right panel indicates the source extraction region, whose radius is $1'.45$ corresponding to 2.00 mm on the sensor.

0.461 ± 0.001 cts s^{-1}). There, the signal detection is statistically significant at $> 8\sigma$, in each of appropriately summed energy bins in the spectrum. Even in the HXD-GSO range, the signal thus exceeds 2% of the background up to ~ 150 keV, although it decreases to $\lesssim 1\%$ at ~ 200 keV. In the subsequent spectral fitting, we utilize the GSO data only in the 70–120 keV range.

Figure 5.29 shows the Crab ratio of NGC 4388 in the 4.5–200 keV band. Below ~ 30 keV, the ratio decreases steeply, indicating that the underlying emission is attenuated by absorption, whose column density is significantly higher than those in NGC 4388 or Mrk 3. Above ~ 40 keV, the Crab ratio stays rather constant up to ~ 200 keV, without showing clear evidence for a high-energy spectral cutoff. As clearly seen from the Crab ratios, this AGN is considerably brighter at ~ 100 keV than the three objects studied so far. At $\lesssim 10$ keV the ratio becomes flatter, but the implied spectrum is still harder than that of the Crab Nebula, implying a photon index of $\Gamma \sim 1$. Therefore, the source spectrum in this energy range can be better interpreted as a reflected continuum rather than an intrinsic emission. This inference is supported also by the strong emission line features, which are clearly seen around 6–8 keV in the inserted figure.

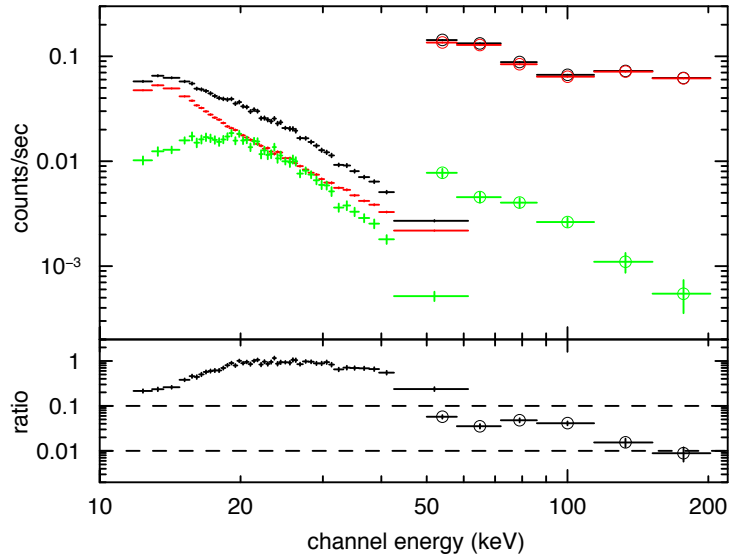

Figure 5.28: The same as Figure 5.2, but for NGC 4945.

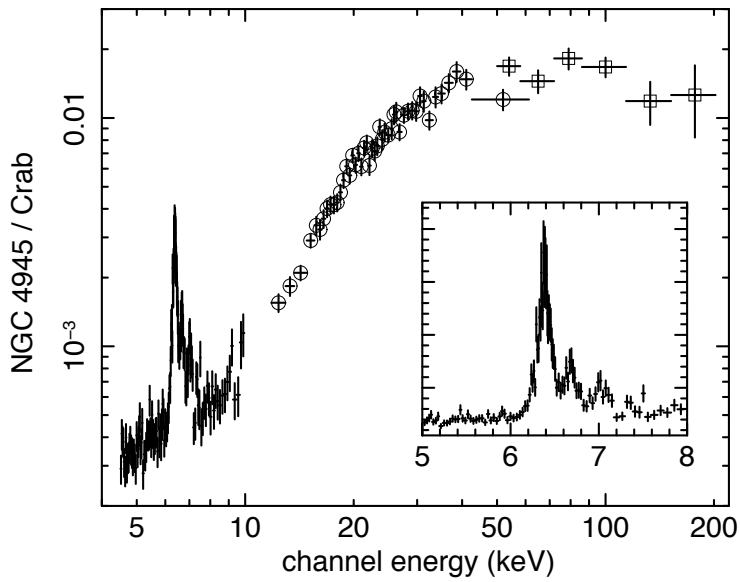

Figure 5.29: The same as Figure 5.3, but for NGC 4945.

5.4.3 Spectral fitting with BC + lines model

As noted in §5.4.2, the intrinsic nuclear emission of NGC 4945 is considered to appear only at $\gtrsim$ 10 keV, while its reprocessed emission dominates the energy spectrum below 10 keV. In order to approximate the background-subtracted XIS and HXD spectra in the energy range of 4.5–120 keV, we first adopted the BC model, consisting of an absorbed intrinsic emission and a cold reflection continuum (see §5.1.5). As before, the energy band between 6.0 and 8.0 keV was not utilized in the fitting. The Galactic absorbing column toward NGC 4945 was set at 1.57×10^{21} cm^{-2} (Heiles and Cleary 1979), and we initially fixed the cutoff energy for the high energy roll over at 200 keV. The data, the best-fit BC model, and the fit residuals are shown in Figure 5.30. As seen in the figure, the BC model roughly reproduced the overall continuum shape. Although the fit is still unacceptable with $\chi^2/\nu = 108.4/51$, the photon index of the intrinsic power-law can be estimated as $\Gamma \sim 1.7$. Furthermore, the absorbing columns, $N_{\rm H} \sim 4.5 \times 10^{24}$ cm $^{-2}$, was confirmed to be significantly higher than those in NGC 4388 an Mrk 3, which makes NGC 4945 another Compton-thick source in addition to Circinus.

Figure 5.30 (right) shows the data/model ratio around the iron line region. It reveals several emission lines, at $\sim$ 6.40 keV, $\sim$ 6.70 keV, $\sim$ 7.05 keV, and possibly at $\sim$ 7.47 keV. We therefore added Gaussians to represent those four features, and found that all of them are statistically significant ($\gtrsim$ 99.9% even with the $\sim$ 7.47 keV one). From their center energies, they can be identified as fluorescent Fe I Kα, Fe I Kβ and Ni I Kα lines, respectively, which indicate that they originate as fluorescence from cold materials. Note that the latter two emission lines have not been detected by any previous missions. Apart from the three neutral lines, the emission line at $\sim$ 6.68 keV agrees in energy with Fe XXV Kα line, suggesting the presence of another reprocessing material which is highly ionized. Although the BC plus lines model thus reproduced the observed continuum and iron line complex roughly well, systematic residuals are clearly recognized at $\lesssim$ 5 keV and $\gtrsim$ 8 keV, which make the fit unacceptable ($\chi^2/\nu = 174.1/92$),

5.4.4 Spectral fitting with BC + ionized plasma models

The reprocessed emission from cold material (i.e., reflection continuum and fluorescent lines) has been modeled successfully by the BC plus lines model, at least in the 5–8 keV range. The presence of the ionized Fe-K line at $\sim$ 6.7 keV, however, suggest that there is a separate soft emission component that may require an independent modeling. One obvious possibility is that the ionized line originates from a hot plasma collisionally heated

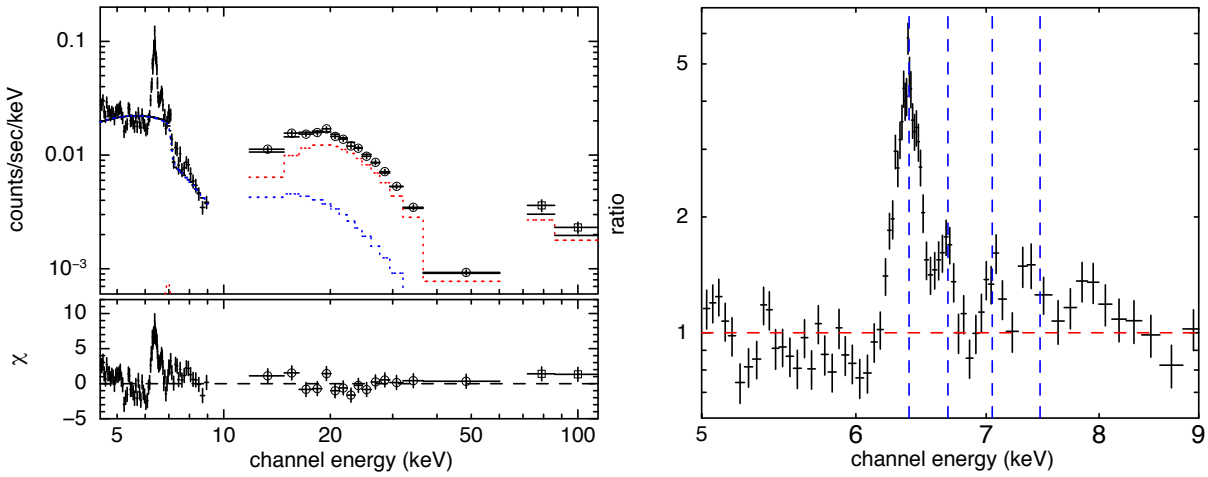

Figure 5.30: The same as Figure 5.4, but for NGC 4945.

by the star-burst activity around the nucleus (Schurch et al. 2002). Such a plasma must also contribute to the soft continuum, which should be modeled together with the ionized iron line. We thus added to the BC model a hot plasma component (`mekal` in XSPEC). We separately modeled the three neutral lines; the Fe I Kβ and Ni I Kα lines by single Gaussians, while the strong Fe I Kα line by the `kalpha` model (§5.1.5). The fit goodness drastically improved compared to the "BC plus lines" model, and became acceptable ($\chi^2/\nu = 96.5/93$). We show in Figure 5.31 the data, the best-fit model, and the fit residuals. The best-fit parameters are summarized in Table 5.5.

An alternative mechanism to produce the ionized ion line is fluorescence in a photo-ionized plasma. Indeed, recent studies with high energy resolution instruments found radiative recombination continua in AGN spectra, which provide clear evidence for photo-ionized gas. These atomic features are typically seen in the highest signal–to–noise spectra of obscured AGNs (e.g., the compilation of Bianchi et al. 2006; Young et al. 2001; Kinkhabwala et al. 2002). According to detailed calculations of the column, ionization state and covering fraction of the gas required to produce the radiative recombination continua and the copious low energy photo-ionized lines in Seyfert 2's, such material must necessarily also scatter some fraction $f_{\rm scat}$ of the photo-ionizing flux (§5.2.3). The scattered continuum has approximately the same shape as the incident AGN emission, i.e., a power-law (Bianchi et al. 2006). This continuum can be seen directly in regions of the spectrum away from the strong line emission (e.g., Mrk 3, Bianchi et al. 2005b; §5.2.3). Hence we explore here the possibility that the Fe XXV Kα line seen in NGC 4945 is from photo-ionized rather than collisionally ionized material, although the RGS data, hampered by poor signal–to–noise ratio of this object at low energies, did not give strong evidence for such a photo-ionized gas (Guainazzi and Bianchi 2007). We thus added to

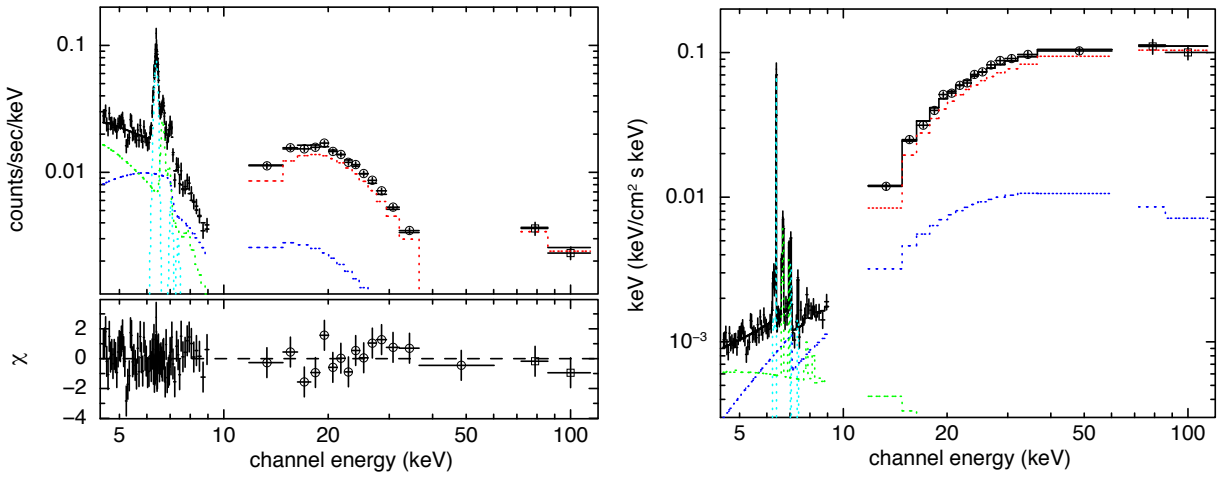

Figure 5.31: The same as Figure 5.4, but for NGC 4945, under the BC plus thermal plasma model. The dashed color lines represent model components: the absorbed intrinsic power-law in red, reflection in blue, emission lines in cyan, and thermal plasma in green.

the BC model, another power-law absorbed only by the Galactic column, with its photon index set to the same as the primary one. The neutral lines are modeled in the same way as the BC plus thermal plasma model, while the Fe XXV Kα line with a single Gaussian, allowing its energy to vary. This model has also reproduced the data successfully, with $\chi^2/\nu = 95.8/91$. We show in Figure 5.32 the data, best-fit model, and the fit residuals. The obtained best-fit parameters are shown in Table 5.5.

5.4.5 Derived parameters

The observed flux of NGC 4945 in the 2–10 keV range is only 3.2×10^{-12} erg s^{-1} cm^{-2}, which is lower than any of the former four sources. However, we found that this source is indeed the most luminous among our sample in the 20–100 keV range, with the observed flux of $L_{20-100} = 2.6 \times 10^{-10}$ erg s^{-1} cm^{-2}. The obtained absorbing columns is $N_{\rm H} \sim$ (4–5) $\times 10^{24}$ cm^{-2}; thus NGC 4945 is a Compton-thick source as well as Circinus. Then, as described in §5.3.4, the intrinsic flux should be estimated by taking the Compton scattering fully into account. From discussion to be conducted later in §5.4.6, the Compton-thick obscuring material in this source must have a rather small solid angle as seen from the central source. In such a case, the intrinsic flux must have been suppressed, at the most extreme case, by a factor of $\sim \exp(-N_{\rm H}\sigma_{\rm T})$. If we assume this extreme case, the unabsorbed intrinsic flux is estimated to be $F^{\rm int}_{2-10} =$ (2–4) $\times 10^{-9}$ erg s^{-1} cm^{-2}, corresponding to the luminosity of $L^{\rm int}_{2-10} =$ (3–6) $\times 10^{42}$ erg s^{-1}, under either the BC plus thermal or the BC plus scattering model, at a distance of 3.7 Mpc. We then obtained the

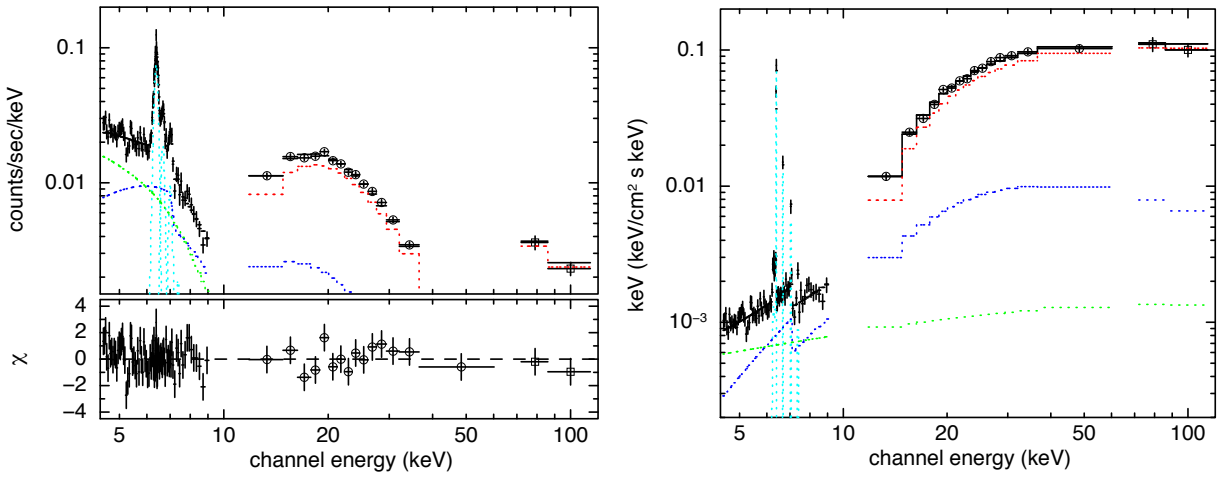

Figure 5.32: The same as Figure 5.4, but for NGC 4945, under the BC plus scattered continuum model. The dashed color lines represent model components in the same way as Figure 5.31.

bolometric luminosity as $\sim$ (3–6) $\times 10^{43}$ erg s^{-1}, corresponding to $\sim$ 20% of the Eddington luminosity for the 1.4×10^6 $M_\odot$ black hole. Thus, this scenario is energetically feasible, though it requires rather high bolometric luminosity. Under this scenario, the reflection fraction should be as small as $f_{\rm refl} \sim 0.1 \cdot \exp(-N_{\rm H}\sigma_{\rm T}) \lesssim 0.01$.

The Fe I Kα line has been found to have an equivalent width of $\sim$ 1.6 keV with respect to the cold reflection component. This value is similar to those obtained in the previous sections, implying that the line and reflected continuum originate at the same location, possibly a visible part of the putative torus (e.g., Matt et al. 1996a). The Compton shoulder parameter $f_{\rm CS}$ was constrained to be $\sim 0.11^{+0.07}_{-0.10}$, which is also consistent with the line originating in a near-Compton-thick reflector.

5.4.6 Time variability

Figure 5.33 shows light curves of NGC 4945 taken with *Suzaku* in five energy ranges. In the upper three panels (with the XIS), the data are binned at the orbital period (5760 sec). The curves in in the lower two panels were extracted from the HXD data, in the same way as in §5.1.7. The three light curves below 10 keV are consistent with being constant. In the energy ranges above 10 keV, in contrast, the source varied by a factor of $\sim$ 2 on a time scale of $\sim$ 20 ks. This agrees with the picture that the reflection from a distant cold material (plus possibly an extended thermal emission or scattering from an ionized medium) dominates the spectrum below 10 keV, while we are seeing the intrinsic AGN emission in the higher energy.

Table 5.5: Best-fit parameters of the two models (see text) to the Suzaku XIS, HXD-PIN, and HXD-GSO spectrum of NGC 4945.

Model Component	Parameter	BC + Thermal	BC + Scattering
Intrinsic PL	Γ	$1.59^{+0.09}_{-0.09}$	$1.60^{+0.09}_{-0.10}$
	$N_{\rm PL}{}^{a}$	$2.2^{+0.6}_{-0.7}$	$2.4^{+0.7}_{-0.7}$
	$N_{\rm H}{}^{b}$	$4.6^{+0.6}_{-0.5}$	$4.7^{+0.5}_{-0.5}$
Reflection	$f_{\rm refl}$	$\sim 0.1^{i}$	$\sim 0.1^{i}$
	$A_{\rm Fe}{}^{c}$	$0.83^{+0.10}_{-0.11}$	$0.86^{+0.11}_{-0.12}$
Mekal	kT^{d}	$6.8^{+0.05}_{-0.08}$	-
	norm	$1.3^{+0.1}_{-0.2} \times 10^{-3}$	-
Scattered PL	$f_{\rm scat}$	-	$\sim 0.01^{i}$
Fe I Kα	$E_{\rm c}{}^{e}$	$6.396^{+0.005}_{-0.005}$	$6.397^{+0.005}_{-0.005}$
	I^{f}	33^{+2}_{-2}	33^{+2}_{-2}
	EW^{g}	$1.6^{+0.2}_{-0.2}{}^{h}$	$1.6^{+0.2}_{-0.2}{}^{h}$
CS	$f_{\rm CS}$	$0.11^{+0.07}_{-0.10}$	$0.10^{+0.08}_{-0.09}$
Fe XXV Kα	$E_{\rm c}{}^{e}$	-	$6.680^{+0.015}_{-0.015}$
	I^{f}	-	$8.3^{+1.0}_{-1.5}$
	EW^{h}	-	$0.5^{+0.1}_{-0.1}$
Fe I Kβ	$E_{\rm c}{}^{e}$	$7.06^{+0.10}_{-0.11}$	$7.04^{+0.12}_{-0.11}$
	I^{f}	$3.0^{+1.2}_{-1.3}$	$4.9^{+1.3}_{-1.8}$
	EW^{g}	$\sim 0.2^{g}$	$\sim 0.2^{g}$
Ni I Kα	$E_{\rm c}{}^{e}$	$7.39^{+0.17}_{-0.16}$	$7.39^{+0.18}_{-0.17}$
	I^{f}	$1.8^{+0.8}_{-0.9}$	$1.1^{+0.8}_{-0.7}$
	EW^{g}	$\sim 0.1^{g}$	$\sim 0.1^{g}$
χ^2/d.o.f.		96.5/93	95.8/91

^{a} 10^{-2} ph keV^{-1} cm^{-2} s^{-1} at 1 keV. ^{b} 10^{24} cm^{-2}.

^{c} Iron abundance of the reflector and absorber. ^{d} Plasma temperature in keV

^{e} Center energy in keV. ^{f} 10^{-6} photons cm^{-2} s^{-1}.

^{g} Equivalent width with respect to the cold reflection.

^{h} Equivalent width with respect to the scattered continuum.

^{i} When the Compton scattering of the intrinsic emission is taking into account, the fractions are further decreased by a factor of $\exp(-N_{\rm H}\sigma_{\rm T})$ (see text).

The detected hard X-ray variations not only elucidates the nature of the emission above $\sim$ 10 keV, but strongly constrain the geometry of the Compton-thick absorver. As described in §5.3.4, when a reprocessing matter has a large solid angle to the central source, a fraction of the photons will be scattered into the line of sight. If, at the same time, the intrinsic emission is highly attenuated through Compton-scatterings by the absorbing matter, the scattered-in photons dominate the spectrum even in the hard X-ray band. Such scattered photons would significantly dilute the time variability of the intrinsic source. Thus, the observed rapid hard X-ray variability in NGC 4945 require that the Compton-thick absorber (reprocessing material) must not have large solid angle as seen from the central source (Madejski et al. 2000). In other words, the Compton-thick absorver is required to be localized into a rather solid angle (including our line of sight) around the AGN.

In order to search the spectra for intensity-correlated changes, we divided the entire observation period into two phases according to the 12–50 keV count rate; "high flux" and "low flux" phases, corresponding to periods when the count rate is higher and lower than 0.275 cts s^{-1}, respectively. The net exposure is 33.7 ks for the high flux phase and 31.7 ks for the low phase. Figure 5.34 shows the spectra of the two phases, in the form of their ratios to the time-averaged spectrum. Above 10 keV, the flux of the high phase is approximately twice as high as that of the low phase, independent of energy. In contrast, data points below 10 keV show no significant difference between the two phases, in agreement with the implication of the light curves. We fitted each spectrum of the two phases by the BC + scattered power-law model, and confirmed that the spectral parameters do not significantly change as the flux varied, except for the normalization of the absorbed power-law component.

It is quite interesting to obtain the varying spectral component, since it must be the pure intrinsic AGN emission without being diluted by any re-processed component. We show in Figure 5.35 the differential spectrum between the two phases, i.e., a spectrum of the high flux phase minus that of the low phase. As shown there, an absorbed power-law reproduces the data successfully ($\chi^2/\nu = 141/216$), with $\Gamma = 1.6^{+0.2}_{-0.3}$, $N_{\rm H} = 4.5^{+0.5}_{-1.0} \times 10^{24}$ cm^{-2}, and $E_{\rm cut} \gtrsim 150$ keV (not constrained). These parameter values agree with those we have derived from the time-averaged spectrum in the previous section. This confirms that the time-averaged spectrum above $\sim$ 10 keV is dominated by the intrinsic AGN component, with little contribution from reprocessed emission.

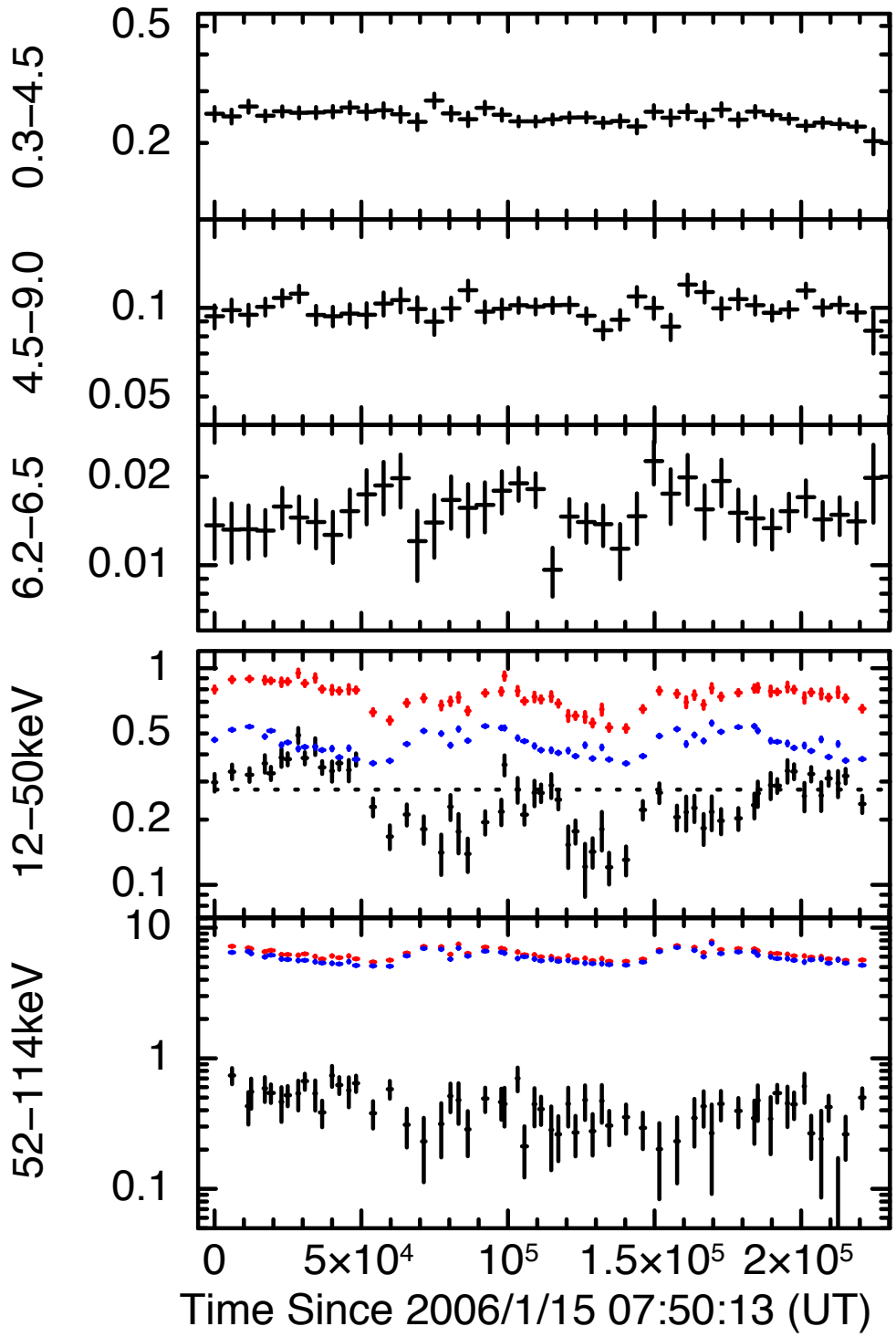

Figure 5.33: Background-subtracted light curves of NGC 4945 taken with Suzaku. The upper three panels show those in 0.3–4.5 keV, 4.5–9.0 keV and 6.2–6.5 keV, respectively, taken with the four XIS sensors, and re-binned with the orbital period of 5760 s. The fourth and fifth panels shows 12–50 keV (HXD-PIN) and 52–114 keV (HXD-GSO) light curves, respectively. In these panels, each bin corresponds to a continuous time interval without data gaps. Dotted line in fourth panels correspond to 0.275 cts s^{-1}, which separate the "high" and "low" flux phase (see text).

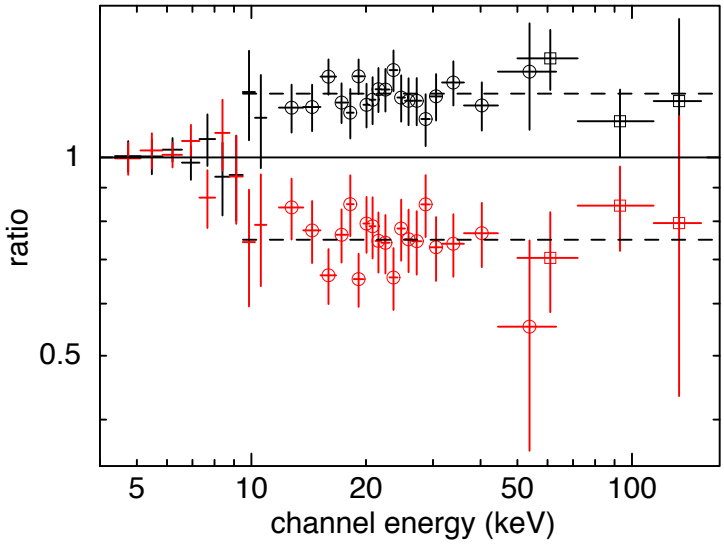

Figure 5.34: Spectra from the "high phase" (black) and "low phase" (red), shown as their ratios to the time averaged spectrum. The XIS, HXD-PIN and HXD-GSO data points are shown in crosses, circles, and squares, respectively.

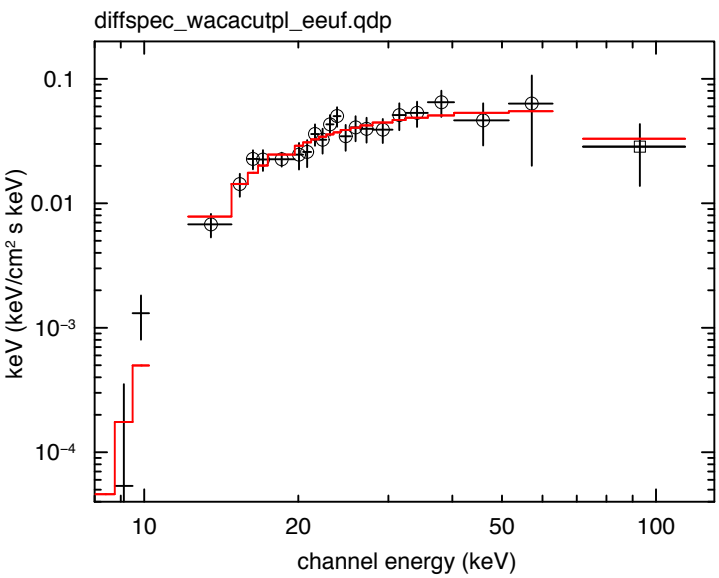

Figure 5.35: Differential $\nu F\nu$ spectrum between the two phases (black points), i.e., high minus low, on which an absorbed power-law model with $\Gamma = 1.6$ is superposed (red line).

5.5 NGC 4258

5.5.1 XIS data analysis

XIS0 images of the NGC 4258 nucleus and inner disk area are shown in Figure 5.36, in the two energy ranges of 0.3–2 keV and 2–10 keV. The soft-band image is dominated by complex unresolved emission with an extent of at least $\sim 4'$, while a bright nuclear point source dominates the hard-band image. In addition, several fainter point-like sources are distributed over the NGC 4258 disk. Thus, compared to the other AGNs in our sample, the nucleus of NGC 4258 has a much lower contrast against other sources in the host galaxy, because of its intrinsically low luminosity. With the higher resolution X-ray telescopes, Pietsch and Read (2002; *XMMNewton*) and Yang et al. (2007; *Chandra*) confirmed that the soft contributions is clearly separated from the harder nuclear emission, and do not contributed to the spectrum above ~ 3 keV.

Although the soft emission extending out from the nucleus (particularly "anomalous arms") is of much interest because of its possible association with the AGN jets (e.g., Wilson et al. 2001), it is beyond the scope of the present thesis. Since the nuclear emission cannot be spatially separated from the extended solar emission in these *Suzaku* images, we thus restrict the following spectral modeling to energies above 3 keV. The source extraction region is indicated by black solid circles in the images, whose radius is $4'.0$ (corresponding to 8.4 kpc in physical size at a distance of 7.2 Mpc). Since there is a point-like source at $2'.2$ south of the nucleus, we excluded a circular region centered on the source, with a radius of $1'.0$ (indicated by a black dashed circle). The background spectra were extracted from source free regions of the same CCDs. A total net exposure of ~ 99 ks was obtained from each XIS sensor, with source count rates of 0.430 ± 0.002 cts s^{-1} from the three FI chips (3.0–9.0 keV), and 0.115 ± 0.001 cts s^{-1} from the BI chip (3.0–8.0 keV).

5.5.2 HXD data analysis and broad-band spectrum

Since 2006 May 24, a quarter of the whole HXD-PIN diodes (WPU0) have been operated with a bias voltage of 400 V, while the others are at 500 V. This is due to anomalous behavior of the noise seen in some of the diodes, when operated with the nominal bias voltage. As described in §3.7.2, the NXB data should be accumulated over several months, under a particular instrumental condition, to construct the data base used in the NXB modeling. Therefore, we used data from the three quarters of the whole HXD-PIN diodes, operated at the time of the NGC 4258 observation with the nominal bias voltage of 500 V.

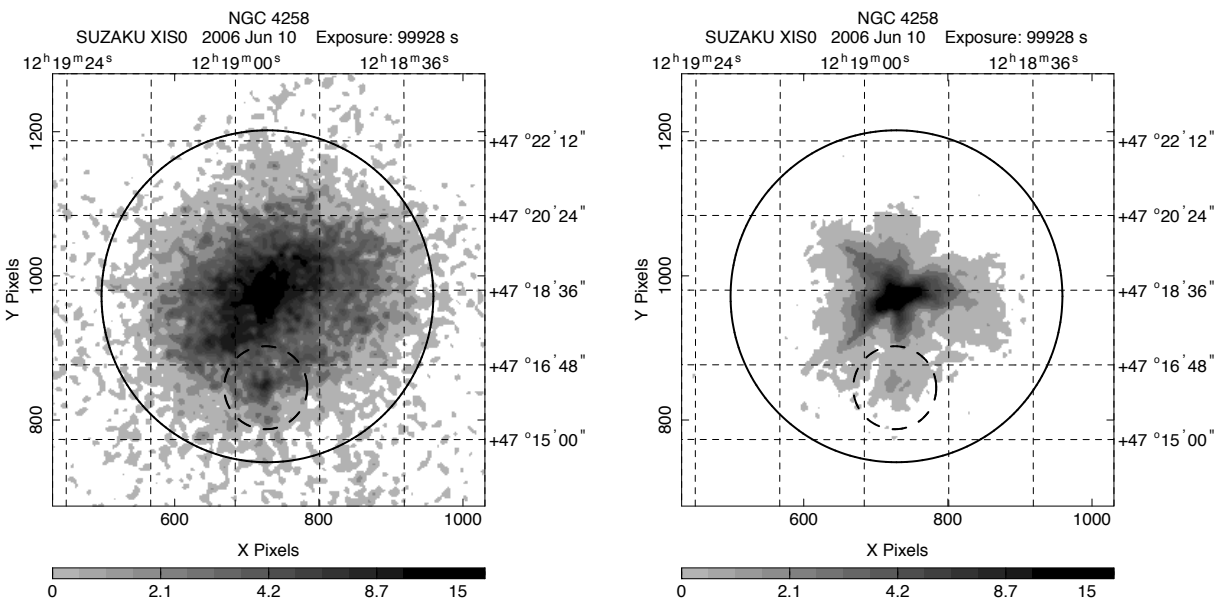

Figure 5.36: The same as Figure 5.1, but for NGC 4258, in the 0.3–2.0 keV (left) and 2-9.0 keV band (right). The source events are extracted within the black solid circle in the panels, excluding those within the black dashed one. The radius of the solid and dashed circles are $4'.0$ and $1'.0$, corresponding to 5.5 mm and 1.4 mm on the sensor, respectively.

We used a modeled NXB event file which is also based on the NXB database constructed from the same three quarters of the detector.

Figure 5.37 shows the HXD-PIN spectra of NGC 4258, in comparison with the HXD-PIN background which includes both the NXB and CXB. The lower panel indicates that the net source count rate is $\sim 10-20\%$ in the energy range of $12-40$ keV. In the following spectral analysis, we use this energy range, in which the source signals are detected at $> 9\sigma$ (statistical) above the background in each of appropriately summed energy bins in the spectrum. The source detection is fully significant even considering the systematic errors ($\pm \lesssim 3\%$; §5.1.2) associated with the NXB modeling. The background-subtracted source count rate in the energy range, with statistical error, is 4.2 ± 0.2 cts s^{-2}, which is $\sim 13\%$ of the background rate (NXB plus CXB, 0.335 ± 0.001 cts s^{-1}). In contrast, the source was not detected with HXD-GSO, with an upper limit which is consistent with an extrapolation from the HXD-PIN signals.

Figure 5.38 shows the source spectra in the 3–40 keV band, normalized to those of the Crab nebula. Similar to the other source in this thesis, the ratio plot reveals an extremely hard spectrum in the 2–5 keV band, which provides clear evidence for the presence of a considerable degree of absorbing column toward the nuclear engine. Above ~ 5 keV, the ratio keeps increasing up to ~ 40 keV with a rather constant but flatter

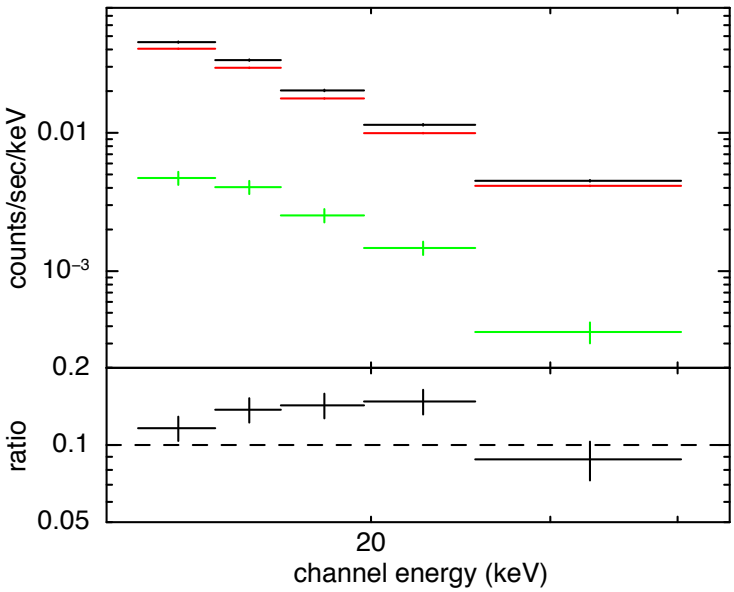

Figure 5.37: The same as Figure 5.2, but for NGC 4258. Only HXD-PIN data are shown.

slope, without showing any clear evidence for an underlying Compton hump which is present in NGC 4388. In the 5–8 keV range (the inset figure), we observe a weak iron line at $\sim$ 6.4 keV, while we do not see any other clear features attributable to the iron line/edge complex. Since the Compton hump and/or the strong line/edge complex are one of the characteristic spectral features of the reflected emission observed from the rest of our sources, their lack in this source suggests that the physical condition around the nucleus of NGC 4258 is somehow different from those of the others.

5.5.3 Spectral fitting

In order to reproduce the 3.0–40 keV spectrum, we began our spectral fitting with a simple absorbed power-law model. The model well reproduced the continuum over the whole energy range, with a photon index of $\Gamma \sim 1.70$ and an absorbing column of $N_{\rm H} \sim 8.3 \times 10^{22}$ cm^{-2}. Significant residuals, however, remained around 6.4 keV, making the fit statistically rather unacceptable ($\chi^2/\nu = 326.8/275$). By adding a narrow Gaussian emission line at $\sim$ 6.4 keV, the fit became acceptable with $\chi^2/\nu = 288.5/273 = 1.06$ ($\Delta\chi^2 = -38.4$). In order to estimate the line width, we allowed the Gaussian to be broad, but this did not improve the fit significantly. The upper limit on the line width is calculated as 65 eV, corresponding to a velocity of $\sim$ 3000 km s^{-1}, or $\sim$ 0.02 pc assuming a Keplerian rotation around the central black hole with $3.6 \times 10^7 M_\odot$.

Although the data have already been reproduced successfully with this simple model,

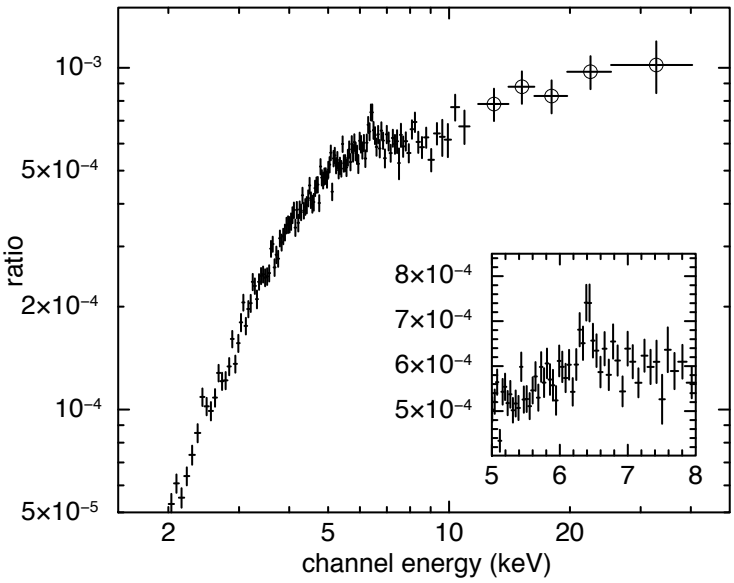

Figure 5.38: The same as Figure 5.3, but for NGC 4258.

we further added to it a reflected continuum component (`pexrav` in XSPEC), to examine whether there is such a signal like in the other sample sources. As indicated in §5.5.2, its inclusion did not improve the fit at all. We obtained a tight upper limit on the reflection fraction, $f_{\rm refl} < 0.1$. Therefore, we do not include the reflected continuum in the following analysis.

Figure 5.39 shows the *Suzaku* spectrum of NGC 4258 averaged over the entire observation exposure, on which the best fit model is superimposed. The data are shown in the raw detector count rate (left) and in an unfolded $\nu F\nu$ plot. We also show in Figure 5.40 confidence counters of the photon index of the intrinsic continuum and the absorbing column. The best-fit parameters are summarized in Table 5.6. The resulting absorbed and unabsorbed fluxes in the 2–10 keV band are 8.0 and 13.0×10^{-12} erg cm^{-2} s^{-1}, respectively, corresponding to luminosities of 5.0 and 8.1×10^{40} erg s^{-1} at 7.2 Mpc. Thus, the bolometric luminosity is estimated to be $\sim 6 \times 10^{41}$ erg s^{-1}. As described in §4.5.5, this is indeed 2 to 3 orders of magnitude lower than those of the other objects in our sample.

5.5.4 Time variability

We show in Figure 5.41 light curves of the NGC 4258 nucleus in five energy ranges, taken with the *Suzaku* XIS (upper 3 panels) and HXD-PIN (bottom panel). The light curves were extracted in the same way as in §5.1.7. The light curves below 2 keV do not show any significant variation, which agree with the idea that the thermal diffuse emission

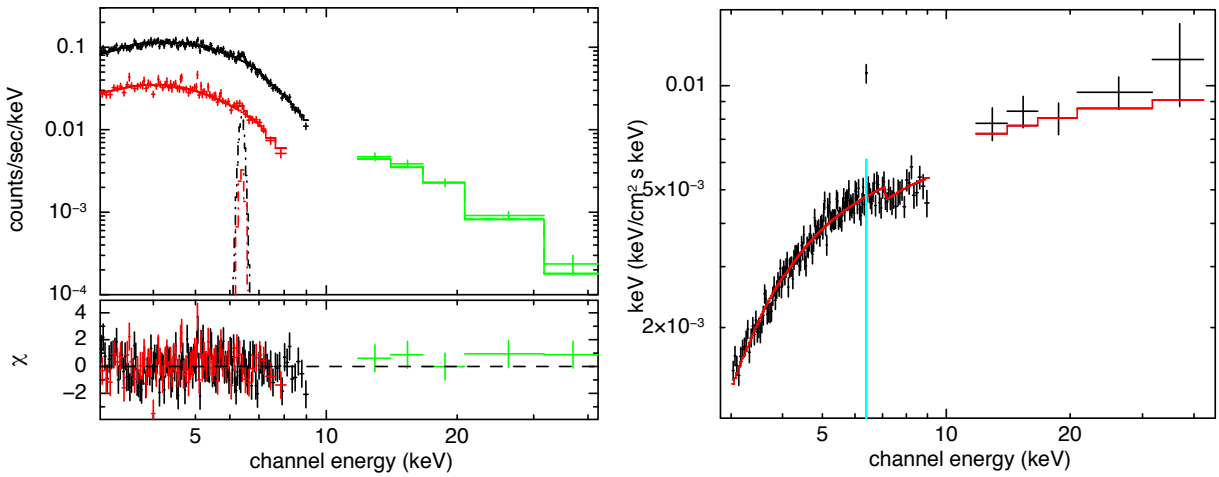

Figure 5.39: The broad-band (3–40 keV) spectra of NGC 4258, on which models are superposed. (Left) The spectrum is shown as the raw count rate of the detector. The crosses shows the data points while the lines are the models. The black, red and green colors correspond to XIS-FI, BI and PIN, respectively. The lower panel shows the residuals from this fit. (Right) The spectrum is shown as a $\nu F\nu$ plot. The data are shown in black points and the models in colored lines; the absorbed intrinsic power-law in red, and emission lines in cyan.

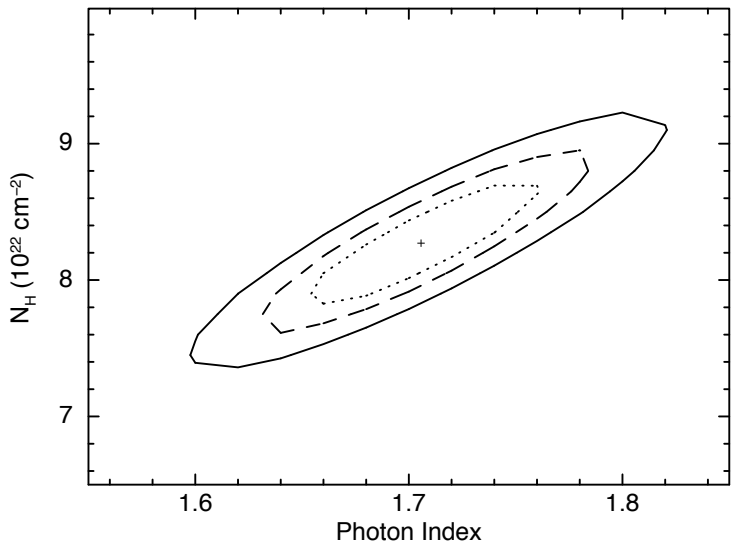

Figure 5.40: The same as Figure 5.6 (left), but for NGC 4258.

Table 5.6: Best-fit parameters of the *Suzaku* spectrum of NGC 4258 over 3.0–40 keV, derived under the model of absorbed power-law plus a narrow Gaussian line.

Model Component	Parameter	Average	High	Low
Intrinsic PL	Γ	$1.70^{+0.06}_{-0.06}$	$1.82^{+0.09}_{-0.12}$	$1.61^{+0.06}_{-0.06}$
	$N_{\rm PL}{}^{a}$	$3.3^{+0.4}_{-0.4}$	$5.0^{+0.7}_{-0.7}$	$2.4^{+0.5}_{-0.5}$
	$N_{\rm H}{}^{b}$	$8.3^{+0.5}_{-0.5}$	$9.6^{+0.8}_{-0.9}$	$7.2^{+0.5}_{-0.6}$
Fe I Kα	$E_{\rm c}{}^{c}$	$6.40^{+0.03}_{-0.03}$	$6.43^{+0.04}_{-0.04}$	$6.38^{+0.03}_{-0.03}$
	I^{d}	$5.5^{+1.5}_{-1.5}$	$6.4^{+1.8}_{-1.8}$	$5.8^{+1.6}_{-1.6}$
	EW	40^{+20}_{-20}	40^{+25}_{-23}	49^{+25}_{-30}
χ^2/d.o.f.		288.5/273	116.8/109	193.0/165

[a] 10^{-3} photons keV^{-1} cm^{-2} s^{-1} at 1 keV. [b] 10^{22} cm^{-2}.

[c] Center energy in keV. [d] 10^{-6} photons cm^{-2} s^{-1}.

dominates in the energy range. In the energy ranges above 2 keV, in contrast, the source flux varied by a factor of ~ 1.5 across the ~ 200 ks gross time coverage, accompanied by some variations in the hardness ratio.

In order to search the spectra for intensity-correlated changes, we divided the entire observation period into two phases according to the 2–10 keV count rate; "high flux" and "low flux" phases, corresponding to periods when the count rate is higher and lower than 0.75 cts s^{-1}, respectively. The two dotted line in Figure 5.41 separates the two phases; high phase between the lines and low phase outside. The net exposure is 34.8 ks (XIS) and 28.1 ks (HXD) for the high flux phase, and 65.1 ks (XIS) and 55.5 ks (HXD) for the low phase. Figure 5.42 shows the spectrum of the high phase, divided by that of the low phase. Above 5 keV, the flux of the high phase is approximately 1.3 times as high as that of the low phase. Interestingly, the ratio becomes lower than unity in the 1–2 keV range, suggesting some variations in the spectral shape between the two phases.

We fitted the spectra from the two phases by the same model as employed in §5.5.3. The fits were acceptable in both cases, and inclusion of reflected continuum made the fit worth as in the time averaged spectrum. The resultant fits and the best-fit parameters are summarized in Figure 5.44 and Table 5.6. We also show in Figure 5.43 confidence contours of the photon index of the primary power-law, Γ ,against the absorbing column, $N_{\rm H}$, separated for the two spectra. Thus, both $N_{\rm H}$ and Γ, or at least $N_{\rm H}$, changed along

with the flux variation, on a time scale of several tens ksec. Previously, a $\sim 30\%$ change in $N_{\rm H}$ across a few years has been known in this source from several *ASCA* observations (Reynolds et al. 2000). A more rapid (in about six weeks) decrease of $N_{\rm H}$ by $\sim 10\%$, accompanying a $\sim 10\%$ flux decrease, has also been reported based on *XMM-Newton* observations (Fruscione et al. 2005). The present observations, therefore, provides the fastest variation in $N_{\rm H}$ so far observed from this source.

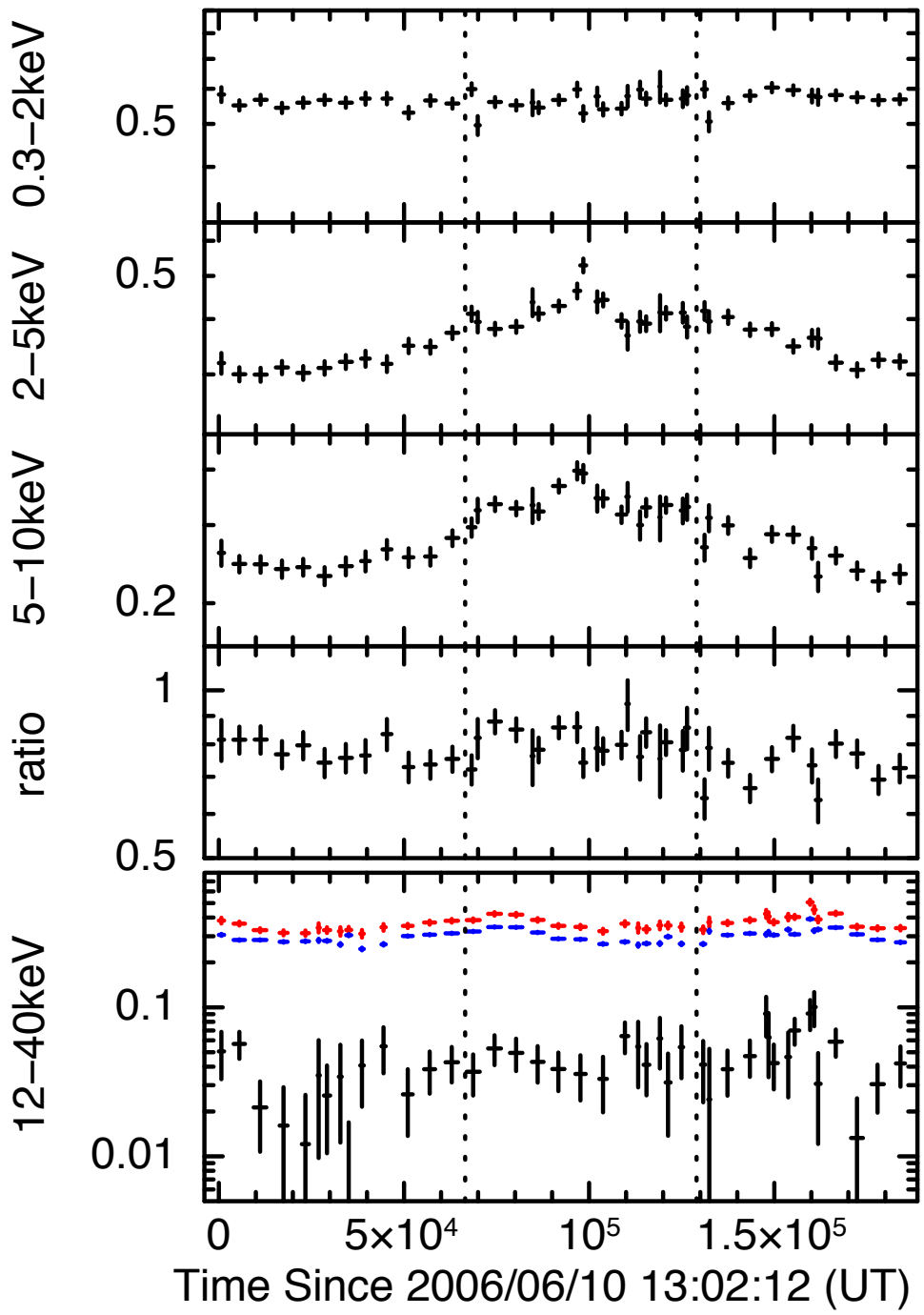

Figure 5.41: Background-subtracted light curves of NGC 4258 taken with *Suzaku* . The upper three panels show those in 0.3–2 keV, 2.0–5.0 keV and 5.0–10.0 keV, respectively, taken with the four XIS sensors. the fourth panel shows the hardness ratio between 5.0–10.0 keV and 2.0–5.0 keV. Each bin corresponds to a continuous time interval without data gaps. The bottom panel shows the HXD-PIN light curves in the 12–40 keV band: the red points indicates background-inclusive raw count rates, blue the modeled background (NXB + CXB), and black the net source count rates. Each bin corresponds to a continuous time interval without data gaps, which can be different from those in the upper panels.

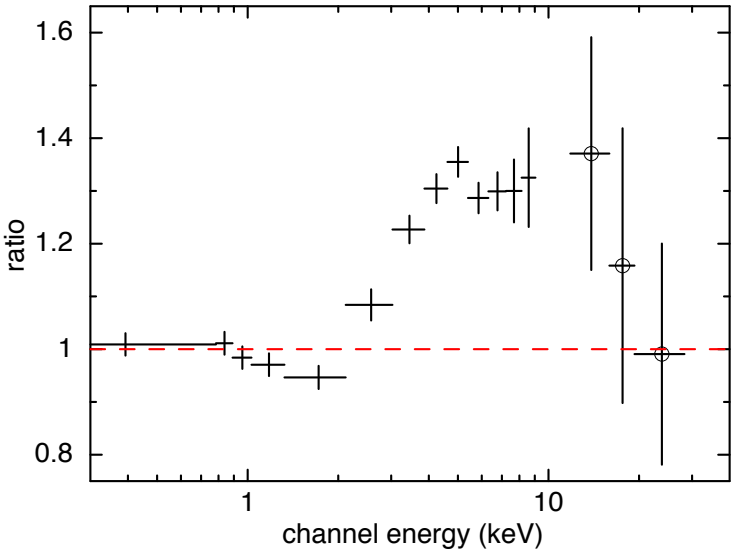

Figure 5.42: Spectra from the "high phase", normalized to that of the "low phase". The XIS and the HXD-PIN data points are shown in crosses and circles, respectively.

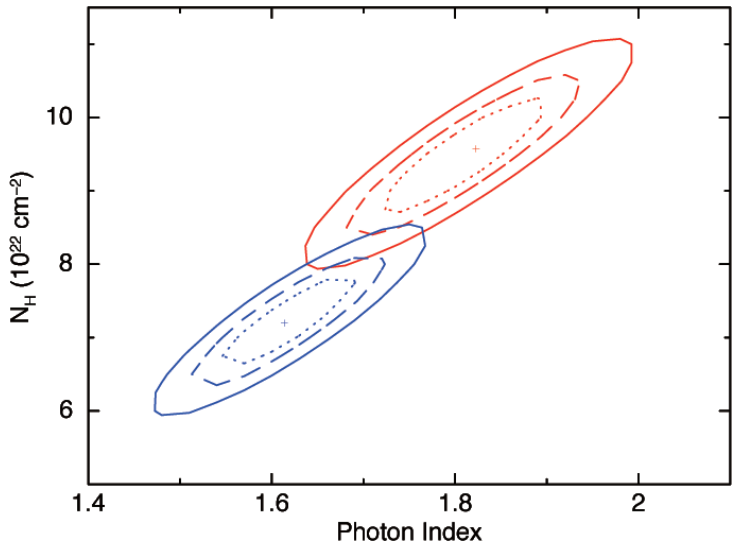

Figure 5.43: The same as Figure 5.40, but for the spectra of the high (red) and low (blue) phase.

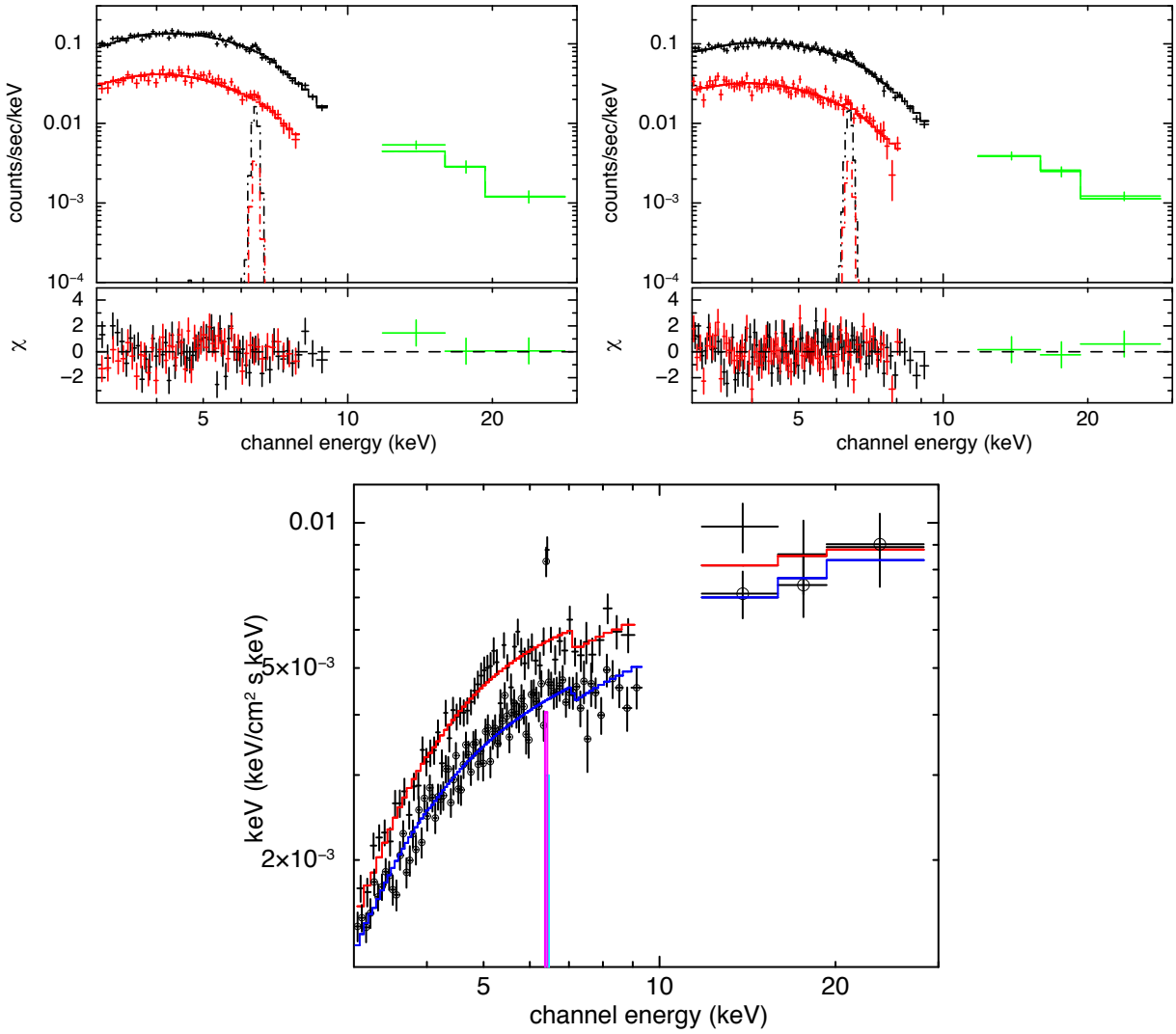

Figure 5.44: The same as Figure 5.39, but for the spectra of the high and low phase. The spectrum is shown as the detector raw count rate in the upper panels: left panel for the high phase and right for the low. The unfolded $\nu F\nu$ plot for both spectra are superimposed. Black crosses, red line and cyan line indicates the data points, intrinsic power-law and emission line of the high phase, respectively. Black circle, blue line, and magenta line those of the low phase.

Chapter 6

DISCUSSION

6.1 Summary of Results

Making use of the *Suzaku* observations in its PV and AO-1 phases, we have investigated X-ray spectra and time variability of a sample of five type 2 Seyfert AGNs, focusing mainly on the $\sim$ 2–150 keV range. Since all these objects are known as water maser emitters, our view direction is restricted to be nearly edge-on to their accretion disks. The superior spectral and timing capability of *Suzaku* , throughout its wide energy range, allowed us to demonstrate that all these edge-on AGNs are indeed highly obscured, and to obtain major spectral and timing results as summarized in Table 6.1. These results, to the first order, agree well with the Unified Scheme (Chapter 1, §2.1.3) of type 1/type 2 AGNs, reinforcing the picture more firmly than ever. We have also obtained a new inference on the "putative torus", of which little has been learned from previous observations. In this section, we briefly summarize these results which we have derived.

6.1.1 Spectral components observed in our sample objects

In Chapter 5, we have successfully and consistently decomposed the X-ray emission from our sample AGNs into (at least) three distinct components. This decomposition is illustrated schematically in Figure 6.1.

The first component is the highly absorbed power-law, which is detectable only in energies above 3–10 keV, extending up to $\gtrsim$ 100 keV. In at least four sources in our sample, this component has been securely identified with the primary AGN emission, seen through thick obscuring materials which have column densities in the range of $N_{\rm H} \sim 10^{23}$ cm^{-2} to a few $\times 10^{24}$ cm^{-2}. We also successfully estimated the intrinsic spectral slope, as well as the

unobscured X-ray flux (Table 6.1), although the latter becomes considerably uncertain as the source become Compton-thick. Figure 6.2 show a scatter plot between the absorbing column and the estimated bolometric luminosity $L_{\rm bol}$. Our sample, though far from being complete, is thus found to cover rather wide ranges in luminosity and absorbing column.

The second component, found in all our sample AGNs except for NGC 4258, is the nuclear emission reflected by some optically-thick materials, reaching us without being further obscured by the absorber that obscures the primary emission. This component in fact consists of three parts; (1) the flat continuum observed in energies below 10 keV, exhibiting a deep Fe-K edge; (2) the "hump" at 20–30 keV visible in the PIN spectra; and (3) several narrow (< several tens eV) emission lines from major elements, including many first detections from these AGNs. We can regard (1) and (2) as originating from the same material, because they can be successfully modeled together as a single reflection component. Furthermore, (3) can also be considered to come from the same material, as judged from the line equivalent widths relative to (1), and from the relative strengths of the Compton down-scattered shoulder associated with the Fe I Kα emission lines (observed from four sources). The reflector is inferred to be neutral or in low ionization states, based on the measured center energies of (3), as well as the observed Kβ / Kα intensity ratio of ~ 0.12. A very important finding is that the strength $f_{\rm refl}$ of this reflected component, relative to the intrinsic AGN emission, is rather high in two objects (NGC 4388 and Mrk 3; Table 6.1), whereas very low in NGC 4945 and NGC 4258. A further consideration continues in section 6.2.

The third component is the highly ionized iron emission/absorption lines, observed from four objects in our sample. This signals the presence of ionized materials somewhere around the nucleus. Such materials are likely to be photoionized under irradiation by the bright nuclear light, although an alternative idea of collisionally ionized plasma cannot be ruled out from this study. Assuming the photoionization scenario to be the case, we expect also to observe another continuum with a similar shape as the primary one, i.e., primary light scattered by the ionized material. At least in one source (Mrk 3), we have found evidence for such scattered continuum.

Besides the identification of these spectral components, another spectral result from *Suzaku* is the constraint on iron abundance of the circum-nuclear materials. Assuming that the absorber and the reflector is different parts of the same matter distribution (possibly the "torus"), we have successfully estimated the iron abundance in some of the sources to be consistent with one solar, or slightly lower than that. Such an abundance estimation has become possible thanks to the high sensitivity of the XIS in the iron edge

region, and to the superior hard X-ray sensitivity of the HXD that allow us to fix the reflection hump.

We show in Figure 6.3 the energy spectra of the five sources in the Crab ratio format. Even from these simple plots, we can nicely review the spectral signature summarized in this section, for the targets with various absorbing columns. In the top object which has the least absorbing columns, the absorbed intrinsic emission emerges at ~ 3 keV, while signatures for the cold reflection are buried under the emission. In the objects plotted lower in the figure, the intrinsic emission are obscured up to higher energies, as the absorbing columns goes higher. Instead, we can see the signatures for the cold reflection more and more clearly at < 10 keV. In the last two objects, the spectra below ~ 10 keV is totally separated from the intrinsic emission which emerges only above ~ 10 keV. This means that these sources are "Compton-thick", where Compton scattering plays a quite important role to make the observed spectral components. This effect is further discussed in §6.2.

6.1.2 Time variability of the emission components

Along with the spectral properties, the time variability can provide a crucial key to our understanding of the environment around the AGNs. During the observations, we observed flux variations from at least 3 AGNs in our sample; NGC 4388, NGC 4945 and NGC 4258. These flux changes are most likely associated only with the absorbed intrinsic component, since neither the reflection continuum nor the emission lines varied in intensity beyond a typical upper limit of $\sim 10\%$. We can hence conclude that the reflecting material is located sufficiently far from the AGN, so that the intrinsic AGN variations are smeared out by the reflected signals due to distributed time delays.

As reported in §5.1.7, the RMS variability of NGC 4388 decreased toward higher energies above 10 keV. This means that the spectral "hump" at 20–30 keV is less variable than the primary emission. This nicely confirms our spectral results, that (1), (2) and (3) of the second spectral component have the same origin.

The detected hard X-ray variations, when combined with the values of $f_{\rm refl}$, provide an important implication that forms the major achievement of the present thesis. This is discussed in §6.2.

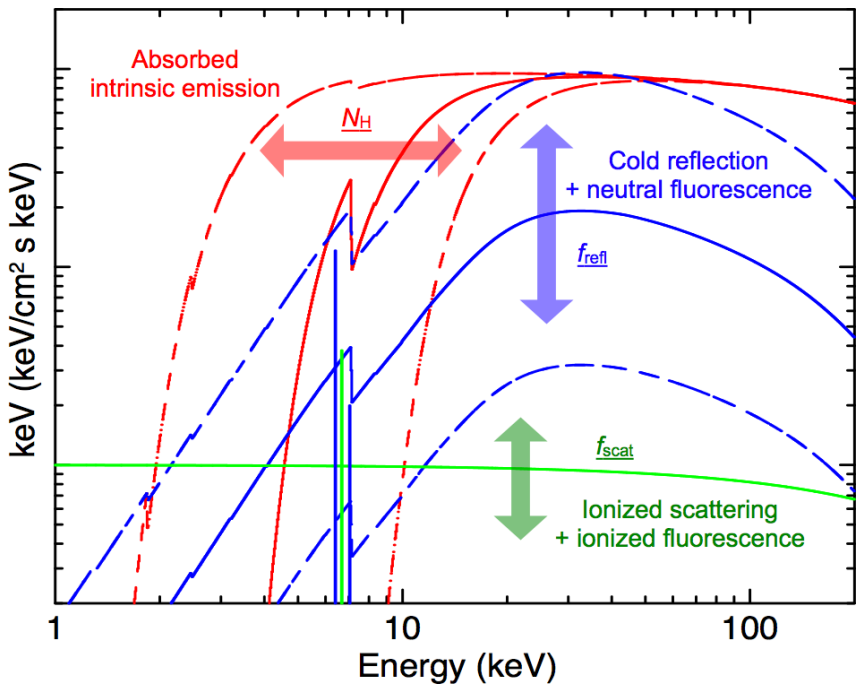

Figure 6.1: A Schematic illustration of the spectral components generally observed in our sample.

6.1.3 The Unified Scheme of AGNs

The Unified Scheme of AGNs (§2.1.3, e.g., Antonucci and Miller 1985; Antonucci 1993) dictates that type 1 and type 2 AGNs are the same objects seen from different directions. The present results provide several pieces of supporting evidence to this view, as described below. The measured photon index of the primary power-law emission, distributing over 1.6–2.0, is consistent with those of type 1 AGNs. In a few sources, we have also constrained (though marginal) the high energy spectral cutoff, at around $E_{\rm cut} \gtrsim 100$ keV which is also consistent with those measured in some of the brightest type 1 AGNs. The luminosity relative to the Eddington ratio (Table 6.1), a few to several tens percent, is not particularly different from those of type 1 AGNs. The large difference in the absorbing column can be explained simply as an inclination effect.

Table 6.1: The observed properties of individual AGNs.

Target name	$M_{\rm BH}$ ($10^6\ M_\odot$)	$L^a_{\rm bol}$ (10^{43} erg s^{-1})	$L_{\rm bol}/L_{\rm Edd}$	Γ %	$N_{\rm H}$ (10^{23} cm^{-2})	$f_{\rm refl}$ -	$F_{\rm var}{}^b$ -
NGC 4388	~ 10	3.0 ± 0.3	~ 2	1.7 ± 0.1	3.7 ± 0.2	1.8 ± 0.3	0.13 ± 0.02
Mrk 3	~ 45	30 ± 3	~ 0.5	1.85 ± 0.1	12 ± 1	1.3 ± 0.3	$0.01^{+0.03}_{-0.01}$
Circinus	1.7 ± 0.3	$4 - 10^c$	$\sim 20 - 50$	$2.0^{+0.1}_{-0.2}$	73 ± 10	$0.30^{+0.15}_{-0.10}$	$0.04^{+0.02}_{-0.04}$
NGC 4945	1.4 ± 0.3	4.5 ± 1.5	~ 25	1.6 ± 0.1	47 ± 5	$0.14^{+0.05}_{-0.04}$	0.32 ± 0.03
NGC 4258	39 ± 3	0.06 ± 0.006	~ 0.01	1.7 ± 0.1	0.7 ± 0.05	< 0.1	0.15 ± 0.02

[a] Bolometric luminosity inferred from X-ray observation except for Circinus.

[b] Fractional RMS variability calculated in the 12–50 keV band. [c] From integrated infrared luminosity.

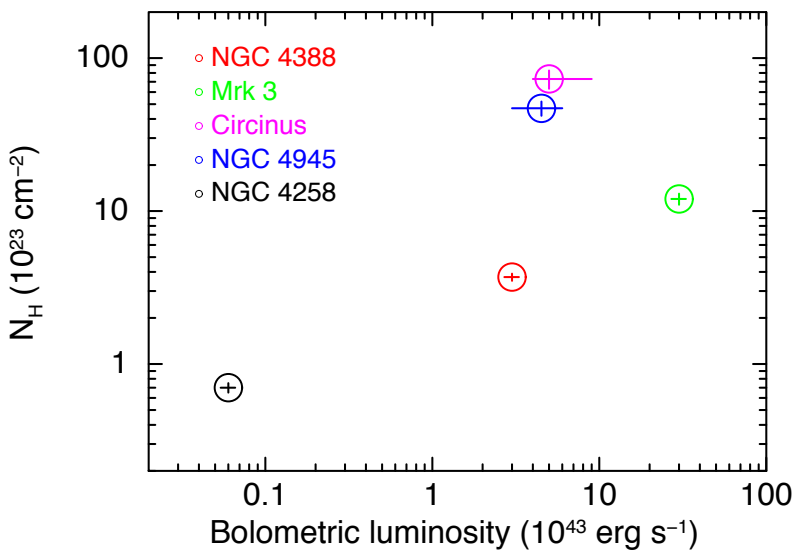

Figure 6.2: A Scatter plot between the bolometric luminosity and absorbing column of our sample AGNs.

6.2 Reflector with Various Covering Factors

6.2.1 Reflection fraction vs time variability

It is known that the time variability of intrinsic emission (defined as fractional RMS variablity $F_{\rm var}$) correlates with the black hole mass (e.g., Papadakis 2004). We show in Figure 6.4 a scatter plot between the black hole mass and the RMS variability $F_{\rm var}^{\rm obs}$ actually observed from our sample AGNs. Thus, the figure roughly reproduces generally accepted view, that $F_{\rm var}$ on a given time scale is inversely proportional to the black hole mass. In addition, we find interesting deviations from this trend, particularly between NGC 4945 and Circinus: they differ in $F_{\rm var}$ almost by an order of magnitude, even though their black hole mass and $L_{\rm bol}/L_{\rm Edd}$ are similar.

As described in the previous section (and in §5.1.7; §5.3.5), the time variability would be suppressed when the reprocessed emission have significant contribution to the total observed flux. To examine this possibility, we show in Figure 6.5 (top) a scatter plot between the reflection fraction, $f_{\rm refl}$, and $F_{\rm var}^{\rm obs}$. In this plot, we have normalized the values of $F_{\rm var}^{\rm obs}$ to those estimated from the black hole mass, $F_{\rm var}^{\rm est}$, referring to a relation by (O'Neill et al. 2005).

Note that the values of $f_{\rm refl}$ used here have not been corrected for the Compton scattering effects. That is, the values of $f_{\rm refl}$ are simply the ratios between the cold reflection and the intrinsic emission, with the latter corrected only for the photo-electric absorption;

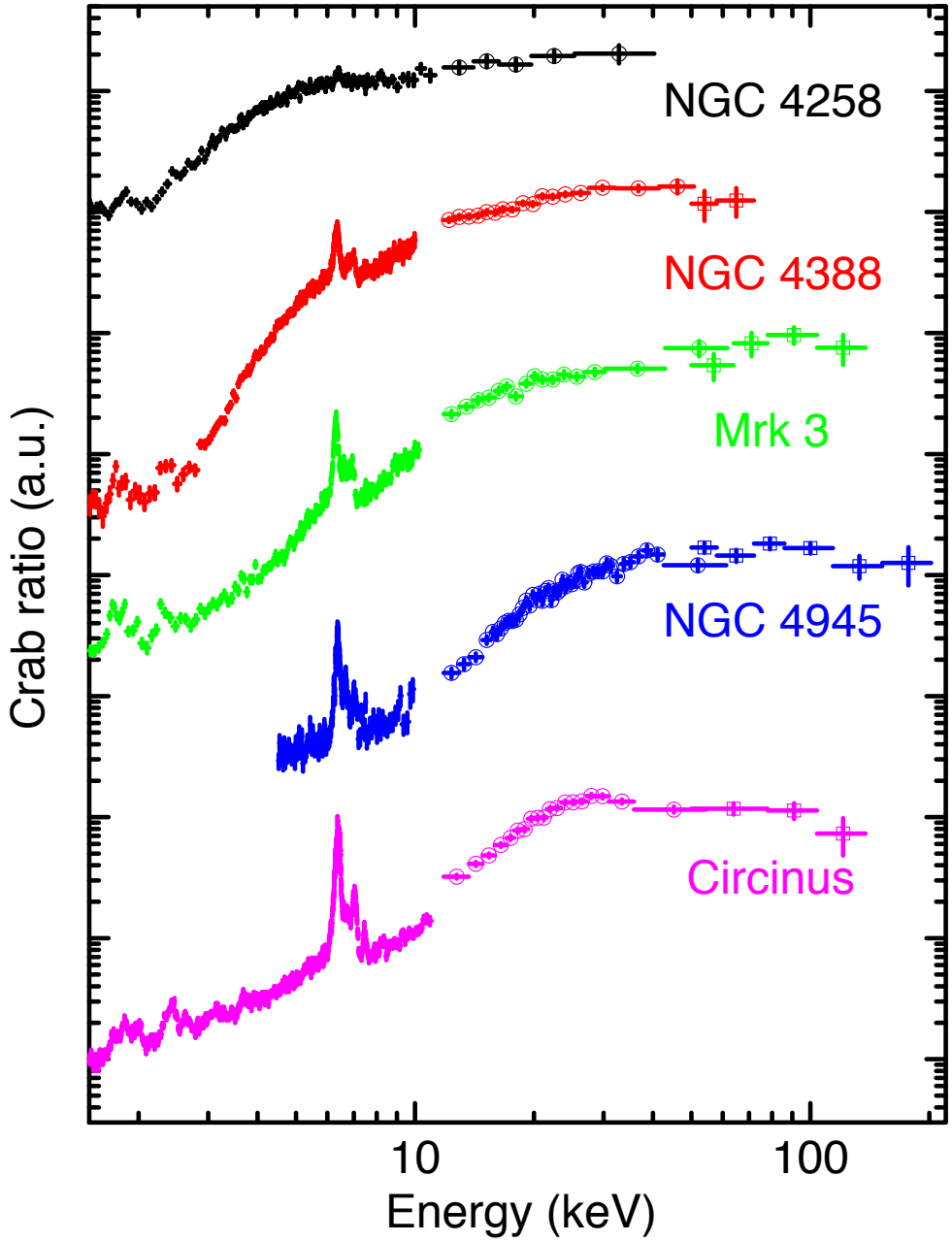

Figure 6.3: Crab ratios of the 5 sources analyzed in this thesis, shown with arbitrary units. Their absorbing columns range between $N_{\rm H} \sim 8 \times 10^{22}$ cm^{-2} and $\sim 7 \times 10^{24}$ cm^{-2}. The absorbing column increases from top to bottom sources.

we consider the effects of the Compton scattering in a comprehensive manner in the next section. The effects of such corrections, however, are negligible in the following discussion, except for the two Compton-thick sources.

Figure 6.5 (top) reveals that NGC 4388 and Mrk 3 have particularly large values of $f_{\rm refl}$, which reach almost unity. This suggests that about 2π of the sky is covered by the reflector as seen from the central engine. (Their values of $f_{\rm refl}$ are reliable, because both are Compton-thin, and hence their direct nuclear emission emerging at $\lesssim 10$ keV accurately fixes $f_{\rm refl}$.) Such a reflector can be readily identified with the putitive "torus", introduced in the unification model of AGN. A large covering factor of the torus agree with the number ratio of type 1 and type 2 AGNs. Since the observed hard X-ray signals are then contributed roughly equally by the varying direct emission and the non-varying reflected component, we expect $F_{\rm var}^{\rm obs} \sim F_{\rm var}^{\rm est}/2$, in a gross agreement with the NGC 4388 data point in Figure 6.5 (top). Note that the black hole mass in Mrk 3 is so high ($M_{\rm BH} \sim 5 \times 10^8 M_\odot$) that the detection of the time variation through the ~ 200 ks observation is not expected. Indeed, we did not observed any time variation from the source.

In Figure 6.5 (top) the contrast between Circinus and NGC 4945 becomes even more interesting; Circinus has only a factor of ~ 2 larger value of $f_{\rm refl}$ than NGC 4945, but its normalized variability is almost an order of magnitude smaller than that of NGC 4945. To further investigate their contrast, we need to fully consider the effect of Compton scattering (see next subsection), because the two objects are the most Compton-thick objects in our sample as shown in Figure 6.5 (bottom).

6.2.2 Compton scattered-out/in through the obscuring material

Although we already discussed in Chapter 5 the effects of Compton scattering by the obscuring materials, let us here consider the issue again, trying to solve the difference between the two Compton-thick sources (Circinus and NGC 4945) in their normalized variability (Figure 6.5). Through such an examination, we at the same time expect to obtain useful information on the geometry of the obscuring matter. As shown in Figure 6.5 (bottom), our line of sight toward their nuclei are obscured by absorbing columns exceeding $N_{\rm H} \sim 4 \times 10^{24}$ cm^{-2}. With such high columns, the absorber becomes optically-thick to Compton scattering (Compton-thick), and hence the flux of intrinsic emission reaching us would be significantly suppressed by a factor of $\exp(-N_{\rm H}\sigma_{\rm T})$, because the primary photons are Comton-scattered out of our line of sight. This is "Scattering-out" effect.

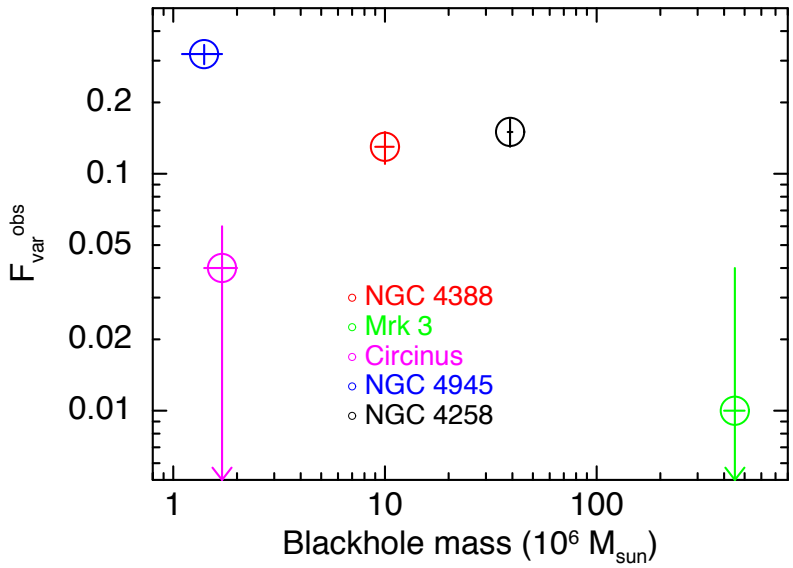

Figure 6.4: A scatter plot between the black hole mass and the observed RMS variability $F_{\rm var}^{\rm obs}$.

In Circinus, the value of $f_{\rm refl}$ is smaller than those in NGC 4388 and Mrk 3, and the flux of the cold reflection component is, actually, ~ 0.3 times that of the total flux at the 12–50 keV range. Thus, we expect that $F_{\rm var}^{\rm obs}/F_{\rm var}^{\rm est}$ would take a value around unity, as is the case in NGC 4388. However, as shown in Figure 6.5 (top), the observed time variability of this source is significantly lower than this prediction. In addition to this problem, we encounter another discrepancy: if we correct the inferred flux of the intrinsic emission for the scatter-out effect by multiplying with a factor of $\exp(N_{\rm H}\sigma_{\rm T}) \sim 130$ (given $N_{\rm H} = 7 \times 10^{24}$ cm^{-2}), the inferred bolometric luminosity would become ~ 8 times as high as the Eddington luminosity. This is physically quite unplausible.

In order to solve these two problems consistently, we need to re-examine the nature of the absorbed intrinsic component. If a Compton thick absorber subtends a large solid angle around the AGN, AGN photons which were first directed away from our line of sight would be partially scattered, inside the thick torus, into our view direction. A schematic illustration of this "scattered-in"component, together with the intrinsic and reflection ones, are shown in Figure 6.6. This component, suffering the photoelectric absorption, is considered to have a similar spectral shape as the absorbed intrinsic emission (e.g., Matt et al. 1999b; Yaqoob 1996), but its time variability would be suppressed like in the reflection component. The relative flux of the scattered-in component depend strongly on the geometry and column density of the obscuring materials (Madejski et al. 2000). We show in Figure 6.7 an example of a spectrum including the scattered-in photons, calculated

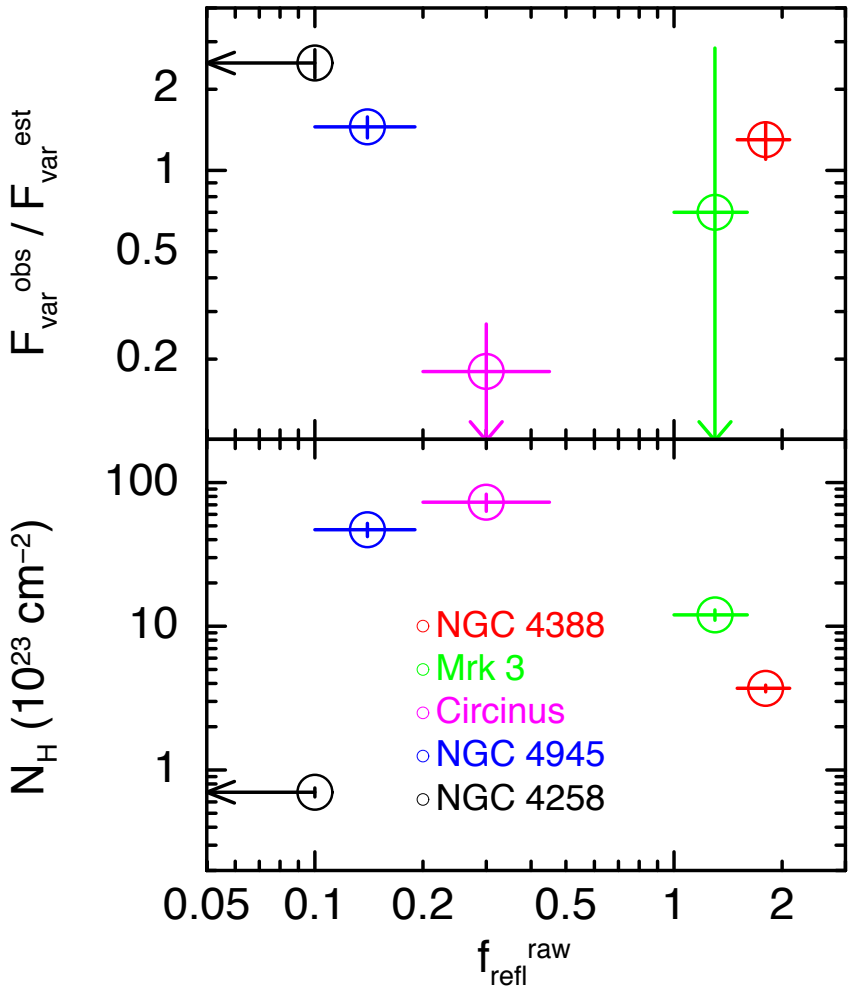

Figure 6.5: The reflection fraction $f_{\rm refl}$, plotted against $F_{\rm var}^{\rm obs}$ normalized to time variation $F_{\rm var}^{\rm est}$ predicted by the black hole mass.

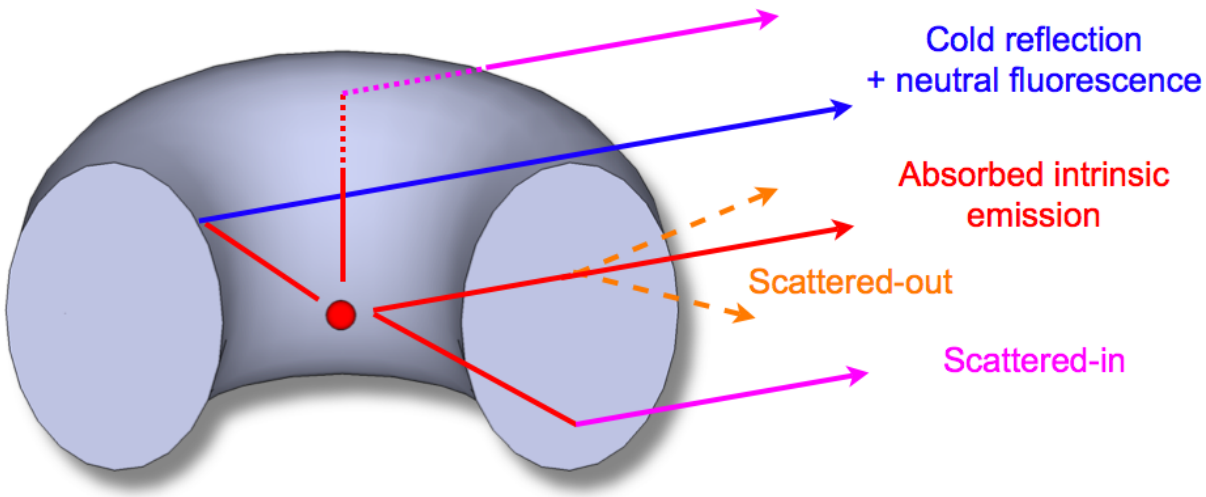

Figure 6.6: Schematic picture of the emission components from an AGN and putative "torus".

assuming that the obscuring matter distributes spherically with uniform density ($N_{\rm H} = 5 \times 10^{24}$ cm^{-2}, Yaqoob 1996). When the intrinsic component is highly attenuated by the scattering-out effect like in the Circinus case, the scattered-in component would dominate what has been considered the absorbed intrinsic emission. If so, the strong suppression of the variability in Circinus can be naturally explained. Furthermore, its intrinsic (corrected for the scatter-out effect) luminosity, calculated by excluding the scattered-in contribution, becomes much lower, and hence $f_{\rm refl}$ gets larger. These considerations conversely imply that the reflector in Circinus has as large as those in NGC 4388 and Mrk 3. In short, the proper consideration of the scattered-in component brings the Circinus galaxy in agreement with the unification of the AGNs.

NGC 4945 is also a Compton-thick source, with the absorbing column close to that in Circinus. The black hole masses are also quite close between the two sources. NGC 4945 exhibits, like the former 3 sources, a clear signature of the optically-thick cold reflector in energies below 10 keV. Nevertheless, in Figure 6.5 (top), NGC 4945 (and NGC 4258 to be considered later) falls on a region which is quite distinct from that occupied by Circinus. Indeed, NGC 4945 varied in energies above 10 keV by a factor of ~ 2 on a time scale as short as ~ 20 ks, and its reflection fraction is constrained to be as small as $f_{\rm refl} \sim 0.1$ even *before* correcting the intrinsic flux for the scattering-out effect. Therefore, unlike Circinus, the emission above 10 keV must be dominated by the direct nuclear component, with little contribution from the reflected or scattered photons. This fact itself is already sufficient to require that the optically-thick reflector in this AGN should have a very small covering

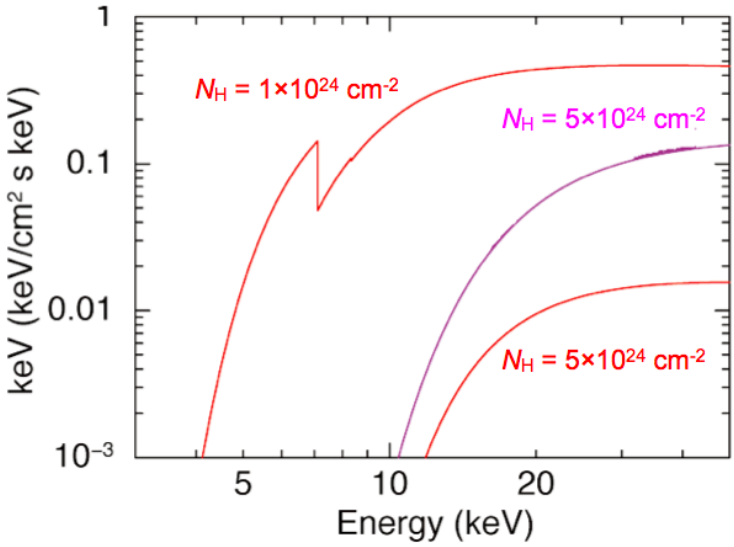

Figure 6.7: An example of spectral calculations showing the effects of scattered-in light (Yaqoob 1996). Red lines show the absorbed intrinsic emission when only the scattering-out effect is considered, for absorbing columns of $N_{\rm H} = 1 \times 10^{24}$ and 5×10^{24} cm^{-2}, respectively. Magenta shows a spectrum when the scattered-in component is added to the absorbed intrinsic emission, with the absorbing column of $N_{\rm H} = 5 \times 10^{24}$ cm^{-2} .

factor around the nucleus, because otherwise the scattered-in photons would smear out the time variability, as in the case of Circinus (Itoh et al. 2008). This conclusion is even enhanced very much, when we correct the intrinsic flux by a factor of $\sim \exp(N_{\rm H}\sigma_{\rm T}) \sim 20$. This correction yields $f_{\rm refl} \lesssim 0.01$.

NGC 4258 is the only source where we failed to find any spectral signature for the cold reflection component. The weakness of iron emission line, iron edge, and Compton-hump have provided, for the first time, a tight constraint on the reflection fraction as $f_{\rm refl} < 0.1$. This, together with the large values of $F_{\rm var}^{\rm obs}/\ F_{\rm var}^{\rm est}$, places NGC 4258 in a similar region on Figure 6.2 (bottom), as NGC 4945. In other words, the accreting cold matter in NGC 4258, of which the clear presence is indicated by the water-masser emission and the X-ray absorption, has such a geometry as to subtend a very small solid angle as seen from the nucleus. The case of NGC 4945 may be similar.

To summarize this important section, we have obtained a new inference on the cold reflectors generally seen in obscured AGNs (putative "torus"); some type 2 AGNs do not have the generally assumed cold reflecting tori with a large covering factor. In such sources, the reflected emission is much lower than those in more "normal" AGNs, as evidenced by the rather enhanced hard X-ray variability and the small values of $f_{\rm refl}$. In

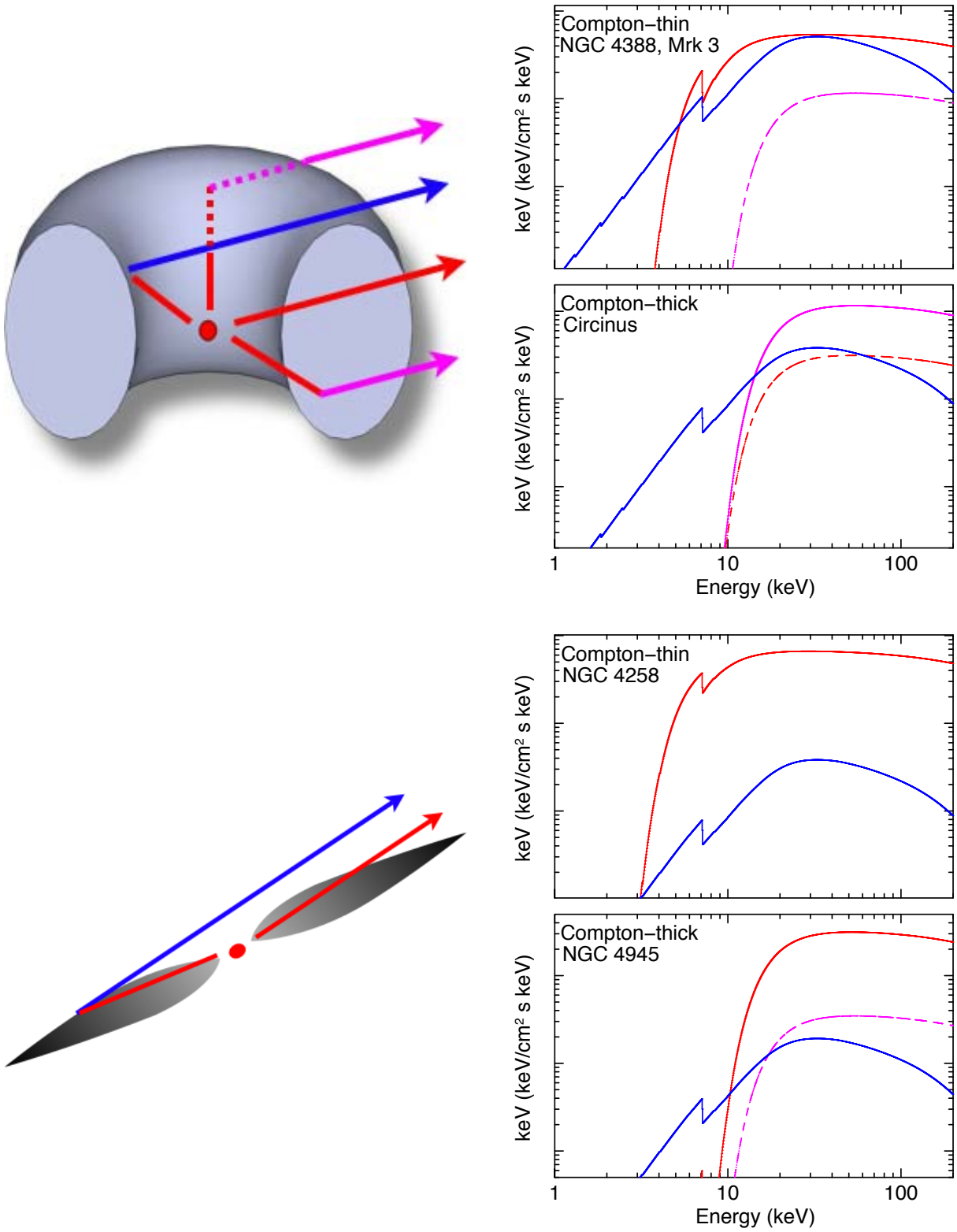

Figure 6.8: Schematic illustrations of the two types of cold-matter distribution inferred in this thesis (left side). (Top left) The normal torus with a large covering factor. (Bottom left) The geometrically-thin, disk-like material which is thought to be present in NGC 4945, and possibly in NGC 4258. (Right side) Schematic drawings of spectral components observed from the corresponding geometry, shown for compton-thin / thick sources. The red, blue and magenta lines show a direct, reflected, and scattered-in emssion as seen from the observer, respectively.

order to explain the "small (or no) reflection" property of these AGNs, we may consider a configuration as illustrated in Figure 6.8 (bottom), that the cold matter has a flat but slightly warped disk geometry, and we are observing the AGN just grazing to it (Itoh et al. 2008). Schematic figures of the two types of tori (normal and disk-like) are shown in Figure 6.8, together with the spectral components observed from each types, depending also on the line-of-sight absorbing columns.

Such AGNs with "small reflection" may, in principle, be present among type 1 AGNs. This inference would significantly affect the study that try to explain the flux and spectrum of the CXB as an assembly of numerous AGNs along the line of sight. The detection of such objects is, however, quite difficult since the direct nuclear emission hide the weak signature of the reflection component. Since accurate measurements of the hard X-ray continua are thought to provide a key to this issue, the improved hard X-ray instruments (the Hard X-ray Imager and the Soft Gamma-Ray Detector) to be onboard the *NeXT* mission will be of great value.

6.3 Prospects

In this section, we consider a possible origin of the difference in the covering fraction of the reflector. Since the obscuring/reflecting materials are infalling to the central black hole, their structure must reflect, at the first order, the amount of matter which accretes per unit time. Thus, we speculate that the accreting material structures the putative toroidal shape, when the nucleus is in a gas-rich environment and hence the mass accretion rate is high. On the other hands, the accreting matter is considered to take a rather geometrically thin disk shape, when the nucleus is relatively gas-starved. This will suppress the reflection fraction and the nuclear obscuration occurs only when our line of sight is grazing to the (possibly warped) thin disk. Figure 6.9 shows a scatter plot of beween $L_{\rm bol}$ and $f_{\rm refl}$. The figure suggest a weak correlation in such a way that a source with a larger $L_{\rm bol}$ (and hence a larger mass accretion rate) has a larger value of $f_{\rm refl}$ (hence a thicker torus). However, the sample is still too small to allow us to draw a definite conclusion at present. To clarify the origin of the geometrical difference of the accreting matter, discovered by the present thesis, we need to acquire broad-band X-ray spectra of a much larger number of obscured AGNs. This will be carried out with the next generation Japanese X-ray satellite *NeXT* (New Exploration X-ray Telescope), scheduled for launch in 2013.

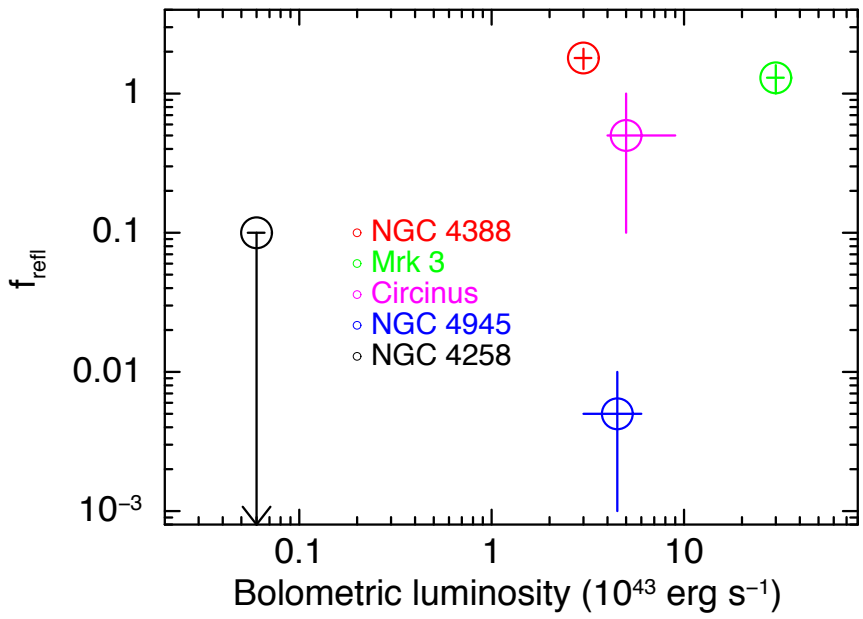

Figure 6.9: Scatter plots of $L_{\rm bol}$ vs $f_{\rm refl}$.

Chapter 7

CONCLUSION

We have selected five Seyfert 2 AGNs from the *Suzaku* PV and GO-1 phase targets; NGC 4388, Mrk 3, Circinus galaxy, NGC 4945, and NGC 4258. All these objects are known to be water maser sources, which restrict our line of sight to nearly edge-on to their accretion disks. Through the analysis of their X-ray spectra and variability, we obtained the following results.

1. The broad-band (a few to $\sim$ 100 keV) X-ray emission observed from our sources has been successfully disentangled into three components; (D) the highly absorbed power-law emission; (R) the nuclear light reflected by an optically thick, cold material; and (S) the nuclear emission scattered by ionized matter. We successfully explained their origin based mainly on the Unified Scheme of AGNs.

2. The component D has been clearly observed from all of our samples, thanks to the broad-band sensitivity of *Suzaku*. This components are highly obscured with the absorbing column densities ranging between $N_{\rm H} = 10^{22.8}$ and $10^{24.8}$ cm^{-2}, and the absorbers were confirmed to be Compton-thick in two out of the five sources; Circinus and NGC 4945. The component can be identified with the nuclear intrinsic emission piercing through obscuring matter, in all the sources except for Circinus. The estimated bolometric luminosity distributes in a fairly wide range, $L_{\rm bol} = 10^{41-44.5}$ erg s^{-1}. Nonetheless, their intrinsic spectral slope are found to be similar to one another, and to those of Seyfert 1 galaxies.

3. Component R has been observed from four sources in three characteristic signatures; (R1) a hard continuum observed in the energy range below $\sim$ 10 keV, accompanied by a sharp Fe-K edge; (R2) several narrow emission lines arising in neutral matter; and (R3) a spectral "hump" at energies around 20 keV. From both the spectral and

time variability aspects, we have shown that these three features can be consistently explained by assuming that they all originate in the same location, namely, a directly visible part of the circum-nuclear matter.

4. In NGC 4388 and Mrk 3, the strength of component R, relative to the nuclear intrinsic emission (component D), $f_{\rm refl}$, have values as large as unity. This suggests that about 2π of the sky is covered by the reflector as seen from the central engine. Such a reflector can be readily identified with the putative "torus", introduced in the unification model of AGN, in which the torus is considered to have a large covering factor based on number ratio of type 1 and type 2 AGNs.

5. From both the hard X-ray time variability and energetics aspects, we have found that the component D measured in Circinus should be identified with the nuclear light scattered by the obscuring material into the line of sight, rather than the nuclear intrinsic emission. Such scattered-in emission is likely to dominate the hard X-ray spectrum, when the obscuring material covers a large solid angle as seen from the central source *and* our view to the nucleus is blocked by the Compton-thick absorber. This in turn suggests the presence of putative "torus" with a large covering factor in Circinus, as in NGC 4388 and Mrk 3.

6. We have found that NGC 4945, another Compton-thick source, exhibits significant time variations in hard X-rays, showing that the contribution of the scattered-in photons is much lower than in Circinus in the energy range. This requires that the obscuring material do not have large covering factor to the central source, as otherwise the variability would be strongly suppressed. Furthermore, the value of $f_{\rm refl}$ have found to be smaller by about 2 orders of magnitude, than those in NGC 4388, Mrk 3, and Circinus. Combining these facts, the obscuring material in NGC 4945 is likely to be localized to a limited solid angle (including our line of sight) around the nucleus. In other words, an inflated thick torus, as invoked in the simplest form of the Unified Scheme, is unlikely to be present in this objects.

7. NGC 4258 is the only source where we have failed to find any significant signature of component R. Instead, we have obtained an upper limit on $f_{\rm refl}$, which is smaller than those in the three "thick torus" objects, by more than an order of magnitude. Thus, the geometrically-thick torus is also unlikely in this source. The obscuring material possibly locates in a similar form as in NGC 4945.

8. We consider that the accreting material assumes the putative toroidal shape, when the nucleus is in a gas-rich environment and hence the mass accretion rate is high. Then, the torus becomes at the same time the absorber for component D, and the reflector for component R. In contrast, the accreting matter is speculated to take a rather geometrically thin disk shape, when the nucleus is relatively gas-starved. This will suppress component R, and the nuclear obscuration occurs only when our line of sight is grazing to the (possibly warped) thin disk.

9. The existence of highly absorbed AGNs with insignificant reflection is expected to have an important implication for the AGN synthesis model of the Cosmic X-ray Background.

References

Abramowicz, M. A., Chen, X., Kato, S., Lasota, J.-P., and Regev, O.: 1995, *ApJL* **438**, L37

Abramowicz, M. A., Czerny, B., Lasota, J. P., and Szuszkiewicz, E.: 1988, *ApJ* **332**, 646

Antonelli, L. A., Matt, G., and Piro, L.: 1997, *A&A* **317**, 686

Antonucci, R.: 1993, *ARA&A* **31**, 473

Antonucci, R. R. J. and Miller, J. S.: 1985, *ApJ* **297**, 621

Avni, Y. and Tananbaum, H.: 1982, *ApJL* **262**, L17

Avni, Y. and Tananbaum, H.: 1986, *ApJ* **305**, 83

Awaki, H., Anabuki, N., Fukazawa, Y., Gallo, L., Ikeda, S., Isobe, N., Itoh, T., Kunieda, H., Makishima, K., Markowitz, A. G., Miniutti, G., Mizuno, T., Okajima, T., Ptak, A., Reeves, J. N., Takahashi, T., Terashima, Y., and Yaqoob, T.: 2008, *PASJ, accepted.*

Awaki, H. and Koyama, K.: 1993, *Advances in Space Research* **13**, 221

Awaki, H., Koyama, K., Inoue, H., and Halpern, J. P.: 1991, *PASJ* **43**, 195

Awaki, H., Koyama, K., Kunieda, H., and Tawara, Y.: 1990, *Nature* **346**, 544

Bassani, L., Dadina, M., Maiolino, R., Salvati, M., Risaliti, G., della Ceca, R., Matt, G., and Zamorani, G.: 1999, *ApJS* **121**, 473

Bauer, F. E., Brandt, W. N., Sambruna, R. M., Chartas, G., Garmire, G. P., Kaspi, S., and Netzer, H.: 2001, *AJ* **122**, 182

Bechtold, J., Dobrzycki, A., Wilden, B., Morita, M., Scott, J., Dobrzycka, D., Tran, K.-V., and Aldcroft, T. L.: 2002, *ApJS* **140**, 143

Beckmann, V., Gehrels, N., Favre, P., Walter, R., Courvoisier, T. J.-L., Petrucci, P.-O., and Malzac, J.: 2004, *ApJ* **614**, 641

Bianchi, S., Guainazzi, M., and Chiaberge, M.: 2006, *A&A* **448**, 499

Bianchi, S. and Matt, G.: 2002, *A&A* **387**, 76

Bianchi, S., Matt, G., Fiore, F., Fabian, A. C., Iwasawa, K., and Nicastro, F.: 2002, *A&A* **396**, 793

Bianchi, S., Matt, G., and Iwasawa, K.: 2001, *MNRAS* **322**, 669

Bianchi, S., Matt, G., Nicastro, F., Porquet, D., and Dubau, J.: 2005a, *MNRAS* **357**, 599

Bianchi, S., Miniutti, G., Fabian, A. C., and Iwasawa, K.: 2005b, *MNRAS* **360**, 380

Boella, G., Butler, R. C., Perola, G. C., Piro, L., Scarsi, L., and Bleeker, J. A. M.: 1997, *A&AS* **122**, 299

Boldt, E.: 1987, *Phys. Rep.* **146**, 215

Boroson, T. A.: 2002, *ApJ* **565**, 78

Braatz, J. A., Henkel, C., Greenhill, L. J., Moran, J. M., and Wilson, A. S.: 2004, *ApJL* **617**, L29

Braatz, J. A., Wilson, A. S., and Henkel, C.: 1996, *ApJS* **106**, 51

Braatz, J. A., Wilson, A. S., and Henkel, C.: 1997, *ApJS* **110**, 321

Brinkmann, W., Siebert, J., and Boller, T.: 1994, *A&A* **281**, 355

Brock, D., Joy, M., Lester, D. F., Harvey, P. M., and Ellis, H. B. J.: 1988, *ApJ* **329**, 208

Butler, R. C. and Scarsi, L.: 1990, in H. S. Hudson and O. H. Siegmund (eds.), *Proc. SPIE Vol. 1344, p. 465-478, EUV, X-Ray, and Gamma-Ray Instrumentation for Astronomy, Hugh S. Hudson; Oswald H. Siegmund; Eds.*, Vol. 1344 of *Presented at the Society of Photo-Optical Instrumentation Engineers (SPIE) Conference*, pp 465–478

Cappi, M., Bassani, L., Comastri, A., Guainazzi, M., Maccacaro, T., Malaguti, G., Matt, G., Palumbo, G. G. C., Blanco, P., Dadina, M., dal Fiume, D., di Cocco, G., Fabian, A. C., Frontera, F., Maiolino, R., Piro, L., Trifoglio, M., and Zhang, N.: 1999, *A&A* **344**, 857

Cecil, G., Wilson, A. S., and de Pree, C.: 1995, *ApJ* **440**, 181

Colbert, E. J. M. and Ptak, A. F.: 2002, *ApJS* **143**, 25

Comastri, A., Setti, G., Zamorani, G., and Hasinger, G.: 1995, *A&A* **296**, 1

Curran, S. J., Johansson, L. E. B., Rydbeck, G., and Booth, R. S.: 1998, *A&A* **338**, 863

Curran, S. J., Rydbeck, G., Johansson, L. E. B., and Booth, R. S.: 1999, *A&A* **344**, 767

Czerny, B. and Elvis, M.: 1987, *ApJ* **321**, 305

Done, C., Madejski, G. M., and Smith, D. A.: 1996, *ApJL* **463**, L63+

Done, C., Madejski, G. M., Życki, P. T., and Greenhill, L. J.: 2003, *ApJ* **588**, 763

Dos Santos, P. M. and Lepine, J. R. D.: 1979, *Nature* **278**, 34

Ebisawa, K., Makino, F., Mitsuda, K., Belloni, T., Cowley, A. P., Schmidtke, P. C., and Treves, A.: 1993, *ApJ* **403**, 684

Ebisawa, K., Życki, P., Kubota, A., Mizuno, T., and Watarai, K.-y.: 2003, *ApJ* **597**, 780

Edelson, R., Turner, T. J., Pounds, K., Vaughan, S., Markowitz, A., Marshall, H., Dobbie, P., and Warwick, R.: 2002, *ApJ* **568**, 610

Elmouttie, M., Haynes, R. F., Jones, K. L., Sadler, E. M., and Ehle, M.: 1998, *MNRAS* **297**, 1202

Elvis, M., Maccacaro, T., Wilson, A. S., Ward, M. J., Penston, M. V., Fosbury, R. A. E., and Perola, G. C.: 1978, *MNRAS* **183**, 129

Elvis, M., Risaliti, G., Nicastro, F., Miller, J. M., Fiore, F., and Puccetti, S.: 2004, *ApJL* **615**, L25

Esin, A. A., McClintock, J. E., Drake, J. J., Garcia, M. R., Haswell, C. A., Hynes, R. I., and Muno, M. P.: 2001, *ApJ* **555**, 483

Fabian, A. C., Rees, M. J., Stella, L., and White, N. E.: 1989, *MNRAS* **238**, 729

Fabian, A. C., Vaughan, S., Nandra, K., Iwasawa, K., Ballantyne, D. R., Lee, J. C., De Rosa, A., Turner, A., and Young, A. J.: 2002, *MNRAS* **335**, L1

Filippenko, A. V. and Sargent, W. L. W.: 1985, *ApJS* **57**, 503

Fiore, F., Pellegrini, S., Matt, G., Antonelli, L. A., Comastri, A., della Ceca, R., Giallongo, E., Mathur, S., Molendi, S., Siemiginowska, A., Trinchieri, G., and Wilkes, B.: 2001, *ApJ* **556**, 150

Ford, H. C., Harms, R. J., Tsvetanov, Z. I., Hartig, G. F., Dressel, L. L., Kriss, G. A., Bohlin, R. C., Davidsen, A. F., Margon, B., and Kochhar, A. K.: 1994, *ApJL* **435**, L27

Forster, K., Leighly, K. M., and Kay, L. E.: 1999, *ApJ* **523**, 521

Freeman, K. C., Karlsson, B., Lynga, G., Burrell, J. F., van Woerden, H., Goss, W. M., and Mebold, U.: 1977, *A&A* **55**, 445

Frontera, F., Costa, E., dal Fiume, D., Feroci, M., Nicastro, L., Orlandini, M., Palazzi, E., and Zavattini, G.: 1997, *A&AS* **122**, 357

Fruscione, A., Greenhill, L. J., Filippenko, A. V., Moran, J. M., Herrnstein, J. R., and Galle, E.: 2005, *ApJ* **624**, 103

Geant4 Collaboration, Agostinelli, S., Allison, J., Amako, K., Apostolakis, J., Araujo, H., Arce, P., Asai, M., Axen, D., Banerjee, S., Barrand, G., Behner, F., Bellagamba, L., Boudreau, J., Broglia, L., Brunengo, A., Burkhardt, H., Chauvie, S., Chuma, J., Chytracek, R., Cooperman, G., Cosmo, G., Degtyarenko, P., dell'Acqua, A., Depaola, G., Dietrich, D., Enami, R., Feliciello, A., Ferguson, C., Fesefeldt, H., Folger, G., Foppiano, F., Forti, A., Garelli, S., Giani, S., Giannitrapani, R., Gibin, D., Gómez Cadenas, J. J., González, I., Gracia Abril, G., Greeniaus, G., Greiner, W., Grichine, V., Grossheim, A., Guatelli, S., Gumplinger, P., Hamatsu, R., Hashimoto, K., Hasui, H., Heikkinen, A., Howard, A., Ivanchenko, V., Johnson, A., Jones, F. W., Kallenbach, J., Kanaya, N., Kawabata, M., Kawabata, Y., Kawaguti, M., Kelner, S., Kent, P., Kimura, A., Kodama, T., Kokoulin, R., Kossov, M., Kurashige, H., Lamanna, E., Lampén, T., Lara, V., Lefebure, V., Lei, F., Liendl, M., Lockman, W., Longo, F., Magni, S., Maire, M., Medernach, E., Minamimoto, K., Mora de Freitas, P., Morita, Y., Murakami, K., Nagamatu, M., Nartallo, R., Nieminen, P., Nishimura, T., Ohtsubo, K., Okamura, M., O'Neale, S., Oohata, Y., Paech, K., Perl, J., Pfeiffer, A., Pia, M. G., Ranjard, F., Rybin, A., Sadilov, S., di Salvo, E., Santin, G., Sasaki, T., Savvas, N., Sawada, Y., Scherer, S., Sei, S., Sirotenko, V., Smith, D., Starkov, N., Stoecker, H., Sulkimo, J., Takahata, M., Tanaka, S., Tcherniaev, E., Safai Tehrani, E., Tropeano, M., Truscott, P., Uno, H., Urban, L., Urban, P., Verderi, M., Walkden, A., Wander, W., Weber, H., Wellisch, J. P., Wenaus, T., Williams, D. C., Wright, D., Yamada, T., Yoshida, H., and Zschiesche, D.: 2003, *Nuclear Instruments and Methods in Physics Research A* **506**, 250

Gehrels, N., Chincarini, G., Giommi, P., Mason, K. O., Nousek, J. A., Wells, A. A., White, N. E., Barthelmy, S. D., Burrows, D. N., Cominsky, L. R., Hurley, K. C., Marshall, F. E., Mészáros, P., Roming, P. W. A., Angelini, L., Barbier, L. M., Belloni, T., Campana, S., Caraveo, P. A., Chester, M. M., Citterio, O., Cline, T. L., Cropper, M. S., Cummings, J. R., Dean, A. J., Feigelson, E. D., Fenimore, E. E., Frail, D. A., Fruchter, A. S., Garmire, G. P., Gendreau, K., Ghisellini, G., Greiner, J., Hill, J. E., Hunsberger, S. D., Krimm, H. A., Kulkarni, S. R., Kumar, P., Lebrun, F., Lloyd-Ronning, N. M., Markwardt, C. B., Mattson, B. J., Mushotzky, R. F., Norris, J. P., Osborne, J., Paczynski, B., Palmer, D. M., Park, H.-S., Parsons, A. M., Paul, J., Rees, M. J., Reynolds, C. S., Rhoads, J. E., Sasseen, T. P., Schaefer, B. E., Short, A. T., Smale, A. P., Smith, I. A., Stella, L., Tagliaferri, G., Takahashi, T., Tashiro, M., Townsley, L. K., Tueller, J., Turner, M. J. L., Vietri, M., Voges, W., Ward, M. J., Willingale, R., Zerbi, F. M., and Zhang, W. W.: 2004, *ApJ* **611**, 1005

Gehrels, N., Chipman, E., and Kniffen, D. A.: 1993, *A&AS* **97**, 5

Genzel, R., Eckart, A., Ott, T., and Eisenhauer, F.: 1997, *MNRAS* **291**, 219

Genzel, R., Lutz, D., Sturm, E., Egami, E., Kunze, D., Moorwood, A. F. M., Rigopoulou, D., Spoon, H. W. W., Sternberg, A., Tacconi-Garman, L. E., Tacconi, L., and Thatte, N.: 1998, *ApJ* **498**, 579

Genzel, R., Pichon, C., Eckart, A., Gerhard, O. E., and Ott, T.: 2000, *MNRAS* **317**, 348

George, I. M., Nandra, K., Laor, A., Turner, T. J., Fiore, F., Netzer, H., and Mushotzky, R. F.: 1997, *ApJ* **491**, 508

George, I. M., Turner, T. J., Yaqoob, T., Netzer, H., Laor, A., Mushotzky, R. F., Nandra, K., and Takahashi, T.: 2000, *ApJ* **531**, 52

Ghisellini, G., Haardt, F., and Matt, G.: 1994, *MNRAS* **267**, 743

Greenhill, L. J., Booth, R. S., Ellingsen, S. P., Herrnstein, J. R., Jauncey, D. L., McCulloch, P. M., Moran, J. M., Norris, R. P., Reynolds, J. E., and Tzioumis, A. K.: 2003a, *ApJ* **590**, 162

Greenhill, L. J. and Gwinn, C. R.: 1997, *Ap&SS* **248**, 261

Greenhill, L. J., Henkel, C., Becker, R., Wilson, T. L., and Wouterloot, J. G. A.: 1995a, *A&A* **304**, 21

Greenhill, L. J., Jiang, D. R., Moran, J. M., Reid, M. J., Lo, K. Y., and Claussen, M. J.: 1995b, *ApJ* **440**, 619

Greenhill, L. J., Kondratko, P. T., Lovell, J. E. J., Kuiper, T. B. H., Moran, J. M., Jauncey, D. L., and Baines, G. P.: 2003b, *ApJL* **582**, L11

Greenhill, L. J., Moran, J. M., and Herrnstein, J. R.: 1997, *ApJL* **481**, L23+

Greenstein, J. L. and Schmidt, M.: 1964, *ApJ* **140**, 1

Gruber, D. E., Matteson, J. L., Peterson, L. E., and Jung, G. V.: 1999, *ApJ* **520**, 124

Guainazzi, M. and Bianchi, S.: 2007, *MNRAS* **374**, 1290

Guainazzi, M., Matt, G., Antonelli, L. A., Bassani, L., Fabian, A. C., Maiolino, R., Marconi, A., Fiore, F., Iwasawa, K., and Piro, L.: 1999, *MNRAS* **310**, 10

Gursky, H., Giacconi, R., Paolini, F. R., and Rossi, B. B.: 1963, *Physical Review Letters* **11**, 530

Haniff, C. A., Wilson, A. S., and Ward, M. J.: 1988, *ApJ* **334**, 104

Hanson, C. G., Skinner, G. K., Eyles, C. J., and Willmore, A. P.: 1990, *MNRAS* **242**, 262

Heckman, T. M.: 1980, *A&A* **87**, 152

Heckman, T. M., Armus, L., and Miley, G. K.: 1990, *ApJS* **74**, 833

Heiles, C. and Cleary, M. N.: 1979, *Australian Journal of Physics Astrophysical Supplement* **47**, 1

Henkel, C., Peck, A. B., Tarchi, A., Nagar, N. M., Braatz, J. A., Castangia, P., and Moscadelli, L.: 2005, *A&A* **436**, 75

Herrnstein, J. R., Moran, J. M., Greenhill, L. J., Diamond, P. J., Inoue, M., Nakai, N., Miyoshi, M., Henkel, C., and Riess, A.: 1999, *Nature* **400**, 539

Herrnstein, J. R., Moran, J. M., Greenhill, L. J., and Trotter, A. S.: 2005, *ApJ* **629**, 719

Ho, L. C., Filippenko, A. V., and Sargent, W. L. W.: 1997, *ApJS* **112**, 315

Hyman, S. D., Calle, D., Weiler, K. W., Lacey, C. K., Van Dyk, S. D., and Sramek, R.: 2001, *ApJ* **551**, 702

Ichimaru, S.: 1977, *ApJ* **214**, 840

Ikebe, Y., Leighly, K., Tanaka, Y., Nakagawa, T., Terashima, Y., and Komossa, S.: 2000, *MNRAS* **316**, 433

Illarionov, A., Kallman, T., McCray, R., and Ross, R.: 1979, *ApJ* **228**, 279

Ishihara, Y., Nakai, N., Iyomoto, N., Makishima, K., Diamond, P., and Hall, P.: 2001, *PASJ* **53**, 215

Ishisaki, Y., Maeda, Y., Fujimoto, R., Ozaki, M., Ebisawa, K., Takahashi, T., Ueda, Y., Ogasaka, Y., Ptak, A., Mukai, K., Hamaguchi, K., Hirayama, M., Kotani, T., Kubo, H., Shibata, R., Ebara, M., Furuzawa, A., Iizuka, R., Inoue, H., Mori, H., Okada, S., Yokoyama, Y., Matsumoto, H., Nakajima, H., Yamaguchi, H., Anabuki, N., Tawa, N., Nagai, M., Katsuda, S., Hayashida, K., Bamba, A., Miller, E. D., Sato, K., and Yamasaki, N. Y.: 2007, *PASJ* **59**, 113

Isobe, N., Kubota, A., Makishima, K., Gandhi, P., Griffiths, R. E., Dewangan, G. C., Itoh, T., and Mizuno, T.: 2008, *PASJ, accepted.*

Isobe, N., Tashiro, M., Makishima, K., Iyomoto, N., Suzuki, M., Murakami, M. M., Mori, M., and Abe, K.: 2002, *ApJL* **580**, L111

Itoh, T., Done, C., Makishima, K., Madejski, G., Awaki, H., Isobe, N., Gandhi, P., Dewangan, G. C., Griffiths, R. E., Anabuki, N., Okajima, T., Reeves, J., Takahashi, T., Ueda, Y., Eguchi, S., and Yaqoob, T.: 2008, *PASJ, accepted.*

Itoh, T., Niko, H., Kokubun, M., Makishima, K., Kawaharada, M., Takahashi, I., and Miyasaka, H.: 2005, *Nuclear Instruments and Methods in Physics Research A* **541**, 241

Iwasawa, K., Fabian, A. C., Ueno, S., Awaki, H., Fukazawa, Y., Matsushita, K., and Makishima, K.: 1997, *MNRAS* **285**, 683

Iwasawa, K., Koyama, K., Awaki, H., Kunieda, H., Makishima, K., Tsuru, T., Ohashi, T., and Nakai, N.: 1993, *ApJ* **409**, 155

Iwasawa, K., Wilson, A. S., Fabian, A. C., and Young, A. J.: 2003, *MNRAS* **345**, 369

Iwasawa, K., Yaqoob, T., Awaki, H., and Ogasaka, Y.: 1994, *PASJ* **46**, L167

Iyomoto, N. and Makishima, K.: 2001, *MNRAS* **321**, 767

Jansen, F., Lumb, D., Altieri, B., Clavel, J., Ehle, M., Erd, C., Gabriel, C., Guainazzi, M., Gondoin, P., Much, R., Munoz, R., Santos, M., Schartel, N., Texier, D., and Vacanti, G.: 2001, *A&A* **365**, L1

Johnson, W. N., Grove, J. E., Kinzer, R. L., Kroeger, R. A., Kurfess, J. D., Strickman, M. S., McNaron-Brown, K., Grabelsky, D. A., Purcell, W. R., Ulmer, M. P., Jung, G. V., and Cameron, R. A.: 1993, in *Bulletin of the American Astronomical Society*, Vol. 25 of *Bulletin of the American Astronomical Society*, pp 1390–+

Kamae, T., Gunji, S., Hirayama, M., Kubo, H., Miyazaki, S., Saito, Y., Sekimoto, Y., Suzuki, K., Takahashi, T., and Tamura, T.: 1992, in E. Aprile (ed.), *Gamma-ray detectors; Proceedings of the Meeting, San Diego, CA, July 21, 22, 1992 (A93-30101 11-35), p. 2-13.*, Vol. 1734 of *Presented at the Society of Photo-Optical Instrumentation Engineers (SPIE) Conference*, pp 2–13

Kaspi, S., Smith, P. S., Netzer, H., Maoz, D., Jannuzi, B. T., and Giveon, U.: 2000, *ApJ* **533**, 631

Kawaharada, M., Hong, S., Murashima, M. M., Kokubun, M., Itoh, T., Makishima, K., Miyawaki, R., Niko, H., Yanagida, T., Mitani, T., Nakazawa, K., Oonuki, K., Takahashi, T., Tamura, K., Tanaka, T., Terada, Y., Fukazawa, Y., Kawano, N., Kawashima, K., Ohno, M., Yamaoka, K., Abe, K., Suzuki, M., Tashiro, M., Yonetoku, D., and Murakami, T.: 2004, in A. D. Holland (ed.), *High-Energy Detectors in Astronomy. Edited by Holland, Andrew D. Proceedings of the SPIE, Volume 5501, pp. 286-295 (2004).*, Vol. 5501 of *Presented at the Society of Photo-Optical Instrumentation Engineers (SPIE) Conference*, pp 286–295

Kay, L. E.: 1994, *ApJ* **430**, 196

Khachikian, E. Y. and Weedman, D. W.: 1974, *ApJ* **192**, 581

Kinkhabwala, A., Sako, M., Behar, E., Kahn, S. M., Paerels, F., Brinkman, A. C., Kaastra, J. S., Gu, M. F., and Liedahl, D. A.: 2002, *ApJ* **575**, 732

Kirsch, M. G., Briel, U. G., Burrows, D., Campana, S., Cusumano, G., Ebisawa, K., Freyberg, M. J., Guainazzi, M., Haberl, F., Jahoda, K., Kaastra, J., Kretschmar, P., Larsson, S., Lubinski, P., Mori, K., Plucinsky, P., Pollock, A. M., Rothschild, R., Sembay, S., Wilms, J., and Yamamoto, M.: 2005, in O. H. W. Siegmund (ed.), *UV, X-Ray, and Gamma-Ray Space Instrumentation for Astronomy XIV. Edited by Siegmund, Oswald H. W. Proceedings of the SPIE, Volume 5898, pp. 22-33 (2005).*, Vol. 5898 of *Presented at the Society of Photo-Optical Instrumentation Engineers (SPIE) Conference*, pp 22–33

Kitaguchi, T., Kokubun, M., Kawaharada, M., Murashima, M., Miyawaki, R., Yanagida, T., Itoh, T., Hirakuri, S., Enoto, T., Sato, M., Makishima, K., Takahashi, T., Nakazawa, K., Watanabe, S., Tanaka, T., Terada, Y., Tamagawa, T., Kubota, A., Fukazawa, Y., Mizuno, M., Takahashi, H., Yamasaki, T., Tashiro, M., Endo, Y., Yamaoka, K., Murakami, T., Yonetoku, D., and Kamae, T.: 2006, in *Hard X-Ray and Gamma-Ray Detector Physics and Penetrating Radiation Systems VIII. Edited by Franks, Larry A.; Burger, Arnold; James, Ralph B.; Barber, H. Bradford; Doty, F. Patrick; Roehrig, Hans. Proceedings of the SPIE, Volume 6319, pp. 63190U (2006).*, Vol. 6319 of *Presented at the Society of Photo-Optical Instrumentation Engineers (SPIE) Conference*

Kokubun, M., Makishima, K., Takahashi, T., Murakami, T., Tashiro, M., Fukazawa, Y., Kamae, T., Madejski, G. M., Nakazawa, K., Yamaoka, K., Terada, Y., Yonetoku, D., Watanabe, S., Tamagawa, T., Mizuno, T., Kubota, A., Isobe, N., Takahashi, I., Sato, G., Takahashi, H., Hong, S., Kawaharada, M., Kawano, N., Mitani, T., Murashima, M., Suzuki, M., Abe, K., Miyawaki, R., Ohno, M., Tanaka, T., Yanagida, T., Itoh, T., Ohnuki, K., Tamura, K.-I., Endo, Y., Hirakuri, S., Hiruta, T., Kitaguchi, T., Kishishita, T., Sugita, S., Takahashi, T., Takeda, S., Enoto, T., Hirasawa, A., Katsuta, J., Matsumura, S., Onda, K., Sato, M., Ushio, M., Ishikawa, S.-N., Murase, K., Odaka, H., Suzuki, M., Yaji, Y., Yamada, S., Yamasaki, T., Yuasa, T., and The Hxd Team: 2007, *PASJ* **59**, 53

Kondratko, P. T., Greenhill, L. J., Moran, J. M., Lovell, J. E. J., Kuiper, T. B. H., Jauncey, D. L., Cameron, L. B., Gómez, J. F., García-Miró, C., Moll, E., de Gregorio-Monsalvo, I., and Jiménez-Bailón, E.: 2006, *ApJ* **638**, 100

Koratkar, A. and Blaes, O.: 1999, *PASP* **111**, 1

Korista, K. T., Alloin, D., Barr, P., Clavel, J., Cohen, R. D., Crenshaw, D. M., Evans, I. N., Horne, K., Koratkar, A. P., Kriss, G. A., Krolik, J. H., Malkan, M. A., Morris, S. L., Netzer, H., O'Brien, P. T., Peterson, B. M., Reichert, G. A., Rodriguez-Pascual, P. M., Wamsteker, W., Anderson, K. S. J., Axon, D. J., Benitez, E., Berlind, P., Bertram, R., Blackwell, Jr., J. H., Bochkarev, N. G., Boisson, C., Carini, M., Carrillo, R., Carone, T. E., Cheng, F.-Z., Christensen, J. A., Chuvaev, K. K., Dietrich, M., Dokter, J. J.,

Doroshenko, V., Dultzin-Hacyan, D., England, M. N., Espey, B. R., Filippenko, A. V., Gaskell, C. M., Goad, M. R., Ho, L. C., Huchra, J. P., Jiang, X. J., Kaspi, S., Kollatschny, W., Laor, A., Luminet, J.-P., MacAlpine, G. M., MacKenty, J. W., Malkov, Y. F., Maoz, D., Martin, P. G., Matheson, T., McCollum, B., Merkulova, N., Metik, L., Mignoli, M., Miller, H. R., Pastoriza, M. G., Pelat, D., Penfold, J., Perez, M., Perola, G. C., Persaud, J. L., Peters, J., Pitts, R., Pogge, R. W., Pronik, I., Pronik, V. I., Ptak, R. L., Rawley, L., Recondo-Gonzalez, M. C., Rodriguez-Espinosa, J. M., Romanishin, W., Sadun, A. C., Salamanca, I., Santos-Lleo, M., Sekiguchi, K., Sergeev, S. G., Shapovalova, A. I., Shields, J. C., Shrader, C., Shull, J. M., Silbermann, N. A., Sitko, M. L., Skillman, D. R., Smith, H. A., Smith, S. M., Snijders, M. A. J., Sparke, L. S., Stirpe, G. M., Stoner, R. E., Sun, W.-H., Thiele, U., Tokarz, S., Tsvetanov, Z. I., Turnshek, D. A., Veilleux, S., Wagner, R. M., Wagner, S. J., Wanders, I., Wang, T., Welsh, W. F., Weymann, R. J., White, R. J., Wilkes, B. J., Wills, B. J., Winge, C., Wu, H., and Zou, Z. L.: 1995, *ApJS* **97**, 285

Kormendy, J.: 1988, *ApJ* **325**, 128

Kormendy, J. and Richstone, D.: 1995, *ARA&A* **33**, 581

Koyama, K., Inoue, H., Tanaka, Y., Awaki, H., Takano, S., Ohashi, T., and Matsuoka, M.: 1989, *PASJ* **41**, 731

Krongold, Y., Nicastro, F., Brickhouse, N. S., Elvis, M., Liedahl, D. A., and Mathur, S.: 2003, *ApJ* **597**, 832

Kruper, J. S., Canizares, C. R., and Urry, C. M.: 1990, *ApJS* **74**, 347

Kubota, A., Tanaka, Y., Makishima, K., Ueda, Y., Dotani, T., Inoue, H., and Yamaoka, K.: 1998, *PASJ* **50**, 667

Laor, A., Fiore, F., Elvis, M., Wilkes, B. J., and McDowell, J. C.: 1997, *ApJ* **477**, 93

Leighly, K. M.: 1999, *ApJS* **125**, 297

Liu, B. F., Mineshige, S., Meyer, F., Meyer-Hofmeister, E., and Kawaguchi, T.: 2002, *ApJ* **575**, 117

Lumsden, S. L., Heisler, C. A., Bailey, J. A., Hough, J. H., and Young, S.: 2001, *MNRAS* **327**, 459

Lynden-Bell, D.: 1969, *Nature* **223**, 690

Madau, P., Ghisellini, G., and Fabian, A. C.: 1993, *ApJL* **410**, L7

Madejski, G., Done, C., Życki, P. T., and Greenhill, L.: 2006, *ApJ* **636**, 75

Madejski, G., Życki, P., Done, C., Valinia, A., Blanco, P., Rothschild, R., and Turek, B.: 2000, *ApJL* **535**, L87

Magdziarz, P. and Zdziarski, A. A.: 1995, *MNRAS* **273**, 837

Maiolino, R., Alonso-Herrero, A., Anders, S., Quillen, A., Rieke, M. J., Rieke, G. H., and Tacconi-Garman, L. E.: 2000, *ApJ* **531**, 219

Maiolino, R., Krabbe, A., Thatte, N., and Genzel, R.: 1998, *ApJ* **493**, 650

Makishima, K., Fujimoto, R., Ishisaki, Y., Kii, T., Loewenstein, M., Mushotzky, R., Serlemitsos, P., Sonobe, T., Tashiro, M., and Yaqoob, T.: 1994, *PASJ* **46**, L77

Makishima, K., Maejima, Y., Mitsuda, K., Bradt, H. V., Remillard, R. A., Tuohy, I. R., Hoshi, R., and Nakagawa, M.: 1986, *ApJ* **308**, 635

Malizia, A., Bassani, L., Stephen, J. B., Di Cocco, G., Fiore, F., and Dean, A. J.: 2003, *ApJL* **589**, L17

Marconi, A., Risaliti, G., Gilli, R., Hunt, L. K., Maiolino, R., and Salvati, M.: 2004, *MNRAS* **351**, 169

Matt, G.: 2002, *MNRAS* **337**, 147

Matt, G., Brandt, W. N., and Fabian, A. C.: 1996a, *MNRAS* **280**, 823

Matt, G., Fabian, A. C., and Reynolds, C. S.: 1997a, *MNRAS* **289**, 175

Matt, G., Fiore, F., Perola, G. C., Piro, L., Fink, H. H., Grandi, P., Matsuoka, M., Oliva, E., and Salvati, M.: 1996b, *MNRAS* **281**, L69

Matt, G., Guainazzi, M., Frontera, F., Bassani, L., Brandt, W. N., Fabian, A. C., Fiore, F., Haardt, F., Iwasawa, K., Maiolino, R., Malaguti, G., Marconi, A., Matteuzzi, A., Molendi, S., Perola, G. C., Piraino, S., and Piro, L.: 1997b, *A&A* **325**, L13

Matt, G., Guainazzi, M., Maiolino, R., Molendi, S., Perola, G. C., Antonelli, L. A., Bassani, L., Brandt, W. N., Fabian, A. C., Fiore, F., Iwasawa, K., Malaguti, G., Marconi, A., and Poutanen, J.: 1999a, *A&A* **341**, L39

Matt, G., Pompilio, F., and La Franca, F.: 1999b, *New Astronomy* **4**, 191

Mauersberger, R., Henkel, C., Whiteoak, J. B., Chin, Y.-N., and Tieftrunk, A. R.: 1996, *A&A* **309**, 705

Miller, J. S. and Goodrich, R. W.: 1990, *ApJ* **355**, 456

Miller, J. S., Goodrich, R. W., and Mathews, W. G.: 1991, *ApJ* **378**, 47

Mineo, T., Fiore, F., Laor, A., Costantini, E., Brandt, W. N., Comastri, A., Della Ceca, R., Elvis, M., Maccacaro, T., and Molendi, S.: 2000, *A&A* **359**, 471

Miniutti, G., Fabian, A. C., Anabuki, N., Crummy, J., Fukazawa, Y., Gallo, L., Haba, Y., Hayashida, K., Holt, S., Kunieda, H., Larsson, J., Markowitz, A., Matsumoto, C., Ohno, M., Reeves, J. N., Takahashi, T., Tanaka, Y., Terashima, Y., Torii, K., Ueda, Y., Ushio, M., Watanabe, S., Yamauchi, M., and Yaqoob, T.: 2007, *PASJ* **59**, 315

Mitsuda, K., Bautz, M., Inoue, H., Kelley, R. L., Koyama, K., Kunieda, H., Makishima, K., Ogawara, Y., Petre, R., Takahashi, T., Tsunemi, H., White, N. E., Anabuki, N., Angelini, L., Arnaud, K., Awaki, H., Bamba, A., Boyce, K., Brown, G. V., Chan, K.-W., Cottam, J., Dotani, T., Doty, J., Ebisawa, K., Ezoe, Y., Fabian, A. C., Figueroa, E., Fujimoto, R., Fukazawa, Y., Furusho, T., Furuzawa, A., Gendreau, K., Griffiths, R. E., Haba, Y., Hamaguchi, K., Harrus, I., Hasinger, G., Hatsukade, I., Hayashida, K., Henry, P. J., Hiraga, J. S., Holt, S. S., Hornschemeier, A., Hughes, J. P., Hwang, U., Ishida, M., Ishisaki, Y., Isobe, N., Itoh, M., Iyomoto, N., Kahn, S. M., Kamae, T., Katagiri, H., Kataoka, J., Katayama, H., Kawai, N., Kilbourne, C., Kinugasa, K., Kissel, S., Kitamoto, S., Kohama, M., Kohmura, T., Kokubun, M., Kotani, T., Kotoku, J., Kubota, A., Madejski, G. M., Maeda, Y., Makino, F., Markowitz, A., Matsumoto, C., Matsumoto, H., Matsuoka, M., Matsushita, K., McCammon, D., Mihara, T., Misaki, K., Miyata, E., Mizuno, T., Mori, K., Mori, H., Morii, M., Moseley, H., Mukai, K., Murakami, H., Murakami, T., Mushotzky, R., Nagase, F., Namiki, M., Negoro, H., Nakazawa, K., Nousek, J. A., Okajima, T., Ogasaka, Y., Ohashi, T., Oshima, T., Ota, N., Ozaki, M., Ozawa, H., Parmar, A. N., Pence, W. D., Porter, F. S., Reeves, J. N., Ricker, G. R., Sakurai, I., Sanders, W. T., Senda, A., Serlemitsos, P., Shibata, R., Soong, Y., Smith, R., Suzuki, M., Szymkowiak, A. E., Takahashi, H., Tamagawa, T., Tamura, K., Tamura, T., Tanaka, Y., Tashiro, M., Tawara, Y., Terada, Y., Terashima, Y., Tomida, H., Torii, K., Tsuboi, Y., Tsujimoto, M., Tsuru, T. G., Turner, M. J. L. ., Ueda, Y., Ueno, S., Ueno, M., Uno, S.,

Urata, Y., Watanabe, S., Yamamoto, N., Yamaoka, K., Yamasaki, N. Y., Yamashita, K., Yamauchi, M., Yamauchi, S., Yaqoob, T., Yonetoku, D., and Yoshida, A.: 2007, *PASJ* **59**, 1

Mitsuda, K., Inoue, H., Koyama, K., Makishima, K., Matsuoka, M., Ogawara, Y., Suzuki, K., Tanaka, Y., Shibazaki, N., and Hirano, T.: 1984, *PASJ* **36**, 741

Miyaji, T., Hasinger, G., and Schmidt, M.: 2000, *A&A* **353**, 25

Miyoshi, M., Moran, J., Herrnstein, J., Greenhill, L., Nakai, N., Diamond, P., and Inoue, M.: 1995, *Nature* **373**, 127

Moorwood, A. F. M., Lutz, D., Oliva, E., Marconi, A., Netzer, H., Genzel, R., Sturm, E., and de Graauw, T.: 1996a, *A&A* **315**, L109

Moorwood, A. F. M., van der Werf, P. P., Kotilainen, J. K., Marconi, A., and Oliva, E.: 1996b, *A&A* **308**, L1+

Moran, E. C., Barth, A. J., Kay, L. E., and Filippenko, A. V.: 2000, *ApJL* **540**, L73

Moran, E. C., Kay, L. E., Davis, M., Filippenko, A. V., and Barth, A. J.: 2001, *ApJL* **556**, L75

Mushotzky, R. F., Marshall, F. E., Boldt, E. A., Holt, S. S., and Serlemitsos, P. J.: 1980, *ApJ* **235**, 377

Nakai, N.: 1989, *PASJ* **41**, 1107

Nandra, K., George, I. M., Mushotzky, R. F., Turner, T. J., and Yaqoob, T.: 1997, *ApJ* **476**, 70

Nandra, K. and Pounds, K. A.: 1994, *MNRAS* **268**, 405

Narayan, R. and Yi, I.: 1994, *ApJL* **428**, L13

Nelson, C. H.: 2000, *ApJL* **544**, L91

Oliva, E., Marconi, A., Cimatti, A., and Alighieri, S. D. S.: 1998, *A&A* **329**, L21

Oliva, E., Origlia, L., Maiolino, R., and Moorwood, A. F. M.: 1999, *A&A* **350**, 9

Oliva, E., Salvati, M., Moorwood, A. F. M., and Marconi, A.: 1994, *A&A* **288**, 457

O'Neill, P. M., Nandra, K., Papadakis, I. E., and Turner, T. J.: 2005, *MNRAS* **358**, 1405

Ormes, J. F.: 1996, *Current Perspectives in High Energy Astrophysics*, Collected Works, NASA Goddard Space Flight Center Greenbelt, MD United States

Ota, N., Murakami, T., Sugizaki, M., Kaneda, M., Tamura, T., Ozawa, H., Kamae, T., Makishima, K., Takahashi, T., Tashiro, M., Fukazawa, Y., Kataoka, J., Yamaoka, K., Kubo, S., Tanihata, C., Uchiyama, Y., Matsuzaki, K., Iyomoto, N., Kokubun, M., Nakazawa, T., Kubota, A., Mizuno, T., Matsumoto, Y., Isobe, N., Terada, Y., Sugiho, M., Onishi, T., Kubo, H., Ikeda, H., Nomachi, M., Ohsugi, T., Muramatsu, M., and Akahori, H.: 1999, *Nuclear Instruments and Methods in Physics Research A* **436**, 291

Ott, M., Whiteoak, J. B., Henkel, C., and Wielebinski, R.: 2001, *A&A* **372**, 463

Papadakis, I. E.: 2004, *MNRAS* **348**, 207

Paul, J., Ballet, J., Cantin, M., Cordier, B., Goldwurm, A., Lambert, A., Mandrou, P., Chabaud, J. P., Ehanno, M., and Lande, J.: 1991, *Advances in Space Research* **11**, 289

Peng, Z., Gu, Q., Melnick, J., and Zhao, Y.: 2006, *A&A* **453**, 863

Perola, G. C., Matt, G., Cappi, M., Fiore, F., Guainazzi, M., Maraschi, L., Petrucci, P. O., and Piro, L.: 2002, *A&A* **389**, 802

Phillips, M. M. and Malin, D. F.: 1982, *MNRAS* **199**, 905

Pietsch, W. and Read, A. M.: 2002, *A&A* **384**, 793

Pietsch, W., Vogler, A., Kahabka, P., Jain, A., and Klein, U.: 1994, *A&A* **284**, 386

Pinkney, J., Gebhardt, K., Bender, R., Bower, G., Dressler, A., Faber, S. M., Filippenko, A. V., Green, R., Ho, L. C., Kormendy, J., Lauer, T. R., Magorrian, J., Richstone, D., and Tremaine, S.: 2003, *ApJ* **596**, 903

Pogge, R. W. and De Robertis, M. M.: 1993, *ApJ* **404**, 563

Prieto, M. A., Meisenheimer, K., Marco, O., Reunanen, J., Contini, M., Clenet, Y., Davies, R. I., Gratadour, D., Henning, T., Klaas, U., Kotilainen, J., Leinert, C., Lutz, D., Rouan, D., and Thatte, N.: 2004, *ApJ* **614**, 135

Reynolds, C. S.: 1997, *MNRAS* **286**, 513

Reynolds, C. S., Nowak, M. A., and Maloney, P. R.: 2000, *ApJ* **540**, 143

Rice, W., Lonsdale, C. J., Soifer, B. T., Neugebauer, G., Kopan, E. L., Lloyd, L. A., de Jong, T., and Habing, H. J.: 1988, *ApJS* **68**, 91

Risaliti, G.: 2002, *A&A* **386**, 379

Risaliti, G. and Elvis, M.: 2004, in A. J. Barger (ed.), *Supermassive Black Holes in the Distant Universe*, Vol. 308 of *Astrophysics and Space Science Library*, pp 187–+

Risaliti, G., Maiolino, R., and Salvati, M.: 1999, *ApJ* **522**, 157

Sako, M., Kahn, S. M., Paerels, F., and Liedahl, D. A.: 2000a, *ApJL* **543**, L115

Sako, M., Kahn, S. M., Paerels, F., and Liedahl, D. A.: 2000b, *ApJ* **542**, 684

Sambruna, R. M., Brandt, W. N., Chartas, G., Netzer, H., Kaspi, S., Garmire, G. P., Nousek, J. A., and Weaver, K. A.: 2001, *ApJL* **546**, L9

Schmidt, M., Hasinger, G., Gunn, J., Schneider, D., Burg, R., Giacconi, R., Lehmann, I., MacKenty, J., Trumper, J., and Zamorani, G.: 1998, *A&A* **329**, 495

Schurch, N. J., Roberts, T. P., and Warwick, R. S.: 2002, *MNRAS* **335**, 241

Serlemitsos, P. J., Soong, Y., Chan, K.-W., Okajima, T., Lehan, J. P., Maeda, Y., Itoh, K., Mori, H., Iizuka, R., Itoh, A., Inoue, H., Okada, S., Yokoyama, Y., Itoh, Y., Ebara, M., Nakamura, R., Suzuki, K., Ishida, M., Hayakawa, A., Inoue, C., Okuma, S., Kubota, R., Suzuki, M., Osawa, T., Yamashita, K., Kunieda, H., Tawara, Y., Ogasaka, Y., Furuzawa, A., Tamura, K., Shibata, R., Haba, Y., Naitou, M., and Misaki, K.: 2007, *PASJ* **59**, 9

Setti, G. and Woltjer, L.: 1989, *A&A* **224**, L21

Seyfert, C. K.: 1943, *ApJ* **97**, 28

Shakura, N. I. and Syunyaev, R. A.: 1973, *A&A* **24**, 337

Shirai, H., Fukazawa, Y., Sasada, M., Ohno, M., Yonetoku, D., Yokota, S., Fujimoto, R., Murakami, T., Terashima, Y., Awaki, H., Ikeda, S., Ozawa, M., and Tsuru, G.: 2008, *PASJ, accepted.*

Stark, A. A., Gammie, C. F., Wilson, R. W., Bally, J., Linke, R. A., Heiles, C., and Hurwitz, M.: 1992, *ApJS* **79**, 77

Takahashi, T., Abe, K., Endo, M., Endo, Y., Ezoe, Y., Fukazawa, Y., Hamaya, M., Hirakuri, S., Hong, S., Horii, M., Inoue, H., Isobe, N., Itoh, T., Iyomoto, N., Kamae, T., Kasama, D., Kataoka, J., Kato, H., Kawaharada, M., Kawano, N., Kawashima, K., Kawasoe, S., Kishishita, T., Kitaguchi, T., Kobayashi, Y., Kokubun, M., Kotoku, J., Kouda, M., Kubota, A., Kuroda, Y., Madejski, G., Makishima, K., Masukawa, K., Matsumoto, Y., Mitani, T., Miyawaki, R., Mizuno, T., Mori, K., Mori, M., Murashima, M., Murakami, T., Nakazawa, K., Niko, H., Nomachi, M., Okada, Y., Ohno, M., Oonuki, K., Ota, N., Ozawa, H., Sato, G., Shinoda, S., Sugiho, M., Suzuki, M., Taguchi, K., Takahashi, H., Takahashi, I., Takeda, S., Tamura, K.-I., Tamura, T., Tanaka, T., Tanihata, C., Tashiro, M., Terada, Y., Tominaga, S., Uchiyama, Y., Watanabe, S., Yamaoka, K., Yanagida, T., and Yonetoku, D.: 2007, *PASJ* **59**, 35

Takahashi, T., Nomachi, M., Fukazawa, Y., Tashiro, M., Ezawa, H., Hamaya, M., Horii, M., Isobe, N., Iyomoto, N., Kataoka, J., Kamae, T., Kawaguti, G., Kubo, H., Kubo, S., Kubota, A., Kokubun, M., Makishima, K., Matsuzaki, K., Matsumoto, Y., Mizuno, T., Mori, K., Morita, N., Murakami, T., Nakazawa, K., Obayashi, H., Odagi, I., Onishi, T., Ota, N., Ozawa, H., Sato, K., Sugiho, M., Sugizaki, M., Taguchi, K., Tamura, T., Tanaka, Y., Tanihata, C., Terada, Y., Uchiyama, Y., Yamaoka, K., and Yoshida, A.: 1998, in O. H. Siegmund and M. A. Gummin (eds.), *Proc. SPIE Vol. 3445, p. 155-168, EUV, X-Ray, and Gamma-Ray Instrumentation for Astronomy IX, Oswald H. Siegmund; Mark A. Gummin; Eds.*, Vol. 3445 of *Presented at the Society of Photo-Optical Instrumentation Engineers (SPIE) Conference*, pp 155–168

Takano, S. and Koyama, K.: 1991, *PASJ* **43**, 1

Tanaka, Y., Inoue, H., and Holt, S. S.: 1994, *PASJ* **46**, L37

Tanaka, Y., Nandra, K., Fabian, A. C., Inoue, H., Otani, C., Dotani, T., Hayashida, K., Iwasawa, K., Kii, T., Kunieda, H., Makino, F., and Matsuoka, M.: 1995, *Nature* **375**, 659

Tanihata, C., Kataoka, J., Murakami, T., Ota, N., Ozawa, H., Takahashi, T., Tamura, T., Uchiyama, Y., Watanabe, S., Yamaoka, K., Yonetoku, D., Ezoe, Y., Fukazawa, Y., Isobe, N., and Iyomoto, N.: 1999, in O. H. Siegmund and K. A. Flanagan (eds.), *Proc. SPIE Vol. 3765, p. 645-663, EUV, X-Ray, and Gamma-Ray Instrumentation for Astronomy X, Oswald H. Siegmund; Kathryn A. Flanagan; Eds.*, Vol. 3765 of *Presented at the Society of Photo-Optical Instrumentation Engineers (SPIE) Conference*, pp 645–663

Tashiro, M. S., Abe, K., Angelini, L., Barthelmy, S., Gehrels, N., Ishikawa, N., Kaluzienski, L. J., Kawai, N., Kelley, R. L., Kinugasa, K., Kodaira, H., Kohmura, T., Kubota, K., Maeda, Y., Maeno, S., Murakami, H., Murakami, T., Nakagawa, Y. E., Nakazawa, K., Nousek, J., Okuno, S., Onda, K., Reeves, J. N., Ricker, G., Sato, G., Sonoda, E., Suzuki, M., Takahashi, T., Tamagawa, T., Torii, K., Ueda, Y., Urata, Y., Yamaoka, K., Yamauchi, M., Yonetoku, D., Yoshida, A., and Yoshinari, S.: 2007, *PASJ* **59**, 361

Terashima, Y., Iyomoto, N., Ho, L. C., and Ptak, A. F.: 2002, *ApJS* **139**, 1

Tift, W. G. and Cocke, W. J.: 1988, *ApJS* **67**, 1

Tran, H. D.: 1995, *ApJ* **440**, 597

Tran, H. D.: 2001, *ApJL* **554**, L19

Tran, H. D., Miller, J. S., and Kay, L. E.: 1992, *ApJ* **397**, 452

Trotter, A. S., Greenhill, L. J., Moran, J. M., Reid, M. J., Irwin, J. A., and Lo, K.-Y.: 1998, *ApJ* **495**, 740

Tully, R. B.: 1988, *Science* **242**, 310

Turner, J. L. and Ho, P. T. P.: 1994, *ApJ* **421**, 122

Turner, T. J., George, I. M., Nandra, K., and Mushotzky, R. F.: 1997, *ApJ* **488**, 164

Turner, T. J., Urry, C. M., and Mushotzky, R. F.: 1993, *ApJ* **418**, 653

Ueda, Y., Akiyama, M., Ohta, K., and Miyaji, T.: 2003, *ApJ* **598**, 886

Ueda, Y., Eguchi, S., Terashima, Y., Mushotzky, R., Tueller, J., Markwardt, C., Gehrels, N., Hashimoto, Y., and Potter, S.: 2007, *ApJL* **664**, L79

Ueno, S., Koyama, K., Nishida, M., Yamauchi, S., and Ward, M. J.: 1994a, *ApJL* **431**, L1

Ueno, S., Mushotzky, R. F., Koyama, K., Iwasawa, K., Awaki, H., and Hayashi, I.: 1994b, *PASJ* **46**, L71

Vaughan, S. and Fabian, A. C.: 2004, *MNRAS* **348**, 1415

Veilleux, S. and Bland-Hawthorn, J.: 1997, *ApJL* **479**, L105+

Veilleux, S. and Osterbrock, D. E.: 1987, *ApJS* **63**, 295

Veron-Cetty, M.-P. and Veron, P.: 1989, *A Catalogue of quasars and active nuclei*, ESO Scientific Report, Garching: European Southern Observatory (ESO), 1989, 4th ed.

Vignali, C., Brandt, W. N., Schneider, D. P., Anderson, S. F., Fan, X., Gunn, J. E., Kaspi, S., Richards, G. T., and Strauss, M. A.: 2003, *AJ* **125**, 2876

Vignati, P., Molendi, S., Matt, G., Guainazzi, M., Antonelli, L. A., Bassani, L., Brandt, W. N., Fabian, A. C., Iwasawa, K., Maiolino, R., Malaguti, G., Marconi, A., and Perola, G. C.: 1999, *A&A* **349**, L57

Vogler, A. and Pietsch, W.: 1999, *A&A* **352**, 64

Wandel, A., Peterson, B. M., and Malkan, M. A.: 1999, *ApJ* **526**, 579

Wang, J.-M. and Netzer, H.: 2003, *A&A* **398**, 927

Weisskopf, M. C., Wu, K., Tennant, A. F., Swartz, D. A., and Ghosh, K. K.: 2004, *ApJ* **605**, 360

Whiteoak, J. B. and Gardner, F. F.: 1979, *Proceedings of the Astronomical Society of Australia* **3**, 319

Wilkes, B. J., Schmidt, G. D., Smith, P. S., Mathur, S., and McLeod, K. K.: 1995, *ApJL* **455**, L13+

Williams, O. R., Turner, M. J. L., Stewart, G. C., Saxton, R. D., Ohashi, T., Makishima, K., Kii, T., Inoue, H., Makino, F., Hayashida, K., and Koyama, K.: 1992, *ApJ* **389**, 157

Wilson, A. S., Shopbell, P. L., Simpson, C., Storchi-Bergmann, T., Barbosa, F. K. B., and Ward, M. J.: 2000, *AJ* **120**, 1325

Wilson, A. S., Ward, M. J., and Haniff, C. A.: 1988, *ApJ* **334**, 121

Wilson, A. S., Yang, Y., and Cecil, G.: 2001, *ApJ* **560**, 689

Woo, J.-H. and Urry, C. M.: 2002, *ApJ* **579**, 530

Yamaoka, K., Sugita, S., Ohno, M., Takahashi, T., Fukazawa, Y., Terada, Y., Tamagawa, T., Abe, K., Endo, Y., Onda, K., Matsumura, S., Tashiro, M., Soojing, H., Sato, G., Nakazawa, K., Takahashi, T., Miyawaki, R., Enoto, T., Kokubun, M., Makishima, K., and Murakami, T.: 2006, in *Space Telescopes and Instrumentation II: Ultraviolet to Gamma Ray. Edited by Turner, Martin J. L.; Hasinger, Günther. Proceedings of the SPIE, Volume 6266, pp. 626643 (2006).*, Vol. 6266 of *Presented at the Society of Photo-Optical Instrumentation Engineers (SPIE) Conference*

Yang, Y., Li, B., Wilson, A. S., and Reynolds, C. S.: 2007, *ApJ* **660**, 1106

Yaqoob, T.: 1996, in *Bulletin of the American Astronomical Society*, Vol. 28 of *Bulletin of the American Astronomical Society*, pp 1316–+

Young, A. J., Wilson, A. S., and Shopbell, P. L.: 2001, *ApJ* **556**, 6

Zamorani, G., Henry, J. P., Maccacaro, T., Tananbaum, H., Soltan, A., Avni, Y., Liebert, J., Stocke, J., Strittmatter, P. A., Weymann, R. J., Smith, M. G., and Condon, J. J.: 1981, *ApJ* **245**, 357

Zhang, J. S., Henkel, C., Kadler, M., Greenhill, L. J., Nagar, N., Wilson, A. S., and Braatz, J. A.: 2006, *A&A* **450**, 933

List of Tables

3.1 Basic parameters and performance of the *S*uzaku XRT-I. 33
3.2 The characteristics of the *Suzaku* XIS. 37
3.3 The characteristics of the *Suzaku* HXD. 40
3.4 The best-fit parameters and 90% confidence errors for the spectra of the Crab Nebula. 56
3.5 The best-fit parameters and 90% confidence errors of the power-law model determined by the 100-300 keV GSO spectra of the Crab Nebula. 61

4.1 *Suzaku* observation log of active galactic nuclei during the performance verification phase, together with M 81 and NGC 4258 observed by our GO-1 proposal. 73
4.2 The selected sample sources and their properties. 78
4.3 *Suzaku* observation log of the five water maser AGNs. 79

5.1 Best-fit parameters of *Suzaku* spectrum of NGC 4388 over 3.0–50 keV, derived with the final model. 96
5.2 The Best-fit parameters of the *Suzaku* spectrum of Mrk 3 over the 3.0–110 keV range, derived under the BC + lines + scattering model (see text). 108
5.3 The line profiles observed in the 3.0–9.0 keV XIS spectrum of Circinus. 117
5.4 Best-fit continuum parameters of wideband spectrum of Circinus over the 3.0–110 keV range. 121
5.5 Best-fit parameters of the two models (see text) to the Suzaku XIS, HXD-PIN, and HXD-GSO spectrum of NGC 4945. 131
5.6 Best-fit parameters of the *Suzaku* spectrum of NGC 4258 over 3.0–40 keV, derived under the model of absorbed power-law plus a narrow Gaussian line. 140

6.1 The observed properties of individual AGNs. 149

List of Figures

2.1 A classification of AGNs. 7
2.2 Nuclear emission line spectrum of the Seyfert 2 galaxy NGC 1068. 9
2.3 Unified Scheme of all types of AGNs. 10
2.4 The line profile of iron Kα in the X-ray spectrum of MCG-6-30-15. 15
2.5 The radial velocity profile of the stars at the center of a galaxy M 31. 16
2.6 Line-of-sight velocity versus distance along the major axis of NGC 4258, derived with the H_2O maser observation. 18
2.7 Average total spectrum and main components in the X-ray spectrum of a type 1 AGN. 22
2.8 2–100 keV *BeppoSAX* best fit X-ray spectra of two representative Seyfert 2 galaxies. 27

3.1 A schematic drawing of the *Suzaku* satellite and its side-view. 30
3.2 A schematic drawing of the X-Ray Telescope (XRT) mounted on the EOB and a photograph of one XRT module. 32
3.3 The effective area of the *S*uzaku XRT-I. 34
3.4 Locations of the optical axis of each XRT module on the focal plane, determined from the observations of the Crab Nebula. 34
3.5 Image, Point-Spread-Function (PSF), and Encircled-Energy Fraction (EEF) of the XRT modules on the focal plane. 35
3.6 A photograph of one of the four *Suzaku* XIS sensors. 36
3.7 The structure of each CCD chip employed by the *Suzaku* XIS. 37
3.8 Effective areas of a single *Suzaku* XIS-BI and FI sensor, including the telescope (XRT-I) response. 38
3.9 XIS background counting rate normalized both with the effective area and the field of view, presented as a function of energy. 38
3.10 A photograph of the sensor part (HXD-S) of the *Suzaku* Hard X-ray Detector (HXD). 39
3.11 Block diagram of the HXD system. 40
3.12 A schematic view of the HXD-S. 44
3.13 Angular responses of a single Well unit, measured by γ-ray irradiation from radio isotopes placed 280 cm away. 45
3.14 The effective area of HXD-PIN and HXD-GSO, shown as a function of energy. . 45
3.15 Signal flows from a Well unit to a WPU board. 48
3.16 Fast-slow diagram for a single Well unit taken with ^{22}Na irradiation, and PSD selection effect on the GSO spectrum. 49
3.17 An energy spectrum of a single PIN diode, where the events coincident between PIN and GSO were accumulated over half a year. 51
3.18 Comparison between the energy resolutions of the 64 PIN diodes measured on-ground and in-orbit. 52
3.19 Energy vs. pulse height relation of a single PIN diode. 52
3.20 An in-orbit background spectrum of a single PIN diode. 53
3.21 The background spectra summed over the 64 PIN diodes, extracted under various anti-coincidence conditions. 54

3.22 HXD-PIN spectra of the Crab nebula obtained at the XIS-nominal and the HXD-nominal positions. 56
3.23 A typical in-orbit GSO background spectrum of a single Well unit. 58
3.24 GSO energy scale in a single well-counter unit, compared with the calibration points. 59
3.25 Background spectra of scintillators from a single well-counter unit, under various PSD cut conditions. 60
3.26 GSO background spectra processed with various anti-coincidence conditions, summed over 16 well-counter units. 60
3.27 Background-subtracted GSO spectra (summed over the 16 Well units) of the Crab Nebula, taken at the XIS and the HXD nominal pointing positions. 61
3.28 Light curves of the PIN-UD count rate summed over the 16 units, "cleaned" events of PIN plus that of GSO, and geomagnetic cut-off rigidity, taken from an observation of a blank sky field. 63
3.29 Light curves of 9-78 keV PIN NXB folded with T_SAA, accumulated over $\sim$ half a year, and COR which is experienced by *Suzaku* folded in the same way as a function of T_SAA. 65
3.30 Typical light curves of $u(t)$, and $v(t)$ defined by eq. (3.4). 65
3.31 A long-term evolution of averaged GSO NXB spectra during the first half year in orbit. 66
3.32 An example of fake GSO NXB spectra, derived from the background model. . . . 68
3.33 A comparison of in-orbit detector background of the HXD with those of *RXTE* (the PCA and HEXTE) and the *BeppoSAX* PDS. 68
3.34 The hard X-ray spectra of the Crab nebula, obtained with the *Suzaku* HXD-PIN ($<$ 90 keV) and GSO ($>$ 40 keV). 69

4.1 *Suzaku* XIS 2 images of NGC 4388, in energy ranges of 0.3–2 keV and 2–10 keV. 80
4.2 The same as Figure 4.1, but for MKN 3. 80
4.3 The same as Figure 4.1, but for the Circinus galaxy. 80
4.4 The same as Figure 4.1, but for NGC 4945. 81
4.5 The same as Figure 4.1, but for NGC 4258. 81

5.1 Background-inclusive *Suzaku* XIS images of NGC 4388, in the 0.3–3.0 keV and 3-9.0 keV band. 88
5.2 HXD-PIN and HXD-GSO spectra of NGC 4388. 89
5.3 The background-subtracted *Suzaku* spectra of the nucleus of NGC 4388, normalized to those of the Crab nebula. 91
5.4 The broad-band (3.0–50 keV) spectra of NGC 4388, compared with the BC model which was determined by ignoring the 6.0–8.0 keV band. 94
5.5 The same as Figure 5.4, but under the final model. 95
5.6 Confidence (68%, 90%, 99%) contours of the photon index of the primary continuum vs. the absorbing column, and those of the photon index vs. high cutoff energy. 95
5.7 Confidence (68%, 90%, 99%) contours of of the width of Fe I Kα vs. the fraction of the Compton shoulder $f_{\rm CS}$. 97
5.8 A fractional RMS variability of NGC 4388. 98
5.9 Background-subtracted light curves of NGC 4388 taken with *Suzaku* 100
5.10 The same as Figure 5.1, but for Mrk 3, in the 0.3–2.0 keV and 2.0-9.0 keV band. 102
5.11 The same as Figure 5.2, but for Mrk 3. 103
5.12 The same as Figure 5.3, but for Mrk 3. 104
5.13 The same as Figure 5.4, but for Mrk 3. 106
5.14 The same as Figure 5.13, but with the final model. 107
5.15 The same as Figure 5.6, but for Mrk 3. 107
5.16 The same as Figure 5.7, but for Mrk 3. 107
5.17 Background-subtracted light curves of Mrk 3 taken with *Suzaku* 110
5.18 The same as Figure 5.1, but for Circinus, in the 0.3–3.0 keV and 3.0-9.0 keV band. 112
5.19 The same as Figure 5.2, but for Circinus. 113

5.20 The same as Figure 5.3, but for Circinus. 114
5.21 The XIS raw count rate spectra of Circinus on which cold reflection model are superimposed, and the residuals from the fit, with the energy in linear scale. . . . 115
5.22 The same as Figure 5.21, but for the cold reflection plus 11 emission lines and two absorption lines model. 116
5.23 The XIS + HXD spectrum of Circinus in detector raw count rate. 120
5.24 The same as Figure 5.21, but under the wideband modeling incorporating a highly attenuated intrinsic AGN emission. 120
5.25 Background-subtracted light curves of Circinus taken with *Suzaku* XIS, in the energy ranges of 0.2–2, 2–4, 4–6, 6–9, and 6.1–6.6 keV. 122
5.26 Background-subtracted light curves of Circinus taken with *Suzaku* HXD-PIN, in the energy ranges of 12–60, 12–25 and 25–60 keV. 123
5.27 The same as Figure 5.1, but for NGC 4945, in the 0.3–4.5 keV and 4.5-9.0 keV (right) band. 125
5.28 The same as Figure 5.2, but for NGC 4945. 126
5.29 The same as Figure 5.3, but for NGC 4945. 126
5.30 The same as Figure 5.4, but for NGC 4945. 128
5.31 The same as Figure 5.4, but for NGC 4945, under the BC plus thermal plasma model. 129
5.32 The same as Figure 5.4, but for NGC 4945, under the BC plus scattered continuum model. 130
5.33 Background-subtracted light curves of NGC 4945 taken with Suzaku. 133
5.34 Spectra from the "high phase" and "low phase", shown as their ratios to the time averaged spectrum. 134
5.35 Differential $\nu F\nu$ spectrum between the two phases, i.e., high minus low, on which an absorbed power-law model with $\Gamma = 1.6$ is superposed. 134
5.36 The same as Figure 5.1, but for NGC 4258, in the 0.3–2.0 keV and 2-9.0 keV (right) band. 136
5.37 The same as Figure 5.2, but for NGC 4258. 137
5.38 The same as Figure 5.3, but for NGC 4258. 138
5.39 The broad-band (3–40 keV) spectra of NGC 4258, on which models are superposed. 139
5.40 The same as Figure 5.6(left), but for NGC 4258. 139
5.41 Background-subtracted light curves of NGC 4258 taken with *Suzaku* 142
5.42 Spectra from the "high phase", normalized to that of the "low phase". 143
5.43 The same as Figure 5.40, but for the spectra of the high and low phase. 143
5.44 The same as Figure 5.39, but for the spectra of the high and low phase. 144

6.1 A Schematic illustration of the spectral components generally observed in our sample. 148
6.2 A Scatter plot between the bolometric luminosity and absorbing column of our sample AGNs. 150
6.3 Crab ratios of the 5 sources analyzed in this thesis, shown with arbitrary units. . 151
6.4 A scatter plot between the black hole mass and the observed RMS variability $F_{\rm var}^{\rm obs}$. 152
6.5 The reflection fraction $f_{\rm refl}$, plotted against $F_{\rm var}^{\rm obs}$ normalized to time variation $F_{\rm var}^{\rm est}$ predicted by the black hole mass. 153
6.6 Schematic picture of the emission components from an AGN and putative "torus". 155
6.7 An example of spectral calculations showing the effects of scattered-in light (Yaqoob 1996). 156
6.8 Schematic illustrations of the two types of cold-matter distribution inferred in this thesis, and schematic drawings of spectral components observed from the corresponding geometry, shown for compton-thin / thick sources. 157
6.9 Scatter plots of $L_{\rm bol}$ vs $f_{\rm refl}$. 159

Acknowledgments

I am deeply grateful to Prof. Kazuo Makishima for his guidance and support throughout the five years of my graduate course, as well as his careful reading and checking of this thesis. I am also grateful to Prof. M. Kokubun for his continuous training and encouragements during the first four years of my course. I express my special gratitude to Prof. C. Done for her kind guidance, and many helpful ideas and comments on the main theme of this thesis. I also acknowledge Prof. G. Madejski for his ideas and discussions.

I express my acknowledgment to Dr. K. Nakazawa for his support and discussions on this research throughout the last one year. I would like to thank all the former and present members of Makishima group, especially Y. Ezoe, J. Kotoku, I. Takahashi, Y. Okada, H. Takahashi, M. Kawaharada, M. Murashima, R. Miyawaki, T. Yanagida, H. Niko, S. Hirakuri, T. Kitaguchi, T. Enoto, M. Sato, S. Yamada, T. Yuasa, S. Okuyama, T. Ueda, and Y. Uehara for their sharing and assistance of my school life. I owe a great deal to all the scientists and engineers who worked or are working on the development and operation for the *Astro-E/Astro-E2/Suzaku* project.

I give my best gratitude to my wife and son, who shared my life during the hardest period of my research. Their continuous support and understanding have been essential to complete this work.